

NUMERICAL AND EXPERIMENTAL STUDY OF SOIL-ATMOSPHERE EXCHANGE  
PROCESSES ACROSS AN UNDULATING SOIL SURFACE INFLUENCED BY  
THE NEAR-SURFACE ATMOSPHERIC BOUNDARY LAYER

by

Bo Gao

A thesis submitted to the Faculty and the Board of Trustees of the Colorado School of Mines in partial fulfillment of the requirements for the degree of Doctor of Philosophy (Civil and Environmental Engineering).

Golden, Colorado

Date \_\_\_\_\_

Signed: \_\_\_\_\_

Bo Gao

Signed: \_\_\_\_\_

Dr. Kathleen M. Smits

Thesis Advisor

Golden, Colorado

Date \_\_\_\_\_

Signed: \_\_\_\_\_

Dr. Junko Munakata Marr

Professor and Head

Department of Civil and Environmental Engineering

## ABSTRACT

Soil-atmosphere exchange processes are critical to a wide range of applications, such as greenhouse gas release to the atmosphere,  $^{222}\text{Rn}$  transport into buildings, geothermal heat production, global water cycle and land management, which are closely related to the environmental health and protection, climate change, and energy supply. Given the importance, this research aims to investigate soil-atmosphere exchange processes with a special focus on bare-soil evaporation, a process of mass, momentum, and heat transfer between the soil and the atmosphere, by interweaving experimental and numerical approaches. A critical feature of bare soil involves undulating surfaces due to either natural or manual processes. The near-surface boundary layer is significantly influenced by the surface geometry besides of atmospheric conditions. The combined influence of soil undulations and the near-surface boundary layer results in distinct exchange behaviors compared to a hydrodynamically smooth surface. This topic has not been studied systematically due to the lack of appropriate models and high-fidelity datasets.

Therefore, the overarching goal of this research is to advance our understandings of the mass, momentum, and heat transfer between the soil and the atmosphere by including the combined influence of undulating soil surfaces and the corresponding near-surface atmospheric boundary layer to ultimately improve the representation of such processes in hydrological modeling effort. Accordingly, three phases are defined. First, a fundamental study to investigate the undulating-surface evaporation behaviors under a laminar boundary layer was conducted. A fully coupled model describing the mass, momentum, and heat transfer between the soil and the atmosphere was developed and validated through a laboratory experiment using wind tunnel – soil tank system. This model was then used to investigate the influence of atmospheric conditions, soil

properties, and soil surface configurations on evaporation. Results demonstrate that soil undulations affect evaporation by influencing the diffusion in the laminar boundary layer and the capillary flow inside the soil, resulting in a heterogeneous distribution of local evaporative flux along the undulating soil surface. Second, the above model was extended by incorporating turbulence and used to investigate undulating-surface evaporation under turbulent airflow. Hot-wire Anemometry was first employed to measure the velocity profiles above the undulating surface. Results confirmed the presence of recirculation zones in the valleys and the corresponding locally low evaporative flux. Turbulent airflow was found to enhance evaporation and the surface configurations affect local evaporation by influencing the vapor distribution and surface water availability, especially as recirculation zones form. As a joint result of turbulence and undulations, the influence of wind speed on the evaporation was restricted. Third, a reduced model concept was adopted from perspectives of applications, which simplifies the soil-atmosphere exchange via a flux top boundary condition based on Monin-Obukhov similarity theory. The vapor roughness length ( $z_{0v}$ ) and momentum roughness length ( $z_{0m}$ ) are two major parameters in this model characterizing the mass and momentum transfer between the soil surface and the atmosphere. The relationship between  $z_{0v}$  and  $z_{0m}$ , and the subsequent aerodynamic resistance were parameterized through direct measurements of the velocity field above the undulating soil surface. Four laboratory experiments with unique design were conducted and Particle Imaging Velocimetry was employed to collect the velocity field information. Results show that  $z_{0v}$  is roughly smaller than  $z_{0m}$  by 3 to 7 orders of magnitude, owing to the undulating surface and the ratio of  $z_{0v}$  to  $z_{0m}$  are significantly influenced by the surface configuration and wind speed. The newly formulized aerodynamic resistance was then used to evaluate the evaporation rate for laboratory and field experiments, demonstrating the efficacy of the approach.

## TABLE OF CONTENTS

ABSTRACT.....	iii
TABLE OF CONTENTS.....	v
LIST OF FIGURES .....	xi
LIST OF TABLES .....	xviii
ACKNOWLEDGEMENTS .....	xix
CHAPTER 1 INTRODUCTION.....	1
1.1 Motivation and Problems.....	1
1.2 Research Goal and Objectives .....	4
1.3 Methodology.....	5
1.3.1 Laboratory Experiments .....	6
1.3.2 Numerical Modeling and Model Parameterization .....	6
1.4 Research Phases.....	8
1.5 Thesis Outline.....	9
CHAPTER 2 BACKGROUND AND LITERATURE REVIEW .....	11
2.1 Background of Soil Evaporation .....	11
2.1.1 Processes of Mass, Momentum and Heat Transfer .....	11
2.1.2 Evaporation Stages .....	13
2.2 Mathematical Description for Soil Evaporation.....	16
2.2.1 Fully Coupled Model.....	16
2.2.2 Semi-coupled Model .....	18
2.2.3 Penman-Monteith Equation.....	22

2.3	Boundary Layer .....	23
2.3.1	Laminar and Turbulent Flow .....	24
2.3.2	Flow Above a Flat Plate .....	25
2.3.3	Flow Above an Undulating Surface .....	28
2.3.4	Atmospheric Boundary Layer .....	30
2.4	Undulating Soil Surfaces .....	33
2.4.1	Classification of Surface Roughness .....	34
2.4.2	Invalid Flat-surface Assumptions for an Undulating Surface .....	35
2.4.3	Investigation of Roughness Lengths for Momentum, Vapor, and Heat.....	37
2.5	Effect of Airflow on Soil-Atmosphere Interaction.....	40
2.6	Effect of Surface Roughness on Soil-Atmosphere Interaction Under Turbulent Flow .....	42
2.6.1	Micro-scale Surface Roughness .....	42
2.6.2	Regional-scale Surface Topography.....	43
2.6.3	Macro-scale Undulating-surface Evaporation.....	44
2.7	Hypotheses.....	46
CHAPTER 3	EVAPORATION FROM AN UNDULATING SOIL SURFACE UNDER LAMINAR AIRFLOW.....	49
3.1	Abstract.....	49
3.2	Introduction .....	50
3.3	Mathematical Model.....	57
3.3.1	Governing Equations for Free Flow .....	58
3.3.2	Governing Equations for Porous Media Flow.....	59
3.3.3	Coupling Conditions on the Interface.....	62

3.3.4	Boundary Conditions and Initial Conditions .....	64
3.4	Experimental Setup.....	65
3.4.1	Sand Properties .....	65
3.4.2	Experimental Apparatus .....	66
3.4.3	Experimental Procedures.....	68
3.5	Results and Analysis.....	69
3.5.1	Comparison of Numerical and Experimental Results .....	69
3.5.2	Typical Evaporation Rate Curve .....	74
3.5.3	Effects of Atmospheric Conditions .....	77
3.5.4	Effects of Soil Properties.....	80
3.5.5	Effects of Macroscale Roughness .....	82
3.6	Conclusions .....	87
CHAPTER 4	EVAPORATION FROM AN UNDULATING SOIL SURFACE UNDER TURBULENT AIRFLOW .....	90
4.1	Abstract.....	90
4.2	Introduction .....	91
4.3	Extension of Coupled Free Flow and Porous Media Flow Model .....	95
4.4	Experimental Setup and Results.....	101
4.4.1	Experimental Apparatus .....	102
4.4.2	Experimental Procedures.....	103
4.4.3	Experimental Results and Model Verification .....	106
4.5	Numerical Analysis of Evaporation from Undulating Surfaces .....	109
4.5.1	Laminar and Turbulent Flow Conditions .....	110
4.5.2	Influence of Wind Speed.....	112

4.5.3	Influence of Aspect Ratio .....	115
4.5.4	Influence of Permeability .....	117
4.5.5	Influence of Size of Sand .....	117
4.6	Conclusions .....	118
CHAPTER 5	DETERMINATION OF VAPOR AND MOMENTUM ROUGHNESS LENGTHS ABOVE AN UNDULATING SOIL SURFACE BASED ON PIV-MEASURED TURBULENT VELOCITY PROFILES .....	122
5.1	Abstract.....	122
5.2	Introduction .....	123
5.3	Formulation Theory .....	128
5.4	Experimental Setup.....	131
5.4.1	Experimental Facility and Materials .....	132
5.4.2	Experimental Cases .....	136
5.4.3	Experimental Procedures.....	136
5.5	Determination of Vapor and Momentum Roughness Lengths.....	138
5.5.1	Estimation of Turbulent Flow Parameters.....	138
5.5.2	Determination of the Derived Coefficients in $\ln(z_{0v}/z_{0m})$ .....	139
5.5.3	Results and Analysis.....	141
5.6	Calculation of Aerodynamic Resistance and Evaporative Flux .....	147
5.6.1	Aerodynamic Resistance .....	148
5.6.2	Evaporative Flux for Laboratory Experiments.....	148
5.6.3	Evaporative Flux for a Field Experiment .....	151
5.7	Conclusions .....	153
CHAPTER 6	CONCLUSIONS AND RECOMMENDATIONS .....	156

6.1	Summary.....	156
6.2	Major Conclusions.....	158
6.3	Recommendations for Future Research.....	162
APPENDIX A EQUATIONS USED IN CHAPTER 3 AND CHAPTER 4.....		165
A.1	Van Genuchten Model.....	165
A.2	Millington and Quirk Model.....	165
APPENDIX B APPENDIX OF CHAPTER 4 .....		167
B.1	Power-Law Turbulent Boundary Layer and Blasius Laminar Boundary Layer.....	167
B.2	Figure of Blue Dye Deposition at Sand Surface.....	168
APPENDIX C APPENDIX OF CHAPTER 5 .....		169
C.1	Mathematical Description of the Undulating Soil Surface.....	169
C.2	Figures of the Determined Turbulent Flow Parameters .....	169
C.3	Figures of the Fitted $Da_0^{-1}$ and $Cd_0^{-1/2}$ with $\ln(Re_0)$ .....	172
APPENDIX D SAND MATERIAL.....		174
D.1	Sand Properties .....	174
APPENDIX E MEASUREMENT EQUIPMENT AND TECHNIQUES .....		175
E.1	Soil Moisture Measurements .....	175
E.2	Soil Temperature Measurements .....	176
E.3	Atmospheric Relative Humidity and Temperature Measurements .....	177
E.3.1	VP-4.....	177
E.3.2	SHT35-DIS-F .....	178
E.4	Soil Surface Relative Humidity and Temperature Measurements .....	179
E.4.1	EHT .....	179

E.4.2	AKCP-sensorProbe8 and Sensors .....	179
E.5	Wind Velocity Field Measurements .....	180
E.5.1	Pitot Static Tube .....	180
E.5.2	Hot-wire Anemometry.....	181
E.5.3	Particle Image Velocimetry .....	182
APPENDIX F	SUPPLEMENTAL ELECTRONIC FILES: EXPERIMENTAL AND MODELING OUTPUT DATA .....	184
APPENDIX G	SUPPLEMENTAL ELECTRONIC FILES: COPYRIGHT PERMISSION DOCUMENTS .....	185
REFERENCES	.....	186

## LIST OF FIGURES

Figure 2.1	Schematic of soil-atmosphere interactions in the interfacial area. The interfacial area includes shallow subsurface, near-surface atmosphere, and the interface (i.e. soil surface). .....	12
Figure 2.2	Schematic of the evaporation stages, including Stage I, Transition, and Stage II. Dark blue, light blue, and white color represent the saturated, unsaturated, and dry soil zones, respectively. The red line denotes the location of the vaporization plane, which is defined as the top surface of the unsaturated zone. ....	15
Figure 2.3	Two-dimensional configuration (subdomains and boundary conditions) where $C_v$ is the water vapor concentration; $T$ is temperature; $u$ is wind speed; $J$ is flux for $T$ , $u$ , and $C_v$ ; $\lambda$ is wave length; and $\gamma$ is half of the wave amplitude. ....	18
Figure 2.4	The schematic of boundary layer evolution above a flat plate (Mosthaf et al., 2014). (a) From the leading edge, a constant speed profile at low Reynolds number forms laminar boundary layer. As $x$ extends, the laminar boundary layer thickness becomes thicker and transforms to turbulent boundary layer after transition. The turbulent boundary layer is mainly composed of three sublayers: viscous sublayer, turbulent flow layer, and the upper mainstream. $\delta_{99,\text{laminar}}$ and $\delta_{99,\text{turbulent}}$ are the thickness of the laminar and turbulent boundary layer, respectively. (b) and (c) show the boundary layer for wind speed ( $v$ ), vapor concentration ( $C_v$ ), and temperature ( $T$ ); and the corresponding thickness for wind speed ( $\delta_v$ ), vapor concentration ( $\delta_C$ ), and temperature ( $\delta_T$ ) in laminar and viscous sublayer. ....	26
Figure 2.5	Schematic of atmospheric boundary layer (ABL) in meteorology. There are several types of soil surface (e.g., flat surface, rough surface with hills and buildings, rough surface with vegetation). From the surface upwards, ABL mainly consists of interfacial sublayer, inner region, and outer region. The dynamic sublayer is the lowest sublayer of the inner region where universal logarithmic law is valid. There may be some overlaps between these sublayers, which are not showed in this figure. ....	30
Figure 2.6	Schematic of the normalized vapor density (i.e. vapor concentration) profile in the interfacial sublayer and inner region in single logarithmic coordinate. Dynamic sublayer is the lowest part of the inner region where universal logarithmic profiles are valid. $z$ is the vertical position, $d_0$ (m) is the zero-plane displacement, $z_{0v}$ (m) is the vapor roughness length, $\rho_{v,s}$ and $\rho_{v,\text{ref}}$ ( $\text{kg}/\text{m}^3$ ) are the vapor density at surface and the reference plane, respectively; $E$ ( $\text{kg}\cdot\text{m}^{-2}\cdot\text{s}^{-1}$ ) is the evaporative flux. ....	32

Figure 3.1	Two-dimensional configuration (subdomains and boundary conditions) where $C_v$ is the water vapor concentration, $T$ is the temperature, $u$ is the wind speed, $J$ is the flux for $T$ , $u$ and $C_v$ , $\lambda$ is the wave length, and $\gamma$ is half of the wave amplitude.....	57
Figure 3.2	Schematic of the experimental system. ....	67
Figure 3.3	Comparison of the simulated and observed cumulative evaporation over time (rhombus marks: the observed data from experiment; dash line: the simulated results).....	70
Figure 3.4	(a) Comparison of subsurface moisture evolution with time (rhombus marks in a = the observed data from experiment; dash line = simulated results by modeling) and (b) moisture profile at $x = 10$ cm.....	71
Figure 3.5	Schematic of the distribution and location of the moisture sensors. ....	72
Figure 3.6	(a) Evolution of soil moisture with time in the experiment at four points located 5 cm below the wavy surface. The corresponding marks of these four points are #1, #6, #14, and #18 shown in Figure 3.5. The horizontal location of these four points are $x = 10, 20, 40,$ and $50$ cm, respectively. (b) Evolution of soil moisture with time at two points, #2 and #10 (Figure 3.5), which are located along the same horizontal line. The horizontal location of these two points are $x = 10$ and $30$ cm, respectively. Points #2 and #10 are 10 and 2.5 cm below the wavy surface, respectively.....	73
Figure 3.7	The experimental moisture distribution along one horizontal line where the sensors #2, #6, #10, #14, and #19 are located at $t = 1, 10,$ and $11$ days. The horizontal location of these five sensors are $x = 10, 20, 30, 40,$ and $50$ cm, respectively. Sensors #2 and #19 are 10 cm below the wavy surface; sensors #6 and #14 are 5 cm below the wavy surface; and sensor #10 is 2.5 cm below the wavy surface.....	74
Figure 3.8	Typical evaporation rate curve by coupling model.....	75
Figure 3.9	(a) Impact of air flow velocity (wind speed) on evaporation rate ( $C_{v,inlet} = 0.006 \text{ kg/m}^3$ , $T_{inlet} = 293.15 \text{ K}$ , $K = 1\text{E-}10 \text{ m}^2$ , $\phi = 0.312$ , $\alpha = 8$ , $n = 5$ , $\text{AR} = 1/6$ ). (b) Effect of ambient vapor concentration on evaporation rate ( $u_{g,inlet} = 0.10 \text{ m/s}$ , $T_{inlet} = 293.15 \text{ K}$ , $K = 1\text{E-}10 \text{ m}^2$ , $\phi = 0.312$ , $\alpha = 8$ , $n = 5$ , $\text{AR} = 1/6$ ). .....	78
Figure 3.10	Water saturation distribution at the surface during stage I ( $t = 1$ day) under different air flow velocities ( $C_{v,inlet} = 0.006 \text{ kg/m}^3$ , $T_{inlet} = 293.15 \text{ K}$ , $K = 1\text{E-}10 \text{ m}^2$ , $\phi = 0.312$ , $\alpha = 8$ , $n = 5$ , $\text{AR} = 1/6$ ). ....	79
Figure 3.11	(a) Effect of intrinsic permeability on evaporation rate ( $u_{g,inlet} = 0.10 \text{ m/s}$ , $C_{v,inlet} = 0.006 \text{ kg/m}^3$ , $T_{inlet} = 293.15 \text{ K}$ , $\phi = 0.312$ , $\alpha = 8$ , $n = 5$ , $\text{AR} = 1/6$ ). (b) Effect of van Genuchten parameter $n$ on evaporation rate ( $u_{g,inlet} = 0.10$	

	$m/s, C_{v,inlet} = 0.006 \text{ kg/m}^3, T_{inlet} = 293.15 \text{ K}, K = 1E-10 \text{ m}^2, \phi = 0.312, \alpha = 8, AR = 1/6$ ).....	81
Figure 3.12	(a) Effect of wave numbers on evaporation rate ( $u_{g,inlet} = 0.10 \text{ m/s}, C_{v,inlet} = 0.006 \text{ kg/m}^3, T_{inlet} = 293.15 \text{ K}, K = 1E-10 \text{ m}^2, \phi = 0.312, \alpha = 8, n = 5$ ). (b) Effect of aspect ratio (AR) on evaporation rate ( $u_{g,inlet} = 0.10 \text{ m/s}, C_{v,inlet} = 0.006 \text{ kg/m}^3, T_{inlet} = 293.15 \text{ K}, K = 1E-10 \text{ m}^2, \phi = 0.312, \alpha = 8, n = 5, 3$ waves).....	85
Figure 3.13	Distribution of vapor concentration ( $\text{kg/m}^3$ ) in the free-flow region and saturation in the porous media ( $AR = 1/4$ , the arrows show the gas flow direction and the arrow size is proportional to the gas velocity. Separate scales of the arrows are used in free-flow region and porous media). .....	85
Figure 3.14	(a) Vapor concentration along soil surface with AR of 1/6 and 1/4 at $t = 20$ and 70 days. (b) Normal vapor concentration gradient along soil surface with AR of 1/6 and 1/4 at $t = 20$ and 70 days. AR = aspect ratio.....	86
Figure 3.15	Diffusive flux along soil surface with three waves at $t = 20, 30, 60, 80, 110,$ and 160 days; $AR = 1/6$ .....	87
Figure 4.1	Two-dimensional configuration of subdomains and boundary conditions where $C_v$ is vapor concentration; $T$ is temperature; $U$ is mean wind speed; $J$ is flux for $T$ , total mass, and $C_v$ ; $\lambda$ is wavelength and $\gamma$ is wave amplitude. RANS is Reynolds-averaged Navier-Stokes.....	96
Figure 4.2	Schematic of experimental setup.....	102
Figure 4.3	Schematic of the coordinate system above the soil surface. The red dashed lines are the test columns.....	105
Figure 4.4	Measured dimensionless speed profile at 108 mm upstream of the soil tank. Power-law turbulent and Blasius laminar boundary layer solutions are compared by fitting the measured profile. $u$ (m/s) is the measured wind speed at different locations; $U$ (m/s) is the maximum wind speed in the mainstream, i.e. 6 m/s in this experiment; $\delta^*$ (m) is the displacement thickness. ....	106
Figure 4.5	Observed (a) and simulated (b) wind speed profiles. The dashed line represents the surface. The length of each arrow is proportional to the flow speed.....	107
Figure 4.6	Interpolated speed contours (m/s) using the measured speed profiles in Figure 4.5 (a). S1, S2, S3, and S4 represent the four wavy surfaces, respectively.....	108
Figure 4.7	(a) Comparison of observed and modeled evaporation amount; (b) Comparison of observed and modeled soil moisture at the first-layer	

	moisture sensor ( $x = 10$ cm, $y = -6.5$ cm based on the coordinate system showed in Figure 4.3).....	109
Figure 4.8	Effect of airflow state, comparison of Cases A and B: modeled evolution of the evaporation rate. ....	111
Figure 4.9	Effect of wind speed - comparison of cases A, C, D: (a) evaporation rate; (b) upward diffusive flux along undulating surface at $t = 3, 30$ days; (c) soil surface water saturation at selected peak and valley over time and zoom-in saturation at 0-5 days; (d) vapor concentration ( $C_v$ ) at soil surface at $t = 3$ days. Vapor accumulates especially at the separation points, resulting in low diffusive flux (b).....	114
Figure 4.10	Effect of AR - comparison of case A and E: (a) evaporation rate; (b) water saturation at soil surface at $t = 3, 30$ days; (c) upward and (d) horizontal diffusive flux along surface at $t = 3, 30$ days. ....	116
Figure 4.11	Vapor concentration ( $\text{g/m}^3$ ) in the free flow and water saturation in the porous media at $t = 3$ days.....	116
Figure 4.12	Effect of permeability - comparison of case A and G: (a) evaporation rate; (b) upward diffusive flux along surface at $t = 3, 30$ days.....	117
Figure 4.13	Effect of size of sand represented by $\alpha, n$ - comparison of case E and F: (a) evaporation rate; (b) upward diffusive flux along surface at $t = 3, 30$ days.....	118
Figure 5.1	(a) Schematic of the velocity profile as wind over soil undulations. $u$ is the velocity; $z_{\text{ref}}$ is the reference plane; $d_0$ is the zero-plane displacement height; $z_{0m}$ is the momentum roughness length; $h$ is the thickness of the interfacial sublayer. (b) Schematic of the dimensionless velocity and vapor density profiles in a single-logarithmic coordinate system. The $x$ -axis for velocity and vapor density is $u/U$ and $(\rho_{\text{sat}} - \rho_a)/E$ , respectively. $U$ is the average mainstream velocity; $\rho_{\text{sat}}$ and $\rho_a$ are the saturated vapor density at the soil surface and the reference plane, respectively; $E$ is the evaporative flux; $z_{0v}$ is the vapor roughness length.....	126
Figure 5.2	Schematic of the wind tunnel – soil tank system and various sensors used in the experiments. Weight scale is not included. No.4 is a sinusoidal outlined wavy plate glued on the tank surface. The dimension and arrangement of the six wavy plates are shown in Figure 5.4. No.5 represents soil undulations packed between two wavy plates. No. 7 is an example of one undulation extension shell with 15 cm long, which is attached with one wavy plate to precisely extend each undulation laterally. Sensor wires in soil undulations and at soil surface are placed inside the extensions and extended below the false floor through a hole on the floor (No. 8). The same undulation extensions and holes are set up for all the six wavy plates. ....	134

Figure 5.3	Schematic of the layout and size of the turbulent tripping device. The distance between two blocks was 1.2 cm. The tripping device was placed 50 cm away from the nearest soil undulation.....	135
Figure 5.4	Schematic of the coordinate system above the false floor. A mathematical description of the surface is in the Appendix 0. The $x$ -coordinate is set at the false floor, separating the soil surface and the free flow. The sinusoidal curve is the undulating soil surface. The middle dashed curve is not present for #2 undulations. PIV measurements were conducted in the free flow within $x = -0.05 \sim 0.65$ m, and $z = 0 \sim 0.25$ m. ....	138
Figure 5.5	An example of the data filter and fitting based on the logarithmic law at the profile $x = 0.402$ m. ....	139
Figure 5.6	Comparison of observed and fitted $Da_0^{-1}$ and $Cd_0^{-1/2}$ with $Re_0$ in double logarithm (a) and in single logarithm (b), respectively. This is an example from case #3U3. ....	141
Figure 5.7	Distribution of $\ln(z_{0v} / z_{0m})$ along the undulating surface for (a) #3 undulations; (b) #2 undulations. The red dashed line represents $z_{0v} = z_{0m}$ . Above the line: $z_{0v} > z_{0m}$ ; below the line: $z_{0v} < z_{0m}$ . The gray solid line with the right vertical coordinate is the undulating surface. ....	143
Figure 5.8	PIV-measured velocity field above undulating surfaces for case #3U3 in (a) and #2U3 in (b). Additional figures for all the experiments obtained by PIV measurement are in the Supplement.....	143
Figure 5.9	Selected dimensionless horizontal velocity profiles obtained by PIV: (a) #3U3; (b) #2U3. For each profile, the velocity $u(z)$ is normalized by the maximum $u$ in this profile; the corresponding vertical position $z$ is normalized by the undulation height. The dashed line in each profile represents the coordinate $u = 0$ . The black curve represents the undulating surface. ....	144
Figure 5.10	Observed relative humidity at 5 mm above surface (solid line) and in the mainstream (dashed line) for the four cases: (a) #3U3, (b) #2U3, (c) #3U1, and (d) #2U1. The gray curve with the right vertical coordinate is the undulating soil surface.....	146
Figure 5.11	Measured Reynolds stress by PIV for case (a) #3U1 and (b) #3U3.....	147
Figure 5.12	Comparison of the aerodynamic resistance calculated by experimental data, and the new formula in this paper for: (a) #3U3 and (b) #2U3. The gray curve with the right vertical coordinate is the undulating soil surface.....	148

Figure 5.13	Observed versus simulated evaporation rates based on the laboratory experiments, the aerodynamic resistance formulization method in this paper, and the assumption of $z_{0v} = z_{0m}$ .	150
Figure 5.14	Comparison of the daily evaporation rate by observation from Sep. 23 <sup>rd</sup> to Sep. 29 <sup>th</sup> , 2019, the calculation based on the newly formulized $r_a$ in this study, and the calculation based on the assumption of $z_{0v} = z_{0m}$ .	153
Figure B.1	The cosine curve represents the undulating soil surface in the experiment. Pictures a-d are screenshots of sand surface at four slopes during evaporation in the experiment: (a, c) leeward surfaces, and (b, d) windward surfaces. The blue area is caused by blue dye deposition. More deposition means more evaporation. Picture (e) is the whole photo of the sand surface.	168
Figure C.1	Distribution of the determined turbulent flow parameters for case #3U3: (a) friction velocity $u_*$ , (b) zero-plane displacement $d_0$ , (c) momentum roughness length $z_{0m}$ .	170
Figure C.2	Distribution of the determined turbulent flow parameters for case #3U1: (a) friction velocity $u_*$ , (b) zero-plane displacement $d_0$ , (c) momentum roughness length $z_{0m}$ .	170
Figure C.3	Distribution of the determined turbulent flow parameters for case #2U3: (a) friction velocity $u_*$ , (b) zero-plane displacement $d_0$ , (c) momentum roughness length $z_{0m}$ .	171
Figure C.4	Distribution of the determined turbulent flow parameters for case #2U1: (a) friction velocity $u_*$ , (b) zero-plane displacement $d_0$ , (c) momentum roughness length $z_{0m}$ .	171
Figure C.5	Case #3U1: (a) comparison of observed and fitted $Da_0^{-1}$ with $Re_0$ in double logarithm; (b) comparison of observed and fitted $Cd_0^{-1/2}$ with $\ln(Re_0)$ .	172
Figure C.6	Case #2U3: (a) comparison of observed and fitted $Da_0^{-1}$ with $Re_0$ in double logarithm; (b) comparison of observed and fitted $Cd_0^{-1/2}$ with $\ln(Re_0)$ .	172
Figure C.7	Case #2U1: (a) comparison of observed and fitted $Da_0^{-1}$ with $Re_0$ in double logarithm; (b) comparison of observed and fitted $Cd_0^{-1/2}$ with $\ln(Re_0)$ .	173
Figure E.1	(a) EC-5 sensor; (b) Em50 data logger.	175
Figure E.2	ECT sensor and Em50 data logger.	176
Figure E.3	VP-4 sensor.	177

Figure E.4	SHT3x-DIS sensor. ....	178
Figure E.5	EHT sensor. ....	179
Figure E.6	AKCP single port temperature and humidity sensor. ....	180
Figure E.7	AKCP sensorProbe8. ....	180
Figure E.8	PIV system. Left figure includes a camera and laser installed on two traverses, respectively. Right figure includes a smoking machine (ViCount Compact 1300). ....	183

## LIST OF TABLES

Table 3.1	List of model equations and the primary variables .....	64
Table 3.2	Important porous media properties .....	66
Table 3.3	Average atmospheric experimental data .....	69
Table 4.1	List of model equations and primary variables .....	101
Table 4.2	Modeling scenarios and corresponding variables of interest. Case A is regarded as the reference case .....	110
Table 5.1	A summary of the sensors used in this study .....	133
Table 5.2	All experiment cases conducted in this study .....	136
Table 5.3	Modeled and observed evaporation rate for experimental cases.....	140
Table 5.4	A summary of the derived coefficients in aerodynamic resistance.....	141
Table D.1	Main properties of sand.....	174

## ACKNOWLEDGEMENTS

First of all, I wish to express my deepest gratitude to my advisor, Dr. Kathleen Smits for her continuous support, guidance and encouragement to my Ph.D. study. She does not only assist me with my research, she also offers me invaluable advice for my personal development. I would also like to thank my thesis committee, Dr. Hossein Davarzani, Dr. Reza Hedayat, Dr. Nils Tilton, and Dr. Luis E. Zerpa for all their time and inspiration.

I would like to express my appreciation to Dr. Rainer Helmig and his wonderful research group. Dr. Helmig provided me with insightful ideas and comments for my research and paper. Thomas Fetzer helped me a lot for modeling code and concept. Edward Coltman and I worked together on the experimental project at the University of Colorado Boulder and gave me helpful comments for my paper. I would also like to appreciate the great assistance and guidance from Dr. John Farnsworth and his excellent team members, Jamison Bunnell, Dasha Gloutak, Caleb Grady, Matthew Knickerbocker, Hunter Ringenberg, Samantha Sheppard, Daniel Sinner, and Joseph Straccia for experimental setup and operation.

I gratefully acknowledge the funding support from the National Science Foundation (project award 1447533) and the Deutsche Forschungsgemeinschaft (DFG, HE 2531/14-1) to my Ph.D. program. I am also grateful to the Edna Bailey Sussman Foundation Internship for my experimental project, the Colorado School of Mines Graduate Student Government Travel Grants for my conference attendance and presentations, and the Continuance Grant to finish my thesis.

A whole-hearted thanks to all of my colleagues and friends, Younki Cho, Logan F. Forsythe, Zhen Li, Melissa Mitton, Rosalie O'Brien, Michelle Schwartz, Shanru Tian, Jose R. Velasquez. Thank you all for your assistance in the laboratory and with my course work. Your

help and encouragement support me to keep working hard.

Also, I would like to thank the International office and the office of Civil and Environmental Engineering Department at Colorado School of Mines, and the office of Civil Engineering Department at the University of Texas at Arlington for their help with my relocation from Colorado to Texas.

Finally, a special and heartfelt goes to my mother. I cannot express my gratitude enough for her never-ending support and love.

## CHAPTER 1

### INTRODUCTION

This chapter first provides a general introduction of the motivation and problems in this dissertational research, which is followed by the goal and objectives. Section 1.3 introduces the main methodology employed in this research. The research phases and the corresponding thesis outline are summarized in section 1.4 and 1.5, respectively.

#### **1.1 Motivation and Problems**

The mass, momentum, and heat transfer between a porous medium and an adjacent free flow region across a permeable interface has broad engineering and scientific applications, to name a few but not limited to, food cooking and safety (Halder et al., 2011), cosmetics development (Wilcox et al., 2003; Souto & Müller, 2008), medical care (Erbertseder et al., 2012), fuel cell design (Sundmacher & Scott, 1999; Yuan et al., 2001), underground energy development (Moradi et al., 2015; Huang et al., 2016), leakage of CO<sub>2</sub> and natural gas (Altevogt & Celia, 2004; Oldenburg & Unger, 2004), soil contaminant vapor transport to the atmosphere (Tillman & Weaver, 2005; Yates, 2006; Binning et al., 2007; Petri et al., 2015), etc. In all of these applications, soil-atmosphere exchange is an important component. Even though decades of research in the above fields have been conducted and improved our understanding of the porous media – free flow interaction, some knowledge gaps still exist in the current science on soil-atmosphere exchange processes.

First, from the perspective of fundamental mechanisms, current mathematical models do not accurately account for the complex coupled exchange physics. There involves fluid flow in an unsaturated zone and a clear free flow region, multicomponent transport, phase change, heat

transfer, as well as other (bio-)chemical and physical processes. Note that because of the distinct nature of the porous media and the free flow region, the flow and transport behaviors in the soil and the atmosphere are different. The physical processes inside the soil are influenced by soil properties, such as hydraulic conductivity, porosity, soil-water retention, thermal conductivity and diffusivity, heterogeneity, etc. Especially, soil surface roughness is a crucial factor. In practice, the soil surface is not hydrodynamically smooth but rather composed of roughness from grain scale on millimeters up to hill scale on meters. Especially, the macro-scale undulations at soil surface, usually on several to tens of centimeters, are more common in nature. These undulations may form due to natural processes (e.g., soil erosion, alluvial riverbed) or mechanical manipulation (e.g., agricultural furrow). In agricultural practices, for instance, soil undulations are quite common since tillage changes the soil surface topology. Tillage depth, surface relief, and soil type can influence the evaporation characteristics of the tilled soils (Mwendera & Feyen, 1997). Several studies show that soil undulations affect water infiltration, water storage in surface depressions, and water runoff (Lehrsch et al., 1987; Guzha, 2004). Studies relevant to energy transfer close to soil surface show that the undulating surfaces can alter the absorption and reflectance of sunlight from cultivated soils, which in turn has an important impact on the surface energy balance and the available energy for evaporation (Matthias et al., 2000). Moreover, undulating surfaces resulted from tillage or erosion may change the textures and properties of top soil layers, such as moisture, hydraulic conductivity and porosity, etc. Besides of agricultural practices, the natural bog surface is another representative surface with macro-scale ridges and hummocks. 10 to 20 % of the land in Canada, Russia, and Scandinavia are covered by such kind of surfaces, which plays a significant role in controlling the regional climate. The exchange process between the soil and the atmosphere affect the temperature and soil wetness at these places. This, in turn, influences the conditions for

biological or chemical processes and thus important to the motion and balance of soil carbon (Kellner, 2001; Isabelle et al., 2015). Alternatively, the processes in the atmosphere are affected by the atmospheric conditions, such as wind speed, humidity, temperature, etc. In the atmosphere, the wind may create laminar flow, transition state, and turbulent flow. The wind flow states will affect the flow and transport inside the soil through the permeable soil surface (Clements & Wilkening, 1974; Riley et al., 1999; Poulsen & Møldrup, 2006; Nachshon et al., 2012; Poulsen et al., 2017). In turn, the water vapor formed during evaporation diffuses to the atmosphere may also influence the formation of the atmospheric boundary layer (Pan & Mahrt, 1987). As a consequence of all of these physics mentioned above, an advanced understanding of the soil-atmosphere exchange processes relies on a fully coupled model describing the mass, momentum, and heat transfer between the soil and the atmosphere.

Second, from the perspective of practical applications, reduced model concept is commonly adopted instead of the complex fully coupled model concept. In the reduced model concept, the mass, momentum, and heat transfer between the soil and the atmosphere is parameterized through flux top boundary conditions rather than simulating the physical processes in the atmosphere and across the surface explicitly (e.g. Vanderborght et al., 2017). Some of the influential factors mentioned above are not accurately parameterized into the current reduced models. One crucial factor is the macroscale surface undulations. The boundary layer developed in the vicinity of such undulating soil surfaces is significantly influenced by the surface geometry besides of atmospheric conditions. Thus, the soil undulations and the corresponding near-surface atmospheric boundary layer should be taken into consideration simultaneously. However, current reduced models dealing with soil-atmosphere exchange processes always assume a hydrodynamically smooth surface and thus fail to incorporate the combined impacts (e.g., Camillo

& Gurney, 1986; Lehmann et al., 2008; Shahraeeni et al., 2012; Or et al., 2013a; Vanderborght et al., 2017). Alternatively, an accurate parameterization mainly relies on the fundamental understandings of soil-atmosphere exchange processes as mentioned firstly and also high-resolution experimental data.

Thus, it opens up the third problem, i.e. experimentation techniques. The current laboratory experiments on soil-atmosphere exchange processes do not collect the near-surface boundary layer (e.g., Verma & Cermak, 1974a; Sugita & Kishii, 2002; Davarzani et al., 2014; Haghghi & Or, 2015a), especially the boundary layer developed in the vicinity of an undulating soil surface due to its difficulty. For example, it is difficult to create and keep a fully developed turbulent airflow state, and high-quality measurement of the turbulent flow field is sophisticated. Unique experimental design and velocimetry technology are required to obtain high-fidelity datasets, especially the information of the atmospheric boundary layer, which relies on transdisciplinary collaboration.

Given the problems discussed above, this research is devoted to fill the knowledge gaps resulting from undulating soil surfaces and the concomitant atmospheric boundary layer pattern in soil-atmosphere exchange processes. Particularly, the exchange process during soil evaporation is investigated by both numerical and experimental approaches.

## **1.2 Research Goal and Objectives**

The overarching goal of this research is to advance our understanding of the mass, momentum, and heat transfer between the soil and the atmosphere by including the combined influence of undulating soil surfaces and the corresponding near-surface atmospheric boundary layer to ultimately improve the representation of such processes in hydrological modeling effort. Both the fundamental study at the Representative Element Volumetric (REV) scale and

parameterization at the large scale are considered using experimental and numerical approaches.

The general objectives, specifically described in each chapter, are summarized as follows:

(1) Develop a model based on the fully coupled model concept that can successfully characterize all the physics in soil evaporation process and apply it to providing new insights into soil-atmosphere exchange processes. Special focus is paid on the influence of undulating soil surfaces and the laminar or turbulent boundary layer developed in the vicinity of the undulating surface. (2) Based on the understanding of soil-atmosphere exchange processes from the fully couple model, improve the reduced model that is commonly used in practical applications by parameterizing the influence of undulating soil surfaces and the accompanied near-surface turbulent velocity field on the exchange processes. (3) Generate high-fidelity datasets to test the fully coupled model, improve the parameterization of the reduced model, and investigate the characteristics of evaporation from an undulating soil surface experimentally.

The research is designed to test a number of hypotheses: (1) A fully coupled model including the mass, momentum, and heat transfer physics between the soil and the atmosphere for undulating-surface evaporation is able to describe the soil evaporation process; (2) An undulating soil surface has a significant effect on the development of the boundary layer above it. The combined effects in turn greatly influence soil evaporation behavior; (3) The influence of undulating surfaces and atmospheric boundary layers can be parameterized through vapor and momentum roughness lengths based on laboratory experimental data. The hypotheses will be discussed in detail in section 2.7.

### **1.3 Methodology**

According to the goal and objectives, both experimental and numerical approaches are taken in this research.

### **1.3.1 Laboratory Experiments**

Laboratory experiments are uniquely designed to collect evaporation relevant data and, in the meantime, capture the turbulent boundary layer developed in the vicinity of the undulating soil surface. Compared with the traditional laboratory experiments for soil evaporation using a wind tunnel – soil tank system, the major contribution in this research is the capture of the turbulent velocity field developed in the vicinity of the undulating soil surface. In order to experimentally investigate the combined influence of soil undulation configurations and the near-surface turbulent boundary layer on exchange processes and apply it improve model parameterization, velocimetry technology will be employed to obtain the boundary layer information. Accordingly, the equipment used in the wind tunnel -soil tank system will be designed uniquely to accommodate the requirement of velocimetry operation. Firstly, Hot-wire Anemometry (HWA), a point-by-point measurement method, will be employed to obtain turbulent velocity profiles above the undulating soil surface owing to its easy operability (see CHAPTER 4). In order to experimentally advance understandings in soil-atmosphere exchange processes and ultimately improve the model parameterization, Particle Imaging Velocimetry (PIV) is employed afterwards to visualize the two-dimensional turbulent velocity vector field as well as the distribution of Reynolds stress (see CHAPTER 5).

### **1.3.2 Numerical Modeling and Model Parameterization**

Two model concepts will be adopted considering different studying scales and objectives. Firstly, from the perspective of fundamentally investigating the characteristics and mechanisms of soil-atmosphere exchange processes under different surface configurations and boundary layers, a fully coupled model describing the dynamic mass, momentum, and heat transfer in the soil, in the atmosphere, as well as across their interface will be developed. This model will be first used for

investigation under a given laminar boundary layer and validated through experiments. Then it will be extended by incorporating airflow turbulence to study the special exchange behaviors under a given turbulent boundary layer.

Based on the mechanism understandings from the fundamental studies using the fully coupled model, parameterization of the reduced model widely employed for practical applications will be conducted to incorporate the influence of soil surface undulations and the corresponding turbulent velocity field developed in the vicinity of soil undulations. The model parameterization will be implemented with the high-resolution turbulent flow information collected by the PIV system and validated through evaporation relevant data from experiments. In the meantime, the parameterized model will also be used to advance our understandings in soil-atmosphere exchange processes from the perspective of the reduced characterization.

Both the fully coupled model concept and reduced model concept are able to represent soil-atmosphere exchange processes. The major difference between them is the former explicitly describes the mass, momentum, and heat transfer in the soil and the atmosphere, as well as across the soil-atmosphere interface (i.e. the soil surface) by basic flow and transport equations. As discussed in section 1.2, this model concept includes the complex physical processes in the coupling porous media – free flow system. As a result, the mathematical model will also be complicated either in the expression or in the computation, which decides that this model is not applicable in practical applications. Therefore, for the purpose of applications, a reduced model concept is adopted. In this model, the flow and transport physics in the atmosphere are not simulated explicitly but rather replaced by a flux top boundary condition to represent the soil-atmosphere interaction. This reduced model concept decreases the computation cost largely with a simplified expression. However, an accurate characterization of the exchange processes in the

flux top boundary condition is indispensable for model application and prediction.

#### **1.4 Research Phases**

Based on the objectives, this research is divided into three phases to answer two general research questions. Phase I and II deal with question 1, and phase III deals with question 2.

**Research Question 1:** What is the most appropriate model to characterize the fully coupled mass, momentum, and heat transfer between the soil and the atmosphere and how can we test the model?

**Phase I:** Study of the characteristics and mechanisms of evaporation from an undulating soil surface under a laminar boundary layer.

This phase aims at a fundamental mechanism study at the REV continuum scale by both experimental and numerical approaches. A coupling free flow and porous media flow model will be developed to describe the fully coupled mass, momentum, and heat transfer processes between the soil and the atmosphere during evaporation under a laminar boundary layer. To consider soil undulations, the soil surface is assumed in a sinusoidal-type undulating shape for simplicity. A laboratory experiment will be conducted to validate this model. Further it will be used to analyze how soil properties, soil surface geometries, and atmospheric conditions influence soil-atmosphere exchanges under a given laminar boundary layer.

**Phase II:** Study of the characteristics and mechanisms of evaporation from an undulating soil surface under a turbulent boundary layer.

This phase aims at a fundamental mechanism study at the REV continuum scale by both experimental and numerical approaches. The fully coupled model developed and validated in Phase I will be extended by incorporating turbulent airflow through Reynolds-averaged Navier-Stokes equations. A laboratory experiment in which HWA technology is employed to capture the

turbulent boundary layer above the sinusoidal-type undulating soil surface will be conducted to validate this extended model. Then it will be used to analyze how soil properties, soil surface geometries, and atmospheric conditions influence soil-atmosphere exchanges under a given turbulent boundary layer.

**Research Question 2:** How can we improve the current reduced model oriented for practical applications to incorporate physical understandings of soil-atmosphere exchanges?

**Phase III:** Parameterization of the significant combined influence of soil undulations and the accompanied near-surface turbulent flow into the reduced model to improve the characterization of soil-atmosphere changes at large scales.

This phase aims at model parameterization for the purpose of applications. The widely used reduced model concept is adopted, in which the mass, momentum, and heat transfer between the soil and the atmosphere is simplified through a flux top boundary condition (TBC) based on Monin-Obukhov similarity theory (MOST). The vapor and momentum roughness lengths are two significant parameters in this model characterizing the mass and momentum transfer for vapor flux TBC. To construct the relationship between these two roughness lengths to parameterize the combined influence of soil undulations and the accompanied near-surface turbulent flow, a series of unique experiments will be designed. PIV system will be used to collect high-fidelity datasets recording the near-surface turbulent flow field information.

## **1.5 Thesis Outline**

This dissertation consists of 6 chapters and 6 appendices.

CHAPTER 1: General motivation and problems, research goals and objectives.

CHAPTER 2: Background and literature review.

CHAPTER 3: Evaporation from an undulating soil surface under laminar airflow.

This chapter is based on the paper that has been published in Water Resources Research entitled “Experimental and numerical study of evaporation from wavy surfaces by coupling free flow and porous media flow” by Bo Gao (Primary researcher and author), Hossein Davarzani (Research associate at BRGM), Rainer Helmig (Professor at University of Stuttgart), and Kathleen M. Smits (Associate professor at University of Texas at Arlington). Approval for republication of the manuscript was confirmed from Water Resources Research and all co-authors. This chapter deals with the problem in Phase I.

CHAPTER 4: Evaporation from an undulating soil surface under turbulent airflow.

This chapter is based on the paper that has been published in Vadose Zone Journal entitled “Evaporation from undulating soil surfaces under turbulent airflow through numerical and experimental approaches” by Bo Gao (Primary researcher and author), John Farnsworth (Assistant professor at University of Colorado Boulder), Kathleen M Smits (Associate professor at University of Texas at Arlington). Approval for republication of the manuscript was confirmed from Vadose Zone Journal and all co-authors. This chapter deals with the problem in Phase II.

CHAPTER 5: Determination of Vapor and Momentum Roughness Lengths above an Undulating Soil Surface Based on PIV-measured Velocity profiles.

CHAPTER 6: Major conclusions and recommendation for future research.

## CHAPTER 2

### BACKGROUND AND LITERATURE REVIEW

#### **2.1 Background of Soil Evaporation**

This section is devoted to introducing the basic theory of soil evaporation, including the main physical processes and evaporation stage division.

##### **2.1.1 Processes of Mass, Momentum and Heat Transfer**

As mentioned in CHAPTER 1, soil evaporation combines a series of processes of mass, momentum and heat transfer in the interfacial area where the soil and the atmosphere are closely interacted, as shown by Figure 2.1.

Energy, from either solar radiation or ambient gas temperature gradient, provides the original driving force for the phase change between liquid water and water vapor. Essentially, phase change is determined by the discrepancy of chemical potential owned by the liquid water and water vapor. In brief, if the liquid water has a higher chemical potential, it tends to change to vapor through volatilization, and vice versa. Driven by the energy, liquid water evaporates continuously beneath a soil surface. The generated water vapor occupies part of the soil pores and moves through the soil profiles to the soil surface. Finally, the water vapor releases into the atmosphere, forming a concentration boundary layer. On the other hand, the water loss in the soil induces invasion of the air in the atmosphere into the empty soil pores. This process is mainly controlled by soil retention. The top soil layer, thus, is usually characterized as an unsaturated zone where both gas (including water vapor and dry air) and liquid water co-exist. In this area, the liquid water flow is controlled by capillary, viscous and gravitational forces; while the movement of vapor is mainly determined by the ambient concentration gradient. If the soil water continues to

evaporate and the capillary force is not enough to overcome the viscous and gravitational forces to support water reaching the soil surface, a dry surface layer forms at the top of the soil. Within this dry soil layer, only single gas phase exists while no liquid water. As one component in the gas phase, the transport of water vapor in this layer is mainly controlled by molecular diffusion.

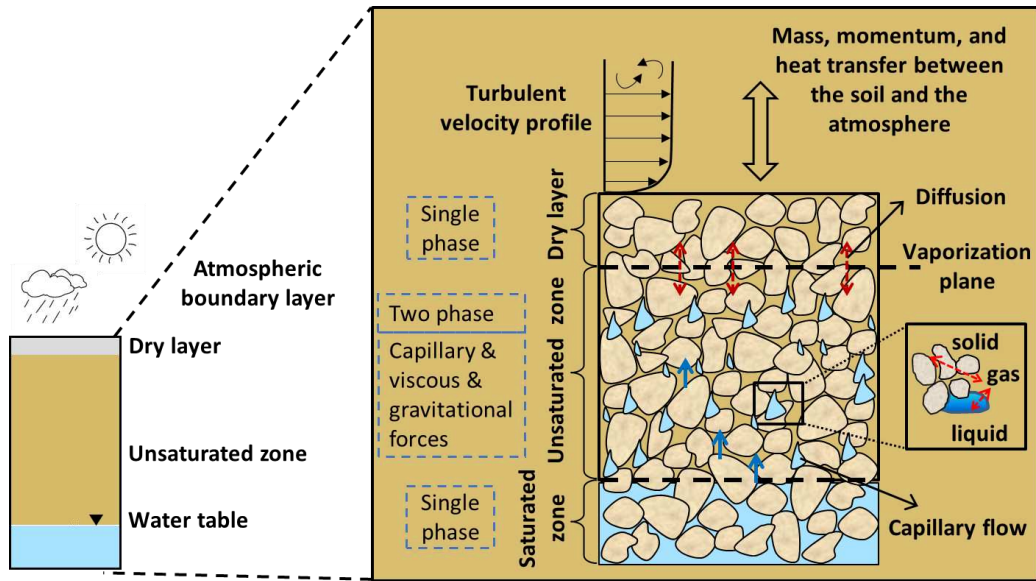


Figure 2.1 Schematic of soil-atmosphere interactions in the interfacial area. The interfacial area includes shallow subsurface, near-surface atmosphere, and the interface (i.e. soil surface).

In the meantime, the atmospheric conditions near the soil surface also execute significant influences on the subsurface motion. The varying solar radiation and the heterogeneous radiation-adsorption/albedo of soil surface due to its undulation will undoubtedly affect soil evaporation. The wind penetrates into large soil pores and induces horizontal gas flow, influencing the vapor transfer by dispersion (Ishihara et al., 1992). As evaporation proceeds, the atmospheric air close to the soil surface becomes gradually saturated and the process will slow down. However, the slow-down may be postponed if the saturated air is displaced by drier air timely. The replacement in the atmosphere depends greatly on the wind speed, the near-surface pressure gradient, and the airflow state (i.e. laminar airflow, turbulent airflow). In particular, if the soil surface is not totally

flat, it may change the development of the boundary layer, causing an early transition from laminar flow to turbulent flow (White & Corfield, 2006; Schlichting & Gersten, 2017). It will, in turn, affect the vapor transport behavior inside soil profiles. Most importantly, it will definitely influence the mass and momentum transfer between the soil surface and the atmosphere, and further influence soil evaporation.

Hence, during soil evaporation, the fully coupled mass, momentum, and heat transfer processes occur dynamically between the soil and the atmosphere. The soil-atmosphere interaction heavily depends on the coupled influences of soil properties (e.g. hydraulic conductivity, porosity, soil retention, thermal conductivity and diffusivity, heterogeneity, soil surface geometry, etc.) and climatological conditions (e.g. atmospheric boundary layer, solar radiation, etc.).

### **2.1.2 Evaporation Stages**

According to the location of the vaporization plane in the soil profiles and the corresponding dominant factors, soil evaporation is usually divided into different stages (Lehmann et al., 2008; Or et al., 2013) identified with distinct evaporation rate. The vaporization plane is defined as the top plane of a saturated or unsaturated zone.

As shown by Figure 2.1, assuming an originally saturated soil column, as evaporation starts, air penetrates into some pores of the top surface layer. The large pores are invaded first. After initial air entry, the evaporation remains at a relatively high-level rate constantly or gradually decrease, see Figure 2.2. Especially if the soil is poorly graded or exposed to a high wind speed, the evaporation curve presents a decreasing trend (Shahraeeni et al., 2012). This period is termed Stage I when the vaporization plane is located at the soil surface. During this stage, evaporation is primarily controlled by atmospheric demand (Hide, 1954; Lemon, 1956). The vapor concentration gradient between the water menisci where the water vapor is nearly saturated and the air decides

the evaporation rate. Stage I is characterized by the hydraulic connection between the soil pore water with the soil surface (i.e. the vaporization plane). In this sense, soil water moves continuously up to the soil surface to evaporate driven by capillarity, which overcomes viscous and gravitational forces.

As evaporation goes on, the top soil surface gradually dries with the drying front receding deeper into the soil column. At the threshold when capillarity becomes not enough to overcome the sum of viscous and gravitational forces, the continuous liquid water network that connects the receding drying front with the soil surface will be disrupted. This indicates the end of Stage I evaporation (Lehmann et al., 2008; Or et al., 2013). The duration of Stage I is mainly decided by two factors. One is the air entry value which corresponds to the capillary pressure when the air begins to invade the initially saturated porous media; the other is the threshold capillary pressure which marks the interruption of the continuity of the liquid network. A characteristic length was proposed to predict the depth of the drying front at the end of Stage I (Lehmann et al., 2008) by considering the balance of capillary, viscous and gravitational forces:

$$L_C = \frac{L_G}{1 + \frac{L_G}{L_V}} \quad (2.1)$$

where  $L_C$  (m),  $L_G$  (m),  $L_V$  (m) are the characteristic length, the gravity length, and the viscous length, respectively. The gravity length is estimated based on (Van Genuchten, 1980) model (Appendix 0) through:

$$L_G = \frac{1}{\alpha(n-1)} \left( \frac{2n-1}{n} \right)^{\frac{2n-1}{n}} \left( \frac{n-1}{n} \right)^{\frac{1-n}{n}} \quad (2.2)$$

where  $\alpha$  ( $m^{-1}$ ) and  $n$  are van Genuchten parameters.

The viscous length is defined as:

$$L_v = \frac{E}{K_{\text{eff}}} \quad (2.3)$$

where  $K_{\text{eff}}$  ( $\text{m}^2/\text{s}$ ) is the effective hydraulic conductivity of the continuous liquid network region;  $E$  ( $\text{m}/\text{s}$ ) is the evaporation rate. Usually, the gravity length is much shorter than the viscous length and thus the characteristic length approximates the gravity length, i.e.  $L_C \approx L_G$ .

As the drying front recedes deeper, an increasing number of soil pore at the top layer become drier. The connection between the drying front with the soil surface (i.e. the vaporization plane) weakens. More water vapor was generated and transports through dry soil pores by diffusion. The evaporation rate falls rapidly until a low but relatively constant level, see Figure 2.2. This period is termed transition stage. Note that during this stage, the vaporization plane still locates at the soil surface. In this sense, soil water can still arrive at the soil surface to evaporate.

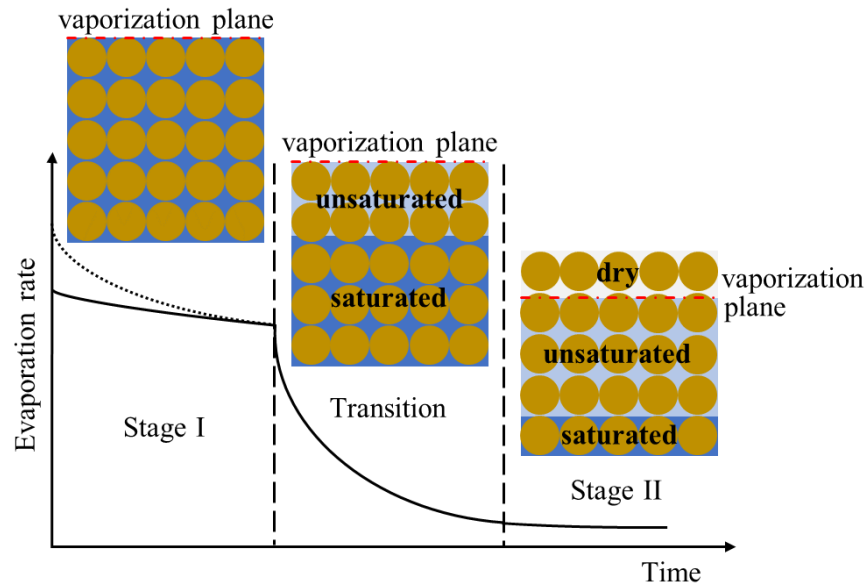


Figure 2.2 Schematic of the evaporation stages, including Stage I, Transition, and Stage II. Dark blue, light blue, and white color represent the saturated, unsaturated, and dry soil zones, respectively. The red line denotes the location of the vaporization plane, which is defined as the top surface of the unsaturated zone.

Once the last menisci pinned at the surface recede into the soil, the drying front disconnects with the soil surface. A dry layer forms where the liquid water is at a residual state and only single gas phase flow exists. The vaporization plane totally recedes into the soil columns. The soil water can only reach the vaporization plane through capillary flow but not the soil surface. The water vapor diffusion in the unsaturated zone and the dry layer mainly dominates the evaporation, resulting in a relatively low and constant evaporation rate. This stage is termed Stage II.

## **2.2 Mathematical Description for Soil Evaporation**

This section introduces three types of mathematical concepts in describing soil evaporation. First is a fully coupled model, i.e. two-phase flow, two-component transport in the porous media coupled with one-phase flow, two-component transport in the free flow under non-isothermal conditions. The second is semi-coupled models considering flow and transport in the porous media with different upper boundary conditions. Especially, the vapor flux top boundary conditions are usually used to estimate bare-soil evaporation rate directly. The third is Penman-Monteith equation which is typically applied to calculate the evapotranspiration (a sum of evaporation from bare soil and vegetation) rate at large scale (e.g. catchment, watershed).

### **2.2.1 Fully Coupled Model**

As already mentioned above, soil evaporation involves coupled mass, momentum, and heat transfer processes and these processes display different behaviors in the porous media and the free flow. However, in most models that describe the soil processes, the soil surface is treated as an upper boundary using a flux or a given constant pressure/temperature condition. In most models that focus on the atmospheric processes, the soil is treated as a lower boundary with prescribed fluxes (Vanderborght et al., 2017). This approach separates the soil and the atmosphere as a single domain independent to each other, which is simple but may result in prediction errors (Seager et

al., 2007). Thus, a fully coupled model is developed to describe the exchange process in the integrated system (Mosthaf et al., 2011; Davarzani et al., 2014; Mosthaf et al., 2014; Thomas Fetzer et al., 2016; Gao et al., 2018, 2020). This section introduces the basic concept and theory of the fully coupled model. The details of the mathematical model refer to CHAPTER 3 and CHAPTER 4.

Figure 2.3 illustrates the schematic of the two-dimensional coupled system. The lower part porous media is the soil subdomain, where two phases (i.e. gas, liquid) and two components (i.e. dry air, water vapor) are existent. The fluid flow follows Darcy's law based on REV assumption. The upper part free flow is the atmosphere subdomain, where single gas phase and two components (i.e. dry air, water vapor) are existent. The fluid flow is assumed incompressible and described by Navier-Stokes equations. For turbulent airflow, the Reynolds-averaged Navier-Stokes equations are applied. The interface between these two subdomains denotes the soil surface. In this research, undulating surfaces are considered. For simplicity, a sinusoidal – shape curve is used to represent the undulating soil surface. At the interface, the total mass flux and stress are continuous at the normal direction between the porous media and the free flow, while a tangential stress is imposed along the tangential direction of the interface. Besides, the temperature and the heat flux, the vapor concentration and the vapor flux are both continuous at the interface. The other boundary conditions are defined based on the specific experimental setup in this research as shown in Figure 2.3. The specific equations are described in CHAPTER 3 and CHAPTER 4.

The advantage of this fully coupled model is it incorporates most of the important processes during soil evaporation dynamically, such as phase change, capillary flow, vapor transport, heat transfer, the exchange between soil and the atmosphere, etc. Thus, it is especially appropriate for a fundamental study to investigate the mechanism of different influential factors on soil

evaporation. In the meantime, this fully coupled model is complex and has a high demand on computation technique, which makes it not applicable for studying a large-scale practical issue.

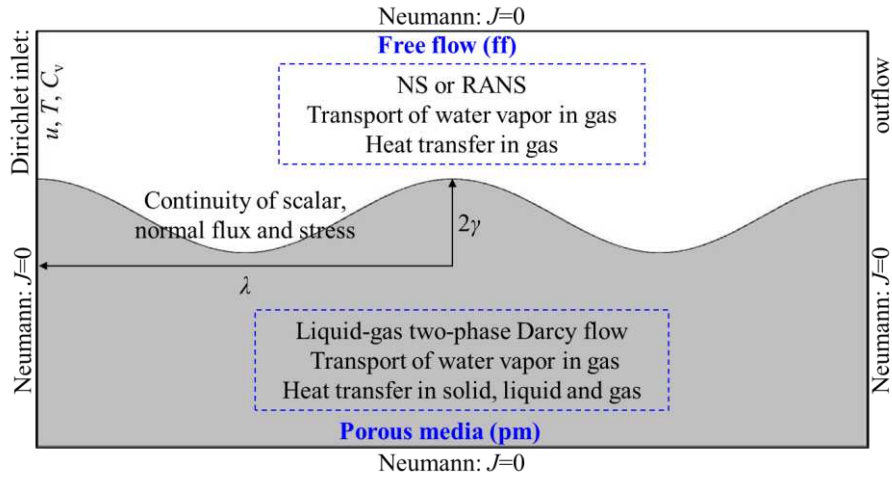


Figure 2.3 Two-dimensional configuration (subdomains and boundary conditions) where  $C_v$  is the water vapor concentration;  $T$  is temperature;  $u$  is wind speed;  $J$  is flux for  $T$ ,  $u$ , and  $C_v$ ;  $\lambda$  is wave length; and  $\gamma$  is half of the wave amplitude.

## 2.2.2 Semi-coupled Model

In this approach, the mass, momentum, and heat transfer processes in the atmosphere are not simulated. Instead, the fluid flow, vapor and heat transfer are considered in the soil by different equations. Besides, a vapor flux or a constant pressure head, and a heat flux or a constant temperature condition are assumed as the top boundary conditions for water vapor transport and heat transfer, respectively. Three models in this concept are introduced based on different mathematical descriptions in the soil (Vanderborgh et al., 2017; Li et al., 2019).

First, one-phase one-component Richards equation is used to model flow and transport in the soil. In this approach, the flow of gas phase is not included, but a pseudo-gas phase, i.e. water vapor is assumed existent in the water phase.

$$\frac{\partial(\rho_w \theta_w)}{\partial t} + \nabla \cdot (\rho_w \mathbf{u}_w) = 0 \quad (2.4)$$

where  $\rho_w$  (kg/m<sup>3</sup>) is the water density;  $\theta_w$  (m<sup>3</sup>/m<sup>3</sup>) is the water content;  $\mathbf{u}_w$  (m/s) is the liquid water velocity following Darcy's law:

$$\mathbf{u}_w = -\frac{\mathbf{K}_{\text{int}} k_{rw}}{\mu_w} (\nabla p_w + \rho_w \mathbf{g}) \quad (2.5)$$

where  $\mathbf{K}_{\text{int}}$  (m<sup>2</sup>) is the intrinsic permeability tensor of porous media;  $k_{rw}$  is the relative permeability of water in the porous media decided by the Van Genuchten (1980) model (Appendix 0);  $\mu_w$  (Pa·s) is the water viscosity;  $p_w$  (Pa) is the water pressure;  $\mathbf{g}$  (m/s<sup>2</sup>) is the gravitation acceleration. In this model, the condition for heat transfer can be either isothermal or non-isothermal. Under a non-isothermal condition, the heat transfer is described by:

$$(\rho c_p)_{\text{eff}} \frac{\partial T}{\partial t} + \nabla \cdot [(\rho_w c_{p,w}) \mathbf{u}_w T] - \nabla \cdot (\lambda_{\text{eff}} \nabla T) = 0 \quad (2.6)$$

where  $(\rho c_p)_{\text{eff}}$  is the effective product of heat capacity and density of liquid water and water vapor;  $T$  (K) is the temperature of the system assuming thermal equilibrium;  $\lambda_{\text{eff}}$  is the effective thermal conductivity of liquid water and water vapor.

Second, "one-and-a-half" phase one-component Richards equation is used to model flow and transport in the soil. In this approach, the flow of gas phase is not included, but the diffusion of vapor in the pseudo-gas phase is considered. The pressure of this pseudo-gas phase is assumed uniform and constant with time, independent of the liquid water phase.

$$\frac{\partial(\rho_w \theta_w)}{\partial t} + \frac{\partial(\rho_w \theta_v)}{\partial t} + \nabla \cdot (\rho_w \mathbf{u}_w) - \nabla \cdot (D_v \nabla C_v) = 0 \quad (2.7)$$

where  $\theta_v$  (m<sup>3</sup>/m<sup>3</sup>) is the vapor content;  $D_v$  (m<sup>2</sup>/s) is vapor diffusion coefficient;  $C_v$  (kg/m<sup>3</sup>) is the vapor concentration. Same with the first approach, the heat transfer condition can be assumed either isothermal or non-isothermal based on equation (2.6).

Third, two-phase two-component non-equilibrium phase change model is used to model flow and transport in the soil. In this approach, a real gas phase flow and the vapor diffusion in the gas phase is simulated. The gas phase pressure is related with the liquid water phase through the Van Genuchten (1980) model (Appendix 0). Since phase change is included, the heat transfer equation is included. A phase change rate term is added in the mass and energy balance equations (Bixler, 1985; Lozano et al., 2008; Halder et al., 2011; Smits et al., 2011). This model is the same with the one used in the porous media subdomain of the fully coupled model. Details are introduced in section 3.3.2 of CHAPTER 3.

The commonly used top boundary conditions at the soil surface for water vapor include:

(1) Potential evaporative flux is used when the soil surface is wet enough that the vapor is saturated.

$$F_v = \frac{\rho_{v,\text{sat}}(z=0) - \rho_{v,a}(z=z_{\text{ref}})}{r_a} \quad (2.8)$$

where  $F_v$  ( $\text{kg}\cdot\text{m}^{-2}\cdot\text{s}^{-1}$ ) is the evaporative flux;  $\rho_{v,\text{sat}}(z=0)$  and  $\rho_{v,a}(z=z_{\text{ref}})$  ( $\text{kg}/\text{m}^3$ ) are the saturated water vapor density at soil surface and the reference plane, respectively;  $r_a$  (s/m) is the aerodynamic resistance usually determined based on the Monin – Obukhov similarity theory (MOST) (e.g., Camillo & Gurney, 1986; Yamanaka et al., 1997; Bittelli et al., 2008).

$$r_a = \frac{\left[ \ln\left(\frac{z_{\text{ref}} - d_0}{z_{0m}}\right) - \psi_m \right] \left[ \ln\left(\frac{z_{\text{ref}} - d_0}{z_{0v}}\right) - \psi_v \right]}{\kappa^2 u_a} \quad (2.9)$$

where  $\psi_m$  and  $\psi_v$  are atmospheric stability correction terms for momentum and vapor transfer, respectively. Under neutral conditions, they are equal to zero as mentioned in section 2.3.4.

(2) Soil resistance  $r_s$  (s/m) is introduced to account for the reduction in evaporation when the soil surface becomes relatively dry and the vapor pressure is lower than the saturated pressure.

$$F_v = \frac{\rho_{v,\text{sat}}(z = z_{\text{vap}}) - \rho_{v,a}(z = z_{\text{ref}})}{r_a + r_s} \quad (2.10)$$

where  $z_{\text{vap}}$  is the vaporization plane where evaporation occurs and the vapor is saturated. The soil resistance is a function of water content in the top soil layer. There have been numerous methods to describe this term empirically, semi-empirically, and theoretically (e.g., Shu, 1982; Camillo & Gurney, 1986; Kondo et al., 1990, 1992; Sellers et al., 1992; van de Griend & Owe, 1994; Sakaguchi & Zeng, 2009; Tang & Riley, 2013).

(3) The vapor density at soil surface whatever the its saturation state is used and no soil resistance is included.

$$F_v = \frac{\rho_v(z = 0) - \rho_{v,a}(z = z_{\text{ref}})}{r_a + r_s} \quad (2.11)$$

where the vapor density at soil surface is determined by:

$$\rho_v = \rho_{v,\text{sat}} \times \text{RH} \quad (2.12)$$

where RH is the relative humidity expressed as (Likos & Lu, 2004):

$$\text{RH} = \exp\left(-\frac{gM_w H_c}{RT}\right) \quad (2.13)$$

where  $M_w$  (kg/mol) is the molecular mass of water;  $H_c$  (m) is the capillary head;  $R$  (8.314 J·mol<sup>-1</sup>·K<sup>-1</sup>) is the universal gas content.

There are two things to note. First, the top boundary conditions for water vapor flux are a simplified representation of mass transfer between the soil and the atmosphere. They are sometimes used to estimate soil evaporation rate (Wallace, 1995; Teng et al., 2014; Haghghi & Or, 2015c; Jefferson & Maxwell, 2015). Second, the selection of the top boundary conditions for vapor transport depends on the evaporation stage (Vanderborght et al., 2017). During stage I when atmosphere dominates, the first condition, i.e. the potential evaporative flux, is employed. When

the soil surface dries out and the effect of vapor diffusion in the soil starts to appear, the second or third condition is applied. When the surface dries to a certain value, i.e. the water pressure head reaches a critical value, a constant water pressure or water content at the soil surface is composed.

In terms of the top boundary conditions for heat transfer at the soil surface, a constant temperature is imposed or heat flux is defined:

$$H = \frac{T(z=0) - T(z=z_{\text{ref}})}{r_h} \quad (2.14)$$

where  $H$  ( $\text{J}\cdot\text{m}^{-2}\cdot\text{s}^{-1}$ ) is the sensible flux;  $r_h$  ( $\text{K}\cdot\text{m}^2\cdot\text{W}^{-1}$ ) is aerodynamic resistance for heat transfer based on the MOST:

$$r_h = \frac{\left[ \ln\left(\frac{z_{\text{ref}} - d_0}{z_{0m}}\right) - \psi_m \right] \left[ \ln\left(\frac{z_{\text{ref}} - d_0}{z_{0h}}\right) - \psi_h \right]}{\kappa^2 u_a} \quad (2.15)$$

where  $\psi_h$  is the atmospheric stability correction term for heat transfer, which is equal to zero under neutral conditions.

Compared with the fully coupled model, the semi-coupled model focuses on the flow and transport processes in the porous media and these physical processes in the atmosphere are not concluded. Instead, they are parameterized in the resistance terms in the top boundary conditions. The advantage is that it can be applied to study the soil evaporation at relatively large scale if only the vertical dimension is considered. However, the drawback lies in the selection of these top boundary conditions and the parameterization of the resistance terms. A poor selection or parameterization may lead to a significant error.

### 2.2.3 Penman-Monteith Equation

Penman-Monteith type equation is a frequently employed method at large scales (e.g., catchment, watershed) to calculate the evapotranspiration rate or used as a top boundary condition

in studying land-atmosphere interaction problems (e.g., Ventura et al., 1999; Sumner & Jacobs, 2005; Isabelle et al., 2015).

Penman (1948) proposed an equation to calculate evaporation rate of an open water by combining energy balance and mass transfer method. This equation was further developed by many researchers and extended to be applied in vegetation evaporation via introducing various resistance terms (e.g., Monteith, 1965; Van Bavel, 1966; Morton, 1983; McIlroy, 1984; Byrne et al., 1988; Shuttleworth, 1993; Garratt, 1994). Penman-Monteith equation (Monteith, 1965) is one of the most widely used method to estimate the evapotranspiration or evaporation rate:

$$\lambda ET = \frac{\Delta(R_n - G) + \rho_a c_p \frac{e_s - e_a}{r_a}}{\Delta + \gamma \left(1 + \frac{r_s}{r_a}\right)} \quad (2.16)$$

where ET ( $\text{kg}\cdot\text{m}^{-2}\cdot\text{s}^{-1}$ ) is the evapotranspiration rate;  $\lambda$  (J/kg) is the latent heat of vaporization;  $R_n$  ( $\text{W}/\text{m}^2$ ) is the net irradiance representing the external source of energy flux;  $G$  ( $\text{W}/\text{m}^2$ ) is the ground flux;  $\rho_a$  ( $\text{kg}/\text{m}^3$ ) is the dry air density;  $c_p$  ( $\text{J}\cdot\text{kg}^{-1}\cdot\text{K}^{-1}$ ) is the specific heat capacity of air;  $e_s$  and  $e_a$  are the saturated vapor pressure at soil surface and in the air, respectively;  $\Delta$  (Pa/K) is the slope of the curve describing saturated vapor pressure versus air temperature;  $\gamma$  (Pa/K) is the Psychrometric constant;  $r_s$  and  $r_a$  (s/m) are the soil and atmospheric resistance terms which have been mentioned above.

### 2.3 Boundary Layer

As mentioned above, the boundary layer generated above the soil surface may have a great impact on the mass, momentum, and heat transfer between the soil and the atmosphere during soil evaporation. This section first presents the basic theory of laminar and turbulent flow state. Then the fundamentals of boundary layer developed above a flat plate and an undulating surface are

introduced, which is followed by the introduction of the atmospheric boundary layer concept in meteorology field.

### 2.3.1 Laminar and Turbulent Flow

Laminar flow denotes that the flow particles following uniform paths with little or no lateral mixing. The motion of the particles in the flow paths is very orderly and one path slides smoothly relative to an adjacent path. The particles close to a solid wall move parallelly to that wall. For a given fluid, laminar flow usually occurs at a low velocity or at the flow beginning.

If increasing the velocity or decrease the viscosity of the fluid, or as the leading edge extends of a laminar flow, the fluid particles may follow erratic paths, causing a high rate of mixing within the fluid. This is referred to as turbulent flow. Between these two flow states, there is transitional flow state, in which both laminar and turbulent flow coexist.

An important parameter to differentiate these flow states is Reynolds number, which is a dimensionless number representing the ratio of the inertial force to the viscous force of the fluid:

$$\text{Re} = ul / \nu \quad (2.17)$$

where Re is Reynolds number,  $u$  (m/s) is the flow velocity,  $l$  (m) is the characteristic length, and  $\nu$  ( $\text{m}^2/\text{s}$ ) is the kinetic viscosity of the fluid. According the definition, the flow state is related to the fluid properties, the flow velocity and the geometry of the flow system.

Laminar flow happens at low Reynolds numbers, in which the viscous force dominates. If there are passive scalars (e.g. smoke particles, gas components) in the flow field, the molecular diffusion controls the transport of these scalars in the flow field. By contrast, turbulent flow occurs at high Reynolds numbers and the inertial force dominates. Chaotic eddies, vortices, and mixing are produced in turbulent flow. Meanwhile, it also generates additional turbulent friction described by Reynolds stress (Pope, 2001; Bailly & Comte-Bellot, 2015). For the transition from a laminar

critical Reynolds numbers  $Re_{cri}$ . The critical Reynolds numbers are distinct for different geometries of the flow system. Usually for a flat plate, the critical Reynolds number approximates  $5 \times 10^5$  (Clark, 1977) using the distance from the leading edge as the characteristic length. For pipe flow, the hydraulic diameter of the pipe is selected as the characteristic length. Experiments demonstrate the laminar flow exists when  $Re_{cri} < 2300$ , while fluid flow develops to fully turbulent when  $Re_{cri} > 2900$  (Holman, 2002; Schlichting & Gersten, 2017).

### 2.3.2 Flow Above a Flat Plate

Figure 2.4 illustrates the schematic of a full boundary layer evolution along a flat plate. At the leading edge there is a constant velocity distribution perpendicular to the plate. For a given fluid, as it starts to flow at a relatively low velocity, a laminar boundary layer usually forms at the upstream region. As the distance from the leading edge increasing, the layer of particles slows down due to the friction between particle layers and particle with the wall. Typically, if the wall is nonpermeable, the flow velocity at the wall is regarded as zero according to a non-slip boundary condition. In the case of a permeable wall such as the case of soil surface, the velocity at the surface should be larger than zero (Beavers & Joseph, 1967; Shavit, 2009). As the vertical position increases, the velocity increases until equal to the value of the outer mainstream, see Figure 2.4. The thickness of the boundary layer  $\delta(x)$  monotonically increases with the position  $x$ . It is defined artificially as the location where the velocity equals to 99% of the mainstream velocity (Schlichting et al., 2000), marked as  $\delta_{99}$ . The thickness of a laminar boundary layer is estimated according to Blasius solution (Blasius, 1907):

$$\delta_{99} = 5 \sqrt{\frac{\nu x}{U_{\infty}}} \quad (2.18)$$

where  $U_{\infty}$  (m/s) is the average mainstream velocity.

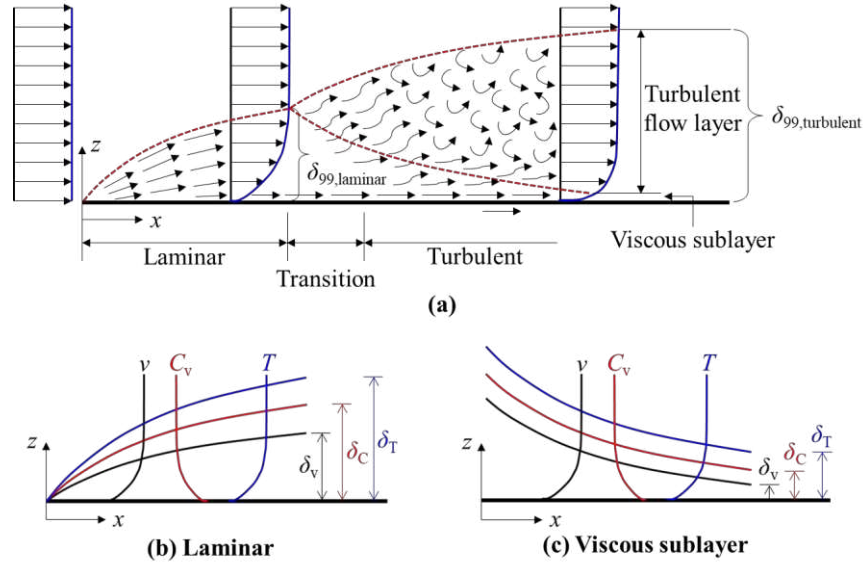


Figure 2.4 The schematic of boundary layer evolution above a flat plate (Mosthaf et al., 2014). (a) From the leading edge, a constant speed profile at low Reynolds number forms laminar boundary layer. As  $x$  extends, the laminar boundary layer thickness becomes thicker and transforms to turbulent boundary layer after transition. The turbulent boundary layer is mainly composed of three sublayers: viscous sublayer, turbulent flow layer, and the upper mainstream.  $\delta_{99,laminar}$  and  $\delta_{99,turbulent}$  are the thickness of the laminar and turbulent boundary layer, respectively. (b) and (c) show the boundary layer for wind speed ( $v$ ), vapor concentration ( $C_v$ ), and temperature ( $T$ ); and the corresponding thickness for wind speed ( $\delta_v$ ), vapor concentration ( $\delta_C$ ), and temperature ( $\delta_T$ ) in laminar and viscous sublayer.

As the laminar boundary layer increases in thickness, it becomes unstable and finally transforms into a turbulent boundary layer downstream as the distance from the leading edge increases. The entire flow field, from the wall upwards, is roughly divided into three sublayers, i.e. the viscous sublayer, the turbulent flow layer, and the outer mainstream flow layer. Adjacent to the wall, in the very thin viscous sublayer, the fluid flow is strongly affected by the effects of the fluid viscosity. Additionally, if the wall surface is permeable, the free flow penetrates into the top layer of the underlying porous media. The kinetic energy of the fluid gradually dissipates during penetration and its velocity decreases to merge with the porous media flow (Manes et al., 2009; Pokrajac & Manes, 2009; Rominger & Nepf, 2011). By contrast, in the turbulent flow layer, the fluid flow is characterized by random fluctuating motion and mainly influenced by the turbulent

fluctuation – induced friction, which is described by Reynolds stress as mentioned above. In the turbulent flow layer, the velocity profile follows logarithmic law (Schlichting et al., 2000):

$$u = \frac{u_*}{\kappa} \ln \left( \frac{z - d_0}{z_{0m}} \right) \quad (2.19)$$

where  $u$  (m/s) is the airflow velocity;  $u_*$  (m/s) is the friction velocity;  $\kappa$  ( $\approx 0.41$ ) is the von Kármán constant;  $z$  (m) is the vertical position;  $d_0$  (m) is the zero-displacement plane;  $z_{0m}$  (m) is the momentum roughness length, which depends on the surface geometry. Visually, it represents the intercept (assuming  $d_0 = 0$ ) of the straight line of the velocity versus elevation in a semi-logarithm coordinate. Below  $z_{0m}$ , the logarithmic law does not apply, which implies  $z_{0m}$  is on the same scale with the viscous sublayer.

Accordingly, besides of velocity, the boundary layer of passive scalars such as temperature and vapor concentration have a similar evolution as shown by Figure 2.4. As the vertical position increases, the temperature increases from a non-zero value to the outer mainstream. The vapor concentration decreases since the generated water vapor releases to soil surface from the inside during evaporation. The thickness of the boundary layer for these passive scalars are different from the velocity. Studies have shown that at the area of laminar boundary layer and the viscous sublayer of the turbulent boundary layer, there is a certain relationship between the scalars and the velocity through the dimensionless Schmidt number and Prandtl number (Bergman et al., 2011):

$$\delta_C = \frac{\delta_v}{Sc^{1/3}} \quad , \quad \delta_T = \frac{\delta_v}{Pr^{1/3}} \quad (2.20)$$

where the subscript “v”, “C”, “T” denote velocity, vapor concentration, and temperature, respectively;  $\delta_i$  ( $i = v, C, T$ ) is the thickness of the laminar boundary layer or the viscous sublayer of  $i$  - variable;  $Sc$  and  $Pr$  are the dimensionless Schmidt number and Prandtl number, respectively. The Schmidt number is defined as the ratio of the momentum diffusivity to the mass diffusivity:

$$Sc = \frac{\nu}{D} \quad (2.21)$$

where  $\nu$  ( $m^2/s$ ) is the kinematic viscosity representing viscous diffusion rate and  $D$  ( $m^2/s$ ) is the diffusion coefficient representing molecular diffusion rate. Similarly, the Prandtl number is defined as the ratio of momentum diffusivity to thermal diffusivity:

$$Pr = \frac{\nu}{D_t} = \frac{c_p \mu}{\lambda} \quad (2.22)$$

where  $D_t$  ( $m^2/s$ ) is the thermal diffusivity,  $\mu$  ( $Pa \cdot s$ ) is the fluid viscosity;  $c_p$  ( $J \cdot kg^{-1} \cdot K^{-1}$ ) is the heat capacity, and  $\lambda$  ( $W \cdot m^{-1} \cdot K^{-1}$ ) is the thermal conductivity.

### 2.3.3 Flow Above an Undulating Surface

In fact, the surface is not ideally smooth or even not hydraulically smooth. A hydraulically smooth surface denotes the surface roughness scale is smaller than the viscous sublayer. As already mentioned above, the surface, especially the soil surface, is always rough with various-scale roughness. The macro-scale soil undulation we are interested in is much larger than the size of the viscous sublayer. The boundary layer developed above such an undulating surface should be totally distinct with that above a flat surface. One phenomenon observed when airflow across macro-scale undulating surface is flow separation and reattachment.

Flow separation denotes the process that a boundary layer detaches a surface and a thickened rotation flow region forms subsequently (Simpson, 1996). It occurs when a fluid passes the thickest part of a streamline body or flows through a widening channel. In such situations, adverse pressure gradient exists along the flow direction. The kinetic energy of the fluid is consumed to overcome the increasing pressure, resulting in decreasing flow velocity and a thickened boundary layer. When the velocity relative the surface reduces to zero, the fluid detaches the surface, signifying that the boundary layer separates, and takes the form of vortices. After the

boundary layer separates, the fluid may attach the surface again at some distance away from the separation point, which is termed as reattachment. The area between the separation point and the reattachment point is called recirculation zone.

Along the flow direction, the fluid has to continuously overcome the friction by consuming kinetic energy. Whenever the kinetic energy is not enough to balance the friction, adverse pressure gradient appears and boundary layer separates. Compared with turbulent flow, flow separation is more common in laminar flow due to its larger viscous friction. Turbulence has more energy due to strong mixing to overcome friction, which makes the flow separation happens more downstream for a turbulent boundary layer.

The presence of a macro-scale undulating surface actually creates a surface condition which is propitious to form an adverse pressure gradient. When the airflow passes the expanding region (i.e. valley) above an undulating surface, it slows down, which lowers its kinetic energy and an adverse pressure gradient may occur. The existence of flow separation and reattachment, as well as the area of the resultant recirculation zone strongly relies on the atmospheric conditions, the undulating surface geometries, and the distribution of surface undulations, etc. (Tampieri, 1987; Poggi & Katul, 2007b; Sherry et al., 2010).

Therefore, the pattern of the boundary layer above an undulating surface has more uncertainties. Different patterns will definitely result in distinct behaviors for mass, momentum, and heat transfer between the soil surface and the mainstream in the atmosphere. This research will study the influence of the undulating surface on soil evaporation from the perspective of both fundamental mechanism and parameterization.

### 2.3.4 Atmospheric Boundary Layer

The above two sections introduce the basic theory of boundary layers. In meteorology, there also exists atmospheric boundary layer (ABL) with similar theory but at a much larger scale. The total ABL may range from a few tens of meters to hundreds of meters dependent on the atmospheric conditions. From the land surface upwards, it is divided into several sublayers (Brutsaert, 2013) as shown by Figure 2.5. It mainly consists of the interfacial sublayer (or roughness sublayer), the inner region (or surface sublayer) with the lowest part called dynamic sublayer, and the outer region (or defect sublayer).

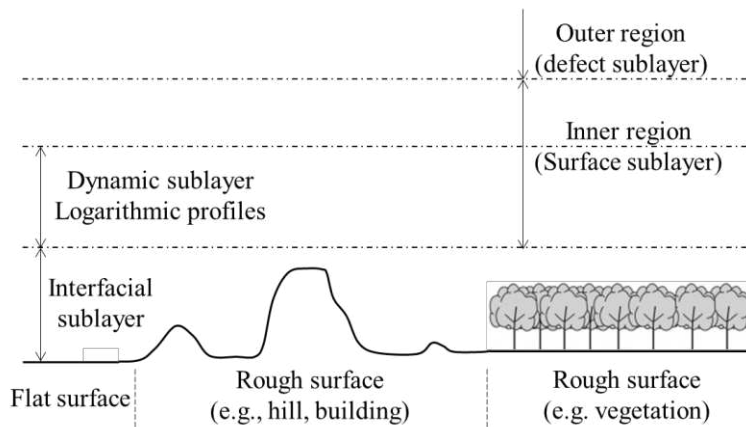


Figure 2.5 Schematic of atmospheric boundary layer (ABL) in meteorology. There are several types of soil surface (e.g., flat surface, rough surface with hills and buildings, rough surface with vegetation). From the surface upwards, ABL mainly consists of interfacial sublayer, inner region, and outer region. The dynamic sublayer is the lowest sublayer of the inner region where universal logarithmic law is valid. There may be some overlaps between these sublayers, which are not showed in this figure.

The interfacial sublayer is defined as the sublayer contacting immediately with the land surface (Brutsaert, 2013) which is strongly affected by the surface conditions, such as buildings, vegetations, soil undulations, etc. In this sublayer, the airflow is not fully turbulent as close to the land surface. The existence of rough elements at land surface (e.g. buildings, vegetations, soil undulations) increases the airflow resistance. These rough obstacles lead to local pressure gradients

which forms extra drags on the airflow, similar with the theory of occurrence of adverse pressure gradient as flow above undulating surfaces in section 2.3.3. Hence, in this sublayer, the viscosity of air plays an important role in the momentum transfer. Accordingly, the mass and heat transfer are mainly dominated by the molecular and thermal diffusivity. Universal logarithmic profiles for velocity, temperature, and water vapor are not valid in this sublayer as shown in Figure 2.6. This is similar with the theory of viscous sublayer defined adjacent to a wall in section 2.3.2, but the scale is hugely different. Actually, the same viscous sublayer defined in section 2.3.2 also exists in this interfacial sublayer which contacts with the surface immediately. But considering such a viscous sublayer is on a millimeter scale (Alfredsson et al., 2011; Haghghi & Or, 2015a), but the interfacial sublayer is on tens of centimeters. This extremely thin viscous sublayer is neglected in ABL. In the interfacial sublayer, the vapor concentration profile is described by:

$$\rho_{v,s} - \rho_{v,\text{ref}} = \frac{E}{u_*} \left[ \text{Da}_0^{-1} - \text{Cd}_0^{-1/2} + \frac{1}{\kappa} \ln \left( \frac{z_{\text{ref}} - d_0}{z_{0m}} \right) \right] \quad (2.23)$$

where the subscript “s” and “ref” represent surface and the reference plane, respectively.  $\rho_{v,i}$  ( $\text{kg}/\text{m}^3$ ) is the vapor density (i.e. vapor concentration) at  $i$ -plane ( $i = s, r$ );  $E$  ( $\text{kg}\cdot\text{m}^{-2}\cdot\text{s}^{-1}$ ) is the evaporative flux;  $\text{Da}_0$  is the interfacial mass transfer coefficient (i.e. interfacial Dalton number);  $\text{Cd}_0$  is the interfacial drag coefficient.

Similarly, the temperature profile is described by:

$$T_s - T_{\text{ref}} = \frac{H}{u_* \rho_g c_p} \left[ \text{St}_0^{-1} - \text{Cd}_0^{-1/2} + \frac{1}{\kappa} \ln \left( \frac{z_{\text{ref}} - d_0}{z_{0m}} \right) \right] \quad (2.24)$$

where  $T_i$  (K) is the gas temperature at  $i$ -plane ( $i = s, r$ );  $H$  ( $\text{J}\cdot\text{m}^{-2}\cdot\text{s}^{-1}$ ) is the sensible heat flux at surface;  $c_p$  ( $\text{J}\cdot\text{kg}^{-1}\cdot\text{K}^{-1}$ ) is the heat capacity;  $\text{St}_0$  is the interfacial heat transfer coefficient (i.e. interfacial Stanton number).

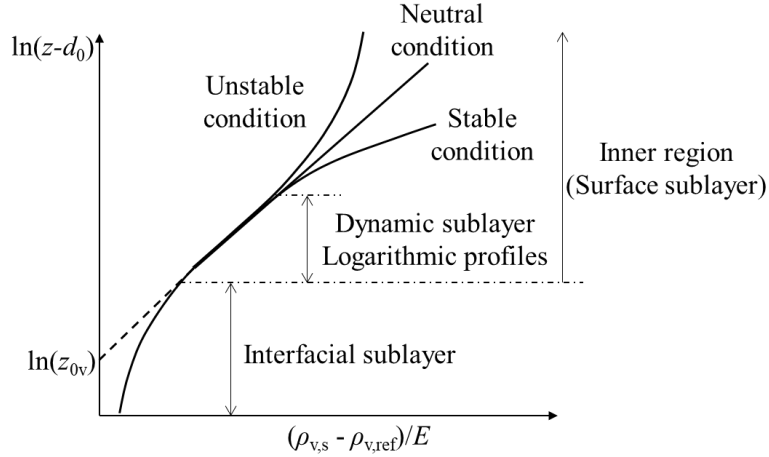


Figure 2.6 Schematic of the normalized vapor density (i.e. vapor concentration) profile in the interfacial sublayer and inner region in single logarithmic coordinate. Dynamic sublayer is the lowest part of the inner region where universal logarithmic profiles are valid.  $z$  is the vertical position,  $d_0$  (m) is the zero-plane displacement,  $z_{0v}$  (m) is the vapor roughness length,  $\rho_{v,s}$  and  $\rho_{v,ref}$  ( $\text{kg}/\text{m}^3$ ) are the vapor density at surface and the reference plane, respectively;  $E$  ( $\text{kg}\cdot\text{m}^{-2}\cdot\text{s}^{-1}$ ) is the evaporative flux.

The dynamic sublayer is located above the interfacial sublayer, which is a fully turbulent flow region. The rough elements at surface, the air viscosity, the molecular and thermal diffusion have negligible effects on the mass, momentum, and heat transfer in this region. Instead, it is the turbulent fluctuation and the accompanying turbulent friction that dominates the motion. Besides, the effect of buoyancy due to the vertical density gradient is also negligible. In this sublayer, the airflow velocity and the passive scalars (e.g. temperature, water vapor concentration) follow the logarithmic law as shown in Figure 2.6. The dynamic sublayer corresponds to the turbulent flow layer introduced in section 2.3.2. The velocity profile in this layer can be characterized the same with equation (2.19). The vapor concentration profile is described by:

$$\rho_{v,s} - \rho_{v,ref} = \frac{E}{\kappa U_*} \ln\left(\frac{z-d_0}{z_{0v}}\right) \quad (2.25)$$

where  $z_{0v}$  (m) is the vapor roughness length. Different from the momentum roughness length  $z_{0m}$ , it depends on both the surface geometry and atmospheric conditions.

Similarly, the temperature profile in this sublayer is described by:

$$T_s - T_{\text{ref}} = \frac{H}{\kappa u_* \rho_g c_p} \ln \left( \frac{z - d_0}{z_{0h}} \right) \quad (2.26)$$

where  $z_{0h}$  (m) is the roughness length for sensible heat, depending on both the surface geometry and atmospheric conditions.

Dynamic sublayer is the lowest part of the surface sublayer where logarithmic profiles are universally satisfied. The sublayer above it is still inside the surface sublayer but the effect of buoyancy due to the vertical density gradient is not negligible. In other words, the stability of atmosphere has to be taken into account. The logarithmic law is only valid under a neutral atmospheric condition (Brutsaert, 2013). Obukhov's stability length  $L$  is introduced to differentiate the atmospheric condition (Obukhov, 1946; Businger & Yaglom, 1971):

$$L = \frac{-u_*^3 \rho_g}{\kappa g \left[ \left( \frac{H}{T_a c_p} \right) + 0.61E \right]} \quad (2.27)$$

where  $T_a$  (K) is a mean reference temperature of the air near the surface. The atmospheric condition is stable for  $L > 0$ , unstable for  $L < 0$ , and neutral if  $L$  is infinitely large. If the atmospheric condition is non-neutral, stability correction terms should be introduced into equations (2.25) and (2.26).

## 2.4 Undulating Soil Surfaces

This research deals with the influence of undulating soil surfaces on evaporation which is formed due to macro-scale surface roughness. Most of the previous studies related to soil evaporation assume a flat surface. Some assumptions, models, and parameter selections in these studies are not valid for undulating surfaces. Both experimental and theoretical approaches are necessary to fill this research gap.

### 2.4.1 Classification of Surface Roughness

Soil surfaces are naturally rough, and the roughness is regarded as the vertical variations relative to an ideally smooth wall. According to the characteristic vertical length scale, Romkens and Wang (1986) described four soil roughness classes (Unger & Cassel, 1991).

(1) Micro-scale roughness, represented by individual sand grains or aggregates with effective diameter smaller than 2 mm.

(2) Macro-scale roughness: random variations in surface elevations due to clods resulted from, for example, tillage on soil. The variation can be up to 10-20 cm and the roughness is non-directionally distributed.

(3) Macro-scale roughness: oriented differences in elevation, such as furrows and ridges in agricultural practice, mainly caused by soil tillage. This kind of variation, usually on the order of dozens of centimeters, is oriented and extends relatively regularly over the entire field.

(4) Quite high-level roughness at the basin scale, such as hills.

The first-class roughness is on a similar order of magnitude with viscous sublayer. The viscous sublayer is the lowest layer of a boundary layer developed above a solid wall (The theory of boundary layer is discussed in detail in the next section.). It is located adjacent with the solid wall directly. The mass and momentum transport in this thin layer are dominated by laminar flow and molecular diffusion (Ounis et al., 1991; Fiolitakis et al., 2014). Fetzer et al. (2016) studied soil evaporation considering micro-scale roughness at soil surface. Negligible effects were observed on the evaporation rate if the roughness scale is on or smaller than the order of viscous sublayer thickness. The fourth-class roughness is commonly found in the study of gas transport in forested hills, turbulent flow over hilly terrain, influence of topography on meteorology, and global hillslope hydrology etc. (Raupach & Finnigan, 1997; Katul et al., 2006; Xu & Yi, 2013; Fan et al.,

2019), far exceeding the goal of this dissertation.

Compared with the first-class micro-scale roughness and fourth-class extremely large-scale roughness, the second and third categories can be measured with a relief meter, a device that measures the elevations of points at regular intervals within a specified area (Unger & Cassel, 1991). These two classes macro-scale roughness have been shown to affect many physical characteristics, such as evaporation, infiltration, solar radiation and reflection, etc. (Zobeck & Onstad, 1987; Unger & Cassel, 1991; Matthias et al., 2000; Cierniewski & Guliński, 2010; Haghighi & Or, 2015a). This dissertational research, thus, will aim at soil evaporation by incorporating roughness of this scale. To avoid confusion, “undulation” rather than “roughness” is used in this research. Accordingly, the surface of soils with undulations is termed undulating soil surface.

#### **2.4.2 Invalid Flat-surface Assumptions for an Undulating Surface**

Most of the studies on soil evaporation are conducted considering a flat surface, whether at small scale (e.g., Yamanaka et al., 1997; Lehmann et al., 2008; Shahræeni et al., 2012; Davarzani et al., 2014) or large scale (e.g., Wallace, 1995; Lawrence et al., 2007; Kool et al., 2014). In terms of the theoretical studies, the common assumptions, modeling approaches, and parameter values adopted in flat-surface evaporation are not valid in the presence of undulating surfaces.

First, a practical three-dimensional evaporation system is typically reduced to be simulated using a one-dimensional model for a flat surface (Vanderborgh et al., 2017), i.e. only the vertical evaporation is considered. But in the case of an undulating soil surface, the evaporative behaviors (e.g., local mass, momentum, and heat transfer, local evaporative flux, etc.) along the surface, in principle, should be distributed distinctively. This is partially caused by the variational distance from the soil surface to the water table. Besides, from the view of atmosphere, the gentle

topographic variations at soil surface alter the airflow direction and allows for convective airflow through the soil at horizontal direction. The local pressure near soil surface may be changed as air flows above an undulating surface. It will, in turn, result in significant changes to the boundary layer pattern relative to a flat surface (Perry et al., 1969; Zilker & Hanratty, 1979; Buckles et al., 1984; Baskaran et al., 1987; Maaß & Schumann, 1996; Cherukat et al., 1998). As a consequence, the mass, momentum, and heat transfer process between the soil and the atmosphere will be markedly affected both locally and globally. In this sense, a two-dimensional model at least should be employed to include the lateral flow and transport process, especially for a fundamental study focusing on mechanism investigation.

Alternatively, for soil evaporation studies at intermediate to large scale, the semi-coupled model and Penman-Monteith equation introduced in section 2.2 are widely adopted. The common feature of these two approaches is that the mass and heat exchange between the soil and the atmosphere is simplified to a vapor / heat flux equation, see equations (2.8)-(2.11) and (2.14)-(2.16). The parameterization of resistance terms (i.e. the aerodynamic resistance and soil resistance) is the heart of all types of the expressions to describe the flux. Generally, for evaporation from a flat and bare soil surface under neutral atmospheric conditions, the roughness lengths for momentum ( $z_{0m}$ ), vapor ( $z_{0v}$ ), and heat ( $z_{0h}$ ) are assumed equal on millimeter scale (e.g., Camillo & Gurney, 1986; Jefferson & Maxwell, 2015). This assumption is not valid in the presence of an undulating surface. The value of  $z_{0m}$  is found dependent on the surface geometry; while  $z_{0v}$  and  $z_{0h}$  rely on both surface geometry and atmospheric boundary layer (Brutsaert, 2013). The macro-scale soil undulations change not only the surface shape, but also the pattern of the atmospheric boundary layer. As a result, the three variables may not be on the same order of magnitude.

### 2.4.3 Investigation of Roughness Lengths for Momentum, Vapor, and Heat

Typically, the roughness lengths for vapor and heat  $z_{0i}$  ( $i = v$  or  $h$ , denoting vapor and heat, respectively) is parameterized in relation with the momentum roughness length  $z_{0m}$  through  $\kappa B^{-1}$  factor, i.e.  $\kappa B^{-1} = -\ln(z_{0i}/z_{0m})$ .  $\kappa (= 0.41)$  is the von Karman constant. For vapor transfer,  $B^{-1}$  is a factor related with the interfacial mass transfer coefficient  $Da_0$  and the interfacial drag coefficient  $Cd_0$  (Brutsaert, 2013). For heat transfer,  $B^{-1}$  is related with the interfacial heat transfer coefficient  $St_0$  and the interfacial drag coefficient  $Cd_0$  (Brutsaert, 2013). In general, both the vapor transfer and heat transfer between the soil and the atmosphere are assumed to be controlled by diffusion and they are typically considered have a similar expression. Therefore, the  $\kappa B^{-1}$  factor is usually constructed for both vapor and heat roughness lengths.

There have been a number of formulations developed empirically, semi-empirically, and theoretically to express  $\kappa B^{-1}$  or  $B^{-1}$  factor (e.g., Verhoef et al., 1997; Kramm et al., 2002; Moriwaki & Kanda, 2006; Vickers & Mahrt, 2006; Liu et al., 2007; Yang et al., 2008; Park et al., 2010; Faivre et al., 2017). A great many datasets have been collected from different surface types (e.g., ocean, bare soil surfaces, soil surfaces with grass, ice or snow, canopy, buildings, etc.) to test these formulations or investigate the values of these roughness lengths or relationship among them (e.g., Sun, 1999; Su et al., 2001; Kramm et al., 2002; Moriwaki & Kanda, 2006; Vickers & Mahrt, 2006; Liu et al., 2007; Yang et al., 2008; Park et al., 2010; Faivre et al., 2017).

As one the most earliest studies, Owen & Thomson (1963) related  $B^{-1}$  factor with the roughness Reynolds number determined by  $Re_0 = u_* z_{0m}/\nu$ , where  $u_*$  (m/s) is the friction velocity and  $\nu$  ( $m^2/s$ ) is the kinetic viscosity:

$$B^{-1} = 2.40 Re_0^{0.45} j^{0.8}, \quad j = Sc, Pr \quad (2.28)$$

where  $j$  denotes Schmidt number and Prandtl number for vapor and heat transfer, respectively.

Garratt & Hicks (1973) tested this model by field data, including various kinds of surfaces and found that for a normal surface covered with vegetation in nature,  $\kappa B^{-1}$  approximated 2 under a wide range of roughness Reynolds number. Afterwards, this constant value was used in some meteorological models. But some studies showed that for a surface with bluff elements or sparse vegetation covers,  $\kappa B^{-1}$  deviated 2 greatly (e.g., Verma & Barfield, 1979; Stewart et al., 1994; Mölder & Lindroth, 2001). Some other studies involving vegetation covered soil surfaces considered that  $\kappa B^{-1}$  relied on leaf area index or the size of leaves (e.g. Qualls & Brutsaert, 1996). Later, Brutsaert (2013) derived a formula based on surface-renewal theory. For a surface with nonpermeable bluff obstacles, this formula is in the form of:

$$B^{-1} = 7.3 \text{Re}_0^{0.25} j^{0.5} - 5, \quad j = \text{Sc}, \text{Pr} \quad (2.29)$$

In case of soil surface covered with ice or snow, Andreas (1987) derived a model based on the above study to predict the roughness length for vapor and heat, which was then widely used in numerical studies (e.g., Morris, 1989; Launiainen & Cheng, 1998; Jordan et al., 1999):

$$\ln \left( \frac{z_{0i}}{z_{0m}} \right) = b_0 + b_1 \ln \text{Re}_0 + b_2 (\ln \text{Re}_0)^2, \quad i = v, h \quad (2.30)$$

where the subscript  $i$  denotes vapor (v) or heat (h);  $b_0$ ,  $b_1$ , and  $b_2$  are coefficients dependent on  $\text{Re}_0$  (Andreas, 1987). Andreas (2002) tested this model with five dataset collected from ice or snow-covered places, in which four were temperature dataset and one was vapor concentration dataset. The results showed that this model matched well with the temperature datasets, while poorly with the vapor datasets. Most recently, Fitzpatrick et al. (2019) used in situ and remote methods to estimate momentum and vapor roughness lengths of two glaciers' surface in Canada over three melt seasons based on eddy covariance observations. Measurement demonstrated the validity of the model proposed by Andreas (1987). Besides, results also showed that the momentum

roughness length was 0.7-4.5 mm for ice-covered surface and 0.5-2.4 mm for snow-covered surface. But the vapor roughness length displayed obvious variations with locations and seasons and differed from the momentum roughness length substantially.

Crago et al. (2005) developed a method based on the complementary evaporation concept (Brutsaert & Stricker, 1979) to estimate the vapor roughness length:

$$\ln\left(\frac{z-d_0}{z_{0v}}\right) = \frac{\kappa u_* \rho}{\left[(2\alpha-1)\frac{\Delta}{\Delta+\gamma} \frac{H+L_e E}{L_e} - E\right] \frac{\Delta+\gamma}{\gamma} \frac{e}{0.622(e_{sat}-e)}} + \psi_v \quad (2.31)$$

where  $z$  (m) is the reference height for temperature and humidity measurement;  $d_0$  (m) is the zero-displacement height;  $\kappa$  is the von Karman constant;  $u_*$  (m/s) is the friction velocity;  $\rho$  (kg/m<sup>3</sup>) is the air density;  $\alpha$  (=1.26) is the Priestley-Taylor parameter;  $\Delta$  (Pa/K) is the slope of the saturation vapor pressure versus temperature;  $\gamma$  is the psychrometric constant;  $H$  (J·m<sup>-2</sup>·s<sup>-1</sup>) is the sensible heat flux;  $L_e$  (J/kg) is the specific latent heat of evaporation;  $E$  (kg·m<sup>-2</sup>·s<sup>-1</sup>) is the evaporation or evapotranspiration rate;  $L_e E$  (J·m<sup>-2</sup>·s<sup>-1</sup>) is the latent heat flux;  $e$  (Pa) and  $e_{sat}$  (Pa) are vapor pressure and saturated vapor pressure at the reference height  $z$ , respectively;  $\psi_v$  is the atmospheric stability correction term. Crago et al. (2005) applied it to a dataset collected from grass-covered soil surface and obtained good prediction. The advantage of this model is that it avoids the measurement of surface temperature or humidity. But it can be only applied based on a strict assumption. That is, a fetch where the surface is statistically homogeneous is present and the fetch should be on the scale of 100 times of the reference height.

There are also formulas of  $\kappa B^{-1}$  constructed based on experimental data.

In case of soil surfaces covered with barley and pasture, Mölder & Lindroth (2001) established an empirical relation between  $\kappa B^{-1}$  factor and the roughness Reynolds number based measured temperature profiles at vertical direction and surface temperature:

$$\kappa B^{-1} = 0.37 \text{Re}_0^{0.3} - (1.2 \text{ or } 1.9) \quad (2.32)$$

where the constant 1.2 and 1.9 are for barley and pasture, respectively.

In case of bog surfaces which are characterized by hummocks and hollows and covered by sparsely vegetation, Mölder & Kellner (2002) established an empirical relation between  $\kappa B^{-1}$  factor and the roughness Reynolds number based on surface temperature measured by an infrared thermometer:

$$\kappa B^{-1} = 1.58 \text{Re}_0^{0.25} - 3.4 \quad (2.33)$$

with momentum roughness length  $z_{0m} \approx 2$  cm. The prediction by this formula was demonstrated between surface with bluff elements and vegetation. This model was used to study the surface energy flux from a Swedish Sphagnum mire (Kellner, 2001), which demonstrated the significance of considering rough elements at soil surface for heat and vapor fluxes from soil surface.

As mentioned by Brutsaert (2013), there is no universal expression for the roughness lengths that is applicable to most situations. There is even no technical standard to show which formulation should be used in a specific situation. The values, and the relationships of the roughness lengths for momentum, vapor, and heat are closely related to the surface type, surface geometry, and atmospheric conditions, etc.

## **2.5 Effect of Airflow on Soil-Atmosphere Interaction**

Soil evaporation essentially deals with mass, momentum, and heat transfer between the soil and the free airflow. The previous studies relevant to the influence of airflow on the soil-atmosphere interactions are roughly divided into the following two categories.

(1) Effect of a mean wind speed on the soil evaporation or the subsurface gas transport

The subsurface gas transport and subsurface-atmosphere gas exchange is widely existent in various research topics, such as soil evaporation, CO<sub>2</sub> emission, methane pipeline leakage, radon

migration into buildings, etc. (e.g., Riley et al., 1999; Davarzani et al., 2014; Basirat et al., 2015; Redeker et al., 2015; Deepagoda et al., 2016). It has been demonstrated somehow related to near-surface wind speed from different research subjects. Davarzani et al. (2014) studied the effect of wind speed on soil evaporation by laboratory experiments and modeling. They found increasing wind speed could increase the evaporation rate in Stage I and short transition, while this impact weakened if further increasing the wind speed. By contrast, the wind speed had negligible effects on the evaporation rate in Stage II when vapor diffusion dominates soil evaporation. Deepagoda et al. (2016) set up a series of laboratory experiments to study the near-surface atmospheric conditions on subsurface methane transport. They showed that the wind speed had a significant effect on methane concentration at surface while not in the subsurface. Levintal et al. (2017, 2019) found wind speed could considerably promote CO<sub>2</sub> transport in high-permeability porous media. Poulsen et al. (2017, 2018) and Poulsen (2019) experimentally demonstrated that wind speed could affect the horizontal gas velocity close to the wind-exposed surface. The main conclusion from most studies similar with the above mentioned is that for single gas phase in the porous media, the near-surface wind speed only influences the gas movement evidently at top surface or deeper if the porous media have a high permeability.

## (2) Effect of air turbulence on the soil evaporation or subsurface gas transport

Different with the wind speed, which denotes a mean value, air turbulence is caused by turbulent airflow (i.e. Reynolds number is larger than the critical value, see section 2.3.1), air pressure fluctuation, or frequent change of wind speed in a wide range. There are numerous theoretical and experimental studies on the air turbulence-affected subsurface gas transport and both laboratory and field experiments have been conducted (e.g., Kimball & Lemon, 1971; Ishihara et al., 1992; Takle et al., 2004; Massman, 2006; Massman & Frank, 2006; Poulsen &

Møldrup, 2006; Maier et al., 2012; Redeker et al., 2015; Poulsen et al., 2017, 2018; Pourbakhtiar et al., 2017). The main conclusion of these studies is that compared with an absolute value of wind speed, air turbulence can influence the subsurface gas transport at a deeper depth, but it still requires that the porous media have a high permeability.

Especially, Haghghi & Or (2013) developed an analytical model to describe the evaporative flux from soil surface into turbulent airflow across the viscous sublayer. This model corresponds to the concept of top boundary condition in the semi-coupled model introduced in section 2.2.2. In this model, the turbulent characteristics were parameterized into the viscous sublayer thickness using eddy exposure time based on surface-renewal theory (Harriott, 1962; Brutsaert, 1975). In brief, this theory considers eddies are loaded by diffusing vapor in the viscous sublayer during their residence and then ejected or renewed by new eddies. This model explicitly quantified the motion of eddies using probability density function method, which had a problem in the reliable determination of the eddy spectrum parameter. Later they proposed a procedure by connecting this viscous sublayer model with MOST-based aerodynamic resistance (see section 2.2.2) to quantify the evaporative flux from soil surface to the upper fully turbulent flow region (Haghghi & Or, 2015c).

## **2.6 Effect of Surface Roughness on Soil-Atmosphere Interaction Under Turbulent Flow**

The studies mentioned in section 2.5 do not include surface roughness. This section discusses the previous studies related to soil-atmosphere interactions considering surface roughness and turbulent airflow.

### **2.6.1 Micro-scale Surface Roughness**

A number of experimental and theoretical studies are found dealing with relevant problems, such as mass transfer across rough porous surface (e.g., Sivykh, 2000; Kim et al., 2020; Lācis et

al., 2020). There are two representative studies that especially contribute to soil evaporation.

Haghighi & Or (2015b) studied evaporation from a soil surface with non-permeable millimeter-scale cylinders on it. The area around a cylinder was divided into three specific zones, i.e. horseshoe vortex, wake region, and unaffected zone (Pattenden et al., 2005), and two cylinders were assumed no interaction with each other. They applied the analytical model developed for evaporative flux into turbulent airflow (Haghighi & Or, 2013) based on the top-boundary-condition concept (see section 2.2.2) to the three specific zones around the cylinders and calculated the average evaporative flux. Results showed the evaporation was enhanced with these protruding elements due to thinner viscous sublayer formed around them. Although the air turbulence is parameterized, this model has a poor application to a large-scale problem. The main reason is that this model explicitly describes the area affected by turbulence. Thus, the locations of the rough elements should be known.

Fetzer et al. (2016) tested the concept of fully coupled model (see section 2.2.1) by simulating soil evaporation under turbulent airflow. The soil surface was assumed with roughness formed by grains. The grain-scale roughness was incorporated into the model via eddy viscosity (Cebeci & Chang, 1978) and coupling condition (Mosthaf et al., 2014). Results showed negligible effect of grain-scale roughness, which is normally on or under the scale of viscous sublayer thickness.

## **2.6.2 Regional-scale Surface Topography**

Most of the studies related to this topic are conducted through regional-scale experiments or modeling in meteorology. The influential factor of concern is not an absolute wind speed or chaotic fluctuations, but layered profiles of wind, humidity, or temperature (see section 2.3.4), which is typically linked with the surface topography, vegetation, canopy, etc. Besides, these

studies focus on the exchange process between the land surface with the upper atmosphere, such as CO<sub>2</sub> transfer between and above canopy or air pollution diffusion (Padro, 1987; Katul et al., 2006; Poggi & Katul, 2007a, 2007b; Chow et al., 2009; Xu & Yi, 2013), water vapor transport due to evapotranspiration (Raupach & Finnigan, 1997; van Heerwaarden, 2011; Liu et al., 2012), etc. In these studies, the land surface is regarded as a bottom boundary and thus the subsurface motion is not included. The main conclusion of the studies in this category is that surface topography or vegetation affects the wind field development, which in turn controls the distribution and movement of the atmospheric scalar through convection or accumulation due to recirculation zones.

### **2.6.3 Macro-scale Undulating-surface Evaporation**

Although rare, there are some studies associated with undulating-surface evaporation by experiments or numerical simulation.

One representative experimental study was conducted by (Verma & Cermak, 1974a, 1974b). They used Styrofoam waves placed on a water-filled pan to experimentally mimic evaporation from undulations. This main finding in this study includes that the mass transfer rate between an undulating surface with the free flow is closely related to the location of recirculation zones (see section 2.3.3 for the definition). The other one is carried out by Sugita and Kishii (2002), who used a wind tunnel together with a lysimeter in their experiments. The results demonstrated the soil evaporation with surface undulations was more sensitive to water table depth and the variation of the undulation intervals could affect the evaporation rate. However, similar with these two studies, the previous experiments relevant to undulating-surface evaporation either focused on only a portion of the overall evaporation stages or failed to simultaneously acquire the atmospheric information. Some other experiments (Cao & Tamura, 2006; Poggi & Katul, 2007a) involving

undulating surfaces used impermeable wavy wall to explore the atmospheric airflow field affected by the surface geometry while no porous media was included.

Alternatively, for modeling work, Fetzer (2018) studied the height and shape of undulations on the system-level evaporation rate using the fully coupled model concept (see section 2.2.1) developed based on DuMu<sup>x</sup> simulator. Since that work aimed at applying DuMu<sup>x</sup> to soil evaporation while not investigating the physical process, the local evaporative behaviors, or the local mass, momentum, and heat transfer features were not discussed. Experiments were not included to validate the numerical simulation. And as mentioned in the last section, this model concept is not applicable for a practical issue. In particular, Haghghi and Or (2015a) conducted an experimental and theoretical study on evaporation from wavy soil surfaces into turbulent airflow. An infrared thermal camera was used to measure soil surface temperature and estimate the surface evaporative flux. This experiment illustrated the clear difference in temperature between peaks and valleys of the undulating surface, denoting distinct local evaporative flux between them. To calculate the evaporative flux theoretically across the viscous sublayer of the wavy surface, they adopted the top-boundary-condition concept (see section 2.2.2) and modified the aerodynamic resistance through an explicit expression for viscous sublayer thickness. The air turbulence was incorporated through the analytical model same with Haghghi and Or (2013, 2015b). The area of recirculation zones formed due to wavy surfaces was expressed as a fixed value. In this way, the influence of the undulating surface was parameterized. However, the boundary layer pattern relies on the specific surface geometry and the atmospheric conditions, which is especially true for the area of recirculation zones (Tampieri, 1987; Poggi & Katul, 2007b; Sherry et al., 2010). Thus, a constant assumption would result in improper parameterization of the undulating surface and boundary layer influenced exchange process. Instead, to account for the

influence, the atmospheric boundary layer information in the presence of the undulating surface should be acquired, which was not considered in their experiment. Besides, the top-boundary-condition concept with parameterization is usually adopted to simplify the description of the mass, momentum, and heat transfer between the soil and the atmosphere. The expression of the boundary layer thickness used in the parameterization is somewhat complex and thus has a poor practical application.

Motivated by the importance of an undulating surface and the corresponding boundary layer on soil-atmosphere interactions during soil evaporation, as well as the current knowledge gap in this problem, this research aims to investigate it from the perspective of both fundamentals and parameterization.

## **2.7 Hypotheses**

According to the importance of the study on undulating-surface evaporation influenced by the near-surface atmospheric boundary layer, as well as the current scarce literature contribution, this research aims to fill this gap based on the following hypotheses to pursue:

(1) A fully coupled model including the mass, momentum, and heat transfer physics between the soil and the atmosphere for undulating-surface evaporation is able to describe the soil evaporation process.

One-dimensional vertical flow and transport model cannot simulate the horizontal or lateral heterogeneity in local evaporative flux. A two-dimensional fully coupled model that characterizes the dynamic soil-atmosphere exchange processes will be developed. Accordingly, the influence of flow and transport at the lateral direction will be minimized in the experimental design.

(2) An undulating soil surface has a significant effect on the development of the boundary layer above it. The combined effects in turn greatly influence soil evaporation behavior.

The macro-scale surface roughness influences the boundary layer pattern. It has been demonstrated numerically and experimentally in fluid dynamic fields at different scales, in which only the free flow and transfer behaviors are considered. In the study of soil evaporation, the boundary layer affected by the surface geometry may further influence the local mass, momentum, and heat transfer between the soil and the atmosphere. Some relevant studies that have been conducted include the effect of wind speed on evaporation or subsurface gas transport (Riley et al., 1999; Poulsen & Møldrup, 2006; Qiao & Zhang, 2010; Davarzani et al., 2014; Levintal et al., 2017; Poulsen et al., 2017, 2018), the effect of air turbulence on subsurface gas movement (Kimball & Lemon, 1971; Ishihara et al., 1992; Maier et al., 2012; Pourbakhtiar et al., 2017), boundary layer influenced gas transport in large scale meteorology (Padro, 1987; Raupach & Finnigan, 1997; Katul et al., 2006; Poggi & Katul, 2007b; Chow et al., 2009; van Heerwaarden, 2011; Xu & Yi, 2013), etc. However, how the near-surface boundary layer pattern under the impact of soil surface geometry influence soil evaporation remain vacant. Alternatively, the boundary layer influenced by the surface geometry shows a feature of locality. The distance between the water table and the undulating soil surface is variational. These two facts can result in a heterogenous distribution of the evaporation flux along the soil surface. Most of the current studies in soil evaporation either assume a flat surface or focus on system-level evaporation rate. An investigation of the local features of the mass, momentum, and heat transfer related to the undulating surface is undetermined.

(3) The influence of undulating surfaces and atmospheric boundary layers can be parameterized through vapor and momentum roughness lengths based on laboratory experimental data.

In terms of the simplified model used in large scale evaporation issues, roughness lengths for momentum, vapor, and heat are important parameters in the description of the soil-atmosphere exchange. Most of the current studies related to soil evaporation assumes a flat surface and the values of these parameters based on this assumption are not valid in the presence of an undulating surface. A theoretical based parameterization, together with the experimental data, to incorporate the influence of soil undulations and the corresponding atmospheric boundary layer is significant. The parameterized roughness lengths based on the laboratory experimental data can be applied to similar soil surface setup. This work can also provide a framework or instruction for similar studies.

## CHAPTER 3

### EVAPORATION FROM AN UNDULATING SOIL SURFACE

#### UNDER LAMINAR AIRFLOW

Modified from an article published in *Water Resources Research*<sup>7</sup> with minor rearrangement

Bo Gao<sup>1,4,5,6</sup>, Hossein Davarzani<sup>2</sup>, Rainer Helmig<sup>3</sup>, Kathleen M. Smits<sup>1,4</sup>

#### 3.1 Abstract

The macroscale roughness of the soil surface has significant influences on the mass/energy interactions between the subsurface and the atmosphere during evaporation. However, most previous works only consider evaporation behavior from flat surfaces. Based on experimental and numerical approaches, the goal of this work is to provide a framework for the understanding of the mechanisms of evaporation from irregular soil surfaces at representative elementary volume scale. A coupling free flow-porous media flow model was developed to describe evaporation under non-isothermal conditions. For simplicity, sinusoidal-type wavy surfaces were considered. To validate this modeling approach, an experiment using an open-ended wind tunnel and soil tank was conducted. The experimental system was instrumented with various environmental sensors to continuously collect atmospheric and subsurface data. Results demonstrate that the surface

---

<sup>1</sup>Department of Civil and Environmental Engineering, Colorado School of Mines, Golden, CO, USA

<sup>2</sup>Bureau de Recherches Géologiques et Minières, Direction Eau, Environnement et Ecotechnologies (D3E), Orléans, France

<sup>3</sup>Department of Hydromechanics and Modelling of Hydrosystems, University of Stuttgart, Stuttgart, Germany

<sup>4</sup>Department of Civil Engineering, University of Texas at Arlington, Arlington, TX, USA

<sup>5</sup>Primary researcher and author

<sup>6</sup>Corresponding author. Direct correspondence to gaobo@mymail.mines.edu.

<sup>7</sup>Reprinted with permission, *Water Resources Research*, 2018, 54(11).

roughness directly affects both atmospheric and diffusion-dominated stages I and II evaporation behavior, respectively. The atmospheric conditions directly affect the boundary layer during stage I. The evaporation rate is determined by the diffusion in the boundary layer, but not that in the porous media. The soil properties exert intrinsic influence on the capillary flow and determine the evaporation amount. The complex interaction between capillarity and the boundary layer leads to a heterogeneous distribution of evaporative flux with undulation (i.e., location along the soil surface) and time. Additionally, more and steeper waves indicate more influence from capillary flow, enhancing evaporation compared to a single wave system with the same wave amplitude, while steeper waves also result in a thicker boundary layer and weaken evaporation.

### **3.2 Introduction**

Evaporation from bare soil surfaces is a key component of the global water cycle, which is closely tied to many industrial activities, climate modeling, weather prediction, agricultural crop growth modeling, and flood forecasting. In arid or semiarid settings, evaporation directly from soil can account for more than half of the total evapotranspiration and therefore critical to its understanding (Huxman et al., 2004). Even though decades of research have improved our understanding of evaporation at the laboratory and regional scales (Budagovskij, 1964; Morton, 1983; Merta et al., 2006; Shuttleworth, 2007; Brutsaert, 2013; Swenson & Lawrence, 2014; Shao et al., 2018), many knowledge gaps still exist in the current science on how the shallow subsurface interacts with the atmosphere during evaporation. Comprehensive understanding of the mechanisms involved in the atmosphere-subsurface interaction is significant to some relevant studies, such as the greenhouse gases emission (Pourbakhtiar et al., 2017) and the remediation of contaminated shallow soil (Weaver & Tillman, 2005). It is also helpful for further modification and improvement of the conventional general circulation models.

To date there have been many experimental and theoretical studies on flat-surface evaporation at different scales. Most previous experimental studies were conducted at the regional scale using different methods, such as eddy covariance, Bowen-Ratio energy balance, lysimeters, and water isotopes (e.g., Kool et al., 2014; Kustas & Agam, 2014). In terms of theoretical studies, the Community Land Model is one of the most frequently used models to simulate the fluid distribution within the whole ecological system (e.g., Oleson et al., 2010). But because of their complexity, these large, global, and regional-scale models/studies are oftentimes aimed at understanding the Earth's climate states or human behavior rather than investigating specific processes, like evaporation. This approach focuses on the entire evaporation amount while oversimplifying the evaporation processes. Another theoretical approach is to use the Penman-Monteith equation alone to calculate evaporation in large-scale hydrological model on the precondition that all the parameters are known (Shao et al., 2018). Other experimental and modeling contributions at smaller scales include those by Lehmann et al. (2008), Shahraeeni et al. (2012), and Haghighi and Or (2013). Based on capillary bundle analysis, Lehmann et al. (2008) proposed a concept called characteristic lengths to define the evaporation stages at the representative elementary volume (REV) scale. REV is defined as the minimum volume of a porous medium sample in which a given geometrical property is independent of the size of the sample (Bear, 2013). It is the fundamental concept of continuum. Shahraeeni et al. (2012) developed a pore-scale model linking the surface water content with the inner capillary flow and the outer boundary layer for simulating evaporation. At the REV scale, Haghighi and Or (2013) employed the advection-diffusion equation in the laminar boundary layer to develop a generalized top boundary condition according to Ohm's law for evaporation, which uses the aerodynamic and soil resistance terms to incorporate the exchange processes between the soil and the atmosphere.

Also, Penman-type equations are oftentimes used as top boundary conditions (Tang & Riley, 2013).

In addition to the above-mentioned approaches, some researchers use more complex models on the basis of REV assumption to describe evaporation from flat surfaces. It is widely accepted that evaporation is a multiphase mass, momentum, and energy exchange process between the soil and the atmosphere, which can be significantly affected by the properties of both the soil (e.g., porosity, permeability, heterogeneity, and thermal and hydraulic conductivity) and the atmosphere (e.g., turbulence, air flow velocity, relative humidity, and radiation). All of these processes are strongly coupled and influence the soil-atmosphere interaction dynamically (Davarzani et al., 2014). The strong coupling between processes leads to highly dynamic interactions between the porous media properties, transport processes, and boundary conditions, resulting in dynamic evaporative behaviors (Sakai et al., 2011). However, the strong coupling at the land-atmosphere interface is rarely considered in most current models or practical application due to numerical model complexity and oftentimes a lack of experimental data needed to verify modeling approaches. But the use of the most complete form of multiphase flow equations in a fully coupled model allows for the investigation of the dominant mechanisms without any preliminary assumptions about the terms that are made in the formulation.

The concept of coupling free flow and porous media flow has been applied in various fields, including proton exchange membrane fuel cells (Baber, 2014), medicine movement inside an organ, multiphase flow through fractured-vuggy reservoirs (Huang et al., 2016), and evaporation from soil (Davarzani et al., 2014; Mosthaf, 2014; Mosthaf et al., 2014). In all these applications, one of the biggest challenges is the coupled interactions between the free flow and porous media flow. In general, there are two main conceptual approaches to describe this coupling, the one-domain and two-domain approaches. The one-domain approach is a simplified method to connect

the free-flow and porous-media regions by assuming that the two regions are continuous in all their physical properties. Thus, only one flow equation, that is, the Brinkman equation (Goyeau et al., 2003), is applied in the entire system. According to the detailed conditions of each domain (i.e., free flow and porous media flow), the Brinkman equation is reduced to either the Navier-Stokes equation (free flow) or Darcy equation (porous media). Therefore, no specific interfacial boundary condition is defined between these two regions. Instead, a transition zone is defined where all the parameters (e.g., permeability and porosity) are continuous. As a result, the choice of these parameters in the transition zone significantly influence the modeling results. Additionally, the Brinkman model has yet to be demonstrated valid for multiphase flow. An alternative method, the two-domain approach, reduces the continuous transition zone to one, no-thickness interface. The Navier-Stokes and Darcy equations are applied separately on either side of this interface. Hence, extra interfacial conditions are imposed. Compared with single-domain approach, this approach has better extensibility, which is able to be extended to multiphase flow. For single-phase flow, similar results can be obtained by these two approaches, while the latter one is more numerically costly. But when multiphases are involved, two-domain approach is physical and accurate. This two-domain approach has been successfully used in multiphase coupling free-flow and porous-media flow problems (Tezduyar et al., 2008; Mosthaf et al., 2011; Baber et al., 2012; Davarzani et al., 2014; Han et al., 2014; Vanderborght et al., 2017).

Mosthaf et al. (2011) discussed the concept of coupling single-phase/two-components free flow and two-phases/two-components porous media flow in detail. They assumed that the interfacial conditions were developed under mechanical, thermal, and chemical equilibrium according to phenomenological explications. The Beavers-Joseph condition (Beavers & Joseph, 1967) was assumed to be valid in the tangential direction of the interface though the condition

originated from parallel single-phase flow. Mosthaf et al. (2014) applied this model to simulate evaporation from a flat, bare soil surface. Fetzer (2012) and Fetzer et al. (2016) extended this model by considering turbulent air flow over flat soil surfaces varying with sand grain roughness. They showed that the effects of the sand grain roughness were only visible for high velocities or large grain sizes. Compared with the above-mentioned methods like energy balance, advection-diffusion equation, and generalized top boundary condition, the coupling free flow and porous media flow model is more complete and physically based. It allows us to improve our understanding of the heat, mass, and momentum transfer processes between the subsurface and the atmosphere during evaporation and provides us guidance for the improvement of simplified parameterizations (e.g., soil and atmospheric resistance terms) by assessing the dominant processes at the interface clearly.

Compared with the studies conducted for flat surfaces, the interaction between the shallow subsurface and the atmosphere is rarely considered for wavy soil surfaces. In this work, the term wavy surface refers to uneven soil surface with macroscale roughness (Canovaro et al., 2007), which is different from the generally recognized surface roughness formed by soil particles. The macroscale roughness here is 1 to 2 orders of magnitude larger than the particle-scale roughness and has a periodicity. In the experiment and modeling of this study, the roughness elements are on tens of centimeters tillage scale, not a hill with big atmosphere in nature. However, the introduction of this macroscale roughness is especially important to agricultural practices (e.g., soil tillage) though this study is only a simple lab-scale model. Tillage practices change the soil surface topology and soil properties, oftentimes resulting in an exposure of soil with high soil moisture content to the atmosphere and hence an increase in evaporation (the reverse can also occur; Unger & Cassel, 1991). Some factors such as tillage depth, surface relief, soil type, and evaporative

demand can influence the drying characteristics of the tilled soils (Mwendera & Feyen, 1997). Therefore, the macroscale surface roughness is one of the important factors which should be taken into consideration. Several studies have shown that soil surface roughness affects water infiltration, water storage in surface depressions, and water runoff (Lehrsch et al., 1987; Guzha, 2004). Studies of energy transport across the soil surface show that the surface roughness can alter the reflectance of sunlight from cultivated soils and thus influence the surface energy balance (Potter et al., 1987; Matthias et al., 2000). Especially, in the case of turbulent atmospheric air flow, the mass and energy exchange process between the subsurface and the atmosphere are more complex for a wavy surface compared to a flat surface due to the formation of separation and reattachment areas, as well as different boundary layers (Perry et al., 1969; Zilker & Hanratty, 1979; Buckles et al., 1984; Baskaran et al., 1987; Maaß & Schumann, 1996; Cherukat et al., 1998). Taylor and Gent (1974) mentioned that the satisfactory inclusion of topography in atmospheric boundary layer models is a nontrivial problem. In other words, the macroscale surface roughness can affect each process associated with land-atmosphere interactions, including radiation, evaporation and drying, saturation distribution, and turbulence (Raupach & Finnigan, 1997). Despite the importance, few mechanistic studies have been conducted on evaporation from bare soil with macroscale roughness. The above-mentioned studies that consider the relief of natural soil surfaces are either limited to field studies for agricultural purposes (Lehrsch et al., 1987; Potter et al., 1987; Mwendera & Feyen, 1997; Matthias et al., 2000; Guzha, 2004) or did not consider the physical processes within the porous media itself (i.e., within the soil; Taylor & Gent, 1974; Maaß & Schumann, 1996; Cherukat et al., 1998; Kruse et al., 2006; Wagner et al., 2011). Particularly, Haghighi and Or (2015a) studied evaporation from wavy porous surfaces into turbulent free flow at the REV scale. In this study, they extended the expression of the aerodynamic resistance term that they developed for flat

surfaces, in which the piecewise boundary layer thickness under turbulent air flow over wavy surfaces was taken into account. They conducted experiments using time domain reflectometry to qualitatively judge the contribution of valleys and ridges to evaporation based on the soil surface temperature distribution. Combined with a simple data analysis technique, the experimental temperature data were used to infer evaporation rates, which they then compared with predictions from the modified top boundary condition equation. This study showed that the mean evaporative flux across the wavy soil surface may be enhanced or suppressed compared with a similar flat surface. The authors inferred that the enhancement and suppression was due to the boundary layer thickness (thicker with wavy surfaces), the larger area present in wavy surfaces compared to flat surfaces and flux suppression in the separation flow region. However, experimental and numerical results demonstrating this behavior were not presented as the simple models cannot describe all the physical processes in evaporation clearly.

The objectives of this study are to (i) develop a coupling free flow and porous media flow model to describe evaporation from wavy surfaces; (ii) perform a controlled bench-scale experiment to validate this model; (iii) improve our understanding of the characteristics of evaporation at the REV scale; (iv) investigate how and why the macroscale surface roughness influences the evaporation. For simplicity, to represent macroscale roughness (i.e., wavy surfaces) sinusoidal-type waves are considered. We emphasize that this study considers tens of centimeters roughness-surface model on lab scale. The results are based on the length scales of the experimental and numerical domains which may not truly mimic more realistic soil-atmosphere continuum scales at tens of thousands of meters due to heterogeneity.

According to the objectives, this chapter is structured as follows: in section 3.3, we present the theoretical background and mathematical model to couple the flow and transport processes

between the atmosphere and subsurface; in section 3.4, the experimental setup is described in detail; the numerical and experimental results are compared in section 3.5, first to validate the numerical model. Finally, the characteristics and influential factors of evaporation from wavy soil surfaces are discussed.

### 3.3 Mathematical Model

In this section, we present the mathematical description of heat and mass transfer of atmospheric air flow over uneven (i.e., wavy) permeable soil surfaces during evaporation. As introduced above, this process can be described by coupling free flow and porous media flow under non-isothermal conditions based on the REV-scale assumption.

This work is implemented on a two-dimensional configuration as shown in Figure 3.1. The width and the height of the whole system is 0.6 m and 0.3 m, respectively. For simplicity, the soil surface is represented by a simple sinusoidal line, which divides the system into two subdomains. The lower part is the shallow soil and the upper part is the free flow close to the soil surface. Wavy surfaces are usually characterized by aspect ratios, which is defined by  $2\gamma/\lambda$  (where  $2\gamma$  and  $\lambda$  are amplitude and wavelength, respectively). According to the two-domain approach, the equations in the atmosphere and the soil are defined separately, which are introduced here in detail.

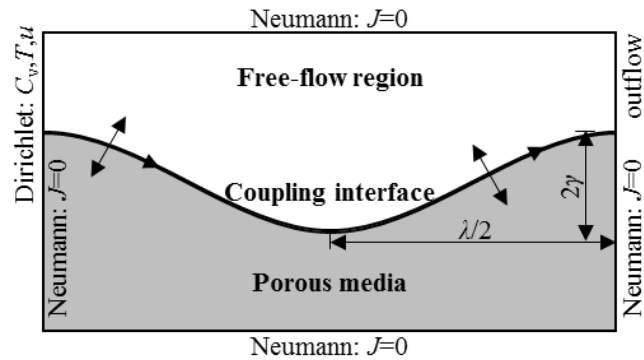


Figure 3.1 Two-dimensional configuration (subdomains and boundary conditions) where  $C_v$  is the water vapor concentration,  $T$  is the temperature,  $u$  is the wind speed,  $J$  is the flux for  $T$ ,  $u$  and  $C_v$ ,  $\lambda$  is the wave length, and  $\gamma$  is half of the wave amplitude.

### 3.3.1 Governing Equations for Free Flow

In the free flow, we assume that a single gas phase exists that is composed of two components, dry air and water vapor. The flow is non-isothermal and incompressible, and gravity is neglected. The fluid flow in the free-flow domain can be described by Navier-Stokes equation, assuming no thermal or solutal expansion (Bird et al., 2004):

$$\nabla \cdot \mathbf{u}_g^{\text{ff}} = 0 \quad (3.1)$$

$$\rho_g \frac{\partial \mathbf{u}_g^{\text{ff}}}{\partial t} + \rho_g (\mathbf{u}_g^{\text{ff}} \cdot \nabla) \mathbf{u}_g^{\text{ff}} = \nabla \cdot \left[ -p_g^{\text{ff}} \mathbf{I} + \mu_g \left( \nabla \mathbf{u}_g^{\text{ff}} + (\nabla \mathbf{u}_g^{\text{ff}})^T \right) \right] \quad (3.2)$$

where the superscript “ff” denotes the free-flow region and the subscript “g” denotes the gas phase.

$\mathbf{u}_g^{\text{ff}}$  (m/s) and  $p_g^{\text{ff}}$  (Pa) are the air flow velocity and pressure in the free-flow region;  $\mathbf{I}$  is the unit matrix;  $\rho_g$  (kg/m<sup>3</sup>) and  $\mu_g$  (Pa·s) are the density and dynamic viscosity of the moist air, both of which depend on temperature and the fraction of water vapor in the gas. Their values are updated real time during calculation.

The component mass balance equation for water vapor in the free-flow region is defined by (Bird, 2002):

$$\frac{\partial (\rho_g w_v^{\text{ff}})}{\partial t} + \nabla \cdot (\rho_g w_v^{\text{ff}} \mathbf{u}_g^{\text{ff}}) - \nabla \cdot [D_v^{\text{ff}} \nabla (\rho_g w_v^{\text{ff}})] = 0 \quad (3.3)$$

where  $w_v^{\text{ff}}$  is the mass fraction of water vapor in the gas phase and  $D_v^{\text{ff}}$  (m<sup>2</sup>/s) is the diffusion coefficient in the free-flow region.

The energy balance equation in the free-flow region is (Kaviany & Kanury, 2002):

$$\left( \rho_g c_{p,g} \right) \frac{\partial T^{\text{ff}}}{\partial t} + \left( \rho_g c_{p,g} \right) \nabla \cdot (\mathbf{u}_g^{\text{ff}} T^{\text{ff}}) - \nabla \cdot (\lambda_g \nabla T^{\text{ff}}) = 0 \quad (3.4)$$

where  $T^{\text{ff}}$  is the temperature (K),  $c_{p,g}$  (J·kg<sup>-1</sup>·K<sup>-1</sup>) is the heat capacity of the moisture air, and  $\lambda_g$

( $\text{W}\cdot\text{m}^{-1}\cdot\text{K}^{-1}$ ) is the thermal conductivity of gas mixture.

### 3.3.2 Governing Equations for Porous Media Flow

We assume that two phases, gas and water, exist in the porous media, and there are two components in the gas: water vapor and dry air. The dissolution of air in the water is neglected and these two fluids are immiscible. The two-phase flow in the porous media is always described by the generalized form of Darcy's law on the REV scale.

The mass balance equations of these two phases are (Bear, 2013):

$$\begin{aligned} \phi \frac{dS_w}{dp_c} \frac{\partial(\rho_w p_c)}{\partial t} + \nabla \cdot (\rho_w \mathbf{u}_w^{\text{pm}}) &= -f_{\text{vw}} \\ \phi \frac{dS_g}{dp_c} \frac{\partial(\rho_g p_c)}{\partial t} + \nabla \cdot (\rho_g \mathbf{u}_g^{\text{pm}}) &= f_{\text{vw}} \end{aligned} \quad (3.5)$$

where the superscript “pm” denotes the porous media and the subscript “w” denotes the water phase.  $S_i$  ( $i = w, g$ ) is the saturation of  $i$  phase,  $\phi$  is the porosity of the porous media,  $p_c$  is the capillary pressure between the water and gas, and  $f_{\text{vw}}$  is the water-gas phase change rate during evaporation.

The phase change between the liquid water and water vapor can be defined by a local equilibrium assumption or by considering the nonequilibrium behavior. In hydrologic studies, it is commonly assumed that the water vapor concentration in the air is always in equilibrium with liquid water in the pores. Under this assumption, the phase exchange happens within a negligible time interval. There are also several studies that demonstrated the importance of considering nonequilibrium phase change in modeling efforts of evaporation (Benet & Jouanna, 1982; Armstrong et al., 1994; Smits et al., 2011).

Halder et al. (2011) discussed the equilibrium and nonequilibrium formulation of phase change in detail. Under the equilibrium assumption, the vapor pressure is always equal to the

equilibrium vapor pressure at a given temperature and moisture condition. We can calculate the equilibrium vapor pressure based on Kelvin's equation and then the vapor concentration according to Henry's law. Thus, the phase change rate,  $f_{vw}$ , comes out of the solution since all the terms on the left-hand side of the component mass balance equation (Eq. (3.3)) are known (Halder et al., 2011). In other words, this source term is implicit under the equilibrium assumption, which is difficult to incorporate in the numerical calculation. On the other hand, when we consider nonequilibrium, there is a time interval,  $\Delta t$ , for the system to reach equilibrium after phase change (i.e., evaporation or condensation). A commonly used nonequilibrium phase change rate term is defined by (Bixler, 1985; Smits et al., 2011):

$$f_{vw} = \frac{b\phi(S_w - S_{rw})RT}{M_w}(\rho_{v,eq} - \rho_v) \quad (3.6)$$

where  $b$  is a fitting parameter,  $R$  is the universal gas constant ( $8.314 \text{ J}\cdot\text{mol}^{-1}\cdot\text{K}^{-1}$ ),  $M_w$  is molecular mass ( $\text{kg}/\text{mol}$ ),  $\rho_{v,eq}$  is the density of vapor at equilibrium ( $\text{kg}/\text{m}^3$ ), and  $\rho_v$  is the vapor density at any condition ( $\text{kg}/\text{m}^3$ ). The vapor density at equilibrium is defined by

$$\rho_{v,eq} = \rho_{v,sat} \exp\left(\frac{M_w p_c}{\rho_w RT}\right) \quad (3.7)$$

according to Kelvin's equation, where  $\rho_{v,sat}$  is the saturated vapor density ( $\text{kg}/\text{m}^3$ ). The saturated vapor density is estimated empirically (Campbell, 1985):

$$\rho_{v,sat} = \frac{\exp(31.37 - 6014.79T^{-1} - 7.92 \times 10^{-3}T)}{T} \times 10^{-3} \quad (3.8)$$

Clearly, this results in an explicit source term representing liquid-gas phase change rate in the mass balance equation. According to Halder et al. (2011), the equilibrium time is around  $10^{-6}$  s for a  $1\text{-}\mu\text{m}$  distance assuming only pure molecular diffusion exists. In other words, it is meaningless to introduce nonequilibrium phase change if all the transport time scales are much

more than the equilibrium time at the same length scale. However, the nonequilibrium phenomenon cannot be ignored if the pore size is equal to or less than 0.1 mm. Therefore, in our simulation where the pore size is approximately 0.1 mm, it is necessary to take the nonequilibrium phase change into consideration. The integrated constant coefficient in Eq. (3.6),  $B = bRT/M_w$ , denotes the reciprocal of the equilibrium time. As the fitting parameter  $b$  becomes infinitely large, the nonequilibrium phase change term will reduce to an equilibrium state.

The velocity in Eq. (3.5) is determined by Darcy's law:

$$\mathbf{u}_i^{\text{pm}} = -\frac{K_{\text{int}} k_{ri}}{\mu_i} (\nabla p_i^{\text{pm}} + \rho_i \mathbf{g}) \quad , \quad i = \text{w, g} \quad (3.9)$$

where  $K_{\text{int}}$  is the intrinsic permeability of the soil;  $k_{ri}$  ( $i = \text{w, g}$ ) is the relative permeability of  $i$ -phase. van Genuchten model is used for the water retention curve and relative permeability (van Genuchten, 1980) see Appendix 0;  $\mathbf{g}$  is the gravitational acceleration.

The mass balance equation for the two components in the gas is described by (Bear, 2013):

$$\phi \frac{\partial (\rho_g w_v^{\text{pm}} S_g)}{\partial t} + \nabla \cdot (\rho_g w_v^{\text{pm}} \mathbf{u}_g^{\text{pm}}) - \nabla \cdot [D_v^{\text{pm}} \nabla (\rho_g w_v^{\text{pm}})] = f_{\text{vw}} \quad (3.10)$$

where  $D_v^{\text{pm}}$  is the effective diffusion coefficient in the porous media, which is determined by:

$$D_v^{\text{pm}} = \phi S_g \tau D_v \quad (3.11)$$

where  $D_v$  is the gas phase diffusion coefficient (Campbell, 1985) and  $\tau$  is the tortuosity of the porous media, which is estimated according to Millington and Quirk model (Millington & Quirk, 1961) see Appendix 0.

The governing equation for temperature in the porous media is given by (Whitaker, 1977):

$$(\rho c_p)_{\text{eff}} \frac{\partial T^{\text{pm}}}{\partial t} + \nabla \cdot \left[ \sum_{i=\text{w, g}} (\rho c_{p,i}) \mathbf{u}_i^{\text{pm}} T^{\text{pm}} \right] - \nabla \cdot (\lambda_{\text{eff}} \nabla T^{\text{pm}}) = -L f_{\text{vw}} - Q_s \quad (3.12)$$

$$\left(\rho c_p\right)_{\text{eff}} = \phi S_w \rho_w c_{p,w} + \phi S_g \rho_g c_{p,g} + (1-\phi) \rho_s c_{p,s} \quad (3.13)$$

where  $c_{p,i}$  is the heat capacity of  $i$ -phase ( $i = w, g, s$ ) ( $\text{J}\cdot\text{kg}^{-1}\cdot\text{K}^{-1}$ );  $\lambda_i$  is the thermal conductivity of  $i$ -phase ( $i = w, g, s$ ) ( $\text{J}\cdot\text{kg}^{-1}\cdot\text{K}^{-1}$ );  $\lambda_{\text{eff}}$  is the effective thermal conductivity of all the phases including water, gas and solid grain, which is defined by (Nield & Bejan, 2006):

$$\lambda_{\text{eff}} = \phi S_w \lambda_w + \phi S_g \lambda_g + (1-\phi) \lambda_s \quad (3.14)$$

The subscript “s” in Eq. (3.13) and (3.14) denotes the solid phase.  $Q_s$  and  $L$  in Eq. (3.12) describe the energy losses from the soil tank and latent heat during water vaporization (Moradi et al., 2015).

### 3.3.3 Coupling Conditions on the Interface

Since different model concepts are used in the free-flow and porous media regions, extra interfacial conditions are necessary to couple the two subdomains (Mosthaf et al., 2011; Davarzani et al., 2014; Fetzer et al., 2016) based on the assumption of local mechanical, chemical and thermal equilibrium.

#### (1) Continuity of total mass flux

Considering there is only a gas phase that exchanges between the free-flow region and the porous media, the continuity of total mass flux in the normal direction of the interface should be:

$$\left(\rho_g \mathbf{u}_g^{\text{ff}}\right) \cdot \mathbf{n}^{\text{ff}} = -\left(\rho_g \mathbf{u}_g^{\text{pm}}\right) \cdot \mathbf{n}^{\text{pm}} \quad (3.15)$$

where  $\mathbf{n}$  denotes the normal vector of the interface.

#### (2) Continuity of normal stress

The normal stress at the interface is continuous:

$$\left\{ \left[ p_g^{\text{ff}} \mathbf{I} - \mu_g \left( \nabla \mathbf{u}_g^{\text{ff}} + \left( \nabla \mathbf{u}_g^{\text{ff}} \right)^T \right) + \rho_g \left( \mathbf{u}_g^{\text{ff}} \cdot \nabla \right) \mathbf{u}_g^{\text{ff}} \right] \mathbf{n}^{\text{ff}} \right\} \cdot \mathbf{n}^{\text{ff}} = p_g^{\text{pm}} \quad (3.16)$$

### (3) Slip condition of tangential stress

In the tangential direction of the interface, the traditional Beavers-Joseph-Saffman (BJS) condition (Beavers & Joseph, 1967; Mosthaf et al., 2011; Mosthaf, 2014) is used to describe the tangential stress jump:

$$\left[ \mathbf{u}_g^{\text{ff}} + \frac{\sqrt{K_{\text{int}}}}{\alpha_{\text{BJ}}} \left( \nabla \mathbf{u}_g^{\text{ff}} + (\nabla \mathbf{u}_g^{\text{ff}})^{\text{T}} \right) \mathbf{n}^{\text{ff}} \right] \cdot \mathbf{t}_i^{\text{ff}} = 0, \quad i \in \{1, 2, \dots, d-1\} \quad (3.17)$$

where  $\mathbf{t}^{\text{ff}}$  denotes the tangential vector at the interface,  $d$  is the dimension of the modeling system and  $\alpha_{\text{BJ}}$  is the slip coefficient. The value of the slip coefficient depends on the properties of the porous media and the fluids, as well as the grain-size roughness of the interface, which is often empirically determined. According to Mosthaf (2014), Davarzani et al. (2014) and Huang et al. (2016), the slip coefficient has little influence on the model output. Thus, we set the slip coefficient to 0.01 for this study. In most studies, the BJS tangential condition is implemented under the condition that a single fluid phase exists throughout the whole system and the fluid flows parallel to the permeable porous media surface (Beavers & Joseph, 1967). However, because we assume laminar air flow velocity and the hypothesis that the two-phase water-gas at the top of the porous media has little influence on the tangential condition, we assume the BJS is still applicable in our model.

### (4) Continuity of temperature and heat flux

Assuming local thermodynamic equilibrium, the temperature and the heat flux at the interface are continuous (Mosthaf et al., 2011; Davarzani et al., 2014; Mosthaf, 2014):

$$T^{\text{ff}} = T^{\text{pm}} \quad (3.18)$$

$$\left[ (\rho_g c_{p,g}) \mathbf{u}_g^{\text{ff}} T^{\text{ff}} - \lambda_g \nabla T^{\text{ff}} \right] \cdot \mathbf{n}^{\text{ff}} = - \left[ \sum_{i=w,g} (\rho c_{p,i}) \mathbf{u}_i^{\text{pm}} T^{\text{pm}} - \lambda_{\text{eff}} \nabla T^{\text{pm}} \right] \cdot \mathbf{n}^{\text{pm}} \quad (3.19)$$

(5) Continuity of vapor concentration and vapor flux is described by (Mosthaf et al., 2011; Mosthaf, 2014):

$$w_v^{\text{ff}} = w_v^{\text{pm}} \quad (3.20)$$

$$\left[ \rho_g w_v^{\text{ff}} \mathbf{u}_g^{\text{ff}} - D_v^{\text{ff}} \nabla (\rho_g w_v^{\text{ff}}) \right] \cdot \mathbf{n}^{\text{ff}} = - \left[ \rho_g w_v^{\text{pm}} \mathbf{u}_g^{\text{pm}} - D_v^{\text{pm}} \nabla (\rho_g w_v^{\text{pm}}) \right] \cdot \mathbf{n}^{\text{pm}} \quad (3.21)$$

A summary of the equations to be solved and their corresponding primary variables is listed in Table 3.1.

Table 3.1 List of model equations and the primary variables

	Equation Type	Equation Number	Primary Variables
Free-flow subdomain	Total mass continuity and Navier-Stokes	(3.1), (3.2)	$\mathbf{u}_g^{\text{ff}}, p_g^{\text{ff}}$
	Component mass balance for gas phase	(3.3)	$w_v^{\text{ff}}$
	Energy balance	(3.4)	$T^{\text{ff}}$
Porous- media subdomain	Total mass balance and Darcy's law	(3.5), (3.9)	$p_w^{\text{pm}}, p_g^{\text{pm}}$
	Component mass balance	(3.10)	$w_v^{\text{pm}}$
	Energy balance	(3.12)	$T^{\text{pm}}$

### 3.3.4 Boundary Conditions and Initial Conditions

As shown in Figure 3.1, the left, right and bottom boundaries of the porous media are closed where Neumann conditions are applied:

$$-\mathbf{n}^{\text{pm}} \cdot \mathbf{u}_i^{\text{pm}} = 0, \quad (i = w, g) \quad (3.22)$$

We assume that the center line of the free-flow region has the largest wind speed, which is considered as the top boundary, thus the following no viscous stress and normal flow conditions should be satisfied:

$$\begin{aligned} \mathbf{u}_g^{\text{ff}} \cdot \mathbf{n}^{\text{ff}} &= 0 \\ \left[ \mu_g \left( \nabla \mathbf{u}_g^{\text{ff}} + (\nabla \mathbf{u}_g^{\text{ff}})^T \right) \right] \mathbf{n}^{\text{ff}} - \left\{ \left[ \mu_g \left( \nabla \mathbf{u}_g^{\text{ff}} + (\nabla \mathbf{u}_g^{\text{ff}})^T \right) \right] \cdot \mathbf{n}^{\text{ff}} \right\} \mathbf{n}^{\text{ff}} &= 0 \end{aligned} \quad (3.23)$$

The left boundary of the free-flow region is set as the inlet, where a laminar inflow with a constant average velocity, constant vapor concentration and temperature are specifically defined. The right boundary of the free-flow region is the outlet and the manometer pressure is zero.

Initially, the porous media region is saturated with water. The vapor concentration in the free-flow region and the temperature of the whole system are the same as the inflow boundary. The mathematical model is implemented using COMSOL Multiphysics 5.2a (Comsol, 2016) based on the finite element method. The whole computation system was discretized with triangular mesh by 13,162 elements (71262DOFs). Local mesh refinement was applied at the interface due to possible formation of large gradients. An initialization was set up before the real calculation. The included linear parallel sparse direct solver (PARDISO) was used to implicitly solve the models.

### **3.4 Experimental Setup**

To validate the above mathematical model, we designed an experimental system to simulate evaporation from a wavy soil surface. A series of data, including soil moisture, temperature, and pressure, as well as ambient relative humidity, temperature, and pressure are collected. This section presents the sand material properties, experimental apparatus and procedures in detail.

#### **3.4.1 Sand Properties**

A uniform silica sand, Accusand #50/70 (effective sieve number, Unimin Corp., Ottawa, MN) was used for this experiment. This sand has been widely characterized and used in previous works at the laboratory scale (Sakaki & Illangasekare, 2007; Davarzani et al., 2014; Moradi et al., 2015). Therefore, the key hydraulic/thermal properties are known (Table 3.2) and not used as fitting parameters so that the key physics can be more accurately described. This sand has low organic content and 99.8% quartz content, with a rounded grain shape. The uniformity coefficient,

defined as  $d_{60}/d_{10}$ , is approximately 1.2 and the mean grain size  $d_{50}$  is 0.26 mm (Zhang et al., 2008). The porosity of the packed soil tank is about 0.364, similar to the experiments in (Zhang et al., 2008; Forsythe, 2017). The capillary pressure ( $p_c$ ) and water content ( $\theta_w$ ) relationship was measured using a small Tempe cell apparatus (Forsythe, 2017). For convenience in numerical modeling, the van Genuchten model in Appendix 0 was first used to fit the experimental  $p_c - \theta_w$  data, and the fitting parameters  $\alpha$  and  $n$  were obtained. Relevant properties of the porous media are listed in Table 3.2.

Table 3.2 Important porous media properties

Porosity	Bulk density	Saturated hydraulic conductivity	Intrinsic permeability	Residual water content	Thermal conductivity		Van Genuchten parameters ( $m = 1-1/n$ )	
$\phi$	$\rho_b^a$	$K_{sat}^a$	$K_{int}^a$	$\theta_r^a$	$\lambda_{dry}^a$	$\lambda_{sat}^a$	$\alpha^b$	$n^b$
-	$\text{g/cm}^3$	$\text{m/s}$	$\text{m}^2$	-	$\text{W}\cdot\text{m}^{-1}\cdot\text{K}^{-1}$		$\text{m}^{-1}$	-
0.364	1.69	0.00036	$3.5\times 10^{-11}$	0.005	0.367	3.297	5	7

<sup>a</sup>Deepagoda et al. (2016)

<sup>b</sup>Forsythe (2017)

### 3.4.2 Experimental Apparatus

A controlled bench-scale laboratory experiment was conducted using a low-velocity open-return wind tunnel that was interfaced with a 2-D soil tank as shown in Figure 3.2. The ductwork forming the wind tunnel is made of galvanized steel and oriented with the 2-D soil tank to channel air flow across the test section. To produce and control the wind, an in-line fan (Suncourt Pro Model DB6GTP) was connected to a velocity controller and a damper. The wind speed was continuously measured using a pre-calibrated pitot static tube (Dwyer Instruments, Inc.; Model 167-12; Accuracy  $\pm 5\%$ ) placed at the centerline of the tunnel. The soil tank was constructed with acrylic glass with length of 60 cm, height 30 cm, and width 9 cm. Compared with the length and width, the tank is thin and therefore can be considered as a two-dimensional tank.

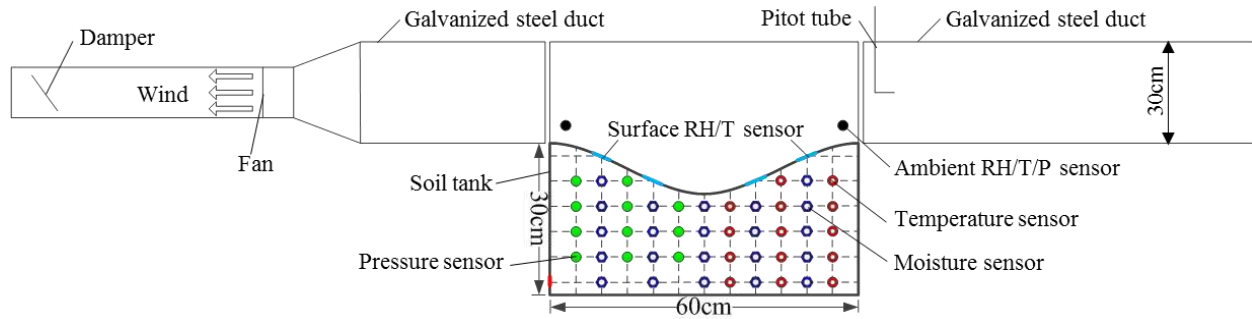


Figure 3.2 Schematic of the experimental system.

As shown in Figure 3.2, 22 moisture sensors (Decagon Devices Inc., ECH<sub>2</sub>O EC-5, moisture frequency 70 MHz, accuracy  $\pm 3\%$ ) were spaced at 10-cm increments horizontally and 5-cm increments vertically throughout the tank. Measurements were collected as analog to digital converter counts and then converted to soil moisture using the two-point  $\alpha$ -mixing model (Sakaki et al., 2008). The subsurface temperature was monitored using 14 temperature sensors (Decagon Devices Inc., RT-1, accuracy  $\pm 0.5$  °C for measurement from 5 to 40 °C). Eleven pressure sensors (Tensiometer, Soilmoisture Equipment Corp., Goleta, CA; pressure transducer, Omega Engineering, Inc., Stamford, CT, Model PX26 Series, accuracy  $\pm 1\%$  psi for the range 0-250 psi, operating temperature: -40 to 85 °C) were located throughout the tank to measure the pore water pressure. The moisture, temperature, and pressure sensors were inserted horizontally through the sides of the acrylic tank to minimize their volume within the tank and hence their effect on the flow processes within the tank. At the soil surface, there were four sensors distributed uniformly to record the surface relative humidity and temperature (Decagon Services, Inc., EHT RH/temperature, accuracy  $\pm 2\%$  from 5 to 90% RH;  $\pm 3\%$  from 90 to 100% RH; temperature accuracy  $\pm 0.25$  °C). The relative humidity/temperature sensors were placed in contact with the soil grains directly. In addition, four VP-4 sensors (Decagon Devices, Inc.; resolution 0.1% RH, 0.1 °C temperature, and 0.01 kPa pressure; accuracy  $\pm 5\%$  RH,  $\pm 0.5$  °C temperature,  $\pm 0.4$  kPa pressure)

were located above the soil surface (two at the inlet of the free-flow region, two at the outlet, see Figure 3.2) to measure the atmospheric relative humidity, temperature, and pressure. All the moisture, temperature, and relative humidity sensors were connected to Em50 series data loggers (Decagon Services, Inc., ECH<sub>2</sub>O System) to store the corresponding data hourly.

### **3.4.3 Experimental Procedures**

The subsurface moisture, temperature, and pressure sensors were tested and calibrated first and then inserted into the corresponding locations of the soil tank. The tank was then wet-packed with #50/70 silica sand (Accusand, Unimin Corporation, Ottawa, MN) in incremental 2-cm layers to achieve a uniform bulk density (Sakaki & Illangasekare, 2007). The soil surface was constructed using a prefabricated metal mold as a sinusoidal-type wavy shape with a wave amplitude of 5 cm, as shown in Figure 3.2. We did our best to make sure the water table was initially at the soil surface. However, because of the wavy shape, a small amount of water accumulated at the bottom of each wave (i.e., in the valley) which was unavoidable based on the soil properties. Before starting the experiment, the soil surface was covered with plastic wrap to prevent evaporation. The side and the bottom walls of the tank did not allow for fluid flow and the valve at the bottom of the tank was shut off so that no water was supplied at the bottom boundary. Then, the tank was placed on a scale (Sartorius Model 11209-95, Range 65 kg, Resolution  $\pm 1$  g) to continuously monitor the water loss from the system. The wind tunnel fan was then set to a constant low speed of 0.08 m/s. A low wind speed was selected to maintain laminar flow conditions ( $Re \approx 580$ ), considering the design of the soil tank, the wind tunnel, and the measurement accuracy of the pitot tube. Thus, turbulence could be neglected. Finally, the plastic wrap was removed from the soil surface and the experiment was initiated; the experiment was run for 46 days.

### 3.5 Results and Analysis

In this section, the experimental and numerical results are first compared to validate our modeling approach. This is followed by a discussion of the evaporation behavior at the REV scale and an analysis of several factors such as atmospheric conditions, soil properties, and surface geometry.

#### 3.5.1 Comparison of Numerical and Experimental Results

Experimental and numerical results are first compared to verify the coupling model presented in section 3.3. Experimental data to include the wind speed and temperature in the air flow and the vapor concentration (determined based on the relative humidity) were used as the boundary conditions in the simulation (see Table 3.3). It is important to note that the laboratory central heating system was turned on at day 18 of the experiment. Therefore, the average ambient temperature increased by  $\sim 3$  °Kelvin, according to the data. Thus, the simulation was divided into two sections due to the changes of boundary conditions (see Table 3.3). This change influenced the one fitting parameter of the model,  $b$ , in the phase change rate expression. For  $t \leq 18$  days  $b$  was  $1.2 \times 10^{-4}$  s/m<sup>2</sup> and for  $5.8 \times 10^{-5}$  s/m<sup>2</sup> after 18 days by fitting the cumulative evaporation data. The corresponding equilibrium time  $1/B$  (The definition of  $B$  is shown in 3.3.2) for phase change is on the order of magnitude  $O(10^{-1})$ , which is similar to other transport time scales (e.g., capillary diffusion and heat flow, Halder et al., 2011). It also indicates that nonequilibrium phase change should be taken into consideration.

Table 3.3 Average atmospheric experimental data

Time	Wind speed (m/s)	Temperature (K)	Vapor concentration (kg/m <sup>3</sup> )	Pressure (kPa)
$t \leq 18$ days	0.08	293.8	0.0064	82.54
$t > 18$ days	0.08	296.3	0.0036	82.54

Figure 3.3 shows the comparison of the simulated and observed cumulative evaporated mass over time. Generally, there is a good agreement between the simulated and experimental results with a  $R^2$  value of 0.987. The observed soil evaporation curve shows relatively gentle changes with time and does not present obvious drying stages owing to the very low wind speed (0.08 m/s) in this experiment. The evaporation remained in stage I for about 30 days and came to stage II without an obvious transition period.

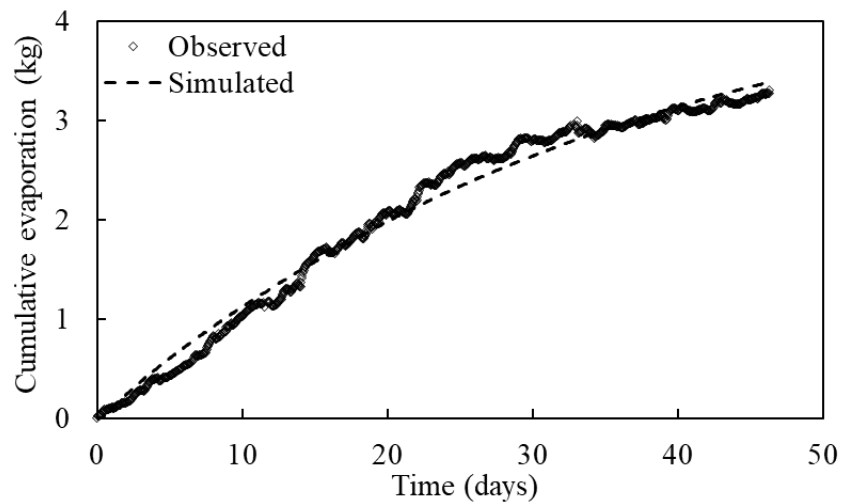


Figure 3.3 Comparison of the simulated and observed cumulative evaporation over time (rhombus marks: the observed data from experiment; dash line: the simulated results).

Figure 3.4a shows the time distribution of soil moisture for four measurement depths (7.5, 12.5, 17.5, and 22.5 cm below the soil surface). The numerical model could predict the evolution of the soil moisture well at the early times but failed to capture the moisture at later times (i.e., approximate  $t = 20$  days). The  $R^2$  values for the depths 7.5, 12.5, 17.5, and 22.5 cm are 0.93, 0.92, 0.92, and 0.92, respectively. Figure 3.4b compares the observed and simulated moisture profiles at  $x = 10$  cm (the first moisture sensor column) at three different times (10, 20, and 35 days). The  $R^2$  values for this comparison are 0.99, 0.98, and 0.97 at times  $t = 10$  days,  $t = 20$  days and  $t = 35$  days, respectively. Figure 3.4b also indicates that the model cannot give a good prediction of the

soil moisture evolution after 20 days. This could be due to, in part, the change in the bulk density of the soil with depth that is oftentimes seen in both experiments and field conditions (Assouline, 2006). In addition, the accuracy of the soil moisture sensors and the local heterogeneity formed during soil packing as discussed in section 3.4 could also contribute to this difference. Another consideration is the definition of some of the fluid properties in the numerical simulations (e.g., density, viscosity, and diffusion coefficient). All these properties are empirically derived, which could lead to compounding inaccuracies in modeling results. However, the numerical model performs relatively well.

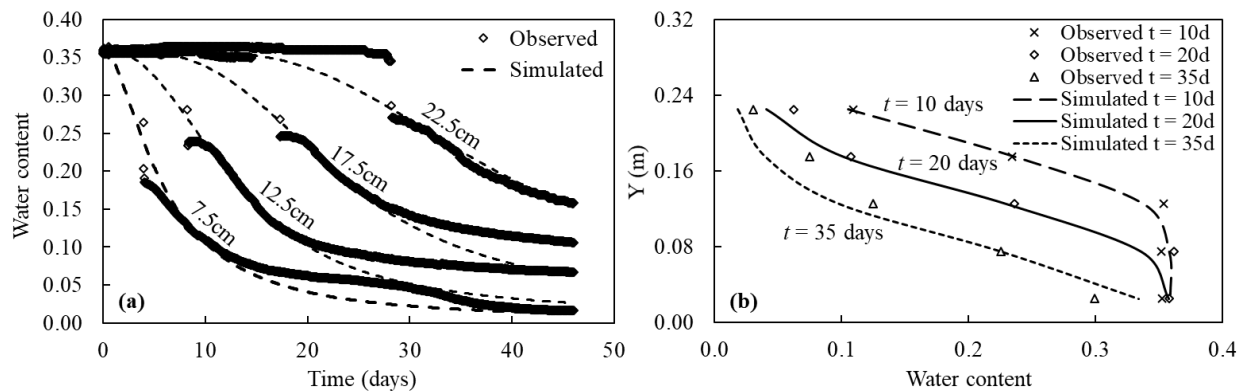


Figure 3.4 (a) Comparison of subsurface moisture evolution with time (rhombus marks in a = the observed data from experiment; dash line = simulated results by modeling) and (b) moisture profile at  $x = 10$  cm.

Figure 3.5 displays the distribution and location of the moisture sensors used in the experiment. We selected seven locations labeled as #1, #2, #6, #10, #14, #18, and #19 to investigate the soil moisture dynamics below the wavy surface with time. The horizontal coordinates of the seven points are  $x = 10, 10, 20, 30, 40, 50,$  and  $50$  cm, respectively. The sensors #2, #6, #10, #14, and #19 are located along the same horizontal plane. The sensor locations #1, #6, #14, and #18 are 5 cm below the wavy surface; #2 and #19 are 10 cm below the surface; and #10 is 2.5 cm below the surface.

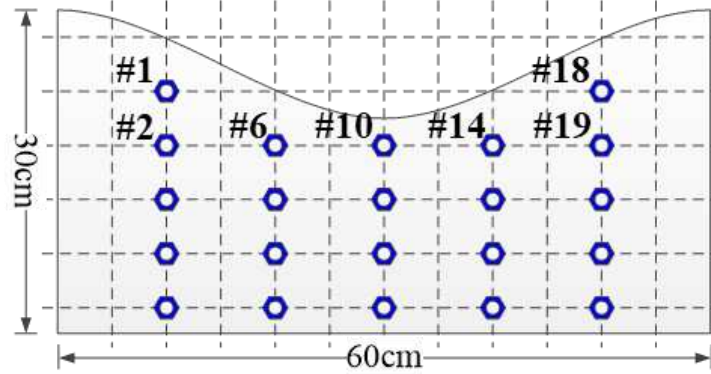


Figure 3.5 Schematic of the distribution and location of the moisture sensors.

Figure 3.6a shows the evolution of soil moisture with time (from 0 to 25 days) at four points (#1, #6, #14, and #18), which are 5 cm below the wavy surface. The experimental curves from the left to the right in Figure 3.6a corresponds to the measurement locations #18, #1, #14, and #6. Relatively, sensors #14 and #18 are located closer to the air intake compared with #6 and #1. The air flows from right to left. The wind slows down when it flows downward and accelerates when it climbs up. Thus, the viscous boundary layer has the largest thickness at the valley and the boundary layer thickness should be symmetrical to the vertical center axis of the soil tank. However, we consider that the vapor is carried from right to the left and accumulates more at the left. The vapor concentration gradient should be smaller at the uphill. That is why we see that #18 evaporates faster than #1 and #14, faster than #6. The four points are all located 5 cm below the surface. But the water at #1 and #18 evaporates first, although #1 is farther from the fan compared with #14. One may notice that the moisture recorded by sensor #18 has a quick decrease and then an increase during the half day of the beginning. This may be due to the local heterogeneous distribution of water, water supply from the surrounding soil, and/or measurement error, since this phenomenon is only seen at location #18.

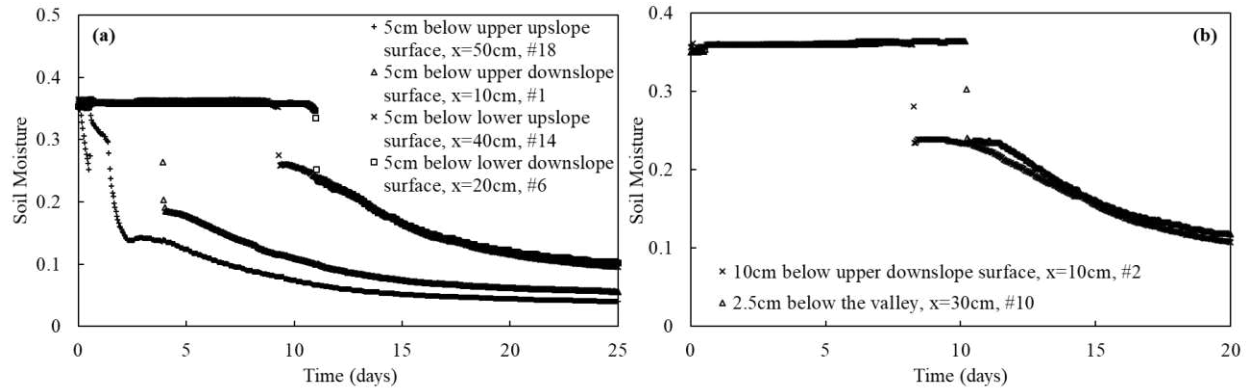


Figure 3.6 (a) Evolution of soil moisture with time in the experiment at four points located 5 cm below the wavy surface. The corresponding marks of these four points are #1, #6, #14, and #18 shown in Figure 3.5. The horizontal location of these four points are  $x = 10, 20, 40,$  and  $50$  cm, respectively. (b) Evolution of soil moisture with time at two points, #2 and #10 (Figure 3.5), which are located along the same horizontal line. The horizontal location of these two points are  $x = 10$  and  $30$  cm, respectively. Points #2 and #10 are 10 and 2.5 cm below the wavy surface, respectively.

Figure 3.6b shows the evolution of soil moisture with time (from 0 to 20 days) at points #2 and #10. Sensor #2 is located below the upper downslope surface and #10 is just below the valley, while they are at the same horizontal line. Clearly, evaporation first happens at #2 although #10 is much close to the surface. Figure 3.7 shows the moisture distribution along one horizontal line where the sensors #2, #6, #10, #14, and #19 are located at 1, 10, and 11 days. Obviously, the soil loses water at the peaks first (from the two sides to the middle). But the moisture distribution and the evolution of the distribution are not symmetric to  $x = 30$  cm as explained above. Therefore, Figure 3.6 and Figure 3.7 demonstrate that evaporation from a wavy surface is not the same along the surface and the peaks evaporate prior to the valleys. Detailed analyses are presented in the later simulated results.

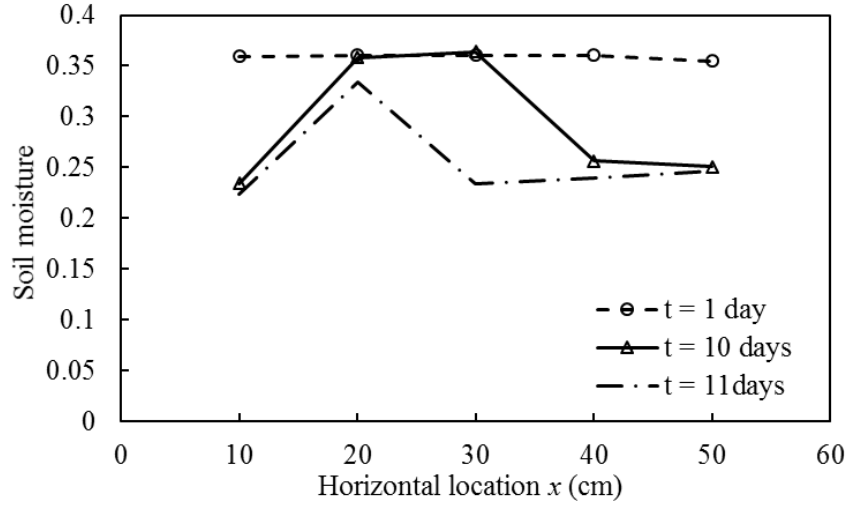


Figure 3.7 The experimental moisture distribution along one horizontal line where the sensors #2, #6, #10, #14, and #19 are located at  $t = 1, 10,$  and  $11$  days. The horizontal location of these five sensors are  $x = 10, 20, 30, 40,$  and  $50$  cm, respectively. Sensors #2 and #19 are 10 cm below the wavy surface; sensors #6 and #14 are 5 cm below the wavy surface; and sensor #10 is 2.5 cm below the wavy surface.

### 3.5.2 Typical Evaporation Rate Curve

Figure 3.8 shows the simulated evaporation rate (solid line) and diffusive flux (dashed line) over time. Although not shown, the observed evaporation rate showed similar behavior (see section 3.5.1 for experimental results). The evaporation rate in Figure 3.8 was calculated according to the loss of water in the porous media subdomain (see Figure 3.1) by:

$$\text{Loss}_{w,\text{pm}} = \rho_w (\phi - \theta_g) V_{\text{pm}} \quad (3.24)$$

where  $V_{\text{pm}}$  is the volume of the porous media subdomain.

The dashed line in Figure 3.8 was calculated based on Fick's law along the soil surface:

$$E = \int D \nabla (\rho_g w_v) dl \quad (3.25)$$

where  $D$  is the diffusion coefficient, which equals  $D_v^{\text{pm}}$  in the porous media and  $D_v^{\text{ff}}$  in the free-flow region,  $w_v$  is the fraction of vapor in gas and  $l$  denotes the length of the soil surface.

The porous media diffusion coefficient  $D_v^{pm}$  was used here to obtain the dashed line in Figure 3.8, representing the amount of water vapor generated in the porous media that leaves the soil via diffusion per day. The amount of vapor loss across the surface due to advection was ignored here due to the assumption of very slow laminar flow.

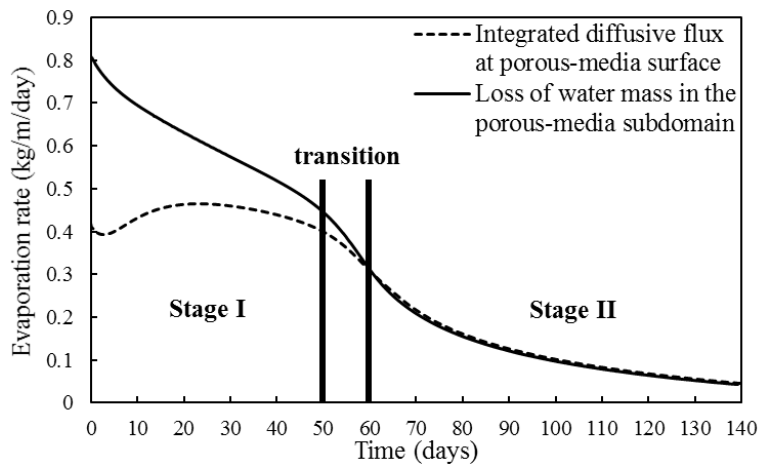


Figure 3.8 Typical evaporation rate curve by coupling model.

The shape of the evaporation rate curve is controlled by two factors. One is the continuous capillary water flow, which can provide liquid water to the vaporization plane where it changes phase and evaporates. The other is vapor diffusion inside the soil. During stage I, the vaporization plane is at the soil surface as there is continuous water replenishing the soil surface due to capillary flow. However, the top part of the porous media gradually becomes unsaturated. Water vapor moves via diffusion through this unsaturated zone and leaves the porous media across the boundary layer to the atmosphere. During stage I, the effect of water flow due to capillarity (capillary flow) is much more important than vapor diffusion in the porous media and the evaporation rate is relatively constant or decreases slowly. As less and less water reaches the soil surface, the influence of vapor diffusion in the porous media increases gradually. As the influence of diffusion increases, the evaporation rate decreases sharply; this is usually referred to as the transition

between stages I and II. However, even though the importance of diffusion increases, during this transition, the capillary flow still dominates. Theoretically speaking, if we just use Fick's law in this unsaturated zone to calculate the evaporation, we will underestimate the evaporation rate since continuous capillary flow still plays an important role in this zone (see stage I and transition in Figure 3.8). Therefore, for stage I, the evaporation rate can accurately be determined by calculating the water mass loss in the porous media subdomain (Eq. (3.24)) and the solid line in Figure 3.8. Differently, the vapor moves across the boundary layer only by diffusion. Thus, Fick's law can be used for the estimation of evaporation rate during stage I and the transition stage within the boundary layer only (i.e., not in the porous media).

When evaporation enters stage II, the continuous water flow can no longer reach the soil surface and a dry zone forms near the soil surface. At the same time, the vaporization plane continues to recede into the porous media (i.e., moves down). The continuous water arrives at this receding vaporization plane and changes to vapor. The vapor moves across both the dry zone of the porous media and the boundary layer totally by diffusion. That is to say, the evaporation rate obtained by Fick's law in the dry zone equals that in the boundary layer; and both of them are equal to the value calculated by water mass loss in the porous media subdomain (see stage II and the solid line in Figure 3.8). Thus, we can locate the exact time of the onset of stage II, which is the time when Fick's law is valid in the porous media to calculate the evaporation rate. Here we discussed the relationship of the two methods, the loss of water and Fick's law, to calculate the evaporation rate at the REV scale (Figure 3.8). Interested readers can refer to Lehmann et al. (2008) for a similar discussion but based on pore-scale understanding. Based on these theories, nearly all the different shape evaporation rate curves influenced by various factors can be explained and understood.

Davarzani et al. (2014) simulated cumulative evaporation under different wind speeds, atmospheric vapor concentrations, permeability, etc. for a flat soil surface. Mosthaf et al. (2014) also studied the influence of permeability, van Genuchten parameters, etc. on the evaporation rate behavior for flat surfaces. They concluded that larger wind speeds and lower vapor concentrations result in higher evaporation rates in stage I and a shorter transition to stage II; changing permeability does not change the evaporation in stage I significantly but increasing permeability increases the transition; a lower van Genuchten parameter  $n$  leads to a prolonged stage 1. However, they did not explain the characteristics and mechanisms of the evaporation curves for different factors during both stages of evaporation. Because both cumulative evaporation and evaporation rate are comprehensive concepts based on the REV assumption, some local characteristics and the value of cumulative evaporation as well as evaporation rate may be distinct for different surface configurations. But compared with a flat surface, similar influences of the atmospheric conditions and soil properties on the evaporation rate (or cumulative evaporation) can be seen in the case of wavy surfaces. Therefore, in the following two sections, only some representative factors are discussed in order to provide the reader a clearer understanding of how and why these factors respond during the entire evaporation process. The particular differences due to the surface configuration will be analyzed in detail in section 3.5.5. The analyses in the following three sections are all based on numerical modeling results.

### **3.5.3 Effects of Atmospheric Conditions**

Atmospheric conditions to include wind speed, relative humidity, and temperature provide the necessary external conditions for the entire evaporation system. Conceivably, they may affect evaporation directly through changing the characteristics of the boundary layer, which connects the atmosphere and the soil.

Figure 3.9a shows the evaporation rate under different ambient air flow wind speeds of 0.05, 0.10, and 0.15 m/s; Figure 3.9b shows the evaporation rate under different ambient vapor concentrations of 0.003, 0.006, and 0.012 kg/m<sup>3</sup>. The vapor concentrations were selected based on the corresponding ambient relative humidity of 17.4%, 34.7%, and 69.4% under 20 °C.

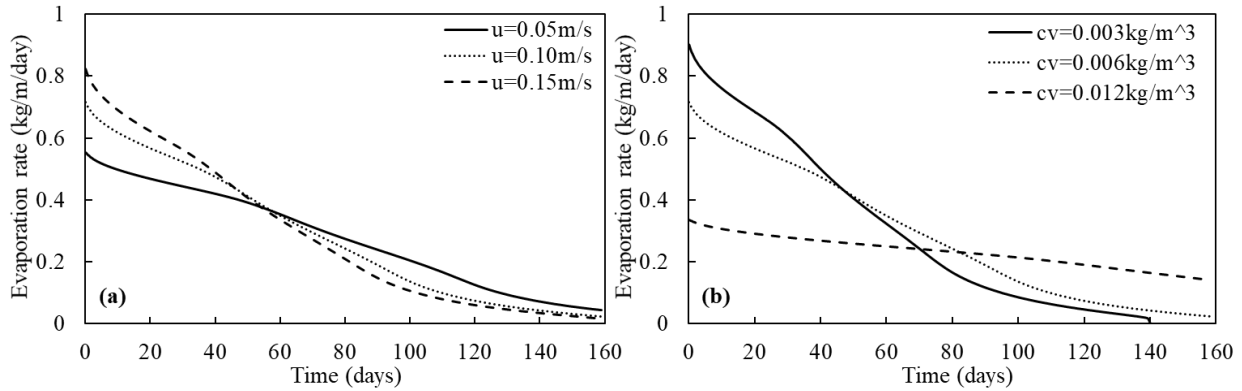


Figure 3.9 (a) Impact of air flow velocity (wind speed) on evaporation rate ( $C_{v,inlet} = 0.006 \text{ kg/m}^3$ ,  $T_{inlet} = 293.15 \text{ K}$ ,  $K = 1\text{E-}10 \text{ m}^2$ ,  $\phi = 0.312$ ,  $\alpha = 8$ ,  $n = 5$ ,  $AR = 1/6$ ). (b) Effect of ambient vapor concentration on evaporation rate ( $u_{g,inlet} = 0.10 \text{ m/s}$ ,  $T_{inlet} = 293.15 \text{ K}$ ,  $K = 1\text{E-}10 \text{ m}^2$ ,  $\phi = 0.312$ ,  $\alpha = 8$ ,  $n = 5$ ,  $AR = 1/6$ ).

From the discussion in section 3.5.2, we know that the capillary flow provides water to the surface and dominates during stage I; the evaporation rate is decided by the vapor diffusion in the boundary layer. The boundary layer for a flat surface can be defined as a function of wind speed according to the definition:

$$\delta_m = 5 \sqrt{\frac{\mu_g x}{\rho_g U_\infty}} \quad (3.26)$$

where  $U_\infty$  is the average atmospheric wind speed in the free-flow region and  $x$  is the abscissa value. As the wind speed decreases, the thickness of the boundary layer for a flat surface increases. This trend is assumed to be the same in the case of wavy surfaces. Under low wind speeds, the application of Fick's law inside the boundary layer will result in a lower evaporation rate than at

high wind speeds. In addition, the water content near the soil surface and the vapor concentration gradient within the boundary layer will change slowly. Thus, stage I will be relatively long, as shown in Figure 3.9.

Figure 3.10 depicts the distribution of the surface water saturation at  $t = 1$  day. Different from the water saturation along the flat surface, the water evaporates first at the ridges. The increasing wind speed requires higher demand of evaporation, which also results in lower soil surface moisture. Combined with the consideration of the thinner boundary layer, one can infer that the local diffusive flux at the ridges should be larger than that of the valley at least at the beginning of the evaporation. It will be discussed in detail in the later section.

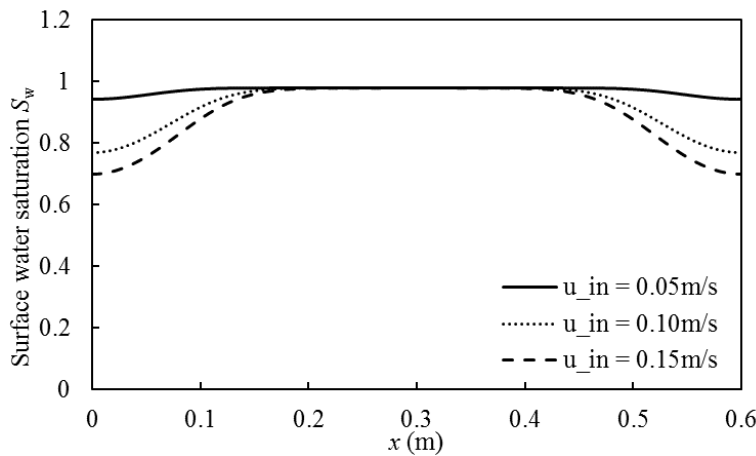


Figure 3.10 Water saturation distribution at the surface during stage I ( $t = 1$  day) under different air flow velocities ( $C_{v,inlet} = 0.006 \text{ kg/m}^3$ ,  $T_{inlet} = 293.15 \text{ K}$ ,  $K = 1\text{E-}10 \text{ m}^2$ ,  $\phi = 0.312$ ,  $\alpha = 8$ ,  $n = 5$ ,  $AR = 1/6$ ).

Similarly, under low ambient vapor concentrations (e.g.,  $c_v = 0.003 \text{ kg/m}^3$ ), the difference of vapor concentration between the porous media and the free flow is large, and the corresponding gradient within the boundary layer is high. Thus, during stage I when the evaporation rate is decided by the vapor diffusion in the boundary layer, the evaporation rate will be higher for a lower ambient vapor concentration. However, both wind speed and ambient vapor concentration are

external influential factors which have no impact on the total evaporative mass over time. Higher evaporation rates at the early stage then result in smaller evaporation rates at later stages. Thus, one can see that the curves in both Figure 3.9a and Figure 3.9b cross at some day and finally converge to zero.

In summary, the ambient conditions (e.g., wind speed and vapor concentration) affect the behavior of the boundary layer directly, which further affect the evaporation rate during stage I when vapor diffusion occurs in the boundary layer but not the long-term evaporative mass over time. This also demonstrates our conjecture mentioned above.

#### **3.5.4 Effects of Soil Properties**

Phase change from liquid water to water vapor occurs at the vaporization plane within the porous media. The soil properties, like permeability, porosity, and soil-water retention, are the internal or intrinsic conditions controlling the evaporation. They affect evaporation by influencing the capillary flow and thus influencing the vapor concentration at the soil surface. In this section, we show the influence of the intrinsic permeability and the van Genuchten parameter  $n$ , as examples of the effects of soil properties on evaporation.

Figure 3.11a presents the evaporation rate for different permeability porous media, assuming other properties of the porous media remain constant. The basic theory is still that the capillary flow dominates during stage I and the evaporation rate is decided by the vapor diffusion in the boundary layer. At early stage I, since the surface moisture is high and the vapor concentration gradient inside the boundary layer is relatively stable, permeability has little influence. Permeability is an intrinsic property of the porous media, representing the ability of fluid to flow through the porous media; high permeability correlates with higher capillary flow and hence more water moving to the vaporization plane with time. Therefore, media with a high

permeability will have longer stage I evaporation. For low-permeability media, the unsaturated or dry zone will emerge early, resulting in the early appearance of stage II. Since the ability of the capillary flow may vanish early in the large-permeability porous media, its influence, though also small, lasts relatively long in the low-permeability porous media. Therefore, from Figure 3.11 a we can see that at late stage II, the evaporation rate of the porous media with higher permeability may be slightly lower.

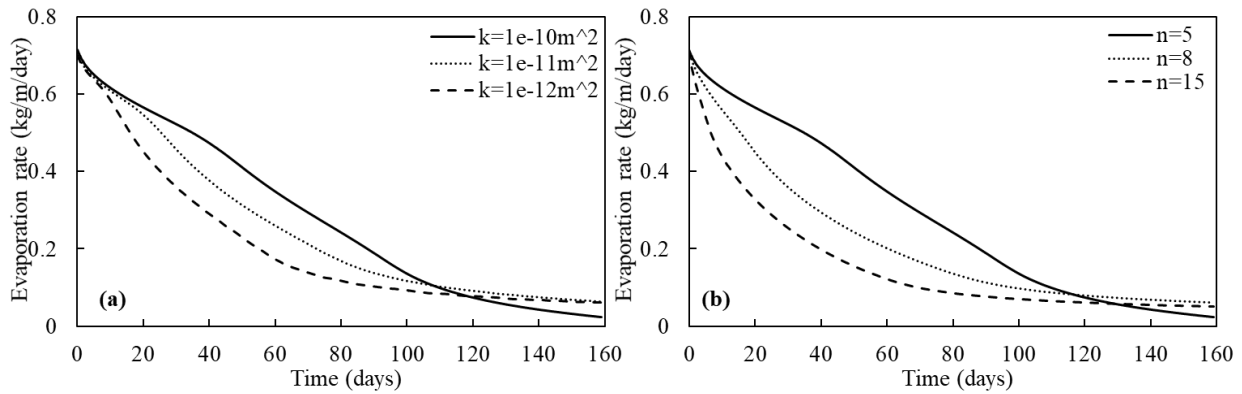


Figure 3.11 (a) Effect of intrinsic permeability on evaporation rate ( $u_{g,inlet} = 0.10$  m/s,  $C_{v,inlet} = 0.006$  kg/m<sup>3</sup>,  $T_{inlet} = 293.15$  K,  $\phi = 0.312$ ,  $\alpha = 8$ ,  $n = 5$ , AR = 1/6). (b) Effect of van Genuchten parameter  $n$  on evaporation rate ( $u_{g,inlet} = 0.10$  m/s,  $C_{v,inlet} = 0.006$  kg/m<sup>3</sup>,  $T_{inlet} = 293.15$  K,  $K = 1E-10$  m<sup>2</sup>,  $\phi = 0.312$ ,  $\alpha = 8$ , AR = 1/6).

Figure 3.11b demonstrates the influence of the van Genuchten parameter,  $n$  on the evaporation rate. This parameter affects both the air entry value (a large  $n$  correlates to a high air entry value) and the shape of the soil-water retention curve, especially during water drainage. Again, capillary flow dominates during stage I, and the evaporation rate is decided by the vapor diffusion in the boundary layer. First, for a soil with a high  $n$  value, more effort is needed for the atmospheric air to overcome the soil resistances, mainly those from water gravity and hence enter the porous media and displace the water at the vaporization plane. In other words, it is relatively difficult to keep the surface water content at a high value by capillary flow after the surface water evaporates. Thus, the high  $n$  value lowers both the vapor concentration at the surface and the vapor

concentration gradient in the boundary layer, leading to a lower evaporation rate than that for a small  $n$  value. After air eventually enters the porous media, water drainage is easier for large- $n$  material. Capillary flow plays a more important role but will not last long, increasing the evaporation process and resulting in a shorter stage I and faster transition to stage II.

Unlike the atmospheric conditions which affect the boundary layer directly, the soil properties have a direct influence on the continuous capillary flow. The capillary flow determines the volume of water moving to the vaporization plane and how much vapor exists at the surface, which is related with the vapor concentration gradient (vapor diffusion) in the boundary layer.

### **3.5.5 Effects of Macroscale Roughness**

The effects of atmospheric conditions and soil properties on the evaporation from wavy surfaces are discussed in the last two sections. The author also ran simulations to test their effects in the case of flat surface and found that the curves present similar trend but not the same value due to the macroscale roughness. This section focuses on the wavy surfaces and make clear the influences and the corresponding mechanisms.

The two main factors that may affect the macroscale roughness are the number of surface waves and their aspect ratio. The former denotes the soil surface undulations, while the latter represents the undulation steepness. The aspect ratio is defined by (Haghighi & Or, 2015a):

$$AR = 2\gamma / \lambda \quad (3.27)$$

where  $\gamma$  and  $\lambda$  are the amplitude and length of the wavy surface, respectively.

The comparison of evaporation rate under different aspect ratios and number of surface waves is shown in Figure 3.12a and b, respectively. Both increasing the number of surface waves and aspect ratio will increase the area of the vaporization plane in stage I, which provides better opportunity for the contribution of capillary flow. In the case of more waves (Figure 3.11), the

evaporation rate is larger and sustained longer in stage I. However, as previously mentioned, since the total amount of water for evaporation is determined by the intrinsic properties of the porous media, a higher evaporation rate in stage I results in a lower evaporation rate in stage II. Capillary flow contributes more to stage I evaporation when there are more waves, leading to a shorter transition to stage II due to the limitation of capillary flow and the increasing contribution from vapor diffusion inside the porous media.

Similarly, high aspect ratios also result in a large influence of capillary flow. However, the aspect ratio may also influence the vapor diffusion in the boundary layer, which decides the evaporation rate. Figure 3.13 shows the distribution of vapor concentration in the free-flow region and water saturation in the porous media at  $t = 40$  days. The arrows represent the gas flow direction, and the size of the arrow is proportional to the magnitude of the velocity. Clearly, the vapor accumulates in the valley. Additionally, the near-surface vapor concentration inside the valley increases as the atmospheric air flows from left to the right as shown in Figure 3.14a. The convex parts correspond to the vapor concentration in the valleys. As what has been mentioned in section 3.5.1, the distribution of the vapor along the surface is partially due to the surface wind speed distribution. From left to right, the wind slows down when it flows downward and accelerates when it climbs up. The boundary layer has the largest thickness at the valley within a wavy element. Considering the accumulation of vapor along the surface, the vapor concentration gradient should be smaller at the uphill in a wavy element and becomes increasingly smaller at the later wavy elements (see Figure 3.13 and Figure 3.14b). Increasing the aspect ratio will also increase the accumulation of vapor in the valley, resulting in a thicker boundary layer or lower vapor concentration gradient at the soil surface. This is demonstrated by the comparison of the vapor concentration gradient at the soil surface with aspect ratio (AR) of 1/6 and 1/4 at  $t = 20$  days shown

in Figure 3.14b. Therefore, under the reverse effects of capillary flow and vapor diffusion in the boundary layer, the evaporation rate from a large-aspect ratio surface is smaller in stage I, as shown in Figure 3.12b. If the aspect ratio is infinitely small, the wavy surface reduces to a flat surface. Compared with a wavy surface, the boundary layer of a flat surface is thinner and thus the evaporation rate is larger during stage I as determined by the vapor diffusion in the boundary layer. Likewise, when the influence of capillary flow starts to decline, vapor diffusion in the porous media begins to dominate and the evaporation comes to stage II after a faster decrease during the transition. The higher evaporation rate in stage I leads to faster drop in the transition and lower evaporation rate in stage II. When the vapor diffusion in the porous media becomes a dominant factor during stage II, the vaporization plane has receded downward, which indicates no water can reach the soil surface. Thus, the vapor diffusion across the boundary layer or the vapor concentration gradient at the soil surface will have little influence for different aspect ratios, especially at the surface peaks, due to the higher priority of losing the influence of capillary flow. The comparison of the vapor concentration gradient at the surface with the aspect ratios (AR) of 1/6 and 1/4 at 70 days as shown in Figure 3.14b indicates this explanation. Figure 3.12b shows that the 70 days is approximately the end of the transition. We can also see from Figure 3.14a that at the 70 days, there is still a difference in the vapor concentration between the peaks and valleys of the soil surface. In other words, capillary flow still affects the valleys. This is why the vapor concentration gradients at the valleys are different between the 1/6-AR and 1/4-AR surfaces. Further, one may infer that when the capillary flow loses its influence in the porous media on evaporation, the vapor concentration gradient curve for different aspect ratios becomes constant (approximately a horizontal line). Complementarily speaking, although we could compare the evaporation from wavy and flat soil surface by adjusting AR in the simulation, the comparison is

not that meaningful in this study. One of the reasons why we focus on wavy surfaces is that it can be considered as a flat surface with simplified permeable obstacles. The substantial mechanisms controlling wavy- and flat-surface evaporation are the same. The only difference stems from the roughness (namely simplified permeable obstacles), which is discussed in this section in detail.

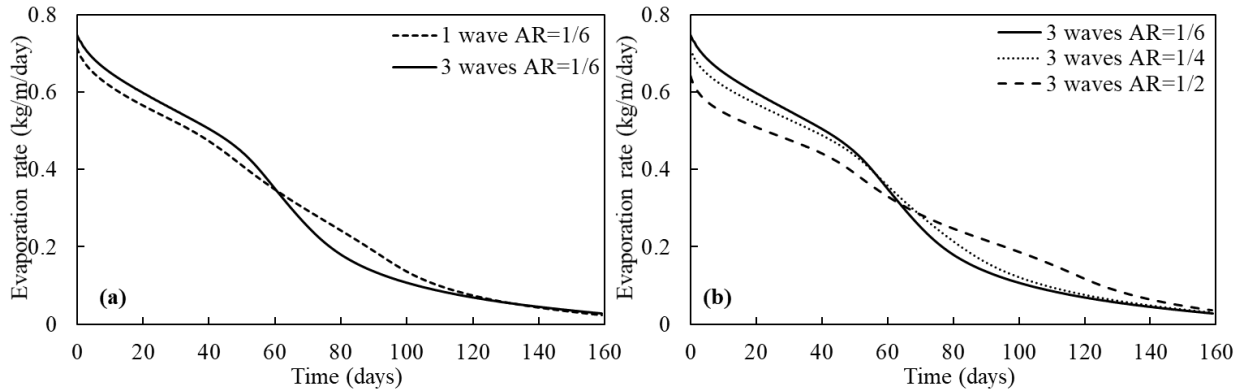


Figure 3.12 (a) Effect of wave numbers on evaporation rate ( $u_{g,inlet} = 0.10$  m/s,  $C_{v,inlet} = 0.006$  kg/m<sup>3</sup>,  $T_{inlet} = 293.15$  K,  $K = 1E-10$  m<sup>2</sup>,  $\phi = 0.312$ ,  $\alpha = 8$ ,  $n = 5$ ). (b) Effect of aspect ratio (AR) on evaporation rate ( $u_{g,inlet} = 0.10$  m/s,  $C_{v,inlet} = 0.006$  kg/m<sup>3</sup>,  $T_{inlet} = 293.15$  K,  $K = 1E-10$  m<sup>2</sup>,  $\phi = 0.312$ ,  $\alpha = 8$ ,  $n = 5$ , 3 waves).

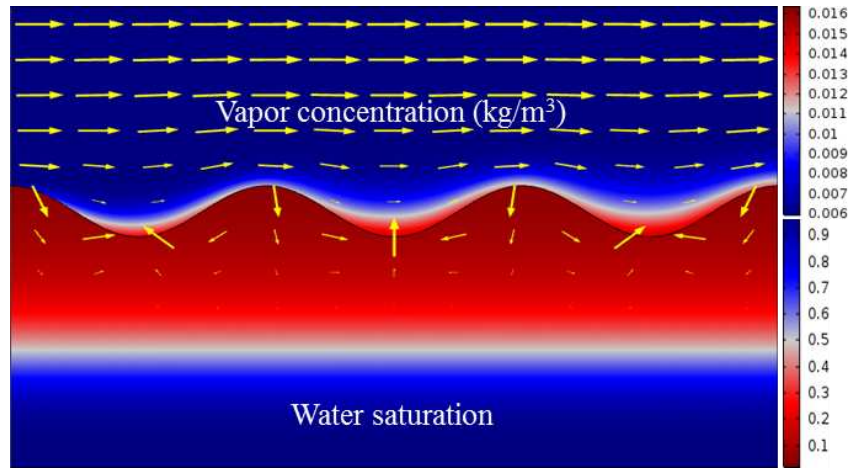


Figure 3.13 Distribution of vapor concentration (kg/m<sup>3</sup>) in the free-flow region and saturation in the porous media (AR = 1/4, the arrows show the gas flow direction and the arrow size is proportional to the gas velocity. Separate scales of the arrows are used in free-flow region and porous media).

Figure 3.14b shows the changes in the vapor concentration gradient along a wavy soil surface with different aspect ratios at 20 and 70 days, demonstrating the nonhorizontal distribution of the evaporative flux along the wavy surface (see Figure 3.15). For the whole system, since the vapor accumulates in the posterior valleys (see Figure 3.13 and Figure 3.14a) resulting in a relatively small vapor concentration gradient, evaporation weakens from inlet to outlet (left to right) and decreases integrally over time. Within one wavy element, the ridge contributes more to the evaporation first when the capillary flow is available at the ridge. It leads to the water lost first at the ridges, which has been shown in Figure 3.10. Due to less and less continuous water available at the ridges, the vapor concentration gradient decreases, resulting in lower local evaporative flux. As the capillary flow vanishes at the ridge and still exists at the valley, the valley contributes more to evaporation while vapor diffusion dominates at the ridge of the porous media, contributing less although the concentration boundary layer at the valley is thicker than that of the ridge. As capillary flow loses its influence gradually and the evaporation from the whole system is dominated by vapor diffusion in the porous media, the difference of the evaporation between the wavy elements becomes small. The evaporation comes to stage II.

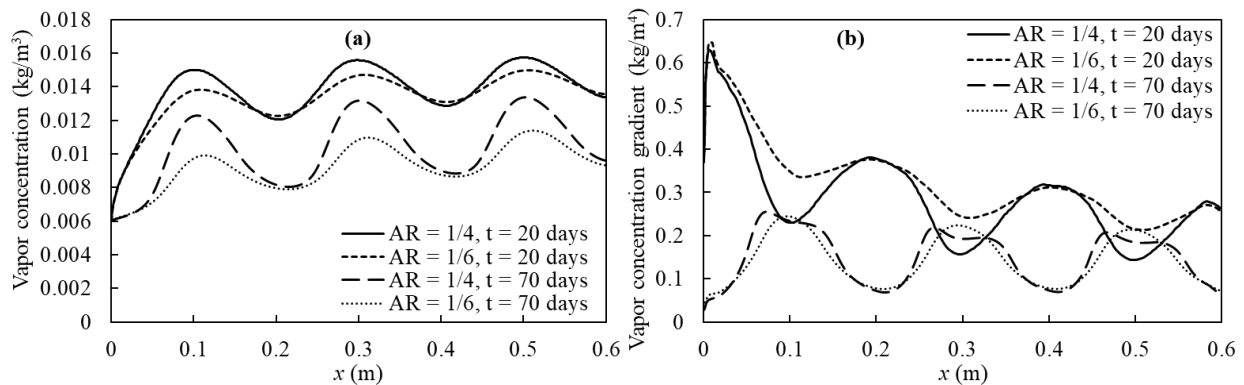


Figure 3.14 (a) Vapor concentration along soil surface with AR of 1/6 and 1/4 at  $t = 20$  and 70 days. (b) Normal vapor concentration gradient along soil surface with AR of 1/6 and 1/4 at  $t = 20$  and 70 days. AR = aspect ratio.

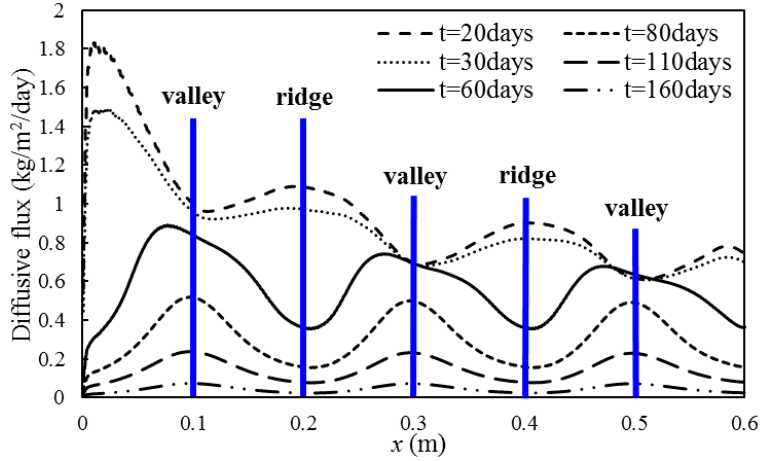


Figure 3.15 Diffusive flux along soil surface with three waves at  $t = 20, 30, 60, 80, 110,$  and  $160$  days;  $AR = 1/6$ .

In summary, the influence of the surface geometry is relatively complex, since it is related to both the capillary flow and the boundary layer. More waves and steeper waves indicate more influence from capillary flow, enhancing evaporation; while steeper waves also result in a thicker boundary layer and weakens evaporation. Especially, in the case where a generalized top boundary condition consisting of resistance terms is used for the estimation of the evaporation rate from an irregular surface, how to quantify the boundary layer remains an open question.

### 3.6 Conclusions

With the goal of coupling free flow and porous media flow to describe evaporation from wavy soil surfaces, we developed a numerical model that describes mass and energy transport processes in and between the subsurface and the atmosphere. The model consists of fluid flow, component and energy equations. What makes this model unique compared with more commonly used evaporation models is that all of the equations are separately defined in both the subsurface and the atmosphere and coupled at the domain interface. To validate the numerical results, we designed a benchmark lab experimental system to simulate evaporation from a wavy soil surface.

At the REV scale, the evaporation stages and the shape of evaporation rate curve is controlled by continuous capillary flow and vapor diffusion within the porous media and across the boundary layer. In theory, the evaporation rate equals the total vapor diffusion in the boundary layer during all evaporation stages. Based on this theory, the influence of atmospheric conditions, soil properties, and macroscale surface roughness on the trend of the evaporation rate curve were discussed. Ambient conditions (e.g., wind speed and temperature) affect the evaporation rate by directly affecting vapor diffusion across the boundary layer. The soil properties directly affect the continuous capillary flow which then influence the vapor concentration gradient in the boundary layer. The macroscale surface roughness directly affects both the capillary flow and vapor diffusion in the boundary layer. The two main parameters that determine the surface geometry, surface waves, and aspect ratio, have reverse effects on the evaporation. Increasing the number of surface waves exposes more area (i.e., larger vaporization plane), which allows capillary flow to contribute more during evaporation stage I, resulting in a larger evaporation rate. Although a higher aspect ratio should lead to the same effect, it thickens the boundary layer and changes the vapor diffusion in the boundary layer as well, resulting in a reverse effect compared with the case of more waves. Particularly, the wavy surface reduces to a flat surface when the aspect ratio is infinitely small. Compared with the relatively constant evaporative flux at a flat soil surface, the flux from a wavy surface changes with surface geometry, which is also controlled by both capillary flow and the boundary layer.

This study assumes that the air flow in the atmosphere is laminar; however, turbulent flow is more common in nature and easily emerges near wavy surfaces. Therefore, on-going work will incorporate turbulence into the coupled numerical model. Additionally, the laboratory experiment presented herein targets mechanism study and model validation. Considering the application of

this experiment in the field or at least within a lysimeter-controlled area, several factors should be taken into account. The first is the definition of a roughness size. The influence of aggregate roughness at the soil surface should be distinguished from the macroscale roughness defined in this paper. Second, in field experiments, natural wind speed cannot be controlled. Turbulent and laminar air flow from random directions may appear alternately, and the soil surface may move when exposed to strong wind conditions. Finally, because of the complexity of natural conditions, added factors would need to be incorporated into the model to account for, as an example, solar radiation, precipitation, and runoff. We expect that this study as well as the planned follow-on work, however, is useful to improving models for evaporation prediction on the engineering scale.

## CHAPTER 4

### EVAPORATION FROM AN UNDULATING SOIL SURFACE

#### UNDER TURBULENT AIRFLOW

Modified from an article published in *Vadose Zone Journal*<sup>5</sup> with minor rearrangement

Bo Gao<sup>1,3</sup>, John Farnsworth<sup>2</sup>, Kathleen M. Smits<sup>1,3,4</sup>

#### 4.1 Abstract

Evaporation from undulating soil surfaces is rarely studied due to limited modeling theory and inadequate experimental data linking dynamic soil and atmospheric interactions. The goal of this paper is to provide exploratory insights into evaporation behavior from undulating soil surfaces under turbulent conditions through numerical and experimental approaches. A previously developed and verified coupled free flow and porous media flow model was extended by incorporating turbulent airflow through Reynolds-averaged Navier–Stokes equations. The model explicitly describes the relevant physical processes and the key properties in the free flow, porous media, and at the interface, allowing for the analysis of coupled exchange fluxes. An experiment aiming to simultaneously collect the data of the boundary layer and soil evaporation in the area around the soil–atmosphere interface was conducted using a wind tunnel integrated with a soil tank. The turbulent boundary layer above the undulating soil surface was captured using high-resolution hot-wire anemometry, confirming the presence of recirculation zones in the undulating

---

<sup>1</sup> Department of Civil and Environmental Engineering, Colorado School of Mines, Golden, CO, 80401, U.S.A

<sup>2</sup> Ann and H.J. Smead Department of Aerospace Engineering Sciences, University of Colorado Boulder, Boulder, CO 80309, United States

<sup>3</sup> Department of Civil Engineering, University of Texas at Arlington, Arlington, TX, 76010

<sup>4</sup> Corresponding author. Direct correspondence to [kathleen.smits@uta.edu](mailto:kathleen.smits@uta.edu).

<sup>5</sup> Reprinted with permission, *Vadose Zone Journal*, 2020, 19(1).

valleys and locally low evaporative flux. Experimental data were used to validate the extended model, and modeling results demonstrate that turbulent airflow enhances evaporation and shortens the duration of Stage I. The surface geometry significantly affects the local evaporative flux by influencing the vapor distribution, concentration gradient, and water availability at the soil surface, especially when recirculation zones form in the valleys. As a joint result of turbulence and surface undulations, the influence of wind speed on both the local and system-level evaporation rate is restricted.

## **4.2 Introduction**

Evaporation is a key component of soil–atmosphere interactions and is influenced by both the soil properties and the atmospheric conditions (Davarzani et al., 2014). The influences are especially critical in the near-surface area, which involves the interplay of the soil and the atmosphere. Although decades of relevant studies (Clements & Wilkening, 1974; Ishihara et al., 1992; Katul et al., 2006; Poulsen & Møldrup, 2006; Bowling & Massman, 2011; Shokri, 2014; Poulsen et al., 2018) have been conducted, many gaps still exist in our current knowledge of mass and energy exchange between the soil and the atmosphere. One knowledge gap is in our understanding of the influence of the soil surface, which in most cases is not hydrodynamically smooth but rather in the form of undulations at all scales. The undulations may form due to natural processes (e.g., soil erosion, alluvial riverbed) or mechanical manipulation (e.g., agricultural furrow). Unlike a flat surface, topographic variations can induce turbulence adjacent to the soil surface, changing the development of the boundary layer and further affecting the mass and energy exchanges between the soil and the atmosphere (Haghighi & Or, 2015a). However, the characteristics and mechanisms of the influence of surface undulations linked with near-surface turbulence on the soil–atmosphere exchange processes during soil evaporation are not clear, being

limited by both experimental techniques and appropriate theoretical models.

Particularly, the soil undulations of interest in this study are on the order of several to dozens of centimeters (macroscale surface roughness). There has been some published literature on surface undulations at this scale using laboratory experiments (Verma & Cermak, 1974a, 1974b; Zilker & Hanratty, 1979; Dawkins & Davies, 1981; Athanassiadou & Castro, 2001; Sugita & Kishii, 2002; Poggi & Katul, 2007b; Dobberschütz, 2014) or numerical simulations (Brutsaert, 1979; Maaß & Schumann, 1996; Cherukat et al., 1998; De Lemos & Silva, 2003; Silva & De Lemos, 2003; Ross, 2008). In terms of the representative experiments, Verma and Cermak (1974a) used Styrofoam waves placed on a water-filled pan to simulate water evaporation from soil undulations and concluded that the mass transfer rate from an undulating surface was closely linked with the location of the recirculation zones (RZs). Sugita and Kishii (2002) used a lysimeter–wind tunnel system with a low water table to study the effect of macroscale roughness distribution on evaporation. Their work demonstrated that the variation of the roughness intervals could affect the evaporation rate. Most previous experiments focused on only a portion of the overall evaporation process (i.e., atmosphere-dominated Stage I or soil-dominated Stage II) or failed to simultaneously acquire atmospheric information. Other experiments (Poggi et al., 2007) used wavy impermeable surfaces to explore how the surface geometry affected the atmospheric velocity field while no porous media information was obtained. Alternatively, previous modeling studies of fluid flow over undulating surfaces generally focused on the boundary layer development by different methods such as large eddy simulation (LES) and direct numerical simulation (DNS) (Maaß & Schumann, 1996; Ross, 2008). Some worked on the mathematical expression of the coupling of free flow and porous media flow over a curved interface (De Lemos & Silva, 2003; Silva & De Lemos, 2003; Davarzani et al., 2014). Previous modeling studies

indicate that boundary layer development is influenced by surface geometry, yet these studies did not apply their results to evaporation.

The boundary layers developed above soil surfaces can be laminar, turbulent, transition, or even more complicated depending on the surface geometry. Low-speed airflow over a surface generally develops a laminar boundary layer. This boundary layer becomes unstable as the downstream distance from the boundary layer origin increases and the boundary layer thickness grows. After a point of instability is reached, the original laminar boundary layer gradually transitions to a fully turbulent boundary layer. This onset of instability and transition is defined by the critical Reynolds number, which accounts for the influence of both the local streamwise position and the free flow speed on boundary layer transition. The addition of roughness to a smooth surface reduces the critical Reynolds number for the development of a turbulent boundary layer (White & Corfield, 2006; Schlichting & Gersten, 2016). This then causes transition to occur at an earlier streamwise position for a constant flow speed, or at a lower flow speed for a constant streamwise position. As a result, turbulent boundary layers commonly exist in nature due to the presence of roughness at a broad range of scales and long boundary layer development lengths in a geophysical environment. If the surface roughness is on a certain scale (e.g., soil undulations), an adverse pressure gradient may occur along the leeward sides of undulating surfaces, reducing the air speed and potentially inducing flow separation (Calhoun & Street, 2001; Finnigan & Belcher, 2004; Poggi & Katul, 2007b). Although some studies identified the importance of atmospheric turbulence on subsurface gas transport (Maier et al., 2012; Pourbakhtiar et al., 2017; Poulsen et al., 2018; Levintal et al., 2019), few studies in hydrology, so far, have considered the interplay of turbulent airflow and undulating surfaces on soil evaporation. Particularly, Haghghi and Or (2015a) conducted a study on evaporation from wavy soil surfaces into turbulent airflow.

Experimentally, the soil surface temperature was measured by an infrared thermal camera and was used to estimate surface evaporative flux. The difference in the temperature and evaporative flux between the peaks and valleys were identified. However, the corresponding turbulent boundary layer was not measured to connect with the evaporation disparity. Haghghi and Or (2015a) used a top-boundary-condition formula to calculate the evaporation rate. The effect of turbulence was incorporated by modifying the aerodynamic resistance term, and an explicit expression was used to describe the mean boundary layer thickness. Although appropriate for system level evaporation estimates (Huntingford et al., 1995; Villagarcía et al., 2007; Swenson & Lawrence, 2014), the top-boundary-condition type formulas cannot explicitly quantify the dynamic mass and energy transfer between the soil and the atmosphere. Hence, the formula proposed in Haghghi and Or (2015a) is not necessarily suitable for a fundamental study of soil–atmosphere interactions like the work presented herein.

Given the abovementioned limitations of modeling theory and current experiments, the purpose of this study is to establish a benchmark understanding of the interlinked behavior of the atmosphere and porous media during evaporation from undulating soil surfaces under turbulent conditions. This study builds upon our previous work (Gao et al., 2018), in which the mechanisms and characteristics of evaporation from undulating soil surfaces under laminar conditions were investigated. Specifically, there are three main objectives in this paper: (a) testing the application of hot-wire anemometry (HWA) to measure the turbulent atmospheric boundary layer above undulating soil surfaces; (b) extending the coupled free flow and porous media flow model developed in Gao et al. (2018) by including turbulent airflow to simulate the dynamic soil–atmosphere interactions; and (c) analyzing the influence of wind speed, surface geometry, and soil properties on evaporation from undulating surfaces under turbulent conditions.

### 4.3 Extension of Coupled Free Flow and Porous Media Flow Model

In our previous study, Gao et al. (2018) developed a two-domain model at the representative element volume (REV) scale to estimate evaporation by coupled Navier–Stokes free flow and porous media Darcy flow with appropriate coupling conditions at an undulating free flow–porous media interface. This model describes the full nonequilibrium mass, momentum, and heat transfer processes in the whole evaporation system with undulating soil surfaces under laminar conditions and has been validated with corresponding laboratory experimental data (Gao et al., 2018). Compared with the top-boundary-condition type formulas, this model avoids many parameterized variables and conditions, thereby excluding much of the uncertainty caused by parameterization. Instead, the physical processes involved in soil evaporation, such as mass flow and transport, heat transfer, and phase change, are included by the corresponding mass and energy equations. Moreover, the atmospheric airflow states and the development of the boundary layer affected by the surface geometry, the two main focuses in this study, can be explicitly described and obtained. The modeling outputs not only include the evaporation rate, but also the real-time evolution of global and local variables of interest in the system (e.g., moisture, temperature, vapor concentration, mass and thermal fluxes, etc.). Therefore, this model is particularly qualified for the purpose of understanding the soil–atmosphere interactions in this fundamental REV scale study.

In this work, we extend the model developed in Gao et al. (2018) by incorporating turbulent airflow in the free flow through Reynolds-averaged Navier–Stokes (RANS) equations, in which the Reynolds stress term is expressed by a two-equation model for kinetic energy  $k$  and energy dissipation  $\varepsilon$ , respectively (i.e., RANS with  $k$ – $\varepsilon$  closure model). Among the methods available to simulate turbulent flow (e.g., DNS, LES, and RANS), RANS is widely used in engineering (e.g., Defraeye et al., 2010; Allegrini et al., 2014) because of its high efficiency. Fetzner et al. (2016) and

(Mosthaf, 2014) used RANS with a zero-equation closure model due to its simplicity, convergence success, and relatively low computational cost. However, zero-equation closure models cannot properly account for the historic effects of turbulence (e.g., diffusion and convection of turbulent energy) (Trautz, 2015). Instead, the RANS with  $k-\epsilon$  two-equation closure model is a promising option to simulate turbulent airflow, although extra near-wall flow treatment is necessary.

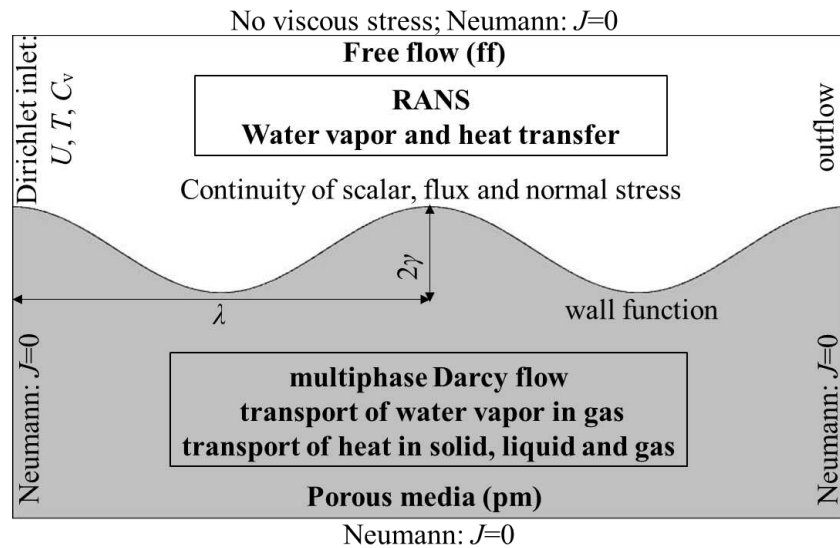


Figure 4.1 Two-dimensional configuration of subdomains and boundary conditions where  $C_v$  is vapor concentration;  $T$  is temperature;  $U$  is mean wind speed;  $J$  is flux for  $T$ , total mass, and  $C_v$ ;  $\lambda$  is wavelength and  $\gamma$  is wave amplitude. RANS is Reynolds-averaged Navier-Stokes.

Figure 4.1 shows the two-dimensional conceptual configuration and boundary conditions for this study. The size of the computation domain and the boundary conditions are decided based on the experimental setup. The whole domain consists of two subdomains: the lower porous media (i.e., soil) and the upper free flow region (i.e., the near-soil-surface atmosphere). The two subdomains are separated by a two-period cosine curve with an aspect ratio (AR) defined by  $2\gamma/\lambda$  ( $\gamma$  and  $\lambda$  are the amplitude and wavelength, respectively), representing the undulating soil surface. In the free flow, a single gas phase is assumed, which is composed of two components (dry air and water vapor). The gas flow is assumed incompressible and gravity is neglected. In the porous

media, two phases, (gas and liquid water) coexist, and the gas is composed of two components (water vapor and dry air). The dissolution of air in water is neglected, and the two fluids are immiscible. Based on these assumptions, a set of equations describing the fluid flow, vapor transport, and heat transfer is defined separately in the free flow and porous media. This mathematical model was discussed in detail in Gao et al. (2018). Only the extended part (i.e., the description of turbulent airflow and the change of interfacial conditions due to turbulence) is introduced below. The additional equations applied in the porous media, and other boundary options are referred to in Gao et al. (2018).

As mentioned above, the turbulent airflow in the free flow region is described by the RANS with  $k$ - $\varepsilon$  closure model. Besides the mass and momentum balance equations, another two partial differential equations are added. One is for the turbulent kinetic energy,  $k$ , and the other is for the energy dissipation,  $\varepsilon$ . The mass and momentum balance equations in the free flow are

$$\nabla \mathbf{u}_g^{\text{ff}} = 0 \quad (4.1)$$

$$\frac{\partial(\rho_g \mathbf{u}_g^{\text{ff}})}{\partial t} + (\rho_g \mathbf{u}_g^{\text{ff}} \nabla) \mathbf{u}_g^{\text{ff}} = \nabla \left\{ -p_g^{\text{ff}} \mathbf{I} + (\mu_g + \mu_{g,T}) \left[ \nabla \mathbf{u}_g^{\text{ff}} + (\nabla \mathbf{u}_g^{\text{ff}})^T \right] \right\} \quad (4.2)$$

where the superscript “ff” denotes the free flow region and the subscript “g” denotes gas phase.

$\mathbf{u}_g^{\text{ff}}$  ( $\text{m} \cdot \text{s}^{-1}$ ) and  $p_g^{\text{ff}}$  (Pa) are the gas flow velocity and pressure in the free flow region.  $\rho_g$  ( $\text{kg} \cdot \text{m}^{-3}$ ) and  $\mu_g$  ( $\text{Pa} \cdot \text{s}^{-1}$ ) are the gas density and dynamic viscosity, depending on the temperature and the fraction of water vapor in the gas (their values are updated in real time during calculation).  $\mu_{g,T}$  is the eddy viscosity in the RANS equations defined by:

$$\mu_{g,T} = \rho_g c_\mu \frac{k^2}{\varepsilon} \quad (4.3)$$

where  $c_\mu$  ( $c_\mu = 0.09$ ) is a constant. The equations for  $k$  and  $\varepsilon$  are

$$\rho_g \frac{\partial k}{\partial t} + \rho_g (\mathbf{u}_g^{\text{ff}} \cdot \nabla) k = \nabla \cdot \left[ \left( \mu_g + \frac{\mu_{g,T}}{\sigma_k} \right) \nabla k \right] + P_k - \rho_g \varepsilon \quad (4.4)$$

and

$$\rho_g \frac{\partial \varepsilon}{\partial t} + \rho_g (\mathbf{u}_g^{\text{ff}} \cdot \nabla) \varepsilon = \nabla \cdot \left[ \left( \mu_g + \frac{\mu_{g,T}}{\sigma_\varepsilon} \right) \nabla \varepsilon \right] + c_{\varepsilon 1} \frac{\varepsilon}{k} P_k - c_{\varepsilon 2} \rho_g \frac{\varepsilon^2}{k} \quad (4.5)$$

where  $\sigma_k$ ,  $\sigma_\varepsilon$ ,  $c_{\varepsilon 1}$  and  $c_{\varepsilon 2}$  ( $\sigma_k = 1.0$ ;  $\sigma_\varepsilon = 1.3$ ;  $c_{\varepsilon 1} = 1.44$ ;  $c_{\varepsilon 2} = 1.92$ ) are model constants and  $P_k$  is the production term given by

$$P_k = \mu_{g,T} \left[ \nabla \mathbf{u}_g^{\text{ff}} : \left( \nabla \mathbf{u}_g^{\text{ff}} + \left( \nabla \mathbf{u}_g^{\text{ff}} \right)^T \right) \right] \quad (4.6)$$

Under turbulent flow conditions, the component mass balance equation in the free flow region is modified by including a turbulent diffusion term (Fetzer, Smits, & Helmig, 2016):

$$\frac{\partial C_v^{\text{ff}}}{\partial t} + \nabla \cdot (C_v^{\text{ff}} \mathbf{u}_g^{\text{ff}}) - \nabla \cdot \left[ (D_v^{\text{ff}} + D_{v,T}^{\text{ff}}) \cdot \nabla C_v^{\text{ff}} \right] = 0 \quad (4.7)$$

where  $C_v^{\text{ff}}$  (kg/m<sup>3</sup>) is the vapor concentration ( $C_v^{\text{ff}} = \rho_g w_v^{\text{ff}}$ ,  $w_v^{\text{ff}}$  is the mass fraction of water vapor in the gas phase),  $D_v^{\text{ff}}$  (m<sup>2</sup>/s) is the diffusion coefficient in the free flow region and  $D_{v,T}^{\text{ff}}$  (m<sup>2</sup>/s) is the eddy diffusivity caused by turbulence. The eddy diffusivity is usually determined from the turbulent Schmidt number,  $Sc_T$ , a dimensionless number describing the ratio between the rates of the turbulent transport of momentum and mass:

$$Sc_T = \frac{\mu_{g,T}}{\rho_g D_{v,T}^{\text{ff}}} \quad (4.8)$$

Likewise, the energy balance equation in the free flow region is also revised by including a turbulence-induced term for conductivity (Fetzer et al., 2016):

$$\left( \rho_g c_{p,g} \right) \frac{\partial T^{\text{ff}}}{\partial t} + \left( \rho_g c_{p,g} \right) \nabla \cdot (\mathbf{u}_g^{\text{ff}} T^{\text{ff}}) - \nabla \cdot \left[ (\lambda_g + \lambda_{g,T}) \cdot \nabla T^{\text{ff}} \right] = 0 \quad (4.9)$$

where  $T^{\text{ff}}$  (K) is the temperature,  $c_{p,g}$  ( $\text{J}\cdot\text{kg}^{-1}\cdot\text{K}^{-1}$ ) is the heat capacity of the moist air and  $\lambda_g$  ( $\text{W}/(\text{m}\cdot\text{K})$ ) is the thermal conductivity of gas mixture.  $\lambda_{g,T}$  ( $\text{W}\cdot\text{m}^{-1}\cdot\text{K}^{-1}$ ) is the eddy thermal conductivity formed due to turbulence. Similar to the turbulent mass transfer, the dimensionless Prandtl number,  $\text{Pr}_T$ , defined by the ratio of momentum and heat transfer eddy diffusivity, is used to determine the eddy thermal conductivity.  $\text{Sc}_T$  and  $\text{Pr}_T$  of gas are about 0.78 and 0.71, respectively, at atmospheric pressure and temperature about 298 K (Mosthaf, 2014).

$$\text{Pr}_T = \frac{c_{p,g}\mu_{g,T}}{\lambda_{g,T}} \quad (4.10)$$

Under turbulent conditions, the near-wall region is different from the mainstream, complicating the calculation of the flow field by turbulent models (Pope, 2001). Although it is possible to modify the  $k$ - $\varepsilon$  turbulent model so that it can describe the flow in near-wall regions, this is not always desirable because of the accompanying high-resolution requirements. Instead, an analytical expression, known as a wall function, is typically used to describe the near-wall flow (Lacasse et al., 2004; Kuzmin et al., 2007). One limitation of this approach is that the wall function assumes that the wall is impermeable, whereas porous surfaces allow for mass exchange between the porous media and the free flow through pores at the interface. However, under turbulent flow, a viscous sublayer exists adjacent to the permeable surface where  $k$ - $\varepsilon$  equations are not applicable. In this case, we assume that the pore-scale mass exchange between the porous media and the free flow at the interface has a negligible influence on the REV-scale evaporation. Hence, the wall function Eq. (4.11), together with the normal continuity of mass, stresses, and fluxes, is applied at the soil surface. The wall function is described by (Kuzmin et al., 2007):

$$\left\{ (\mu_g + \mu_{g,T}) \left[ \nabla \mathbf{u}_g^{\text{ff}} + (\nabla \mathbf{u}_g^{\text{ff}})^T \right] \right\} \mathbf{n} = - \frac{\rho_g \mathbf{u}_g^{\text{ff}}}{\frac{1}{\kappa} \ln \delta_w^+ + B} \quad (4.11)$$

where  $\kappa$  is the von Kármán constant ( $\kappa = 0.41$ ) and  $B$  is a constant set to 0.52 by default;  $\delta_w^+$  is the dimensionless thickness of the viscous sublayer.

At the interface, other normal continuity conditions include:

(1) Continuity of total mass flux

Considering there is only a gas phase that exchanges between the free flow region and the porous media, the continuity of total mass flux in the normal direction of the interface should be

$$\left(\rho_g \mathbf{u}_g^{\text{ff}}\right) \cdot \mathbf{n}^{\text{ff}} = -\left(\rho_g \mathbf{u}_g^{\text{pm}}\right) \cdot \mathbf{n}^{\text{pm}} \quad (4.12)$$

where  $\mathbf{n}$  denotes the normal vector of the interface.

(2) Continuity of normal stress

$$\left\{ \left[ p_g^{\text{ff}} \mathbf{I} - (\mu_g + \mu_{g,T}) \left( \nabla \mathbf{u}_g^{\text{ff}} + (\nabla \mathbf{u}_g^{\text{ff}})^T \right) + \rho_g \left( \mathbf{u}_g^{\text{ff}} \cdot \nabla \right) \mathbf{u}_g^{\text{ff}} \right] \mathbf{n}^{\text{ff}} \right\} \cdot \mathbf{n}^{\text{ff}} = p_g^{\text{pm}} \quad (4.13)$$

(3) Continuity of temperature and heat flux

Assuming local thermodynamic equilibrium, the temperature and the heat flux at the interface are continuous (Mosthaf et al., 2011):

$$\begin{aligned} T^{\text{ff}} &= T^{\text{pm}} \\ \left[ (\rho_g c_{p,g}) \mathbf{u}_g^{\text{ff}} T^{\text{ff}} - (\lambda_g + \lambda_{g,T}) \nabla T^{\text{ff}} \right] \cdot \mathbf{n}^{\text{ff}} &= \\ - \left[ (\rho_g c_{p,g}) \mathbf{u}_g^{\text{pm}} T^{\text{pm}} + (\rho_w c_{p,w}) \mathbf{u}_w^{\text{pm}} T^{\text{pm}} - \lambda_{\text{eff}} \nabla T^{\text{pm}} \right] \cdot \mathbf{n}^{\text{pm}} & \end{aligned} \quad (4.14)$$

(4) Continuity of vapor concentration and vapor flux (Mosthaf et al., 2011):

$$\begin{aligned} C_v^{\text{ff}} &= C_v^{\text{pm}} \\ \left[ C_v^{\text{ff}} \mathbf{u}_g^{\text{ff}} - (D_v^{\text{ff}} + D_{v,T}^{\text{ff}}) \nabla C_v^{\text{ff}} \right] \cdot \mathbf{n}^{\text{ff}} &= - \left[ C_v^{\text{pm}} \mathbf{u}_g^{\text{pm}} - (D_v^{\text{pm}} + D_d^{\text{pm}}) \nabla C_v^{\text{pm}} \right] \cdot \mathbf{n}^{\text{pm}} \end{aligned} \quad (4.15)$$

A summary of the equations and the primary variables is presented in Table 4.1..

Table 4.1 List of model equations and primary variables

Subdomain	Equation Type	Equation Number	Primary Variables
Free flow subdomain	Total mass continuity and RANS	(4.1)(4.2)(4.3) (4.4)(4.5)(4.6)	$\mathbf{u}_g^{\text{ff}}, p_g^{\text{ff}}, k, \varepsilon$
	Component mass balance for gas	(4.7)	$C_v^{\text{ff}}$
	Energy balance	(4.9)	$T^{\text{ff}}$
	Normal mass and stress continuity	(4.12)(4.13)	
	Wall function	(4.11)	
Interface	Temperature and heat flux continuity	(4.14)	
	Vapor concentration and flux continuity	(4.15)	
Porous media subdomain	Total mass balance and Darcy's law	(3.5) (3.9)	$P_w^{\text{pm}}, P_g^{\text{pm}}$
	Component mass balance	(3.10)	$C_v^{\text{pm}}$
	Energy balance	(3.12)	$T^{\text{pm}}$

#### 4.4 Experimental Setup and Results

To provide a preliminary understanding of the behavior of evaporation from undulating soil surfaces under turbulent airflow conditions, we first conducted an experiment using a wind tunnel and soil tank system (Gao et al., 2018), as shown in Figure 4.2. Unique in this work, HWA system was applied to measure the turbulent boundary layer above the undulating soil surfaces. To the authors' knowledge, HWA has not previously been used in such a laboratory experimental system for a soil evaporation study. The main advantage of this method of wind speed measurement compared with sonic anemometers is that the sensor wire is tiny so as to measure the wind speed at one point relatively precisely, and the wire probe can be easily mounted on a high-spatial-resolution traverse. The computer-automated traverse can then accurately locate the sensor to designated positions, allowing for the measurement of wind speed profiles at high spatial resolutions. In this section, the experimental materials, methods, and protocols are discussed.

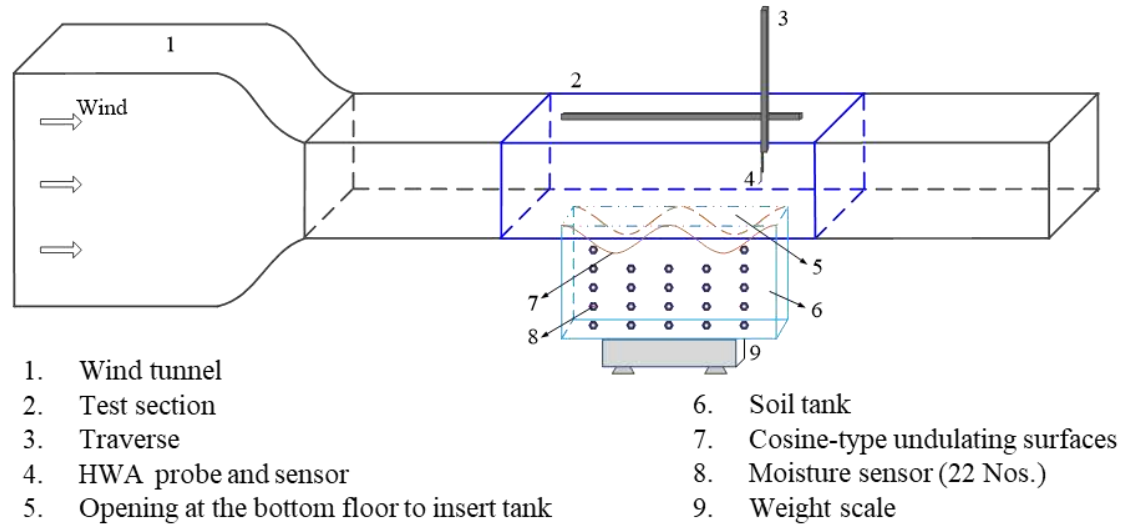


Figure 4.2 Schematic of experimental setup.

#### 4.4.1 Experimental Apparatus

Experiments were conducted using an open-return wind tunnel (Culler & Farnsworth, 2019) in the Experimental Aerodynamics Laboratory at the University of Colorado Boulder (Aerolab, UCB). The wind tunnel has a square test section ( $76 \times 76$  cm) and can maintain a steady wind at both low and intermediate speeds. To accommodate the soil tank, the bottom panel of the wind tunnel was redesigned to allow the top of the soil tank to align precisely with the bottom panel. Hence, the floor of the wind tunnel served as the surface of the soil tank.

The soil tank was constructed with acrylic glass with a length of 60 cm, height of 30 cm, and width of 9 cm. Water content was continuously monitored throughout the tank using 22 ECH2O EC-5 moisture sensors (Decagon Devices, accuracy =  $\pm 3\%$ ). Sensors were inserted into the tank in 10-cm increments horizontally and 5-cm increments vertically (Figure 4.2). Data were collected using a series of five-channel continuous data loggers (Decagon Services, ECH2O System). The soil tank was packed with a uniform silica sand, Accusand #50/70 (effective sieve number, particle diameter  $D_{50} = 0.23$  mm, Unimin Corporation). This sand has been widely

characterized and used in the previous laboratory experiments (Deepagoda et al., 2016; Gao et al., 2018). The porosity of the packed soil tank was  $\sim 0.32$ .

The speed profiles of the boundary layer were measured by the HWA system. In this paper, “velocity” denotes a vector composed of components in different directions; while “speed” denotes the “magnitude” of one velocity component. The HWA system includes a five channel AN-1003 constant temperature anemometer (CTA) from A.A. Lab Systems, a straight single-sensor wire miniature probe (model number 55P11) with the corresponding probe support from Dantec Dynamics, and a software package. The probe has a single  $5\ \mu\text{m}$  diameter, 1.25 mm long plated tungsten wire as a sensor. The probe was mounted on a traverse with the wire perpendicular to the streamwise flow direction, allowing for the time varying measurement of the streamwise speed normal to the sensor.

#### **4.4.2 Experimental Procedures**

Soil moisture sensors were tested and calibrated prior to installation into the corresponding locations of the soil tank. The tank was then wet-packed into a two-period cosine surface configuration with #50/70 silica sand in incremental 2-cm layer to achieve a uniform bulk density (Sakaki & Illangasekare, 2007). The packed sand was saturated below the valleys with blue-dyed water to allow for visualization of drying during the experiment. Soil undulations were then built with fully wet sand. The amplitude and length of one-period undulation were 3.6 and 30 cm, respectively. During packing, some free water was left above the valley surface to keep the undulations saturated via capillary rise. Because the characteristic length of the #50/70 sand is  $\sim 12$  cm (Lehmann et al., 2008) based on the sand properties (Gao et al., 2018), the undulating soil surface was assumed to be close to full saturation at the start of the experiment (also confirmed by soil moisture sensors). Prior to the start of the experiment, the soil tank was covered with plastic

wrap to prevent evaporation. The side and the bottom walls of the tank did not allow for fluid flow, and the valve at the bottom of the tank was shut off so that no water was supplied at the bottom boundary. After packing, the soil tank was placed on a weight scale (Sartorius Model 11209-95, range = 65 kg, resolution =  $\pm 1$  g) to continuously monitor the water loss from the system and hence the system-level evaporation rate. The tank and scale setup were precisely fit into the custom opening of the bottom floor of the wind-tunnel test section and adjusted to make sure the tank surface was aligned flush with the floor (Figure 4.2). The small gap between the opening and the tank was sealed with tape to prevent improper air ventilation. A motorized, computer-controlled traverse was installed from the ceiling of the wind-tunnel test section. The traverse could move horizontally along the mainstream through the opening at the wind tunnel ceiling. The single-sensor wire probe of the HWA system was then mounted on the traverse, allowing for precise positioning of the sensor to the predefined measurement points. The HWA system was then implemented to measure the mean wind speed field point by point above the undulating soil surfaces.

Figure 4.3 shows the reference coordinate system for the HWA measurement points. The  $x$ -axis was set at the tank surface. In the horizontal direction ( $x$ -axis), 12 positions were selected from 0 to 60 cm spaced every 5 cm. In the vertical direction ( $y$ -axis), the measurement range was from -7 cm (the value of the lowest point of the soil surface on a vertical axis) to 10 cm in the free flow region. Piecewise increments in the vertical direction were chosen in order to guarantee the accuracy of measurement:  $\Delta y = 1$  mm ( $h < 1$  cm);  $\Delta y = 2$  mm ( $1$  cm  $< h < 2$  cm);  $\Delta y = 5$  mm ( $h > 2$  cm) where  $h$  is the height above soil surface and  $\Delta y$  is  $y$ -increment. All the test points were set at the lateral center profile of the tank. For each vertical measurement column (the red dashed lines in Figure 4.3), the probe sensor was initially placed at the first measurement point, about 2 mm

away from sand surface. The probe was then moved up under the control of the computer and stopped at the next pre-defined point for 2-3 seconds to measure the wind speed. In this way the sensor collected data point by point until reaching the highest test point ( $y = 10$  cm) at each column. Afterwards, the probe shifted to the next column and repeated the same steps until finishing the measurements at all pre-defined test points. 659 test points in total were collected in this experiment.

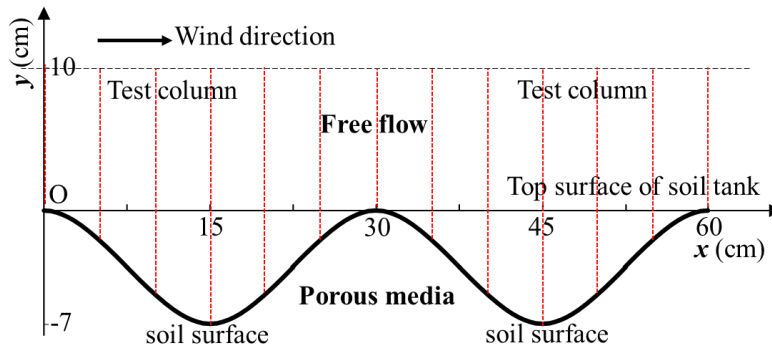


Figure 4.3 Schematic of the coordinate system above the soil surface. The red dashed lines are the test columns.

To start the experiment, the wind tunnel was set to a high wind speed of 6.0 m/s ( $\pm 0.1$  m/s), ensuring the development of a fully turbulent boundary layer over the soil surfaces. HWA measurements were first taken at the column 108 mm upstream of the tank edge ( $x = -108$  mm in Figure 4.3) to verify the generated boundary layer. In the vertical direction, the test points were spaced from  $y = 0$  to  $y = 10$  cm with the same piecewise increment defined above. The solutions of both laminar and turbulent boundary layer equations were used to fit the data to verify the flow state. The fitting results are presented in section 4.4.3. Afterwards, the plastic wrap that covered the top of the tank was removed, any remaining water located above the valleys was drained by a syringe and the evaporation experiment commenced. During evaporation, the soil moisture and weight of the soil tank were monitored every minute. The wind speed profiles were measured by

HWA point by point. The experiment lasted six hours due to the limitation of time and laboratory.

#### 4.4.3 Experimental Results and Model Verification

Prior to presenting the boundary layer profiles above the undulating soil surfaces, the profile measured at 108 mm upstream of the tank is given by Figure 4.4 as compared with different fitting methods. Power-law turbulent boundary layer profiles with different index ( $\beta$ ) values and laminar Blasius solutions are compared with the observations, in which  $\beta = 4.225$  is estimated from the measured data (Appendix 0). A detailed mathematical description of the two boundary layers can be found in (Appendix 0). Figure 4.4 illustrates that the power law matches with the data much better than the Blasius solution, indicating that a turbulent boundary layer was developed along the wind tunnel floor. According to Cheng (2007), a power-law index ( $\beta$ ) varying from 4 to 12 is recommended, and 2 to 6 is suggested in some extreme cases such as macroscale bed roughness. Hence,  $\beta = 4.225$  estimated from experimental data is qualified for the data fitting, consistent with the theory in Cheng (2007).

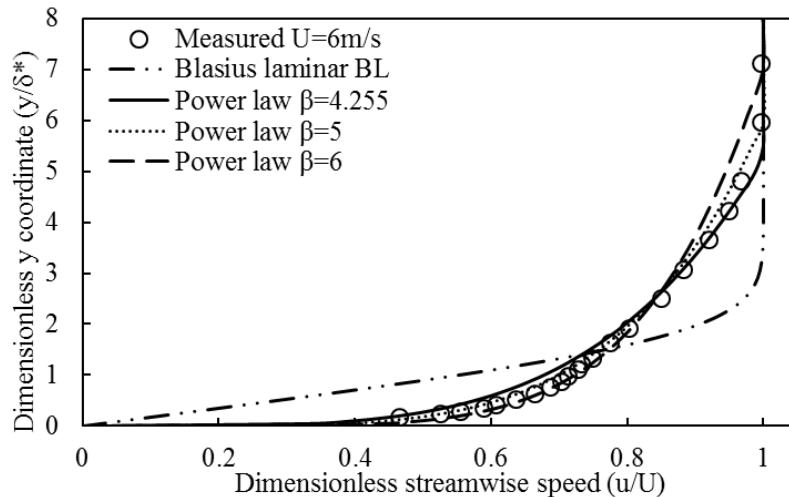


Figure 4.4 Measured dimensionless speed profile at 108 mm upstream of the soil tank. Power-law turbulent and Blasius laminar boundary layer solutions are compared by fitting the measured profile.  $u$  (m/s) is the measured wind speed at different locations;  $U$  (m/s) is the maximum wind speed in the mainstream, i.e. 6 m/s in this experiment;  $\delta^*$  (m) is the displacement thickness.

Figure 4.5 (a) shows the wind speed profiles above the undulating soil surfaces measured via HWA. The speed decreases with the reduction of the vertical position from 6 m/s in the mainstream. In the valley, however, the speed increases again as approaching the soil surface, especially near the leeward side of the valley. Since the HWA with single-sensor wire probe could only measure the average streamwise speed without direction, the changes of the speed with the vertical positions indicate the reverse airflow (i.e. the presence of RZs), thus demonstrating that HWA is able to capture the turbulent boundary layer. The simulated wind speed (Figure 4.5 (b)) using the numerical model described in section 4.3 shows similar trends with the measurements.

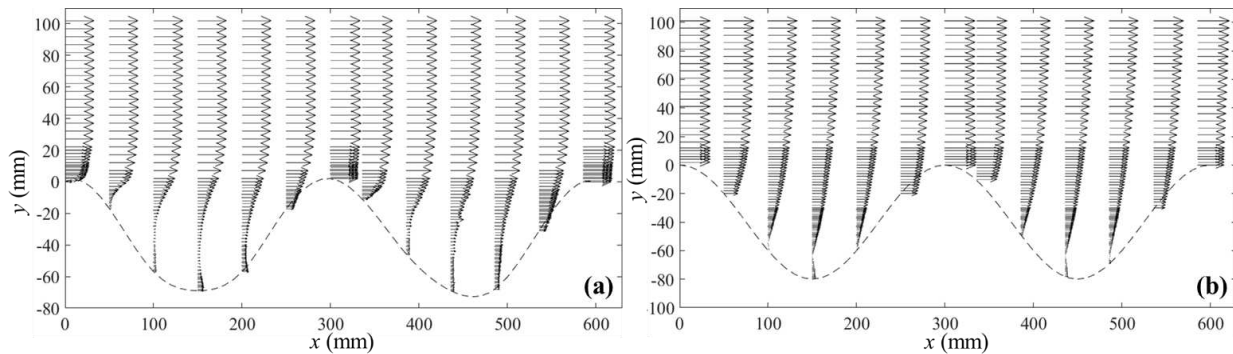


Figure 4.5 Observed (a) and simulated (b) wind speed profiles. The dashed line represents the surface. The length of each arrow is proportional to the flow speed.

However, several experimental limitations are responsible to the difference of the profile between the experiment and modeling. First, the manual surface packing results in small surface variations preventing a perfect cosine shape like that in the model. Second, because of the point by point nature of HWA, it took upwards of 6 hours to obtain two-dimensional speed profiles in this experiment. Although the wind tunnel flow field is very precise, small variations of temperature and pressure in the laboratory during this period can affect the wind field development. Finally, the presence of the traverse and sensor itself in the free flow, albeit small, disrupts the wind field development. Despite these limitations, HWA was able to capture the turbulent

boundary layer development, demonstrating its promise for such uses. This is especially useful as many times non-intrusive methods such as particle imaging velocimetry (PIV) are not available or cost prohibitive. HWA offers a fairly simple yet precise alternative to gain understanding of the boundary layer. However, to overcome some of these limitations, a non-intrusive method will also be explored for future experiments.

Figure 4.6 shows the observed speed contours obtained by kriging interpolation of the measured speed data. The low speed area above the leeward surfaces (surface S1 and S3) are caused by the RZs. The presence of the RZs, which will be expanded upon in section 4.5.2, results in vapor accumulation at leeward surfaces and thus a locally low evaporation rate. This was also observed visually through the deposition of the blue dye on the soil surface (Shokri & Or, 2011). As seen by Figure B1 in Appendix 0, differences in the blue dye deposition are qualitatively very obvious based on the color gradients between the leeward and windward surfaces. The darker blue surfaces correspond to locations of high evaporation rate. Connected with Figure 4.6, this demonstrates that locally lower evaporation appears at the leeward soil surfaces due to the RZs.

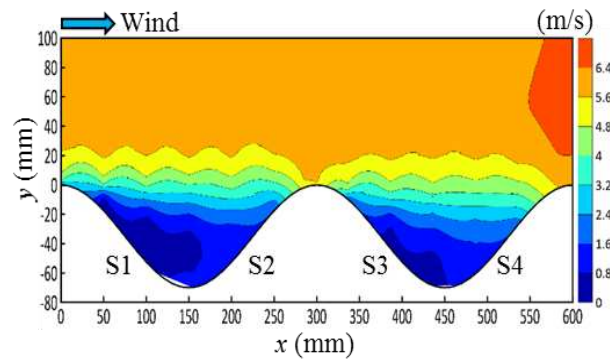


Figure 4.6 Interpolated speed contours (m/s) using the measured speed profiles in Figure 4.5 (a). S1, S2, S3, and S4 represent the four wavy surfaces, respectively.

During the 6-h experiment, the weight of the soil tank and soil moisture were monitored.

Figure 4.7 illustrates the experimental and modeled accumulative evaporation and soil moisture

6.5 cm below the top surface of the tank (~1 cm below the undulating sand surface). The data oscillation at ~2.5 h is due to an unavoidable stop and restart of the wind tunnel for adjustment purposes. As the soil tank was initially saturated, the accumulative evaporation amount increases almost linearly with time at a high evaporation rate (Stage I evaporation). The modeled soil moisture matches the observations well, further verifying the ability of the model to capture the evaporation behavior under turbulent conditions. This will be further discussed in Section 4.5.

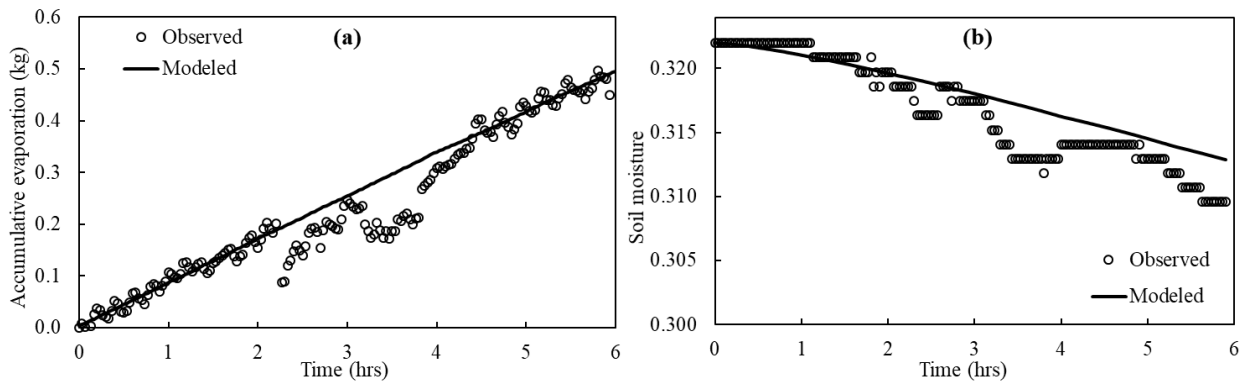


Figure 4.7 (a) Comparison of observed and modeled evaporation amount; (b) Comparison of observed and modeled soil moisture at the first-layer moisture sensor ( $x = 10$  cm,  $y = -6.5$  cm based on the coordinate system showed in Figure 4.3).

#### 4.5 Numerical Analysis of Evaporation from Undulating Surfaces

This section provides theoretical insights into the characteristics of evaporation from undulating soil surfaces under turbulent conditions. Seven cases, A - G, listed in Table 4.2 were simulated. Five variables of interest, i.e. flow state, wind speed, AR, size of sand (represented by van Genuchten parameter  $\alpha$  and  $n$ ), and soil permeability, were studied. For each scenario, the simulated porous media was initially saturated. Additionally, the vapor concentration in the free flow and the temperature of the whole system were set equal to the inflow boundary conditions, i.e.  $6E-3$  kg/m<sup>3</sup> and 22°C, respectively, consistent with experimental conditions. The mathematical model was implemented using COMSOL Multiphysics 5.2a (Comsol, 2016) based on a finite

element method. Quadratic Lagrange elements were used for the dependent variables ( $p_g^{\text{pm}}$ ,  $p_w^{\text{pm}}$ ,  $\mathbf{u}_g^{\text{ff}}$ ); and linear Lagrange elements were applied for the other variables ( $p_g^{\text{ff}}$ ,  $C_v$ ,  $T$ ). The whole computational domain was discretized by triangular meshes with 20,506 elements (156,545 degrees of freedom in total). Local mesh refinement was introduced at the interface of the two subdomains due to the possible formation of large gradients. Before the calculation, the vapor concentration field and flow field were initialized. A backward Euler time discretization was used to generate an implicit solving system. In every time step, a segregated solver was applied. The flow-concentration-heat variables ( $\mathbf{u}_g^{\text{ff}}$ ,  $p_i^j$ ,  $C_v^j$ ,  $T^j$ ,  $i = w, g$ ;  $j = \text{ff, pm}$ ) and turbulent variables ( $k, \varepsilon$ ) were solved in two subgroups. Each group used a damped version of Newton's method. In each iteration, a linearized version of the nonlinear system was solved using multifrontal massively parallel sparse direct solver (MUMPS) and parallel sparse direct solver (PARDISO) for each subgroup, respectively.

Table 4.2 Modeling scenarios and corresponding variables of interest.  
Case A is regarded as the reference case

Case	$U$ (m/s)	AR ( $2\gamma/\lambda$ )	Flow state	Size of sand		Permeability	Variable of interest
				$\alpha$ ( $\text{m}^{-1}$ )	$n$	( $\text{m}^2$ )	
A	1.0	0.27	turbulent	5	7	$1 \times 10^{-10}$	Reference case
B	1.0	0.27	laminar	5	7	$1 \times 10^{-10}$	Flow state
C	3.5	0.27	turbulent	5	7	$1 \times 10^{-10}$	Wind speed
D	6.0	0.27	turbulent	5	7	$1 \times 10^{-10}$	Wind speed
E	1.0	0.15	turbulent	5	7	$1 \times 10^{-10}$	Aspect ratio
F	1.0	0.15	turbulent	8	11	$1 \times 10^{-10}$	Size of sand
G	1.0	0.27	turbulent	5	7	$1 \times 10^{-12}$	Permeability

#### 4.5.1 Laminar and Turbulent Flow Conditions

As discussed in section 4.2, near-surface turbulence can occur even at a low wind speed due to the presence of roughness at a broad range of scales and long leading edge for boundary layer development. Because an inaccurate assumption of flow state may lead to a great error in the

estimation of the evaporation behavior, we first compare the application of laminar (Gao et al., 2018) and turbulent models by case A and B for the same soil at the same low wind speed. This is an important comparison as many models assume laminar conditions without recognition as to the influence of such an assumption.

Figure 4.8 shows the evolution of the evaporation rate calculated based on the assumption of turbulent and laminar conditions.

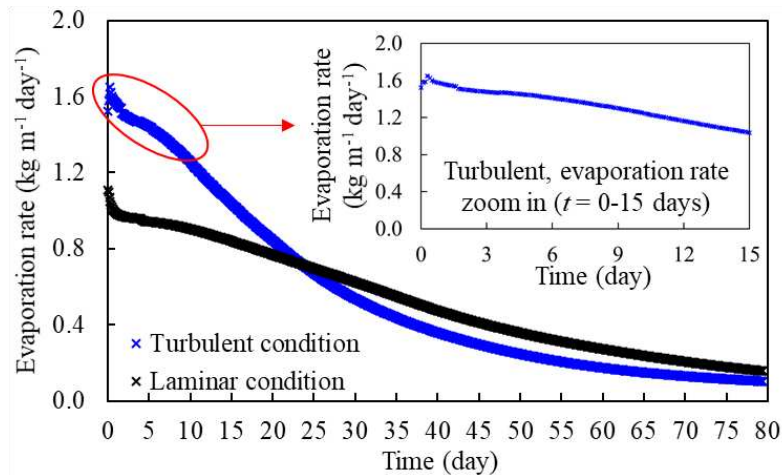


Figure 4.8 Effect of airflow state, comparison of Cases A and B: modeled evolution of the evaporation rate.

From a fully saturated condition as presented here, the evaporation process generally progresses in three stages: (1) the atmosphere-dominated Stage I when the evaporation rate is high and constant or slowly decreases; (2) the transition period when the evaporation rate decreases quickly; and (3) the soil-dominated Stage II when the evaporation rate is low and decreases slowly. Figure 4.8 illustrates that the estimated duration of evaporation stages and evaporation rate by laminar and turbulent models are significantly distinct. Based on the given modeling conditions, the evaporation rate obtained from the turbulent model is obviously higher and stays in Stage I for a shorter time compared with the laminar model. The transition stage occurs at about  $t = 6$  d according to the zoom-in view of the evaporation rate from 0 to 15 d. After a rapid transition, the

evaporation then comes to Stage II when the evaporation rate is lower than that under laminar conditions. Hence, the turbulent airflow promotes Stage I evaporation, shortens Stage I duration, and accelerates the transition to Stage II. The comparison illustrates that an inaccurate assumption of airflow states will definitely result in a miscalculation, especially for the fundamental mechanism studies. In the sections below, as an extension of Gao et al. (2018) in which laminar airflow was assumed, the turbulent model is applied to investigate the influence of turbulence on the evaporation from undulating soil surfaces for various atmospheric and soil conditions.

#### **4.5.2 Influence of Wind Speed**

In this section, the influence of wind speed on the evaporation from undulating surfaces is considered under turbulent conditions by comparing Cases A, C, and D. Figure 4.9a shows the change of system evaporation rate over time under three different wind speeds from 1 to 6 m/s. Speeds were selected to correspond to low, medium and relatively high speed conditions compared to nature, in which 6 m/s was the speed applied in the above experiment. Consistent with Gao et al. (2018) for laminar airflow, increasing wind speed promotes stage I soil evaporation under turbulent airflow. However, in comparison to laminar conditions, the enhancement with an increase in wind speed is quite small under turbulent conditions, especially for high wind speeds. Interestingly, through laboratory experiments, Davarzani et al. (2014) noticed a threshold wind speed over which an increase in wind speed had a limited effect on the evaporation rate, whereas no explanation was provided. This can be understood by our model in which turbulence is incorporated by further investigation of the diffusive flux. According to Fick's law, diffusive flux is controlled by the thickness of viscous sublayer where vapor diffusion dominates, the vapor concentration difference across the viscous sublayer and the diffusion coefficient related with turbulence under turbulent conditions.

Figure 4.9b shows the distribution of the upward diffusive flux along the undulating soil surface at  $t = 3$  and 30 d. Time  $t = 3$  d corresponds to a time when all three test cases are still in Stage I evaporation. At this time, the peaks and valleys contribute to the evaporation almost equally, as shown by their similar diffusive flux. However, when it comes to the third day after the evaporation starts, the water saturation at the peaks has dropped close to 20%, while the valleys still have a 80% saturation (Figure 4.9c). This indicates that the peaks have already lost their potential capacity to keep a high diffusive flux due to the water deficiency, and thus the flux at the peaks will decrease quickly (as seen Figure 4.9b from 3 to 30 d). By contrast, during the fast moisture exhaustion at the peaks, the valleys are still able to continue to provide water to the surface (Figure 4.9c), and they present a larger diffusive flux than the peaks over time (Figure 4.9b). It determines that the valleys are the main contributors during most of the evaporation period. Therefore, the influence of wind speed will be limited to the valleys, as the peaks dry quickly.

However, the diffusive flux at the valleys does not increase a lot with the increase in wind speed, as seen in Figure 4.9b, which can be understood from three aspects. First, RZs are formed in the valleys for the AR set in these three test cases, where the reverse airflow leads to accumulation of water vapor at the leeward surfaces, resulting in locally lower diffusive flux than that at the windward surfaces, especially at the start of RZs (i.e., separation points; Figure 4.9b and Figure 4.9d). Thus, the thickness of the viscous sublayer is also related to the RZs, rather than just the wind speed, like in the case of laminar airflow over a flat surface. Second, under turbulent conditions, the diffusion coefficient (Eq. (4.7)) consists of two terms, one of which is associated with turbulent features (Eq. (4.8)). In this sense, turbulent variables such as kinetic energy and energy dissipation are highlighted, and the impact of wind speed is somewhat undercut. Third, turbulent airflow promotes the whole-system evaporation and decreases the amount of water

reaching the valleys, although slightly (Figure 4.9c), with the increase in wind speed, resulting in less formation of water saturation vapor (Figure 4.9d). The vapor concentration difference across the viscous sublayer will decrease to some degree, which is accompanied by the reduction of the viscous sublayer thickness caused by increasing wind speed. Thus, the change in the diffusive flux is unpredictable.

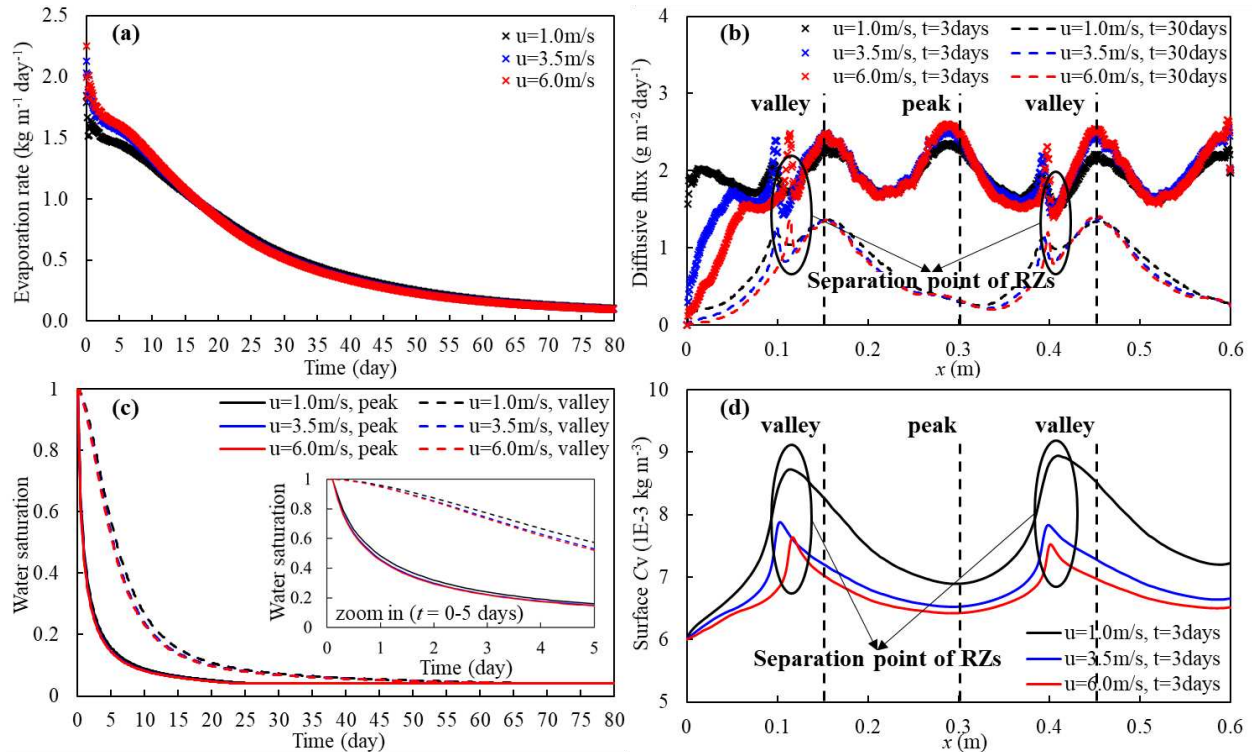


Figure 4.9 Effect of wind speed - comparison of cases A, C, D: (a) evaporation rate; (b) upward diffusive flux along undulating surface at  $t = 3, 30$  days; (c) soil surface water saturation at selected peak and valley over time and zoom-in saturation at 0-5 days; (d) vapor concentration ( $C_v$ ) at soil surface at  $t = 3$  days. Vapor accumulates especially at the separation points, resulting in low diffusive flux (b).

In short, in the case of evaporation from undulating soil surfaces under turbulent conditions, wind speed is not the only key influencing factor for the development of boundary layers, and thus its effect on the local diffusive flux and system-level evaporation rate is somewhat restricted. As for the experiments based on a flat surface in Davarzani et al. (2014), the last two reasons, both

caused by turbulence, account for the existence of a wind speed threshold after which the wind speed has reduced impact on system-level evaporation. Further, this also demonstrates that an accurate assumption of airflow states is significant, especially for REV-scale fundamental studies.

### **4.5.3 Influence of Aspect Ratio**

This section discusses the influence of the undulating soil surface AR by comparing test Cases A and E. As the AR is defined by the ratio of the depth and length of one soil undulation, a larger AR corresponds to a steeper undulating surface. An AR = 0.27 is selected, as it is close to the experimental design, and AR = 0.15 represents a smoother while natural surface.

The comparison of the evaporation rate for the two ARs (Figure 4.10a) shows a rather negligibly faster evaporation rate from the steeper undulating case, but only during Stage I. This can be understood from two aspects. First, large ARs increase the effective surface area in contact with water (Figure 4.10b) through capillarity and thus enhance evaporation mainly in Stage I. However, due to the fast drying of the peak area under turbulent conditions, the enhancement is not significant. Second, RZs form in the valleys for AR = 0.27, where the reverse airflow causes the local accumulation of water vapor at the leeward surfaces as shown in Figure 4.11a. By comparison, no RZ is identified for the smoother surface (AR = 0.15), and thus the vapor spreads more evenly along the soil surface as shown in Figure 4.11b. The vapor distribution in the two cases determines that the surface vapor concentration gradient is lower upward and higher horizontally for the steeper surface than for the smoother surface. In turn, the concentration gradient determines that compared with the smoother surface, the steeper surface has a smaller upward diffusive flux and a larger horizontal flux, as shown by Figure 4.10c and Figure 4.10d, respectively. Further, this determines slight difference in the evaporation rate caused by AR, since evaporation rate equals the integration of surface diffusive flux.

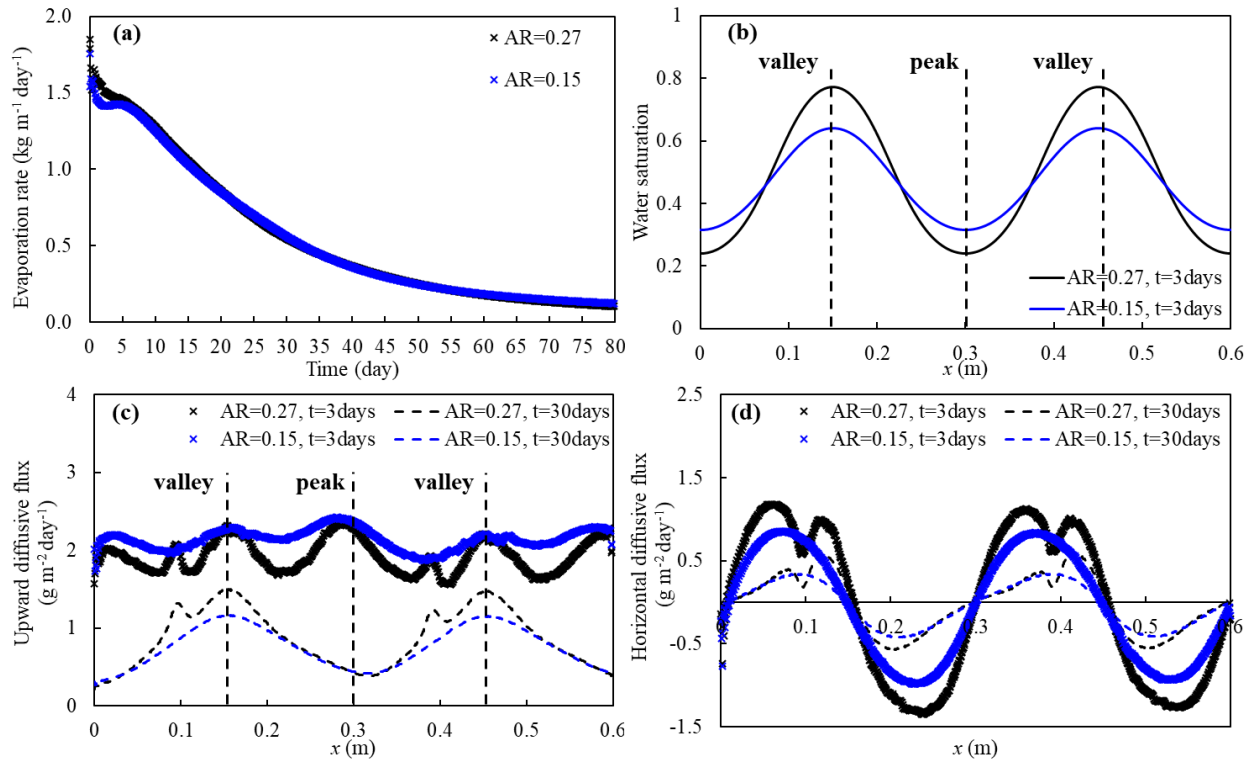


Figure 4.10 Effect of AR - comparison of case A and E: (a) evaporation rate; (b) water saturation at soil surface at  $t = 3, 30$  days; (c) upward and (d) horizontal diffusive flux along surface at  $t = 3, 30$  days.

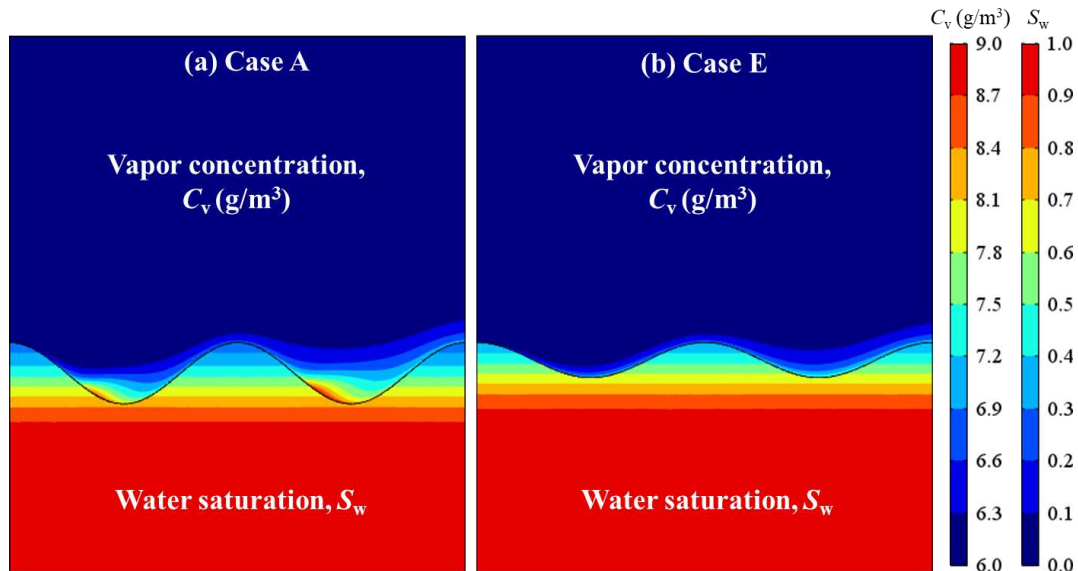


Figure 4.11 Vapor concentration ( $\text{g/m}^3$ ) in the free flow and water saturation in the porous media at  $t = 3$  days.

#### 4.5.4 Influence of Permeability

Permeability is an intrinsic property of the porous media, which determines the continuous flow ability of liquid and gas through the media. Under laminar conditions, higher permeability results in a longer Stage I evaporation for both undulating and flat surfaces (Mosthaf et al., 2014; Gao et al., 2018). In comparison, under turbulent conditions, changes in permeability have little to no effect on the Stage I duration (Figure 4.12a). The reason for the equivalent evaporation rate in Stage I is the adequate water supply at the soil surface for both test cases, which can also be demonstrated by the equal upward diffusive flux at  $t = 3$  d, shown in Figure 4.12b. Alternatively, as mentioned in section 4.5.1, the turbulent airflow shortens the first stage of evaporation. It thus restricts the influence duration of permeability and results in an almost equivalent Stage I period. Therefore, the assumption of laminar conditions may misestimate the influence of soil properties.

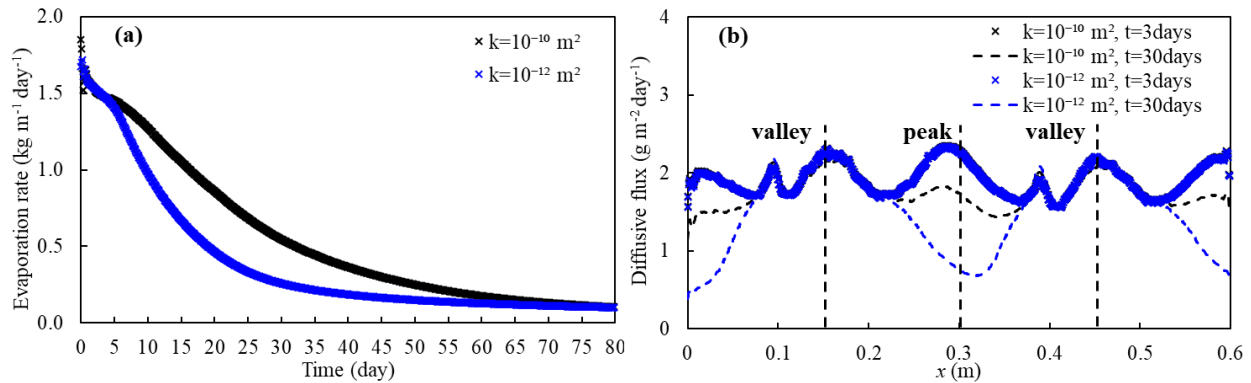


Figure 4.12 Effect of permeability - comparison of case A and G: (a) evaporation rate; (b) upward diffusive flux along surface at  $t = 3, 30$  days.

#### 4.5.5 Influence of Size of Sand

Based on the discussion in the above sections, the turbulent condition shortens the first stage of evaporation and accelerates the transition to Stage II. This phenomenon highlights the importance of water capillarity to the soil evaporation, which is closely associated with the size of sand. The drying characteristic of a sand can be described by the van Genuchten parameters (van

Genuchten, 1980):  $\alpha$  ( $\text{m}^{-1}$ ), which is related to the inverse of the air entry suction; and  $n$  (dimensionless), which is connected with the pore size distribution. The van Genuchten parameters of the #50/70 sand used in this experiment are  $\alpha = 5 \text{ m}^{-1}$  and  $n = 7$  (Gao et al., 2018), and for a coarser sand #12/20, they are approximately  $8 \text{ m}^{-1}$  and 11 (Wallen et al., 2016), respectively. The influence of the combined effect of the air suction and the pore size is numerically studied by comparing the evaporation from #50/70 and #12/20 sand. The evaporation rate shown by Figure 4.13a illustrates that under turbulent conditions, the coarse-sand system evaporates quickly and thus enters transition and Stage II rapidly. Figure 4.13b also shows that the peak area of a coarse sand loses its contribution early, whereas the valley area plays an important role in the system evaporation due to water availability. Hence, Stage I evaporation is not only shortened by turbulent airflow, but it may even disappear in the case of a coarse sand. An inaccurate assumption of the airflow states may lead to wrong estimation of evaporation stages.

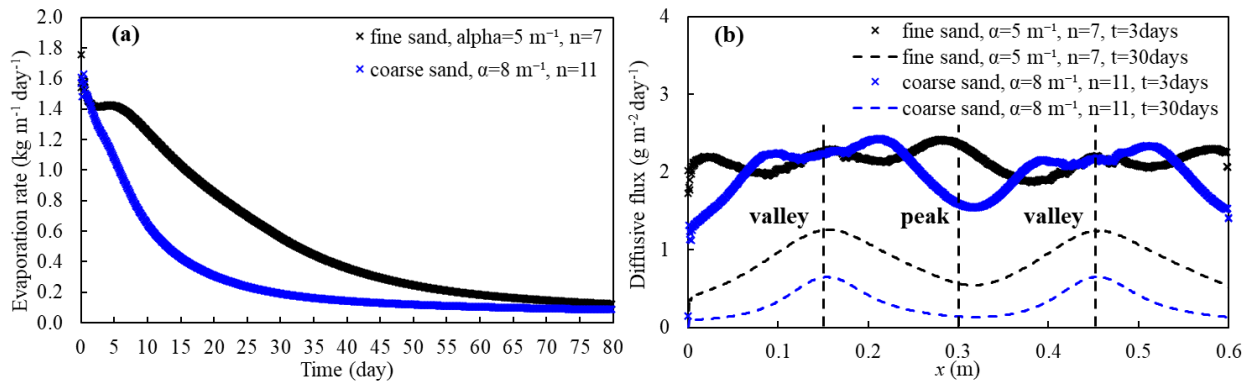


Figure 4.13 Effect of size of sand represented by  $\alpha, n$  - comparison of case E and F: (a) evaporation rate; (b) upward diffusive flux along surface at  $t = 3, 30$  days.

#### 4.6 Conclusions

With the goal of understanding the influence of atmospheric turbulent airflow on the evaporation from undulating soil surfaces, we initiated an explorative study using both modeling and experimental approaches. The coupled free flow and porous media flow model that was

developed and testified in Gao et al. (2018) was modified by incorporating turbulent airflow in the free flow through RANS equations, in which the Reynolds stress term is expressed by a two-equation model for kinetic energy  $k$  and energy dissipation  $\varepsilon$ , respectively (i.e., RANS with  $k$ - $\varepsilon$  closure model). The prominent feature of this coupled model compared with the commonly used parameterized top-boundary-condition-type formulas is that it uses the most basic REV-scale equations to explicitly describe the physical processes during soil evaporation (e.g., mass and heat transfer, phase change, etc.), as well as the atmospheric airflow states and their development as influenced by the surface geometry. In that sense, the uncertainty caused by simplified parameterization can be mostly excluded, and it makes the coupled model particularly appropriate for fundamental studies. In particular, the evaporation rate, as well as other global and local information in the evaporation system (e.g., moisture, temperature, vapor concentration, mass and thermal fluxes, etc.), can be obtained in real time by this method.

A preliminary laboratory experiment was conducted by integrating a soil tank within a wind tunnel to initiate this study. Hot-wire anemometry was for the first time applied in the soil tank–wind tunnel system to measure the wind field for the laboratory study of soil evaporation. The development of the boundary layer above the undulating soil surfaces was successfully measured at high spatial resolutions and RZs were clearly captured in the valley area. Recirculation zones caused locally low-level evaporation at the leeward soil surfaces, which was observed by less dye deposition at leeward surfaces compared with the windward surfaces. Besides, the collected soil moisture and accumulative evaporation amount in the experiment, as well as the HWA-measured wind speed profiles, matched well with the simulation results from the extended coupled model, allowing us to have an initial understanding of the influencing factors using numerical modeling.

From the perspective of modeling, the influence of wind speed, AR, permeability, and size of sand on evaporation from undulating soil surfaces under turbulent conditions was investigated. Compared with laminar conditions, atmospheric turbulent airflow enhances the system-level evaporation rate and shortens the duration of the Stage I due to fast loss of water, especially at the undulation peaks. The undulation valleys play a major role during most of the evaporation period due to their vicinity to the receding water table. First, increasing wind speed has negligible influence on the local evaporation at the peaks while slightly affecting the valleys. The limited influencing area leads to limited contributions of increases in wind speed to the evaporation rate of the whole system. In the meantime, RZs are prone to develop in the undulating surface valleys with certain ARs, which can affect the development of the viscous sublayer and further influence the local diffusive flux. Especially under turbulent conditions, the vapor diffusion within the viscous sublayer is also associated with turbulent features such as kinetic energy and energy dissipation. Under the intertwined circumstances including both soil undulations and atmospheric turbulent airflow, wind speed is no longer particularly important, as is commonly assumed for laminar airflow over a flat surface. Therefore, the influence of wind speed on undulating-surface evaporation under turbulent conditions will be restricted. Second, the surface AR directly determines the presence and extent of the RZs, which play a significant role in the vapor distribution and the diffusive flux at the soil surfaces. Thus, the AR affects evaporation through influencing both the vertical and horizontal diffusive flux out of the soil surface, as well as the surface water availability. Third, permeability shows little impact on the duration of Stage I under turbulent conditions, and further, Stage I may even vanish in the case of a coarse sand.

Additionally, in terms of the experiment, although it is possible to capture the turbulent boundary layer using HWA, the single-sensor wire probe used in this study could only measure

the mean streamwise wind speed. Therefore, further follow-on study is warranted, using particle image velocimetry to capture a full instantaneous boundary layer profile with flow directions. Also, the soil tank used in this experiment was originally designed for a single-period wavy surface presented in Gao et al. (2018). Hence, the locations of the soil moisture sensors were not ideal (i.e., close to the surface of peaks and valleys). A new soil tank will be designed based on the locations of interest to measure moisture and temperature. The soil surface undulations will be built at the tank surface rather than inside the tank to avoid the influence of the side walls of the tank on the airflow development in the valleys. A series of experiments will be carried out considering various variables (e.g., wind speed, undulation space) to obtain more data to further improve the numerical model and understanding of the characteristics of evaporation from undulating surfaces under turbulent airflow.

We expect the planned follow-on work to be useful for improving the models for evaporation prediction on the engineering scale and similar research problems involving interactions between the free flow and porous media flow.

## CHAPTER 5

### DETERMINATION OF VAPOR AND MOMENTUM ROUGHNESS LENGTHS ABOVE AN UNDULATING SOIL SURFACE BASED ON PIV-MEASURED TURBULENT VELOCITY PROFILES

#### 5.1 Abstract

Accurate characterization of soil-atmosphere exchange processes based on Monin-Obukhov similarity theory (MOST) relies on the proper prediction of the vapor roughness length ( $z_{0v}$ ) and momentum roughness length ( $z_{0m}$ ). These two crucial parameters, characterizing the mass and momentum transfer respectively, are heavily related to the boundary layer in the vicinity of the soil surface. The assumption of  $z_{0v}$  approximating  $z_{0m}$  when applying MOST to bare soil evaporation has been widely adopted, without considering the disruption of soil undulations on the near-surface velocity field. The relationship between  $z_{0v}$  and  $z_{0m}$ , which further determines the evaporative flux, remains unclear in the presence of an undulating soil surface. Thus, this study aims to fill this gap through direct measurements of the velocity field developed closed to the undulating soil surface. To achieve this goal, four wind tunnel – soil tank experiments were conducted considering different wind speed and surface configurations. Particle Imaging Velocimetry (PIV) was employed to collect the velocity field information. The experimental data were applied to formulize relationship between  $z_{0v}$  and  $z_{0m}$ . Results demonstrate that  $z_{0v}$  is averagely smaller than  $z_{0m}$  by 3 to 7 orders of magnitude, owing to the undulating soil surface. Combined with the PIV-measured velocity field, the effects of surface configurations and wind speed on the ratio of  $z_{0v}$  to  $z_{0m}$  are demonstrated closely related to the distinct mechanisms of mass and momentum transfer. The newly proposed formulation was then used to evaluate the

evaporative flux for laboratory and field experiments, demonstrating the efficacy of the approach.

## **5.2 Introduction**

Bare soil evaporation is a key component of the global hydrological cycle. Even in the arid or semiarid areas with sparse to moderate plants, evaporation directly from soil makes up about half of the total evapotranspiration (e.g. Allen, 1990; Wilcox et al., 2003; Lawrence et al., 2007). Hence, an accurate estimation of the bare-soil evaporation rate is important to the study of terrestrial water movement, agricultural crop growth, weather forecast, climate change, etc. It requires a rational characterization of soil-atmosphere exchange processes. Even though decades of research have been conducted, knowledge gaps still exist in this issue and a key component of them stems from the soil surface. Typically, the soil surface in nature is hydrodynamically rough due to either the natural processes (e.g. soil erosion, bog area) or mechanical manipulation (e.g., agricultural furrow). The macro-scale soil undulations should theoretically play a significant role in soil-atmosphere exchange processes because of the changes to the soil surface – water table distance and the disruption to the near-surface boundary layer.

Several studies aimed at understanding the fundamental characteristics and mechanisms have been conducted using fully coupled model concept (e.g., Fetzer, 2018; Gao et al., 2018, 2020; Coltman et al., 2020). However, this model is not applicable to a practical bare soil evaporation issue due to its complexity and high computational cost. Therefore, model simplifications are oftentimes made when considering practical applications. One widely adopted simplification involves using a vapor flux top boundary condition to represent the exchange processes (e.g., Mahfouf & Noilhan, 1991; Desborough et al., 1996; Oleson et al., 2004; Kollet & Maxwell, 2008), in which the exchange process between the soil surface and the near-surface atmosphere relates to the aerodynamic resistance derived based on the Monin-Obukhov similarity theory (MOST)

(Brutsaert, 2013). In the aerodynamic resistance, two crucial parameters characterizing the mass (i.e. vapor scalar) and momentum transfer processes are termed the vapor roughness length ( $z_{0v}$ ) and the momentum roughness length ( $z_{0m}$ ), respectively. They are commonly assumed equal for bare-soil evaporation studies. However, since soil undulations modify the boundary layer in the vicinity of the soil surface, and thus influencing the exchange process between the soil surface and the near-surface atmosphere, the relationship between these two parameters remains unclear and requires further investigation. An inaccurate assumption for the relationship between these two parameters when adopting the reduced model concept will result in a false characterization of the exchange processes and deviated prediction of the soil evaporation rate.

According to the reduced model concept mentioned above, the soil-atmosphere exchange process considering vapor flux is described by (Vanderborght et al., 2017):

$$E = \frac{\rho_{\text{sat}}(z_{\text{vap}}) - \rho_{\text{a}}(z_{\text{ref}})}{r_{\text{a}} + r_{\text{s}}(\theta_{\text{w}})} \quad (5.1)$$

where  $E$  ( $\text{kg}\cdot\text{m}^{-2}\cdot\text{s}^{-1}$ ) is the vertical evaporative flux;  $\rho_{\text{sat}}(z_{\text{vap}})$  is the saturated vapor density ( $\text{kg}/\text{m}^3$ ) at the vaporization plane ( $z_{\text{vap}}$ ) of the soil denoted by the top plane of the unsaturated zone;  $\rho_{\text{a}}(z_{\text{ref}})$  is the vapor density ( $\text{kg}/\text{m}^3$ ) in the atmosphere at the reference plane ( $z_{\text{ref}}$ ) where the atmospheric variables (e.g., humidity, velocity) are measured;  $r_{\text{s}}$  is the soil resistance associated with the water content  $\theta_{\text{w}}$  of the top soil layer;  $r_{\text{a}}$  is the aerodynamic resistance for vapor flux depending on the surface geometry and the atmospheric conditions (e.g. wind speed).

Monin-Obukhov similarity theory (MOST) provides a basic theory for the formulation of the aerodynamic resistance. For vapor flux, it takes the form of (Brutsaert, 1975; Parlange et al., 1995; Yamanaka et al., 1997; Sugita & Kishii, 2002):

$$r_{\text{a}} = \frac{\rho_{\text{sat}}(z_{\text{vap}} = z_{\text{s}}) - \rho_{\text{a}}(z_{\text{ref}})}{E} = \frac{1}{u_* K} \ln \left( \frac{z_{\text{ref}} - d_0}{z_{0v}} \right) \quad (5.2)$$

where  $z_{\text{vap}} = z_s$  denotes that the vaporization plane is the soil surface  $z_s$  (m);  $d_0$  (m) is the zero-plane displacement height ( $d_0 = 0$  for a flat bare soil surface);  $z_{0v}$  (m) is the vapor roughness length characterizing the vapor scalar transfer (i.e. mass transfer);  $\kappa$  is the von Kármán constant ( $\kappa = 0.41$ );  $u_*$  (m/s) is the friction velocity determined by the surface shear stress. Usually,  $u_*$  is difficult to obtain experimentally and thus estimated through velocity measurement assuming logarithmic velocity profiles (Brutsaert, 2013):

$$u = \frac{u_*}{\kappa} \ln \left( \frac{z_{\text{ref}} - d_0}{z_{0m}} \right) \quad (5.3)$$

where  $u$  (m/s) is the average mainstream velocity measured at  $z_{\text{ref}}$ ;  $z_{0m}$  (m) is the momentum roughness length characterizing the momentum transfer. By combining Eq. (5.2) and (5.3), the aerodynamic resistance is written as:

$$r_a = \frac{1}{\kappa^2 u} \ln \left( \frac{z_{\text{ref}} - d_0}{z_{0v}} \right) \ln \left( \frac{z_{\text{ref}} - d_0}{z_{0m}} \right) \quad (5.4)$$

The zero-plane displacement height  $d_0$ , the vapor roughness length  $z_{0v}$ , and the momentum roughness length  $z_{0m}$  are three fundamental parameters in characterizing the vapor scalar and velocity profiles. A typical schematic of the velocity profile as wind over surface with soil undulations is shown in Figure 5.1a. Different from a flat or hydrodynamically smooth surface, when soil undulations are present, the vertical origin is not the flat land surface (i.e.  $z_s = 0$ ), but some distance above which is represented by  $d_0$ . Thus,  $d_0$  is solely dependent on the surface geometry while no relationship with the atmospheric conditions. Above  $z = d_0$ , the extension of the velocity profile which is unaffected by the soil undulations intersects with the vertical height coordinate with a thickness  $z_{0m}$ . For mathematical description, the velocity profiles of velocity and vapor density are usually plotted in a dimensionless single-logarithmic coordinate system as shown by Figure 5.1b. The boundary layer close to the soil surface consists of two parts: the interfacial

sublayer (ISL) and the dynamic sublayer (DSL) located just above the ISL. Within the DSL, the impact of soil undulations is negligible and thus the velocity and vapor scalar profiles satisfy the logarithmic law. Within the ISL, a universal logarithmic profile is not valid. This is due to both the existence of the soil undulations and the attenuated turbulence in the ISL that highlights the effect of the viscous shear.  $z_{0v}$  and  $z_{0m}$  denote the heights where the vapor density and velocity are extrapolated from the logarithmic part in the DSL down to the ISL, respectively.

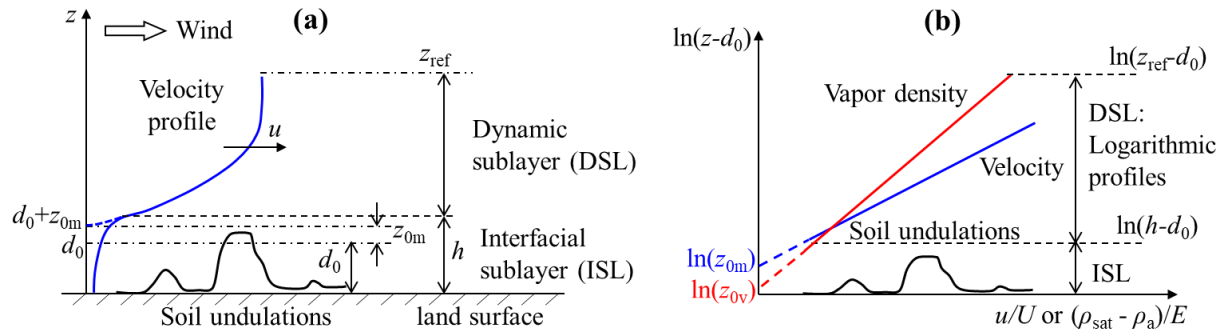


Figure 5.1 (a) Schematic of the velocity profile as wind over soil undulations.  $u$  is the velocity;  $z_{ref}$  is the reference plane;  $d_0$  is the zero-plane displacement height;  $z_{0m}$  is the momentum roughness length;  $h$  is the thickness of the interfacial sublayer. (b) Schematic of the dimensionless velocity and vapor density profiles in a single-logarithmic coordinate system. The x-axis for velocity and vapor density is  $u/U$  and  $(\rho_{sat} - \rho_a)/E$ , respectively.  $U$  is the average mainstream velocity;  $\rho_{sat}$  and  $\rho_a$  are the saturated vapor density at the soil surface and the reference plane, respectively;  $E$  is the evaporative flux;  $z_{0v}$  is the vapor roughness length.

Most of the previous bare-soil evaporation studies using this reduced model concept either assume a flat surface (i.e.  $d_0 = 0$ ) or assume  $z_{0v}$  approximating  $z_{0m}$  with a value on the order of several millimeters to centimeters (e.g., Camillo & Gurney, 1986; Yamanaka et al., 1997; Qiu et al., 2002; Villagarcía et al., 2007; Jefferson & Maxwell, 2015; Rodny et al., 2016). For a soil surface with macro-scale rough elements,  $z_{0m}$  only depends on the soil surface geometry (De Bruin & Moore, 1985; Dong et al., 2001; Vanderborgh et al., 2017), which is also demonstrated by the processed experimental data in this study. In comparison,  $z_{0v}$  is controlled by both the surface geometry and the near-surface velocity field. In the meantime, the surface geometries (e.g.,

undulation size, spacing) also play a crucial role in affecting the near-surface velocity field (Francesco, 1987; Maaß & Schumann, 1996; Poggi & Katul, 2007a; Sherry et al., 2010). For example, flow separation and reattachment may occur due to the adverse pressure gradient formed along the undulating surface. There is a great uncertainty in the feature of the velocity field as air flows across the undulating soil surface, which in turn affects the value of  $z_{0v}$ . Theoretically,  $z_{0v}$  should be different with  $z_{0m}$  from the perspective of the influential factors. Moreover, studies on vapor transfer involving different surface types (e.g., ocean, soil surface with grass, canopy, ice or snow, buildings, etc.) have demonstrated noticeable difference between  $z_{0v}$  and  $z_{0m}$ , and developed distinct expressions to describe their relationship (e.g., Sun, 1999; Su et al., 2001; Kramm et al., 2002; Moriwaki & Kanda, 2006; Vickers & Mahrt, 2006; Liu et al., 2007; Yang et al., 2008; Park et al., 2010; Faivre et al., 2017) considering various surface types and configurations. These studies have raised questions about the validity of the current assumption of  $z_{0v}$  approximating  $z_{0m}$  for soil evaporation in the presence of soil undulations. Further, since these two parameters fundamentally decides the aerodynamic resistance and the subsequent evaporation rate, how much the deviation on the prediction of the evaporation rate would be if assuming  $z_{0v} \approx z_{0m}$  requires to be understood. However, rare studies have been conducted to address this issue (Park et al., 2010).

Therefore, the overarching goal of this study is to understand the soil-atmosphere exchange processes from the perspective of a reduced model concept in the presence of soil undulations. Specifically, there include three main objectives: (1) develop the formulation describing the relationship between  $z_{0v}$  and  $z_{0m}$ , as well as the value of  $d_0$  considering an undulating soil surface based on MOST; (2) understand the dependence of the relationship between  $z_{0v}$  and  $z_{0m}$  on the velocity field developed above the undulating soil surface; (3) validate the formulation by applying it to calculating the evaporation rate for experiments and ascertain the difference of the prediction

compared with the common assumption of  $z_{0v} \approx z_{0m}$ . In order to obtain the velocity field information to formulize the relationship between  $z_{0v}$  and  $z_{0m}$ , Particle Imaging Velocimetry (PIV) technology was employed in the experiments. To the authors' knowledge, it is the first time to use PIV for a laboratory experimental study on soil evaporation.

The paper is organized as follows: in section 5.3, the theory to formulize the relationship of  $z_{0v}$  and  $z_{0m}$ , and the aerodynamic resistance is introduced, producing a group of turbulent flow parameters ( $d_0$ ,  $u_*$ ,  $z_{0m}$ ) and a group of derived coefficients to be determined by experiments. The experimental setup, including the experimental facility, cases, and procedures are presented in detail in section 5.4. With the experimental data, especially PIV-measured near-surface velocity field, the turbulent flow parameters and the derived coefficients in section 5.3 are determined, and thus the relation between  $z_{0v}$  and  $z_{0m}$  is quantified in section 5.5. Besides, the influence of soil surface configuration and the near-surface velocity field on the relationship between  $z_{0v}$  and  $z_{0m}$  is discussed. In section 5.6, the newly formulized aerodynamic resistance is applied to calculate the evaporation rate for the laboratory experiments in this study and a field experiment with similar setup.

### **5.3 Formulation Theory**

This section presents the theory background to formulize the relationship between  $z_{0v}$  and  $z_{0m}$ , and the aerodynamic resistance.

As shown in Figure 5.1, assuming the DSL does not overlap with the ISL and there is a clear interface between them, the aerodynamic resistance is partitioned into two components. One characterizes the resistance between the surface and the upper boundary of the ISL, and the other is between this boundary and some distance above whilst within the DSL:

$$r_a = \frac{\rho_{\text{sat}}(z_s) - \rho_a(z_{\text{ref}})}{E} = \frac{\rho_{\text{sat}}(z_s) - \rho_a(z_h)}{E} \Big|_{\text{ISL}} + \frac{\rho_a(z_h) - \rho_a(z_{\text{ref}})}{E} \Big|_{\text{DSL}} \quad (5.5)$$

where  $z_{\text{ref}}$  (m) is the reference plane in the DSL;  $z_h$  (m) is the upper boundary of the ISL, also the lowest boundary of the DSL.

As mentioned above, it is the viscous shear and surface geometry rather than the turbulent effect that dominate the flow behavior in the ISL. Thus an interfacial mass transfer coefficient  $\text{Da}_0$  (i.e. Dalton number) is introduced to describe the mass transfer between the soil surface and the ISL (Brutsaert, 2013):

$$\text{Da}_0 = \frac{1}{u_*} \frac{E}{\rho_{\text{sat}}(z_s) - \rho_a(z_h)} \Rightarrow \frac{\rho_{\text{sat}}(z_s) - \rho_a(z_h)}{E} \Big|_{\text{ISL}} = \frac{\text{Da}_0^{-1}}{u_*} \quad (5.6)$$

In the DSL, the vapor density is a logarithmic function of the vertical position  $z$  (m) described by (Brutsaert, 2013):

$$\frac{\rho_a(z_h) - \rho_a(z_{\text{ref}})}{E} \Big|_{\text{DSL}} = \frac{1}{\kappa u_*} \ln \left( \frac{z_{\text{ref}} - d_0}{z_h - d_0} \right) \quad (5.7)$$

The velocity at  $z_h$  follows logarithmic law as shown by Eq. (5.3):

$$u_h = \frac{u_*}{\kappa} \ln \left( \frac{z_h - d_0}{z_{0m}} \right) \quad (5.8)$$

where  $u_h$  (m/s) is the velocity at  $z_h$ . Thus, Eq. (5.7) is arranged to:

$$\frac{\rho_a(z_h) - \rho_a(z_{\text{ref}})}{E} \Big|_{\text{DSL}} = \frac{1}{u_*} \left[ \frac{1}{\kappa} \ln \left( \frac{z_{\text{ref}} - d_0}{z_{0m}} \right) - \frac{u_h}{u_*} \right] \quad (5.9)$$

Compared with the ISL, the turbulent effect accounts for a dominant portion and thus the interfacial momentum transfer coefficient  $\text{Cd}_0$  is introduced to describe the momentum transfer between the soil surface and the DSL (Brutsaert, 2013):

$$Cd_0 = \frac{u_*^2}{u_h^2} \quad (5.10)$$

Thus, Eq. (5.9) is written as a function of  $Cd_0$ :

$$\left. \frac{\rho_a(z_h) - \rho_a(z_{ref})}{E} \right|_{DSL} = \frac{1}{\kappa u_*} \ln \left( \frac{z_{ref} - d_0}{z_{0m}} \right) - \frac{Cd_0^{-1/2}}{u_*}. \quad (5.11)$$

Hence, the total aerodynamic resistance is obtained by substituting Eq. (5.6) and (5.11) into (5.5):

$$r_a = \frac{1}{u_*} \left( Da_0^{-1} - Cd_0^{-1/2} \right) + \frac{1}{\kappa u_*} \ln \left( \frac{z_{ref} - d_0}{z_{0m}} \right) \quad (5.12)$$

Comparing Eq. (5.12) with Eq. (5.2), the relationship between  $z_{0v}$  and  $z_{0m}$  is obtained (Brutsaert, 2013):

$$\ln \left( \frac{z_{0v}}{z_{0m}} \right) = -\kappa \left( Da_0^{-1} - Cd_0^{-1/2} \right) \quad (5.13)$$

As mentioned above, the velocity field in the ISL is significantly affected by the soil undulations and the viscous shear. To account for the flow state in the ISL, the roughness Reynolds number is defined by  $Re_0 = u_* z_{0m} / \nu$ , where  $\nu$  ( $m^2/s$ ) is the kinetic viscosity. The mass transfer within the ISL is theoretically related to the roughness Reynolds number. Generally,  $Da_0^{-1}$  is considered as a power function of the roughness Reynolds number of the ISL (e.g., Brutsaert, 1975; Verhoef et al., 1997; Mölder & Lindroth, 2001; Mölder & Kellner, 2002; Park et al., 2010):

$$Da_0^{-1} = a Re_0^b \quad (5.14)$$

$Cd_0^{-1/2}$  is commonly considered as a constant for different situations (e.g., Brutsaert, 1975; Verhoef et al., 1997; Mölder & Lindroth, 2001; Mölder & Kellner, 2002; Park et al., 2010). As a parameter related to the momentum transfer in the ISL, it is considered dependent on the roughness

Reynolds number. In this study, we assume  $Cd_0^{-1/2}$  is a natural logarithmic function of  $Re_0$  after examining the experimental data:

$$Cd_0^{-1/2} = m \ln(Re_0) + n \quad (5.15)$$

By substituting Eq. (5.14) and (5.15) to (5.13) we obtain:

$$\ln\left(\frac{z_{0v}}{z_{0m}}\right) = -\kappa \left\{ a Re_0^b - [m \ln(Re_0) + n] \right\} \quad (5.16)$$

and the aerodynamic resistance (5.12) is arranged to

$$r_a = \frac{1}{u_*} \left\{ a Re_0^b - [m \ln(Re_0) + n] \right\} + \frac{1}{\kappa u_*} \ln\left(\frac{z_{ref} - d_0}{z_{0m}}\right) \quad (5.17)$$

The above derivation process implies that the ratio of  $z_{0v}$  to  $z_{0m}$  essentially compares the difference between mass transfer and momentum transfer. To understand the influence of surface undulations on the soil – atmosphere exchange process, the specific expressions for the ratio of  $z_{0v}$  to  $z_{0m}$ , as well as the aerodynamic resistance, need to be obtained. To determine the derived unknown coefficients  $a$ ,  $b$ ,  $m$ , and  $n$  by Eq. (5.14) and (5.15), the parameters ( $d_0$ ,  $u_*$ ,  $z_{0m}$ ) that characterize the turbulent flow behavior first need to be experimentally determined. In this study, PIV was used to measure the velocity field above the undulating soil surface.

#### 5.4 Experimental Setup

Experiments were carried out in the Experimental Aerodynamics Laboratory at the University of Colorado Boulder, using a wind tunnel – soil tank system. Because wind speed and undulation dimensions such as undulation spacing are two important factors affecting the development of the ISL and DSL, and hence the relationship of  $z_{0v}$  and  $z_{0m}$ . Four experiments were conducted considering two wind speeds and two undulation spacings. This section provides a detailed description of the experimental facility and materials, test cases, and procedures.

#### 5.4.1 Experimental Facility and Materials

Figure 5.2 shows the schematic of the wind tunnel – soil tank system employed for experiments in this study. The open-return wind tunnel (Culler & Farnsworth, 2019) can mimic a steady wind at low and intermediate speeds that naturally exist close to land surfaces. The test section is about 2.4 m long and has a square cross section approximately 0.76 m by 0.76 m. A false floor was built in the wind tunnel to minimize the impact of the soil tank on the development of the turbulent flow and provide a set distance across which the incoming boundary layer would develop. There was one opening on the false floor to allow for the soil tank to align precisely. Thus, the soil tank was totally beneath the false floor and the soil undulations were above the false floor. The soil tank was constructed with acrylic glass with a length of 60 cm, height of 15 cm, and width of 10 cm (the inner size). A narrow tank was selected to avoid the influence of the boundary layers developed on the side walls of the wind tunnel. The soil tank, as well as the soil undulations between two wavy plates, was packed with Accusand #12/20 silica sand (particle diameter  $d_{50} = 1.04$  mm, Unimin Corp., Ottawa, MN). The sand was selected based on two considerations. One is to ensure continuous water reaching the undulating soil surface by capillarity when the water table aligns with the undulation valley (i.e. the tank surface). And in the meantime, the moisture distribution in the undulations has an obvious difference between the valleys and the peaks. The reason for this is explained in section 5.6.2. Particularly, considering that the sharp corners of the soil undulations at the false floor would affect the turbulent flow, six undulation extensions were constructed using a 3D printer and installed as shown in Figure 5.2. All sensor wires were extended below the false floor and not exposed in the free flow to avoid disrupting the velocity field.

Four types of sensors were used in the experiments to measure soil moisture, soil temperature, surface relative humidity and temperature (RH/T), and atmospheric RH/T. A

summary of the information of these sensors is listed in Table 5.1. As shown in Figure 5.2, ten holes were drilled into the wavy plates at the front side of the tank to insert soil moisture sensors. At the same positions on the back side of the tank, another ten holes were drilled on the wavy plates to insert soil temperature sensors. The soil moisture and temperature sensors were connected to a series of five channel Em50 data loggers (Decagon Services, Inc.) to store data continuously during experiments. Six surface RH/T sensors were placed on the middle of the six slope surfaces of the soil undulations respectively. They were connected to an AKCP sensorProbe8 data logger to record data with a time stamp. Seven atmospheric RH/T sensors were used to measure RH/T above the soil surface. They were placed as shown by Figure 5.2. These sensors were connected to several Arduino UNO R3 boards with DS3231M I2C real time clocks (RTC). All the atmospheric sensors were aligned on the same lateral plane using a small (diameter = 2mm) sensor holder to accurately position the sensors (Figure 5.2). The smallest holder still capable of accurately positioning the sensors was considered to help reduce the impact on the development of the ISL and DSL. During PIV measurements, the sensor holder and its associate sensors were removed to guarantee a clear free flow domain. In addition to the abovementioned sensors, ambient conditions were monitored using RH/T sensors installed upstream of the wind tunnel and within the laboratory as reference.

Table 5.1 A summary of the sensors used in this study

Sensor	Measurement	Manufacturer	Resolution	Accuracy
ECH <sub>2</sub> O EC-5	Soil moisture	METER Group, Inc.	0.001 m <sup>3</sup> /m <sup>3</sup>	± 2%
RT-1	Soil temperature	METER Group, Inc.	0.1 °C	±0.5 °C from 5 to 40 °C
AKCP sensor	Surface RH/T	AKCP, Inc.	RH: 1% T: 1°C	RH: ±3%; T: ±0.4°C at 25°C
SHT35-DIS	Atmospheric RH/T	Sensirion, Inc.	RH: 0.01% T: 0.01°C	RH: ±1.5%; T: ±0.1°C from 20°C to 60°C

For each experiment, a constant water table was established at the valley ( $z_s = 0$  cm), which is on the same horizontal plane as the false floor/soil tank interface. This height was selected to ensure continuous water reaching the soil surface at the peaks and valleys, as well as a constant moisture distribution inside the soil undulations. This can be observed and verified by the soil moisture sensors. Under this water table, the atmospheric conditions rather than the soil capillarity dominate the soil evaporation. To keep a constant water table, the water inlet of the soil tank was connected to a water cylinder which was placed to a certain height. During soil evaporation, the water cylinder was replenished continuously by pumping water from a source bucket. The weight of water source bucket was measured using a weight scale (Sartorius Model 11209-95, Range 65kg, Resolution  $\pm 1$ g) to record the accumulative evaporation amount.

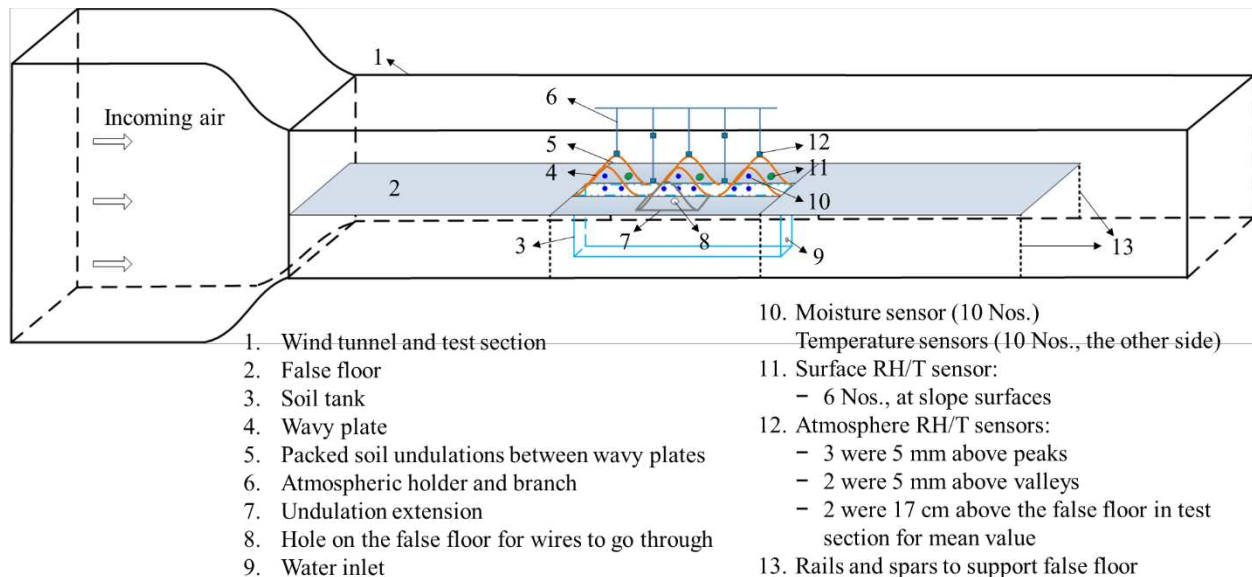


Figure 5.2 Schematic of the wind tunnel – soil tank system and various sensors used in the experiments. Weight scale is not included. No.4 is a sinusoidal outlined wavy plate glued on the tank surface. The dimension and arrangement of the six wavy plates are shown in Figure 5.4. No.5 represents soil undulations packed between two wavy plates. No. 7 is an example of one undulation extension shell with 15 cm long, which is attached with one wavy plate to precisely extend each undulation laterally. Sensor wires in soil undulations and at soil surface are placed inside the extensions and extended below the false floor through a hole on the floor (No. 8). The same undulation extensions and holes are set up for all the six wavy plates.

Above the soil tank, a tripping device was used to establish a fully turbulent flow in front of the soil undulations. As shown in Figure 5.3, the tripping device was composed of two rows of small wood blocks placed in a staggered pattern. The relatively large blocks and the staggered pattern are conducive to promote early transition from a laminar to a turbulent airflow.

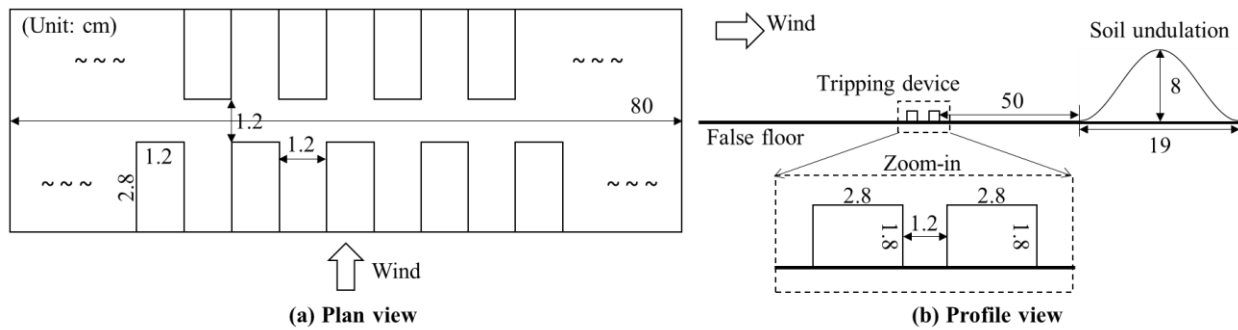


Figure 5.3 Schematic of the layout and size of the turbulent tripping device. The distance between two blocks was 1.2 cm. The tripping device was placed 50 cm away from the nearest soil undulation.

Uniquely, as mentioned above, the turbulent velocity field was measured by means of PIV. Briefly, PIV uses an image analysis technique to track the movement of sufficiently small particles diffused in the flow field and calculates the velocity field based on the particles' motion. The determination of the parameters ( $d_0$ ,  $u_*$ ,  $z_{0m}$ ) relies on an accurate measurement of the undamaged airflow velocity field. As a non-intrusive flow visualization technology, PIV does not disrupt the velocity field during experiments and is therefore has many advantages compared to either point source laser techniques or invasive point source options such as Hot-wire Anemometry. A true instantaneous velocity field, rather than just mean wind speed at several locations, can be obtained in a short time.

In this study, a stereoscopic two-dimensional two-component (2D2C) PIV system (Culler & Farnsworth, 2019) was employed. The system consists of a Quantel Evergreen Nd:YAG laser (maximum output 200 mJ per pulse), one high-speed sCMOS camera (resolution  $2560 \times 2160$

pixels, frame rate 50 fps), two traverses for the positioning of camera and laser head respectively, a ViCount Compact 1300 smoke machine for seeding particles, and a computer with the corresponding software package.

#### 5.4.2 Experimental Cases

Four experiments were conducted for two wind speeds ( $U$ ) and two undulation configurations ( $\#$ ).  $U = 1$  and  $3$  m/s were selected as they represent a range of realistic near-surface wind speed values in nature. Two undulation configurations were selected, resulting in either 2 or 3 ( $\#2$ ,  $\#3$ ) undulations at the surface per tank. Figure 5.2 shows the schematic of  $\#3$  undulations setup. The middle soil undulation and the wavy plates at the corresponding positions were removed for the  $\#2$  undulations experiments. The experimental cases are listed in Table 5.2.

Table 5.2 All experiment cases conducted in this study

Case	Wind speed, $U$ (m/s)	Undulation Nos., $\#$
#3U3	3	3
#3U1	1	3
#2U3	3	2
#2U1	1	2

#### 5.4.3 Experimental Procedures

The empty soil tank was first carefully aligned in the test section as described previously. The water inlet of the tank was connected to the water cylinder through a rubber tube. The tank was then wet-packed with #12/20 silica sand in incremental 1 cm layer to achieve a uniform bulk density (Sakaki & Illangasekare, 2007). The soil undulations were then packed above the tank surface and shaped using a 3D-printed sinusoidal mold. The surface RH/T sensors were placed on the middle of each slope surface. The undulation extensions were anchored on the false floor and attached with the wavy plates and sensor wires were extended below the false floor through the inside of the undulation extensions. The water cylinder was adjusted and fastened at a specific

height to keep a constant water table at the valley (i.e. the tank surface).

Prior to each experiment, a PIV test (introduced in the following) was first conducted to measure the incoming velocity field in front of the soil undulations to confirm the tripping device could induce a fully turbulent flow.

Next, the atmospheric sensor holder was placed in the test section from the opening at the top floor. The atmospheric RH/T sensors were located at the pre-designed positions (Figure 5.2, section 5.4.1) via the five holder branches. All the sensors, the weighting scale and the wind tunnel were then started. The wind speed was set to a value of interest. The soil moisture, soil temperature, and the surface RH/T sensors were set to collect data per minute; the atmospheric RH/T sensors collected data every 10 seconds; and the weighting scale recorded the weight loss of the water source bucket every 30 seconds. The evaporation system was set to run 8 to 12 hours for each case to collect enough data. After one case was finished, the sensors and the weighting scale were stopped. The atmospheric sensor holder was removed out of the test section. PIV system was then employed to measure the velocity field developed above the undulating soil surfaces.

Prior to PIV measurements, the camera and laser head were installed on two computer-automated traverses, allowing for accurate positioning and calibrated. Limited by the calibration area, a view of the entire velocity field in the test section cannot be captured. Therefore, the target area was divided into several sub-views (fourteen and thirteen sub-views for #3 and #2 undulations, respectively). After the wind tunnel was started, a pre-heated smoke machine diffused extremely small oil particles within the wind tunnel until a PIV visible concentration was achieved. The camera and the laser head were moved together in parallel to each sub-view to take images. For each sub-view, one thousand images were taken continuously and averaged by post-processing to obtain a mean velocity field in that sub-view. The averaged velocity fields of all the sub-views

were integrated to obtain an integrated picture of the velocity field.

## 5.5 Determination of Vapor and Momentum Roughness Lengths

The PIV-measured velocity field was first used to estimate turbulent flow parameters ( $d_0$ ,  $u_*$ ,  $z_{0m}$ ), which were then applied to determine the derived unknown coefficients  $a$ ,  $b$ ,  $m$ , and  $n$  in the formulation for vapor and momentum roughness lengths (Eq.(5.16)).

### 5.5.1 Estimation of Turbulent Flow Parameters

The turbulent flow parameters ( $d_0$ ,  $u_*$ ,  $z_{0m}$ ) can be estimated by fitting velocity profiles based on the logarithmic law, see Eq. (5.3).

As shown by the reference coordinate system in Figure 5.4, the wind velocity data  $u(x, z)$  were extracted from PIV measurements every 2 mm horizontally from 5 cm before the soil tank to 5 cm behind the soil tank; and every 2 mm vertically from the false floor to 25 cm above. 351 velocity profiles in total were selected for the fitting process.

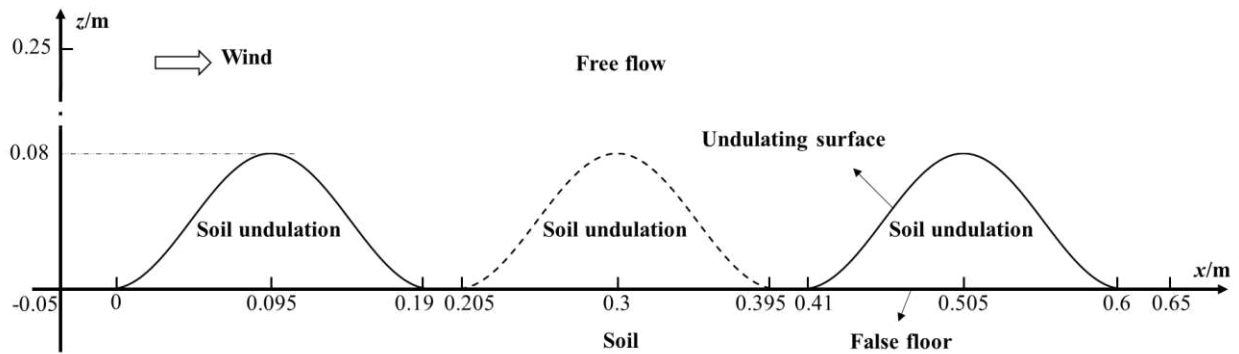


Figure 5.4 Schematic of the coordinate system above the false floor. A mathematical description of the surface is in the Appendix 0. The  $x$ -coordinate is set at the false floor, separating the soil surface and the free flow. The sinusoidal curve is the undulating soil surface. The middle dashed curve is not present for #2 undulations. PIV measurements were conducted in the free flow within  $x = -0.05 \sim 0.65$  m, and  $z = 0 \sim 0.25$  m.

As already mentioned, universal logarithmic profiles are existent in the DSL while not in the ISL due to the influence of soil undulations and air viscosity. Therefore, for each velocity

profile, the data range that was assumed to follow the logarithmic law was screened out first. Figure 5.5 shows an example of the data filter and fitting for one velocity profile ( $x = 0.402$  m, #3U3). The black points are the PIV-measured velocity data. The inflection point of the measured profile is regarded as the start of the velocity data to fit. The end is assumed the point where the velocity is the closest to 99% of the maximum velocity of the profile. As shown in Figure 5.5, the red points are the filtered data to fit Eq. (5.3) and the blue line is the final fitting curve. The nonlinear least-square method with the trust-region-reflective algorithm built in MATLAB was used for the data fitting. Thus, the turbulent flow parameters ( $d_0$ ,  $u_*$ ,  $z_{0m}$ ) for this velocity profile can be obtained and the same operation was implemented for the total 351 profiles.

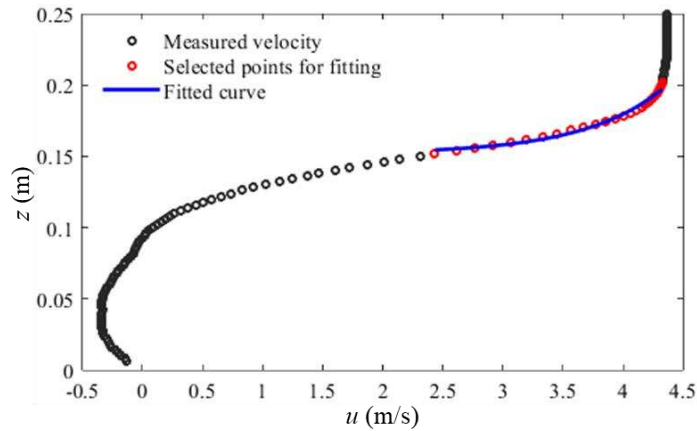


Figure 5.5 An example of the data filter and fitting based on the logarithmic law at the profile  $x = 0.402$  m.

### 5.5.2 Determination of the Derived Coefficients in $\ln(z_{0v}/z_{0m})$

The next step was to determine the coefficients  $a$ ,  $b$ ,  $m$ , and  $n$  in Eq. (5.16) based on the turbulent flow parameters.

Combining Eq. (5.6) and (5.14), one obtains:

$$\frac{u_* \left[ \rho_{\text{sat}}(z_s) - \rho_a(z_h) \right]}{E} \Bigg|_{\text{ISL}} = a \text{Re}_0^b \quad (5.18)$$

For each velocity profile,  $Re_0 (= u_* z_{0m}/\nu)$  and  $u_*$  are known through processing the PIV data as shown in section 5.5.1. However, due to the lack of experimental equipment to measure humidity profiles without interrupting the airflow field, the local values of  $\rho_{sat}(z_s)$ ,  $\rho_a(z_h)$ , and  $E$  for each profile cannot be readily obtained from experiments. Hence, we used the numerical model to simulate the experimental cases with the same setup and conditions. In order to duplicate the experiments numerically, the fully coupled model developed and validated in (Gao et al., 2020) was employed to describe the dynamic mass, momentum, and heat transfer processes in the whole evaporation system. The modeled evaporation rate and the observed evaporation rate were compared as a reference (see Table 5.3) to verify that the modeled results could be used. Thus, the coefficients  $a$  and  $b$  can be determined by fitting Eq. (5.18) via the turbulent flow parameters and the modeling outputs.

Table 5.3 Modeled and observed evaporation rate for experimental cases

Case	Observed (kg/h)	Modeled (kg/h)
#3U3	0.0274	0.0232
#3U1	0.0214	0.0201
#2U3	0.0267	0.0271
#2U1	0.0211	0.0216

Combining Eq. (5.10) and (5.15), in which  $u_h$  is defined by Eq. (5.3), one obtains:

$$\frac{1}{\kappa} \ln \left( \frac{z_h - d_0}{z_{0m}} \right) = m \ln(Re_0) + n \quad (5.19)$$

The terms on the left side of the equation and  $Re_0$  are known from the turbulent flow parameters estimated in section 5.5.1 at each velocity profile. The coefficients  $m$  and  $n$ , thus, can be obtained by fitting Eq. (5.19).

The data fitting for  $a$ ,  $b$ ,  $m$ , and  $n$  was implemented through MATLAB, using the nonlinear least-square method with the trust-region-reflective algorithm.

### 5.5.3 Results and Analysis

The relationship of  $z_{0v}$  and  $z_{0m}$ , as well as the aerodynamic resistance, via the above determination process is presented and analyzed in this section.

Table 5.4 summarizes the derived coefficients  $a$ ,  $b$ ,  $m$ , and  $n$  for the four cases. Figure 5.6 shows an example of  $Da_0^{-1}$  and  $Cd_0^{-1/2}$  obtained by experimental data and the determination process. The comparison figures for the rest cases are in Supplement. Both the value of  $R^2$  in Table 5.4 and Figure 5.6 demonstrate that the fitting results based on the determination process mentioned above are relatively good. As mentioned above,  $Cd_0^{-1/2}$  is usually assumed a constant as some studies use a value varying from 1 to 10 for different situations in heat or mass transfer. But in this study,  $Cd_0^{-1/2}$  changing linearly with  $Re_0$  in a single logarithm is demonstrated in Figure 5.6b.

Table 5.4 A summary of the derived coefficients in aerodynamic resistance

Case	$a$	$b$	$R^2$ , fitting $Da_0^{-1}$	$m$	$n$	$R^2$ , fitting $Cd_0^{-1/2}$
#3U3	16.091	0.107	0.749	-1.068	8.093	0.768
#3U1	9.163	0.177	0.656	-0.786	6.194	0.641
#2U3	15.997	0.147	0.785	-0.954	8.694	0.865
#2U1	10.965	0.116	0.653	-0.860	7.207	0.819

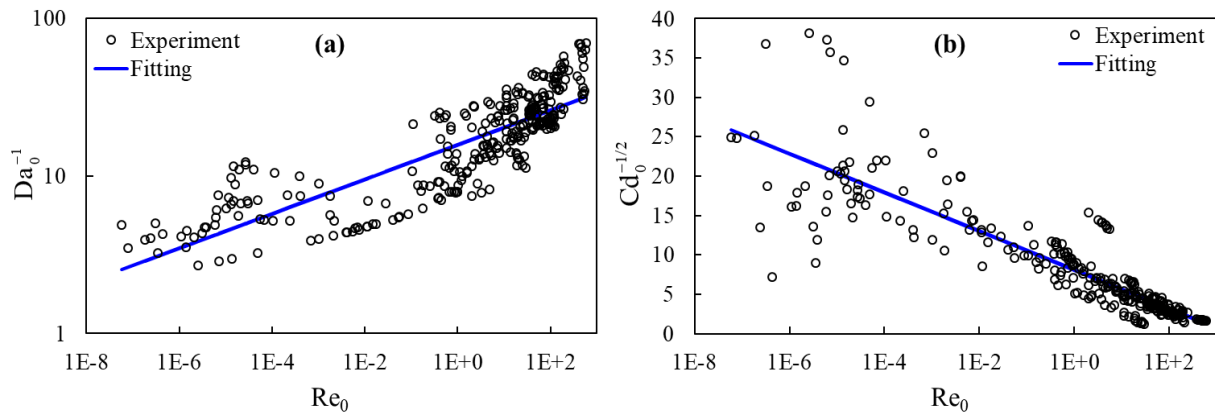


Figure 5.6 Comparison of observed and fitted  $Da_0^{-1}$  and  $Cd_0^{-1/2}$  with  $Re_0$  in double logarithm (a) and in single logarithm (b), respectively. This is an example from case #3U3.

As shown in Table 5.4, the coefficient  $a$  in  $Da_0^{-1}$  presents a similar value for the same wind speed, whereas shows no strong dependence on undulation space. It approaches 16 when the mean speed is approximately 3 m/s and reduces to about 10 when the mean speed decreases to 1 m/s for #3- and #2-undulation setup. Similarly, the coefficient  $m$  in  $Cd_0^{-1/2}$  is also mainly related to the wind speed, close to -1 under 3 m/s and -0.8 under 1 m/s. By contrast, the coefficient  $b$  and  $n$  do not show a certain relationship with the wind speed or undulation space. But they change in a quite narrow range, i.e.,  $b$  ranges from 0.1 to 0.2 and  $n$  roughly ranges between 6 to 8. The fitting results provide a selection guide for a similar scale undulation setup.

After the derived coefficients ( $a$ ,  $b$ ,  $m$ , and  $n$ ) are determined, the relationship of  $z_{0v}$  and  $z_{0m}$  is known according to Eq. (5.16). Figure 5.7 shows the change of  $\ln(z_{0v} / z_{0m})$  along the undulating surface for #3 and #2 undulations. In general, for a given surface configuration, the distribution of  $\ln(z_{0v} / z_{0m})$  under different wind speeds shows a similar pattern. In the presence of soil undulations,  $z_{0v}$  is much lower than  $z_{0m}$  in most of the area. The average difference ranges from 3 to 7 orders of magnitude in the four cases. The large disparity between  $z_{0v}$  and  $z_{0m}$  implies the distinct mechanism of mass and momentum transfer in the near-surface area. The mass (i.e. vapor) transfer is mainly controlled by molecular diffusion as turbulence weakens approaching soil surface. By contrast, both of the viscous shear and the local pressure gradient formed as airflow across soil undulations play an important role in the momentum transfer. The viscous shear stems from two components. One is due to the fluid viscosity and the other is an extra friction produced by turbulence (i.e. Reynolds stress). The effect of the viscous shear and the pressure drag is partially reflected by the flow behaviors which can be observed by the PIV measurement. Figure 5.8 and the selected velocity profiles in Figure 5.9 illustrate the PIV-measured velocity field.

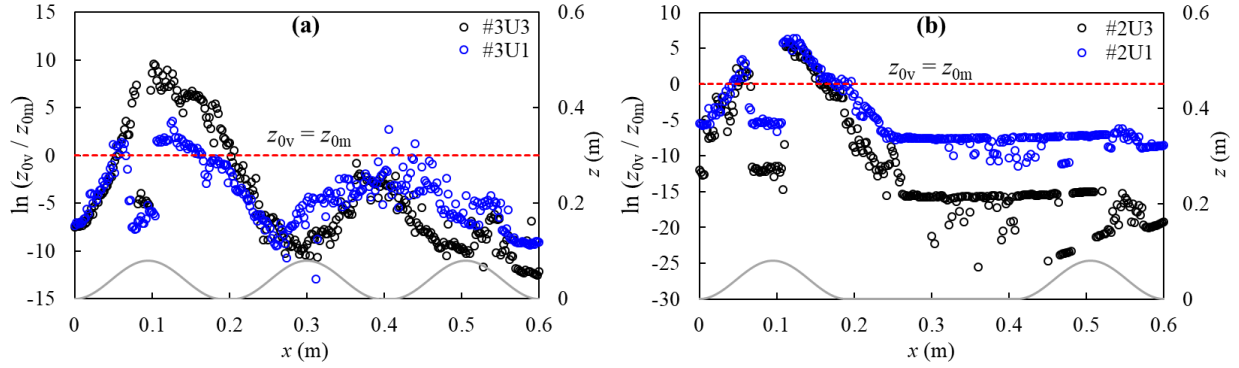


Figure 5.7 Distribution of  $\ln(z_{0v} / z_{0m})$  along the undulating surface for (a) #3 undulations; (b) #2 undulations. The red dashed line represents  $z_{0v} = z_{0m}$ . Above the line:  $z_{0v} > z_{0m}$ ; below the line:  $z_{0v} < z_{0m}$ . The gray solid line with the right vertical coordinate is the undulating surface.

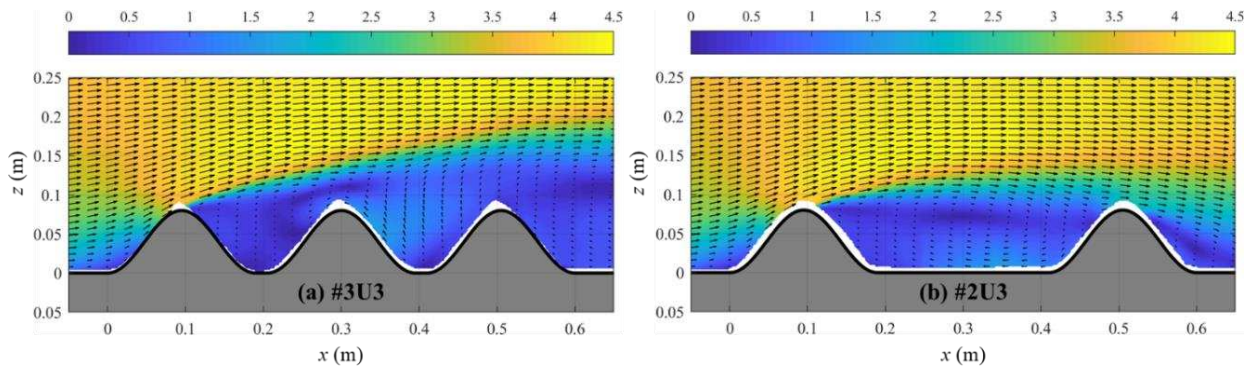


Figure 5.8 PIV-measured velocity field above undulating surfaces for case #3U3 in (a) and #2U3 in (b). Additional figures for all the experiments obtained by PIV measurement are in the Supplement.

In the case of #3 undulations, flow separation is observed at the first undulation peak and a recirculation zone is seen behind the third undulation (negative velocity at  $x > 0.506$  m in Figure 5.9a). Above the middle peak, the air flows back from the second valley into the first valley (negative velocity at  $0.252 < x < 0.402$  m in Figure 5.9a). Flow separation and the accompanied recirculation result from the adverse pressure gradient as air flows along the undulating surface. Inside the valleys, the air mainly flows upward instead of horizontally (Figure 5.9a). Accordingly, the viscous shear effect weakens. In the case of #2 undulations, after the airflow separates at the

first peak, a large recirculation zone occurs between the two undulations Figure 5.8b and negative velocity  $0.142 < x < 0.458$  m in Figure 5.9b). Besides, flow separation happens again at the second peak followed by a small recirculation zone behind the second undulation. Compared with the #3-undulation case, in the #2-undulation setup, the airflow develops a velocity field between the two undulations due to the large space, which is relatively independent on the flow field above the undulations. Under the circumstances, the viscous shear between the undulations plays a more important role than the pressure drag. In addition of the difference in the dominant force between the #3 and #2 undulation cases, the vapor distribution between them is also distinct due to the different flow behaviors. In the #3 undulation setup, the main upward flow motion between undulations results in a small vapor density difference between the soil surface and the mainstream. By contrast, the difference is much larger in the #3 undulation setup due to relatively weak interaction of the velocity field that is between the undulations and the one above the undulations. This is illustrated in Figure 5.10 by comparing Figure 5.10a and Figure 5.10b under 3 m/s, as well as Figure 5.10c and Figure 5.10d under 1 m/s.

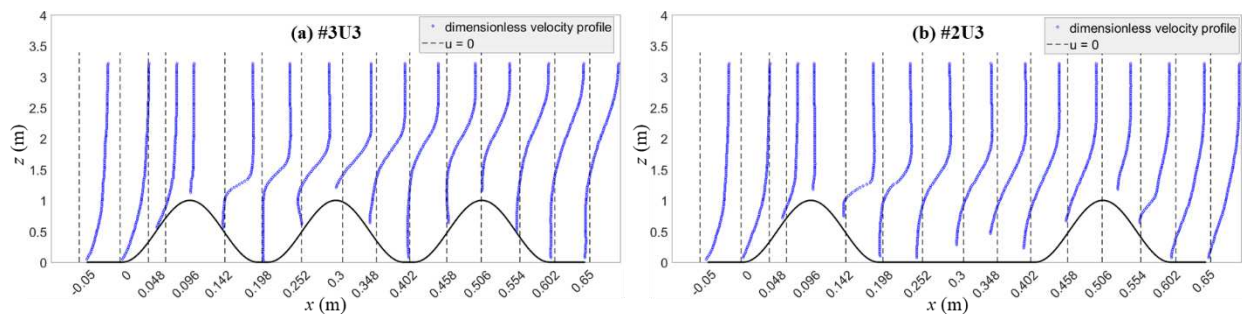


Figure 5.9 Selected dimensionless horizontal velocity profiles obtained by PIV: (a) #3U3; (b) #2U3. For each profile, the velocity  $u(z)$  is normalized by the maximum  $u$  in this profile; the corresponding vertical position  $z$  is normalized by the undulation height. The dashed line in each profile represents the coordinate  $u = 0$ . The black curve represents the undulating surface.

The difference in the force effect between the two surface configurations leads to different momentum transfer behaviors, reflected by  $z_{0m}$ . Likewise, the difference in the vapor distribution leads to different mass transfer behaviors, reflected by  $z_{0v}$ . Thus, the effect of the surface configuration on the distribution of the ratio of  $z_{0v}$  to  $z_{0m}$  along the undulating soil surface can be understood. For momentum transfer, if the pressure drag outweighs the viscous shear such as in the case of #3 undulation setup, one phenomenon is the decrease of the friction velocity, which in turn causes the decrease of  $z_{0m}$  for a given wind speed according to the logarithmic velocity profile Eq. (5.3). For mass transfer, a small vapor density difference between the soil surface and the mainstream weakens the molecular diffusion effect, resulting in an increase of  $z_{0v}$  for a given friction velocity according to the logarithmic humidity profile Eq. (5.2). Consequently, the ratio of  $z_{0v}$  to  $z_{0m}$  will increase, and vice versa.

As shown by Figure 5.7a, as approaching the first undulation peak,  $z_{0v}$  gradually exceeds  $z_{0m}$  and the maxima corresponds to the point where flow separation happens, which corresponds to a significant effect of pressure drag. Then the velocity field develops to a state stepping out of the influence of flow separation at the first peak. Accordingly,  $\ln(z_{0v} / z_{0m})$  gradually falls below zero implying  $z_{0v}$  values smaller than  $z_{0m}$ . When approaching the second valley, the ratio of  $z_{0v}$  to  $z_{0m}$  increases again due to the weakened molecular diffusion, but  $z_{0v}$  remains lower than  $z_{0m}$ . By contrast, in the case of #2 undulations shown by Figure 5.7b, after flow separation, the ratio of  $z_{0v}$  to  $z_{0m}$  decreases to an approximately constant value between the undulations due to the relatively independent velocity field. The highlighted effect of viscous shear and the large vapor density difference between the soil surface and the mainstream result in increased  $z_{0m}$  and decreased  $z_{0v}$ , respectively. Thus, the ratio of  $z_{0v}$  to  $z_{0m}$  in the case of #2 undulations is lower than the #3 undulations, which is shown by comparing Figure 5.7a and Figure 5.7b under the same wind speed.

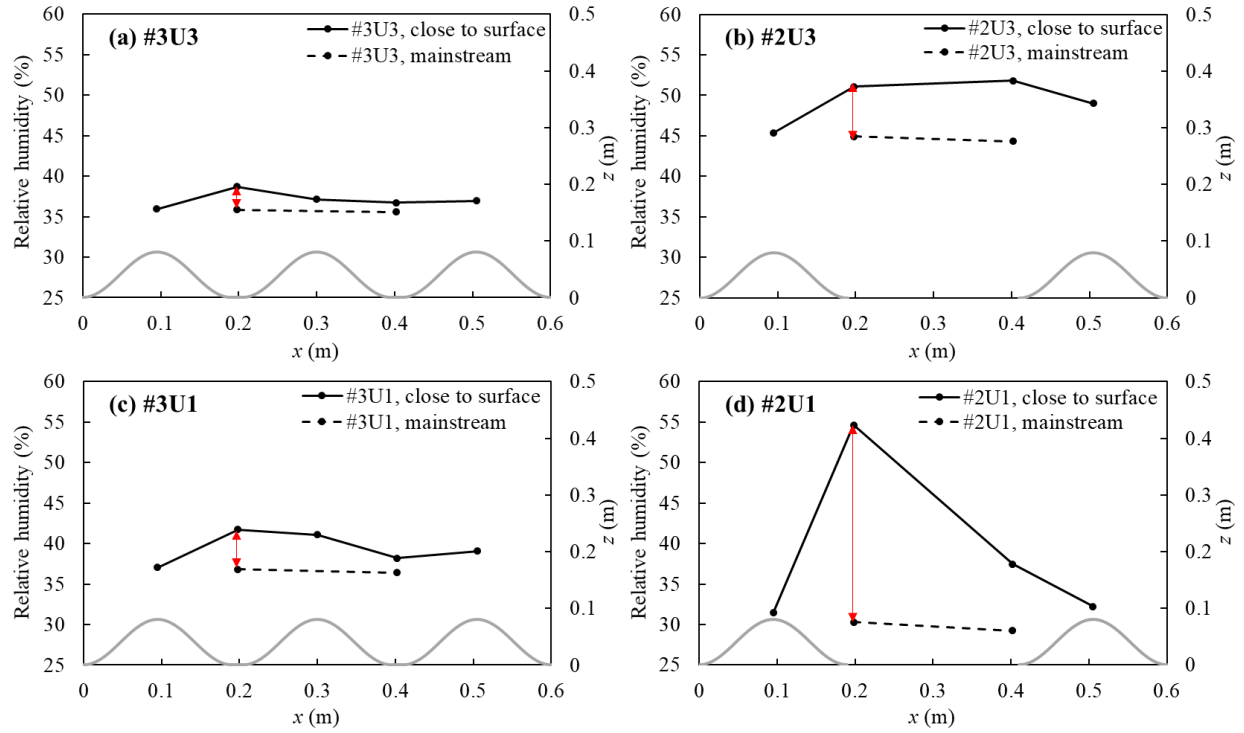


Figure 5.10 Observed relative humidity at 5 mm above surface (solid line) and in the mainstream (dashed line) for the four cases: (a) #3U3, (b) #2U3, (c) #3U1, and (d) #2U1. The gray curve with the right vertical coordinate is the undulating soil surface.

Wind speed also affects the ratio of  $z_{0v}$  to  $z_{0m}$  and the influence is different between the two undulation configurations, which is mainly related to the extra friction in the viscous shear (i.e. Reynolds stress). For a given surface configuration, an increasing wind speed has negligible impacts on the value of  $z_{0m}$  (see figures of  $z_{0m}$  in Supplement), which has also been mentioned in previous studies (De Bruin & Moore, 1985; Dong et al., 2001; Vanderborcht et al., 2017). However, the increase of wind speed strengthens the Reynolds stress (see Figure 5.11) and thus highlights the extra friction, which is presented by an increased friction velocity. Alternatively, a larger wind speed leads to a smaller the vapor density difference between the soil surface and the mainstream, as shown by the comparison of Figure 5.10a and Figure 5.10c for #3 undulation, or Figure 5.10b and Figure 5.10d for #2 undulation. As a synthetical result, a larger wind speed corresponds to a

smaller  $z_{0v}$  according to the logarithmic humidity profile Eq. (5.2) and a smaller ratio of  $z_{0v}$  to  $z_{0m}$ , see Figure 5.7a for #3-undulation setup or Figure 5.7b for #2-undulation setup.

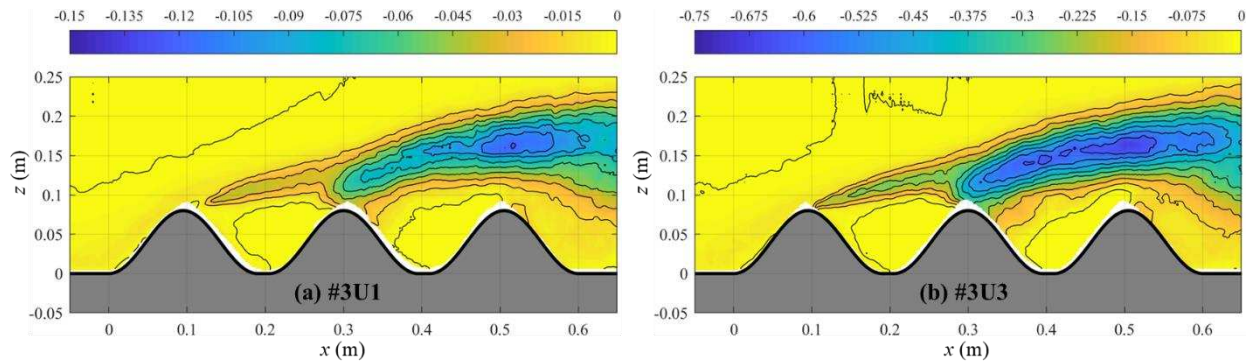


Figure 5.11 Measured Reynolds stress by PIV for case (a) #3U1 and (b) #3U3.

In addition, as mentioned above, due to the relatively independent velocity field between the two undulations in the #2-undulation setup, the greater importance of viscous shear leads to a larger  $z_{0m}$ . In the meantime, less soil surface – mainstream interaction results in a larger vapor density difference between them and thus decreases  $z_{0v}$ . Consequently, the difference between  $z_{0v}$  and  $z_{0m}$  is larger than the #3-undulation setup. This is reflected by the phenomenon that the influence of wind speed on the ratio of  $z_{0v}$  to  $z_{0m}$  is larger for a sparser undulation configuration, as the comparison of Figure 5.7a and Figure 5.7b. The average differences of the ratio between 1 m/s and 3 m/s are 0.17 and 6.78 for #3 and #2 undulations, respectively.

## 5.6 Calculation of Aerodynamic Resistance and Evaporative Flux

After the relationship of  $z_{0v}$  and  $z_{0m}$  is known, the aerodynamic resistance can be investigated. It is then applied to calculate the evaporative flux via Eq. (5.1) based on two datasets. One is from the laboratory experiments carried out in this study as listed in Table 5.2; the other is from a field experiment which included soil undulations in a similar size with the laboratory experiments.

### 5.6.1 Aerodynamic Resistance

The aerodynamic resistance ( $r_a$ ) was calculated via Eq. (5.17) at the 351 selected locations. Figure 5.12 shows the distribution of  $r_a$  along the undulating surface for the wind speed of 3 m/s. Figures for 1 m/s are in the Supplement. The black points are calculated based on the experimental data and the red line is from the new formula in this paper (Eq. (5.17)). In general, the new formula can describe the experimental trends well.  $r_a$  fluctuates dramatically in the vicinity of the first peak owing to the occurrence of flow separation. Before reaching the soil undulations,  $r_a$  is about 100 to 150 s/m ( $x = 0$  in Figure 5.12). At the locations where flow separation happens (i.e., the first peak of both undulation setups, and the second peak of the #2 undulation setup),  $r_a$  casts a maximum value indicating a locally lower evaporative flux at these areas. After flow separation at the first peak,  $r_a$  decreases to a roughly constant level as the velocity field develops to a relatively stable state, approximately 40 to 80 s/m. It is much smaller than the value before airflow contacts the undulation, indicating the existence of soil undulations reduces  $r_a$  compared with a flat surface.

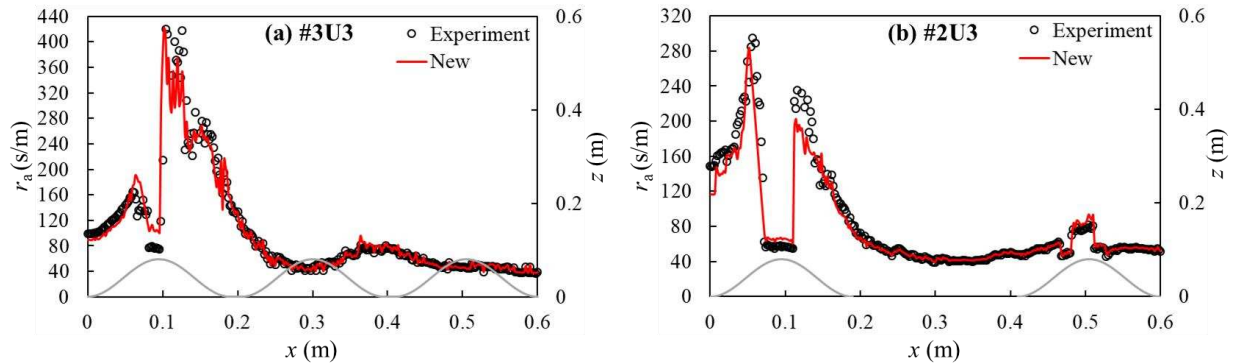


Figure 5.12 Comparison of the aerodynamic resistance calculated by experimental data, and the new formula in this paper for: (a) #3U3 and (b) #2U3. The gray curve with the right vertical coordinate is the undulating soil surface.

### 5.6.2 Evaporative Flux for Laboratory Experiments

After  $r_a$  is obtained, Eq. (5.1) is used to calculate the evaporative flux. The vapor density in the air was calculated from the RH/T data measured at  $z_{\text{ref}} = 17$  cm above the false floor through:

$$\rho_a(z_{\text{ref}}) = \rho_{\text{sat}} \times \text{RH} \quad (5.20)$$

where RH is the relative humidity, and  $\rho_{\text{sat}}$  ( $\text{kg}/\text{m}^3$ ) is the saturated vapor density at the reference plane calculated empirically by (Campbell, 1985):

$$\rho_{\text{sat}} = \frac{\exp(31.37 - 6014.79T^{-1} - 7.92 \times 10^{-3}T)}{T} \times 10^{-3} \quad (5.21)$$

Likewise, the surface RH/T data collected at the slope surfaces were used to calculate the soil surface vapor density at the corresponding locations. The sloped surfaces remained moist so that the soil resistance due to capillary flow at the surface of these locations could be neglected. At the peaks and valleys, the soil temperature measured 2 cm below the soil surface was used to estimate the vapor density based on Eq. (5.21) assuming vapor was saturated. This assumption is reasonable for #12/20 sand according to (Likos & Lu, 2004):

$$\text{RH} = \exp\left(-\frac{gM_w H_c}{RT}\right) \quad (5.22)$$

where  $g$  ( $\text{kg}\cdot\text{m}\cdot\text{s}^{-2}$ ) is the gravitational acceleration;  $M_w$  ( $\text{kg}/\text{mol}$ ) is the molecular mass of water;  $H_c$  (m) is the capillary head decided by the van Genuchten model (Appendix 0);  $R$  ( $\text{J}\cdot\text{mol}^{-1}\cdot\text{K}^{-1}$ ) is the universal gas constant; and  $T$  (K) is the temperature. The relative humidity of #12/20 sand approximates 1 at a low moisture (i.e. high  $H_c$ ).

Since the temperature data at the peaks and valleys were collected beneath the soil surface, soil resistance was calculated at the peaks and valleys. VGO94 model (van de Griend & Owe, 1994) with a broad applicability was used here:

$$r_s = 10 \exp[35.63 \times (0.15 - \theta_w)] \quad (5.23)$$

where  $\theta_w$  is the volumetric water content of the top soil layer. In our experiments, a coarse sand was chosen to generate a clear difference of the moisture at the peaks and valleys. It results in

distinct  $r_s$  at these two locations, and most importantly both are deviated from  $r_a$  by orders of magnitude. In this way, the influence of the soil resistance on the evaluation of  $r_a$  is excluded and this study therefore focuses on the aerodynamic resistance only.

The evaporative flux was estimated at the peaks, valleys, and the slope surfaces where sensors were located. Then the estimated local evaporative flux is integrated along the undulating surface and a total evaporation rate  $E_{\text{est}}$  (kg/h) can be obtained through:

$$E_{\text{est}} = \rho_w \frac{A_s}{l} \int_0^l E_i(x) dx \quad (5.24)$$

where  $\rho_w = 1 \text{ g/cm}^3$  is the water density,  $l = 0.6 \text{ m}$  the length of the tank opening, and  $E_i$  (mm/h) the estimated local evaporative flux at  $i$ -position.  $A_s$  is the area of the undulating surface calculated through  $A_s = w \times s$ , in which  $w$  (m) is the width of the tank opening, and  $s$  (m) is the length of the undulating surface calculated according to Eq. (C.3).

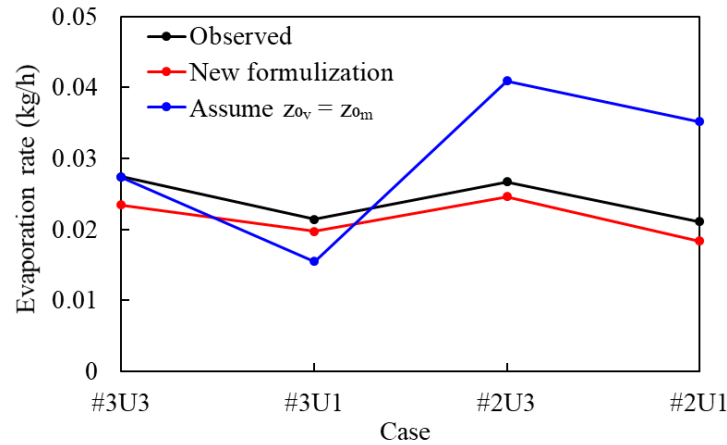


Figure 5.13 Observed versus simulated evaporation rates based on the laboratory experiments, the aerodynamic resistance formulization method in this paper, and the assumption of  $z_{0v} = z_{0m}$ .

The evaporation rate is then compared with the measured total evaporation rate  $E_{\text{obs}}$  (kg/h) in section 5.4, shown by Figure 5.13. Besides, Figure 5.13 also shows the evaporation rate calculated based on the common assumption of  $z_{0v} = z_{0m}$ . The Root Mean Square Errors (RMSE)

based on the new formulation and the common assumption are 0.003 and 0.011, respectively. The comparison indicates that the evaporation rate estimated based on the newly formulized  $r_a$  is relatively rational based on the limited integrated points. By contrast, the result based on the assumption  $z_{0v} = z_{0m}$  commonly made in calculating  $r_a$  deviates from the observed data considerably. This comparison demonstrates the invalidity of the assumption  $z_{0v} = z_{0m}$  for evaporation from an undulating soil surface.

### 5.6.3 Evaporative Flux for a Field Experiment

The newly formulized  $r_a$  was applied to calculate the evaporation rate for a field experiment based on Eq. (5.1). This experiment was carried out using a lysimeter with 10 cm - height soil undulations on the soil surface. It is one of the series of experiments collaborated with Forschungszentrum Jülich running from Aug. 24<sup>th</sup> to Sep. 30<sup>th</sup>, 2019. The data collected from Sep. 23<sup>rd</sup> to Sep 29<sup>th</sup> were used in this section since there was a rainfall on Sep. 23<sup>rd</sup>, 25<sup>th</sup>, and 27<sup>th</sup>. The flat soil surface area of the lysimeter was wet enough so that the vapor pressure could be assumed saturated. The soil resistance within the unsaturated soil undulations was neglected due to the lack of experimental data. Thus, the evaporation rate was assumed approximately equal to the potential evaporation rate from the flat soil surface. During the experiment, the weight of the lysimeter was continuously recorded per hour. The temperature at the flat soil surface area, the mean wind speed and RH/T data at  $z_{ref} = 2$  m above the flat surface were collected every 10 minutes.

Hence, the average daily evaporation rate could be experimentally estimated by the weight change of the lysimeter. The surface temperature and atmospheric RH/T were averaged daily to calculate surface and atmospheric vapor density, respectively, based on Eq. (5.20) and (5.21). To calculate the aerodynamic resistance, the friction velocity in Eq. (5.17) was removed by substituting Eq. (5.3) into Eq. (5.17). Because the value of the friction velocity depends on the

near-surface airflow dynamics and there will be a great uncertainty to assign a value to the friction velocity based on the laboratory experimental data. By contrast, the zero-displacement height  $d_0$  and the momentum roughness length  $z_{0m}$  rely on the surface geometry, which can be estimated according to the above laboratory experiments due to the similar setup. Thus,  $r_a$  is re-arranged to:

$$r_a = \frac{1}{\kappa u} \ln\left(\frac{z-d_0}{z_{0m}}\right) \left\{ a \text{Re}_0^b - [m \ln(\text{Re}_0) + n] \right\} + \frac{1}{\kappa^2 u} \left[ \ln\left(\frac{z-d_0}{z_{0m}}\right) \right]^2 \quad (5.25)$$

The measured average daily wind speed data was approximately 2 m/s which was within the wind conditions in the laboratory experiments. The average turbulent flow parameters obtained in section 5.5.1 were applied, i.e.,  $d_0 = 0.1$  m, and  $z_{0m} = 0.01$  m. Note that the wind speed was measured at 2 m above flat soil surface. The near-surface wind speed should be lower than 2 m/s in principle. Thus, the derived coefficients were assumed close to the cases in which  $u = 1$  m/s, i.e.  $a = 10$ ,  $b = 0.15$ ,  $m = -0.9$ , and  $n = 7.5$  according to section 5.5.3.

Figure 5.14 illustrates the comparison of the daily evaporation rate recorded by the lysimeter and calculated based on the newly formulized  $r_a$  in this study, as well as based on the common assumption of  $z_{0v} = z_{0m}$  in the estimation of the aerodynamic resistance. Generally, the result from the new formulization method of this study is relatively good, while the result using the assumption  $z_{0v} = z_{0m}$  shows a significant deviation from the observed data. The RMSEs based on the new formulation and the common assumption are 0.482 and 2.252, respectively. It indicates the common assumption of  $z_{0v} \approx z_{0m}$  does not perform well in dealing with evaporation from an undulating soil surface. In terms of the calculated results based on this research, underestimation is observed during a rain event and overestimation after rain events. It is theoretically reasonable since two factors were neglected in the estimation. One is the soil resistance within the soil undulations, which plays a significant role if the undulations are not quite wet. The other is the

extensive soil surface area due to the existence of soil undulations, which is important when the whole soil profiles are wet. In this field experiment, during the rainy days (Sep. 23<sup>rd</sup>, 25<sup>th</sup>, and 27<sup>th</sup>), both the flat surface area and the undulations were highly saturated. Thus, the second factor partially accounts for the underestimation of the evaporation rate. After the rainy days, the soil, especially the soil undulations lost moisture, increasing the soil resistance and thus resulting in an overestimation of the evaporative flux on Sep. 24<sup>th</sup>, 26<sup>th</sup>, 28<sup>th</sup>, and 29<sup>th</sup>.

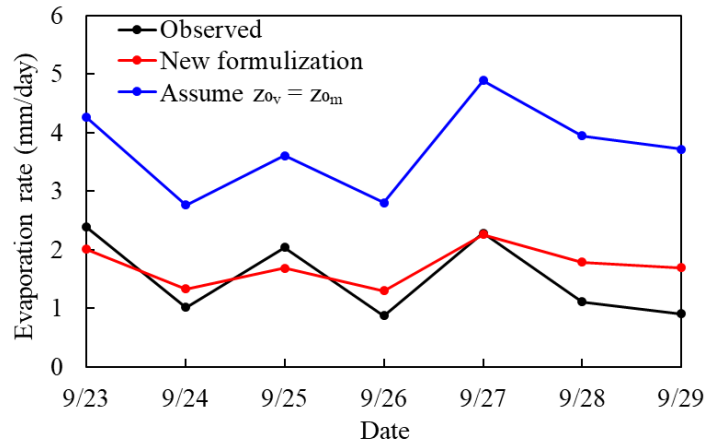


Figure 5.14 Comparison of the daily evaporation rate by observation from Sep. 23<sup>rd</sup> to Sep. 29<sup>th</sup>, 2019, the calculation based on the newly formulized  $r_a$  in this study, and the calculation based on the assumption of  $z_{0v} = z_{0m}$ .

## 5.7 Conclusions

With the goal of understanding the soil-atmosphere exchange processes as the presence of soil undulations under different wind speed from the perspective of practical applications, the reduced model concept in which the exchange processes are simplified by a vapor flux top boundary condition based on Monin-Obukhov similarity theory (MOST) was adopted. In this model, the relationship between the two crucial parameters that characterize the mass and momentum transfer behaviors, i.e. the vapor roughness length ( $z_{0v}$ ) and the momentum roughness length ( $z_{0m}$ ) was formulized. Four experiments were conducted considering two wind speeds (i.e.

1 m/s, 3 m/s) and two undulation configurations (i.e. #2 undulations, #3 undulations). What is unique in this work is the application of the Particle Imaging Velocimetry (PIV) technology to the measurement of the velocity field and the Reynolds stress distribution above the undulating soil surface. The formulation of the relationship between  $z_{0v}$  and  $z_{0m}$  was determined using the PIV-measured velocity field profiles. With the formulized expressions and PIV-collected information, the dependence of the relationship between  $z_{0v}$  and  $z_{0m}$  on the velocity field developed above the undulating soil surface was discussed in detail.

Results show that in the presence of soil undulations,  $z_{0v}$  is much lower than  $z_{0m}$ , averagely for 3 to 7 orders of magnitude, demonstrating the assumption of  $z_{0v} \approx z_{0m}$  does not apply to evaporation from an undulating soil surface. This large dissimilarity of  $z_{0v}$  and  $z_{0m}$  implies the distinct mechanism of vapor scalar and momentum transfer in the near-surface area. Vapor transfer is mainly controlled by the molecular diffusion, while both the viscous shear and the local pressure drag dominates the momentum transfer. The force effect can be reflected by the turbulent flow behaviors observed by PIV. The effect of the surface configurations on the ratio of  $z_{0v}$  to  $z_{0m}$  is closely related to the vapor scalar and momentum transfer mechanisms. When the pressure drag takes more proportion than the viscous shear (e.g. a denser undulation setup), the interaction between the soil surface and the mainstream is strengthened, resulting in a larger ratio of  $z_{0v}$  to  $z_{0m}$ . On the contrary, in an undulation setup, especially in which a relatively independent velocity field is able to form between the undulations, the effect of viscous shear becomes prominent and the soil surface – mainstream interaction is weakened, lowering the ratio of  $z_{0v}$  to  $z_{0m}$ . Additionally, wind speed affects the ratio of  $z_{0v}$  to  $z_{0m}$  mainly owing to the Reynolds stress, which is considered as an extra friction in the viscous shear formed due to turbulence. A larger wind speed highlights the extra friction and causes a larger friction velocity and thus lowers the ratio between  $z_{0v}$  and  $z_{0m}$ .

The influence of wind speed on this ratio is larger for a sparser undulation configuration due to the strengthened viscous shear and the weakened soil surface – mainstream interaction.

The newly formulation was then used to calculate the aerodynamic resistance and the subsequent evaporative flux for the four laboratory experiments in this study and a field experiment with soil undulations of similar scale. Results indicate the existence of soil undulations greatly decreases aerodynamic resistance compared with a flat surface. The average Root Mean Square Error based on the new formulation and the common assumption are 0.003 and 0.011 for the laboratory experiments, and 0.482 and 2.252 for the field experiment, implying the better performance of the new formulation in the estimation of the evaporative flux. It further indicates that the common assumption of  $z_{0v} \approx z_{0m}$  does not apply to bare-soil evaporation in the presence of soil undulations. An inaccurate assumption may result in distinct prediction of the evaporation rate.

This study provides a reference and framework in the estimation of the ratio between  $z_{0v}$  and  $z_{0m}$  when calculating aerodynamic resistance for a soil surface with macro-scale soil undulations. For a similar setup, the four derived coefficients in equation (5.16), which describes the relationship of  $z_{0v}$  and  $z_{0m}$ , are recommended as:  $a \approx 16$  under 3 m/s and  $a \approx 10$  under 1 m/s;  $b$  ranges between 0.1 to 0.2;  $m \approx -1$  under 3 m/s and  $-0.8$  under 1 m/s;  $n$  ranges between 6 to 9. Besides, we expect that this study is useful to improving models for evaporation prediction on the engineering scale.

## CHAPTER 6

### CONCLUSIONS AND RECOMMENDATIONS

This chapter provides a summary of this thesis and the main conclusions from chapter 3-5, followed by the recommendations for future research.

#### **6.1 Summary**

Soil-atmosphere exchange processes have a broad range of applications, in which soil evaporation involving dynamic mass, momentum, and heat transfer between the soil and the atmosphere is an important component. Macro-scale soil undulations commonly occur at soil surfaces due to natural processes (e.g., soil erosion, alluvial riverbed), mechanical manipulation (e.g., agricultural furrow), or can be seen in boggy terrain which comprises a considerable portion of northern countries. Evaporation from such undulating soil surfaces is a key component of the whole water cycle system, and thus significant to the regional climate and ecological balance. Therefore, a well-grounded understanding of the characteristics and mechanisms of the soil evaporation behavior is important not only to the scientific research in soil-atmosphere interactions, but also for the purpose of relatively accurate prediction of the soil water loss.

However, the majority of the previously developed theories and understandings are based on the assumption of a hydrodynamically smooth surface. Yet these current understandings are not fully suitable for the undulating surface-evaporation issues. There are two main reasons. First, the variational distances between the undulating surface and the water table essentially determine the local difference in the evaporative flux along the undulating surface. Second, the macro-scale soil undulations lead to a great uncertainty in the boundary layer development above the undulating surface. Different undulation geometry and distribution may result in distinct boundary layer

pattern. Besides, the boundary layer pattern is also affected by the atmospheric conditions, such as wind speed, pressure fluctuation, etc. The boundary layer pattern directly impacts the mass, momentum, and heat transfer between the soil and the atmosphere. A clear and complete understanding in these physics relies on characterizing fully coupled soil-atmosphere exchange processes, which is rarely seen in relevant fundamental studies especially when turbulent flow state is considered. This fundamental knowledge gap further leads to an inappropriate model parameterization for practical applications.

Given the current knowledge gap, this research aims to provide a critical step toward advancing our understanding of mass, momentum, and heat transfer processes between the soil and the atmosphere from an undulating soil surface under the influence of the near-surface boundary layer. This thesis is divided into three phases based on the overarching goal. First, a fundamental mechanism study on the characteristics of evaporation from an undulating soil surface under a laminar boundary layer was conducted. A fully coupled model was developed to quantify the dynamic mass, momentum, and heat transfer processes. A laboratory experiment using a wind tunnel – soil tank system was carried out to verify the developed model. Second, a fundamental study on the characteristics of evaporation from an undulating soil surface under a turbulent boundary layer was conducted. The fully coupled model developed in the first study was extended by incorporating turbulent airflow through Reynolds-averaged Navier-Stokes equations. Hot-wire Anemometry (HWA) was the first time employed to measure the turbulent boundary layer for a laboratory study of soil evaporation. The presence of recirculation zones in the undulating valleys was confirmed by HWA, corresponding to the observed low evaporation area and thus demonstrated the heterogeneous distribution of the evaporative flux along surface. Besides, results show under the combined influence of turbulence and soil undulations, the effect of wind speed

on system evaporation is restricted. This fully coupled model concept used in the first two phases has a great advantage in fundamental studies for understanding physics. In the last phase, a reduced model concept was adopted, which is commonly applied to practical issues. In this concept, the atmosphere was considered as a top boundary and the exchange processes at the soil surface was simplified by a flux top boundary condition. The influence related to the atmospheric boundary layer was parameterized into the aerodynamic resistance in the top boundary condition. The vapor roughness length ( $z_{0v}$ ) and momentum roughness length ( $z_{0m}$ ) are two major parameters in the aerodynamic resistance to characterize the mass and momentum transfer processes. This phase aims to determine the ratio of  $z_{0v}$  to  $z_{0m}$ , and the subsequent aerodynamic resistance considering the modification of undulating soil surfaces to the near-surface atmospheric boundary layer. The velocity field above the undulating surface measured via Particle Image Velocimetry (PIV) was employed in the parameterization. Combining with the PIV-observed velocity field, the relationship between  $z_{0v}$  and  $z_{0m}$  in the presence of an undulating soil surface was analyzed in detail.

In summary, the fundamental studies using the validated fully coupled model concept demonstrated the significance of the combined influence of soil undulations and the near-surface boundary layer. Based on these mechanism understandings, the model parameterization study was conducted afterwards using the reduced model concept aiming at improving the accuracy of the hydrological modeling.

## **6.2 Major Conclusions**

Research results of each topic are discussed in detail in chapter 3 to 5. At the end of each chapter, the main conclusions are presented, separately. A combination of the three chapters contributes to the overall objective of this dissertation, i.e., advancing our understanding of evaporation from an undulating soil surface under the influence of the near-surface boundary layer.

A summary of the major conclusions of each chapter is presented as follows:

The goal of CHAPTER 3 was to understand the characteristics and mechanisms of evaporation from an undulating soil surface under laminar boundary layer. To achieve this goal, a fully coupled model was developed to simulate the dynamic mass, momentum, and heat transfer processes in the soil-atmosphere system for different atmospheric conditions and soil properties. A laboratory experiment was conducted using wind tunnel – soil tank system, as well as a network of environmental sensors to validate the numerical results. Main results of this study include:

(1) Atmospheric conditions (e.g., wind speed, air temperature, air humidity) affect the evaporation rate by directly affecting vapor diffusion across the boundary layer.

(2) The soil properties (e.g., permeability, soil water retention) affect soil evaporation by directly affecting the continuous capillary flow which then influence the vapor concentration gradient in the boundary layer.

(3) The macro-scale surface undulations directly affect both the capillary flow and vapor diffusion in the boundary layer. Increasing the number of undulations exposes more area for evaporation allowing for more contribution from the capillary flow and resulting in a larger evaporation rate during Stage I. A higher aspect ratio has the same effect, while in the meantime it thickens the boundary layer and impedes the vapor diffusion in the boundary layer as well, which helps lower the evaporation rate.

(4) The local evaporative flux from an undulating surface varies along the surface due to different surface water availability controlled by capillary flow and variational boundary layer thickness along the undulating surface.

The goal of CHAPTER 4 was to understand the characteristics and mechanisms of evaporation from an undulating soil surface under turbulent boundary layer and test the application

of HWA in the boundary layer measurement. To achieve this goal, the fully coupled model developed and validated in CHAPTER 3 was extended by incorporating atmospheric turbulent airflow to simulate the dynamic mass, momentum, and heat transfer processes in the soil-atmosphere system for different atmospheric conditions and soil properties. A laboratory experiment was conducted using wind tunnel – soil tank system, along with HWA to measure the turbulent boundary layer. Main results of this study include:

(1) The turbulent boundary layer developed above the undulating soil surfaces was obtained successfully by HWA at high spatial resolutions. Recirculation zones were clearly captured located in the undulating valleys, where local low-level evaporation was also observed during experiments.

(2) Compared with laminar conditions, atmospheric turbulent airflow enhances the system-level evaporation rate and shortens the duration of the Stage I due to fast loss of water, especially at the undulation peaks. The undulation valleys play a major role during most of the evaporation period due to their vicinity to the receding water table.

(3) Increasing wind speed has negligible influence on the local evaporation at the peaks while slightly affecting the valleys. Together with the turbulence enhancement effect, the influence of wind speed on the system-level evaporation rate for evaporation from an undulating soil surface under turbulent airflow is restricted. Also, the soil permeability shows little impact on the duration of Stage I due to the turbulence enhancement effect, and Stage I may even vanish in the case of a coarse sand.

(4) The aspect ratio of an undulating surface directly determines the presence and extent of the recirculation zones, which controls the vapor distribution and vapor diffusive flux at the soil surfaces. Thus, the AR affects evaporation through influencing both the vertical and horizontal

diffusive flux out of the soil surface, as well as the surface water availability.

The goal of CHAPTER 5 was to improve the parameterization of the reduced model by incorporating the influence of undulating surfaces via direct measurement and investigate the relationship between the vapor roughness length ( $z_{0v}$ ) and the momentum roughness length ( $z_{0m}$ ), two major parameters in the parameterization process. To achieve this goal, four laboratory experiments were conducted using wind tunnel – soil tank system considering different wind speeds and surface undulation configurations. PIV was employed to collect the information of the velocity field developed above the undulating surfaces. Main results of this study include:

(1) In the presence of soil undulations,  $z_{0v}$  is much lower than  $z_{0m}$ , roughly 3 to 7 orders of magnitude, deviating from the assumption commonly used for a flat bare soil surface that  $z_{0v}$  approximates  $z_{0m}$ . Results demonstrate that soil undulations can affect the ratio of  $z_{0v}$  to  $z_{0m}$  significantly, and thus should be taken into consideration when using the reduced model.

(2) The effect of the surface configurations on the ratio of  $z_{0v}$  to  $z_{0m}$  is closely related to the diffusion-controlled mass transfer, and the momentum transfer dominated by both of the viscous shear and the local pressure drag. When the pressure drag takes more proportion than the viscous shear (e.g. a denser undulation setup), the interaction between the soil surface and the mainstream is strengthened, resulting in a larger ratio of  $z_{0v}$  to  $z_{0m}$ . On the contrary, in an undulation setup, especially in which a relatively independent velocity field is able to form between the undulations, the effect of viscous shear becomes prominent and the soil surface – mainstream interaction is weakened, lowering the ratio of  $z_{0v}$  to  $z_{0m}$ .

(3) Wind speed affects the ratio of  $z_{0v}$  to  $z_{0m}$  mainly owing to the Reynolds stress, which is considered as an extra friction in the viscous shear formed due to turbulence. A larger wind speed highlights the extra friction and causes a larger friction velocity and thus lowers the ratio between

$z_{0v}$  and  $z_{0m}$ . The influence of wind speed on this ratio is larger for a sparser undulation configuration due to the strengthened viscous shear and the weakened soil surface – mainstream interaction.

(4) The estimation of the evaporative flux from an undulating soil surface based on the newly formulized aerodynamic resistance performs well by comparing with the experimental data.

### **6.3 Recommendations for Future Research**

This research provides new insights into the mass, momentum, and heat transfer processes between the soil and the atmosphere through investigating the influence of macro-scale undulating surfaces and the near-surface boundary layers. There still remain a number of questions that are worth of further studies. Based on the research in this dissertation, some recommendations for future work are presented as follows.

(1) Add periodic boundary conditions in the fully coupled modeling.

In the fully coupled model, the upstream airflow and vapor transport behavior would have a significant impact on the downstream performance. For example, it is found that the vapor continuously accumulates in the downstream valleys as shown by Figure 3.13. This problem would raise some questions. For instance, how many undulations are enough to display the flow and transport behavior accurately, or which undulating locations should be chosen for behavior analysis. From the perspective of modeling, a solution for this problem is to apply periodic boundary conditions to the free flow subdomain. Further study is needed to fix this modeling issue and compare with the current modeling setup to analyze the difference of the results.

(2) Accurate characterization of the fully coupled model under turbulent boundary layer.

In the fundamental study of evaporation from an undulating soil surface under turbulent boundary layer in CHAPTER 4, a fully coupled model concept was adopted. The model developed and validated in CHAPTER 3 was extended to incorporate turbulent airflow via Reynolds-

averaged Navier-Stokes equations (RANS) with  $k-\varepsilon$  closure model. This turbulent model has a wide application in simulating engineering problems because of its high efficiency. However, this model, in theory, is not valid as close to the wall surface where laminar flow dominates, i.e. the viscous sublayer. Thus, a wall function condition was used at the interface between the free flow and porous media to make up this deficiency. Wall function condition was originally developed based on the assumption of an impermeable wall. Therefore, wall function should not be theoretically correct as a condition used at the permeable soil surface. Although the simulated results are consistent with the experimental results as shown in section 4.4.3, the application of this interfacial condition at the soil surface is not theoretically physical. A physical interfacial characterization remains to be studied in the future. In the meantime, since wall function condition goes along with  $k-\varepsilon$  closure model, a more accurate model to describe the turbulent airflow should be considered if wall function is replaced.

(3) Measurement of humidity profiles above undulating soil surface

In CHAPTER 5, we used the measured velocity field together with simulations using the fully coupled model to parameterize the aerodynamic resistance for the vapor flux top boundary condition. Simulations were employed due to the difficulty to measure the humidity profiles above soil surface without the disruption of velocity boundary layer. In the future research, new experimental approaches can be invented to overcome this challenge.

(4) Linking the parameterization of the viscous sublayer adjacent to the soil surface with the MOST-based aerodynamic resistance.

In CHAPTER 5, we parameterized the aerodynamic resistance based on Monin-Obukhov similarity theory. This theory is valid above the thin viscous sublayer, which is located directly adjacent to the soil surface. In this sense, the viscous sublayer where molecular diffusion

dominates was neglected in the parameterization. In future work, how to include the influence of the viscous sublayer into the parameterized aerodynamic resistance can be taken into consideration.

(5) At what scale do the macro-scale soil undulations display a significant influence on soil evaporation.

According to the research in CHAPTER 3 to CHAPTER 5, the soil undulations play a significant role in the local and system-level evaporation behaviors. The scale on which we conducted simulation or experiments is limited by the laboratory. Field experiments should be carried out in the future to validate these findings and investigate the scale range during which the macro-scale soil undulations have an impact on evaporation.

## APPENDIX A

### EQUATIONS USED IN CHAPTER 3 AND CHAPTER 4

#### A.1 Van Genuchten Model

Soil water retention curve (SWRC) is a basic soil property represented by the relationship between soil water matric potential (or capillary pressure) and soil water content (or water saturation). Van Genuchten (1980) model is the most widely used model to describe SWRC.

$$S_{ew} = \begin{cases} \left[ 1 + (\alpha |p_c / \rho_w g|)^n \right]^{-m} & , p_c > 0 \\ 1 & , p_c \leq 0 \end{cases} \quad (\text{A.1})$$

where  $S_{ew}$  is the normalized water saturation defined by  $S_{ew} = (S_w - S_{rw}) / (1 - S_{rw} - S_{rg})$ ,  $S_{rw}$  and  $S_{rg}$  are residual saturation of water and gas, respectively;  $\alpha$  and  $n$  are van Genuchten fitting parameters ( $m = 1 - 1/n$ );  $p_c$  (Pa) is the capillary pressure;  $\rho_w$  ( $\text{kg/m}^3$ ) is the water density;  $g$  ( $\text{m/s}^2$ ) is the gravitational acceleration.

The relative permeability of water and gas are described by:

$$\begin{aligned} k_{rw} &= S_{ew}^l \left[ 1 - (1 - S_{ew}^{1/m})^m \right]^2 \\ k_{rg} &= (1 - S_{ew})^l (1 - S_{ew}^{1/m})^{2m} \end{aligned} \quad (\text{A.2})$$

where  $k_{ri}$  ( $i = w, g$ ) is the relative permeability of  $i$ -phase,  $i$  denotes water or gas.

#### A.2 Millington and Quirk Model

Millington and Quirk model is a widely used model to calculate the tortuosity of the porous media to predict effective diffusivity. The effective diffusivity  $D_{\text{eff}}$  ( $\text{m}^2/\text{s}$ ) is:

$$D_{\text{eff}} = \frac{\theta_g}{\tau_g} D_g \quad (\text{A.3})$$

where  $\theta_g$  ( $\text{m}^3/\text{m}^3$ ) is the gas phase content in the porous media;  $D_g$  ( $\text{m}^2/\text{s}$ ) is the single-phase

diffusion coefficient for the species diluted in pure gas phase;  $\tau_g$  (dimensionless) is the corresponding tortuosity factor of the porous media, described by the Millington and Quirk model (Millington & Quirk, 1961):

$$\tau_g = \theta_g^{-7/3} \phi^2 \quad (\text{A.4})$$

where  $\phi$  is the porosity.

## APPENDIX B

### APPENDIX OF CHAPTER 4

#### B.1 Power-Law Turbulent Boundary Layer and Blasius Laminar Boundary Layer

##### 1. Power-law turbulent boundary layer

$$\frac{u}{U} = \left( \frac{y / \delta^*}{\beta + 1} \right)^{\frac{1}{\beta}} \quad (\text{B.1})$$

where  $u$  (m/s) is the streamwise time-mean flow speed and  $U$  (m/s) is the maximum flow speed in the mainstream;  $y$  is the surface-normal distance; The power-law index  $\beta$  is determined by

$$\beta = \frac{2}{H - 1}; \quad H = \frac{\delta^*}{\delta^{**}} \quad (\text{B.2})$$

where  $H$  is shape factor;  $\delta^*$  and  $\delta^{**}$  are the displacement thickness and momentum thickness, respectively, calculated from experimental data in CHAPTER 4.

##### 2. Blasius laminar boundary layer

Blasius transformed the second-order partial differential equations governing the growth of the laminar boundary layer on a flat plate under two-dimensional steady and incompressible assumption to a nonlinear, third-order ordinary differential equation by introducing a similarity variable  $\eta$  and dimensionless stream function  $\psi$ :

$$\eta = y / \sqrt{\frac{\nu x}{U}}; \quad f(\eta) = \frac{\psi}{\sqrt{\nu x U}}; \quad f' = \frac{u}{U} \quad (\text{B.3})$$

where  $y$  is the surface-normal distance;  $x$  is the streamwise position;  $\nu$  is the kinetic viscosity;  $U$  is the average freestream speed. This nonlinear, third-order ordinary differential equation can be solved precisely by numerical methods, resulting in a series of  $\eta, f(\eta), f'(\eta) = u/U$  and  $f''(\eta)$ . The calculation shows that  $\eta \approx 4.9$  for  $u/U = 0.99$  when  $y = \delta_{99}$ , where  $\delta_{99}$  is the overall boundary layer

thickness. The displacement thickness  $\delta^*$  is related with the overall thickness  $\delta$  for the flat surface is  $\delta^* = 0.35 \delta_{99}$ . Therefore, the surface-normal distance  $y$  normalized by displacement thickness  $\delta^*$  can be expressed as based on  $\eta$ :

$$\frac{y}{\delta^*} = \frac{\eta}{4.9 * 0.35} \quad (\text{B.4})$$

## B.2 Figure of Blue Dye Deposition at Sand Surface

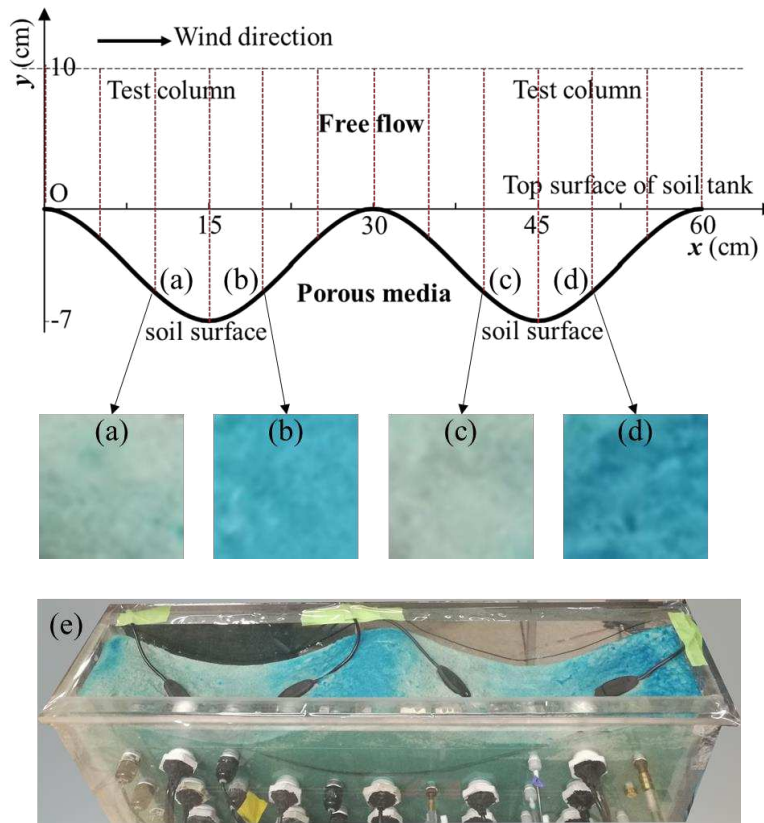


Figure B.1 The cosine curve represents the undulating soil surface in the experiment. Pictures a-d are screenshots of sand surface at four slopes during evaporation in the experiment: (a, c) leeward surfaces, and (b, d) windward surfaces. The blue area is caused by blue dye deposition. More deposition means more evaporation. Picture (e) is the whole photo of the sand surface.

## APPENDIX C

### APPENDIX OF CHAPTER 5

#### C.1 Mathematical Description of the Undulating Soil Surface

(1) #3 undulations

$$\begin{cases} z = -0.04 \cos\left(\frac{2\pi}{0.19}x\right) + 0.04, & 0 \leq x \leq 0.19 \\ z = -0.04 \cos\left[\frac{2\pi}{0.19}(x-0.205)\right] + 0.04, & 0.205 \leq x \leq 0.395 \\ z = -0.04 \cos\left[\frac{2\pi}{0.19}(x-0.41)\right] + 0.04, & 0.41 \leq x \leq 0.6 \\ z = 0, & 0.19 < x < 0.205; 0.395 < x < 0.41 \end{cases} \quad (\text{C.1})$$

(2) #2 undulations

$$\begin{cases} z = -0.04 \cos\left(\frac{2\pi}{0.19}x\right) + 0.04, & 0 \leq x \leq 0.19 \\ z = -0.04 \cos\left[\frac{2\pi}{0.19}(x-0.41)\right] + 0.04, & 0.41 \leq x \leq 0.6 \\ z = 0, & 0.19 < x < 0.41 \end{cases} \quad (\text{C.2})$$

(3) Length of an undulating surface

$$s = \int_a^b \sqrt{1 + [z'(x)]^2} dx \quad (\text{C.3})$$

#### C.2 Figures of the Determined Turbulent Flow Parameters

All fitted turbulent flow parameters in section 5.5.1 for all four cases are displayed by Figure C.1 to Figure C.4.

(1) Case #3U3

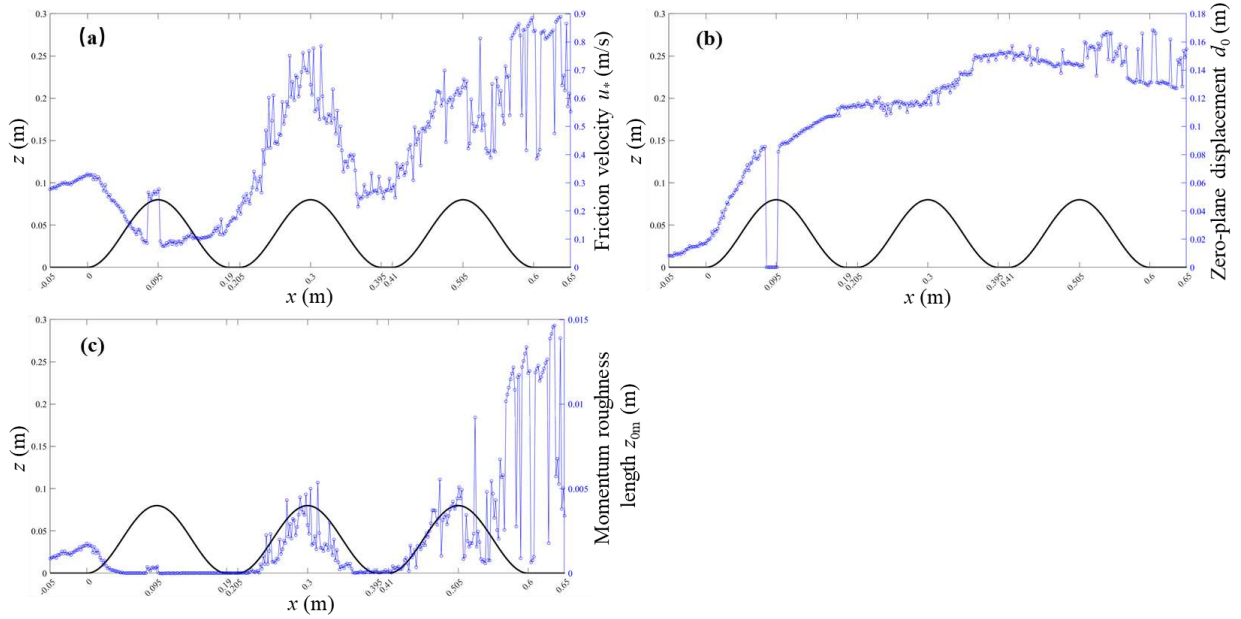


Figure C.1 Distribution of the determined turbulent flow parameters for case #3U3: (a) friction velocity  $u_*$ , (b) zero-plane displacement  $d_0$ , (c) momentum roughness length  $z_{0m}$ .

(2) Case #3U1

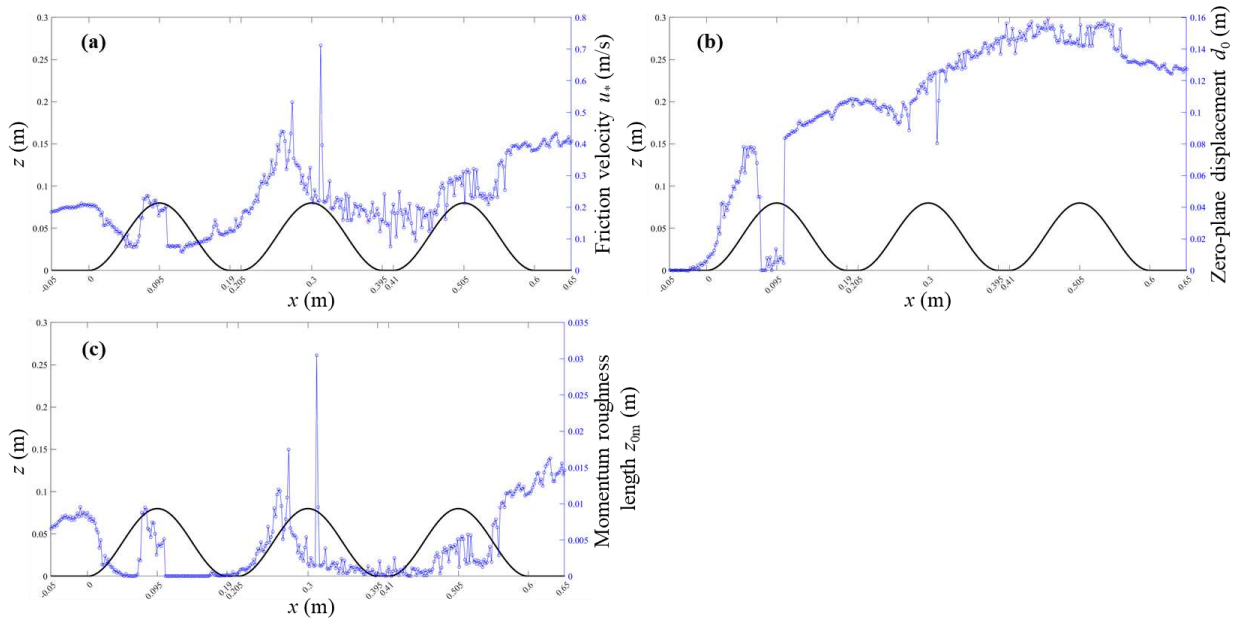


Figure C.2 Distribution of the determined turbulent flow parameters for case #3U1: (a) friction velocity  $u_*$ , (b) zero-plane displacement  $d_0$ , (c) momentum roughness length  $z_{0m}$ .

(3) Case #2U3

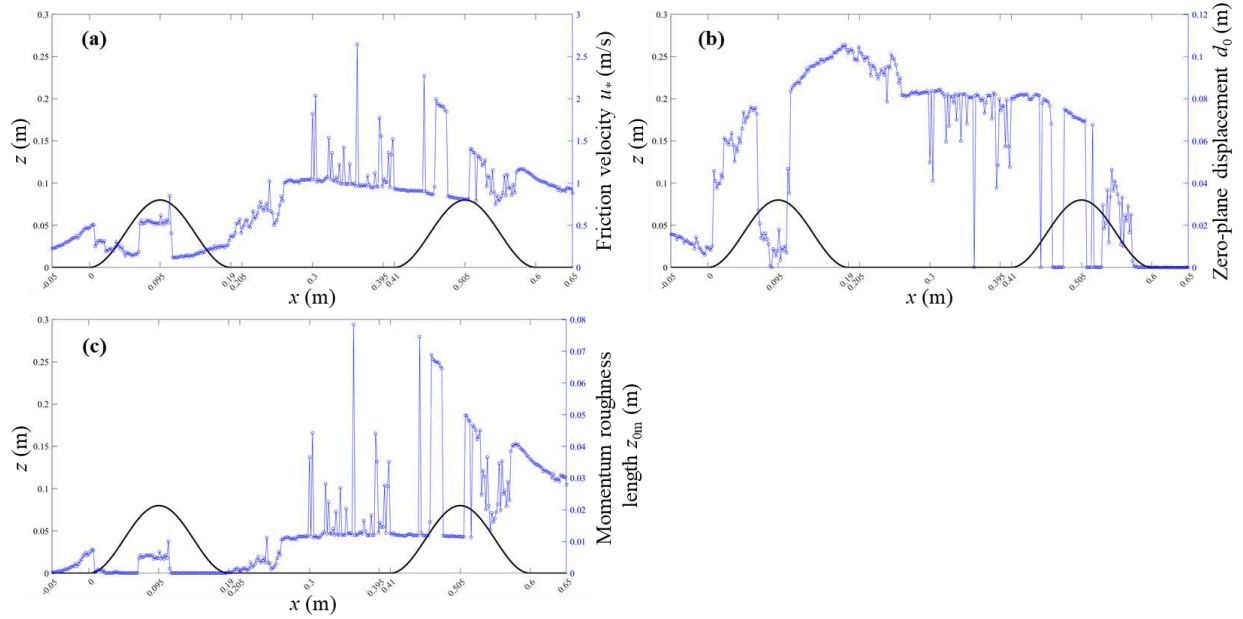


Figure C.3 Distribution of the determined turbulent flow parameters for case #2U3: (a) friction velocity  $u_*$ , (b) zero-plane displacement  $d_0$ , (c) momentum roughness length  $z_{0m}$ .

(4) Case #2U1

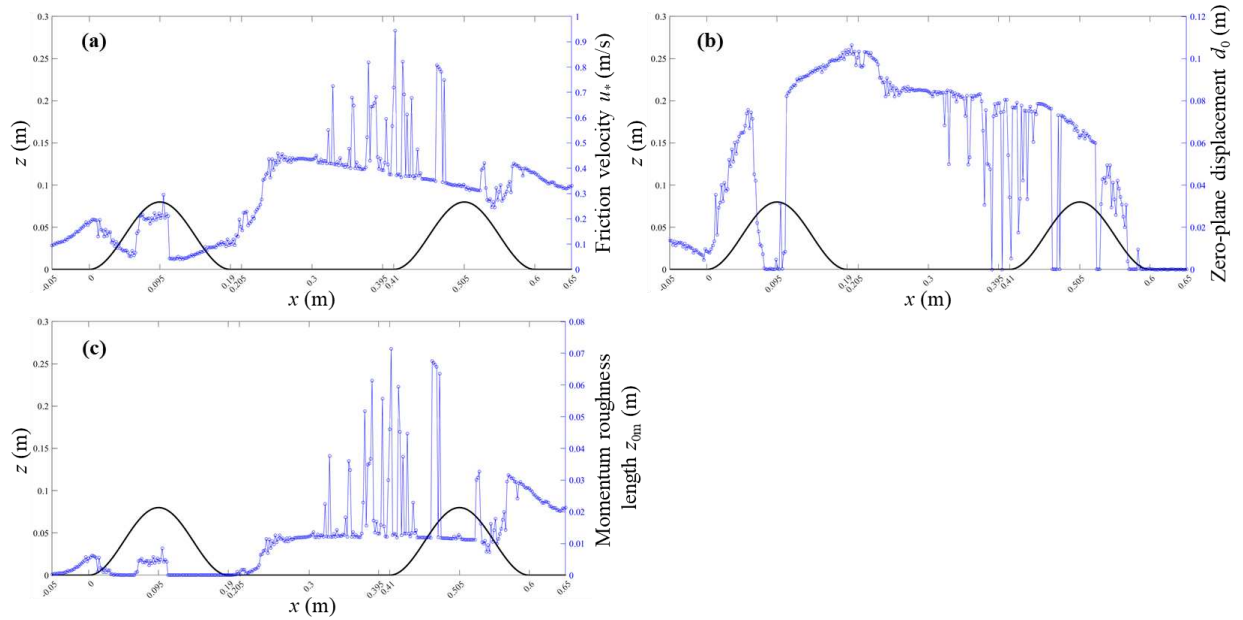


Figure C.4 Distribution of the determined turbulent flow parameters for case #2U1: (a) friction velocity  $u_*$ , (b) zero-plane displacement  $d_0$ , (c) momentum roughness length  $z_{0m}$ .

### C.3 Figures of the Fitted $Da_0^{-1}$ and $Cd_0^{-1/2}$ with $\ln(Re_0)$

(1) Case #3U1

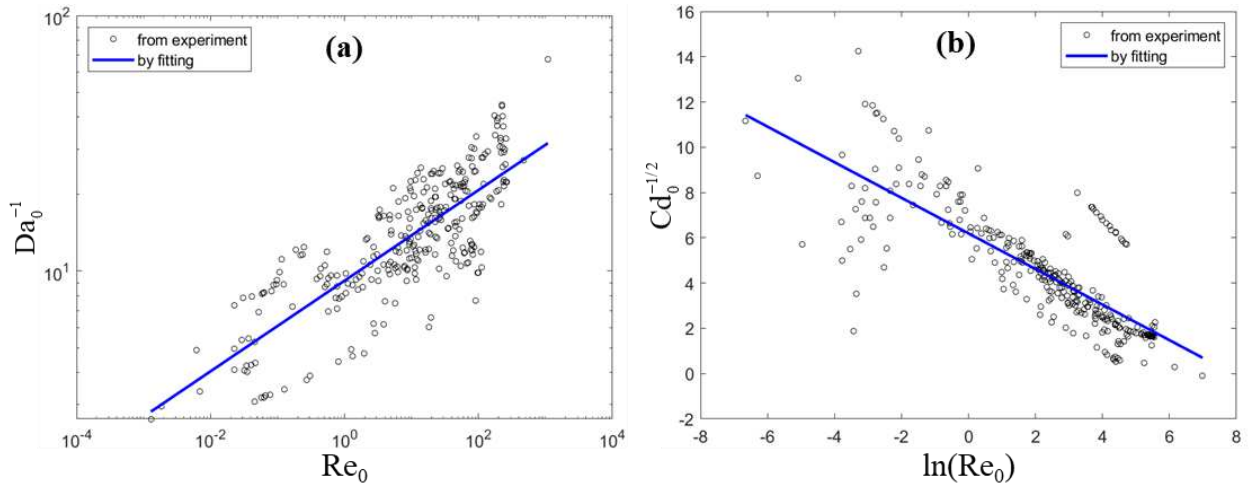


Figure C.5 Case #3U1: (a) comparison of observed and fitted  $Da_0^{-1}$  with  $Re_0$  in double logarithm; (b) comparison of observed and fitted  $Cd_0^{-1/2}$  with  $\ln(Re_0)$ .

(2) Case #2U3

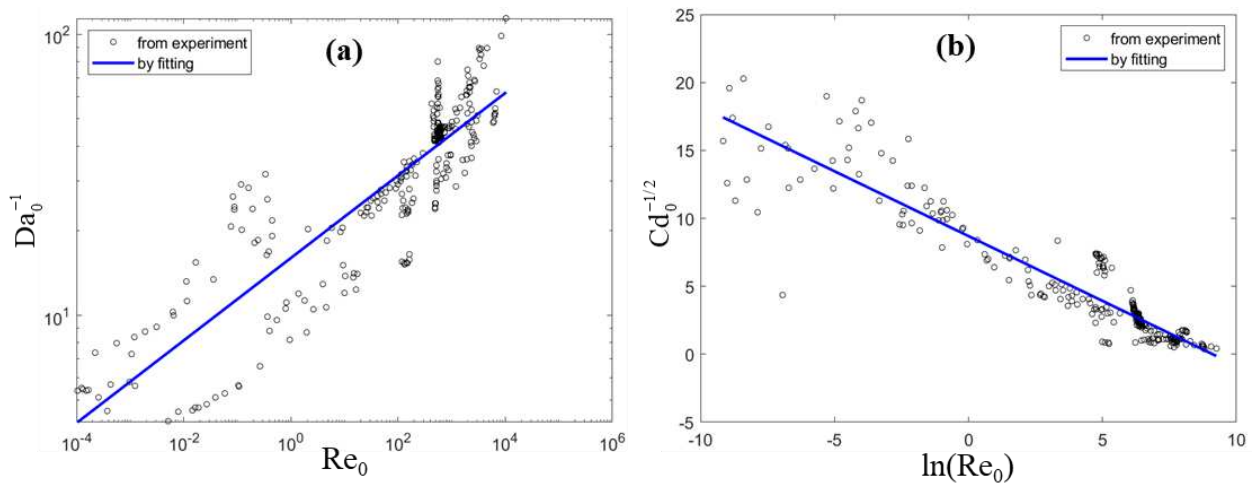


Figure C.6 Case #2U3: (a) comparison of observed and fitted  $Da_0^{-1}$  with  $Re_0$  in double logarithm; (b) comparison of observed and fitted  $Cd_0^{-1/2}$  with  $\ln(Re_0)$ .

(3) Case #2U1

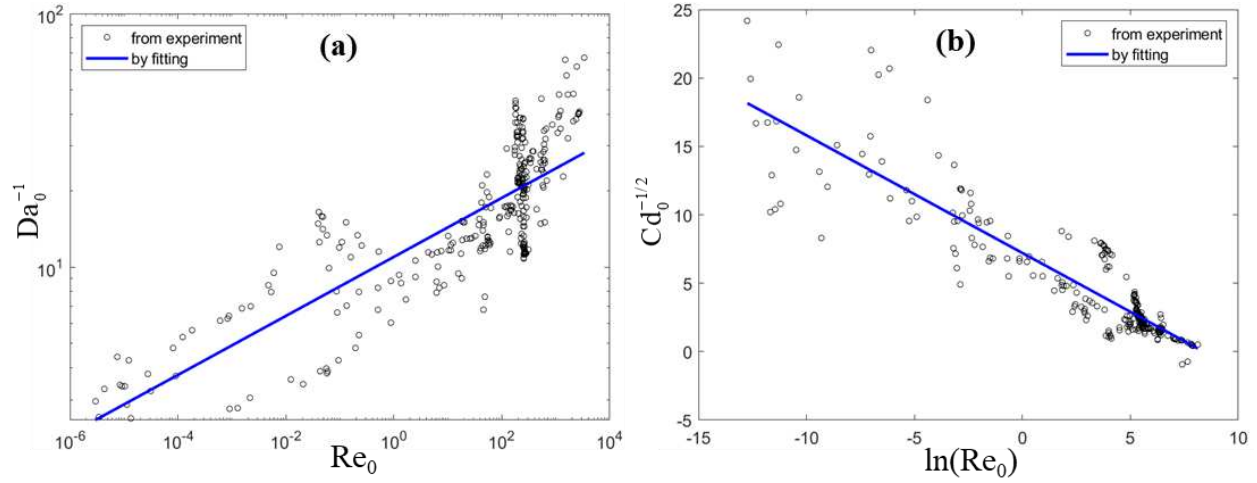


Figure C.7 Case #2U1: (a) comparison of observed and fitted  $Da_0^{-1}$  with  $Re_0$  in double logarithm; (b) comparison of observed and fitted  $Cd_0^{-1/2}$  with  $\ln(Re_0)$ .

APPENDIX D  
SAND MATERIAL

**D.1 Sand Properties**

Two kinds of sands were used in this research, i.e., Accusand #12/20 and Accusand #50/70, from the Unimin Corporation in Ottawa, MN, USA. They are classified according to the effective sieve size and the #12/20 is coarser than the #50/70 sand. 99.8% of the composition is quartz and the grain density is about 2.65 g/cm<sup>3</sup>. The uniformity coefficient of the sands is approximately 1.2 (Sakaki & Smits, 2015). The main properties and van Genuchten parameters (Van Genuchten, 1980) of the two sands are summarized in Table D.1.

Table D.1 Main properties of sand

Sand	$d_{50}$ (mm)	Porosity	Bulk density (g/cm <sup>3</sup> )	Saturated hydraulic conductivity (cm/s)	Thermal conductivity (W·m <sup>-1</sup> ·K <sup>-1</sup> )		Residual water content	Van Genuchten parameters	
					Dry	Saturated		$\alpha$ (m <sup>-1</sup> )	$n$
#12/20	1.03	0.318	1.81	0.376	0.314	2.948	0.006	8.3	11
#50/70	0.26	0.364	1.69	0.036	0.367	3.297	0.005	5	7

Zhang et al., 2008; Sakaki & Smits, 2015; Deepagoda et al, 2016; Forsythe, 2017

## APPENDIX E

### MEASUREMENT EQUIPMENT AND TECHNIQUES

#### E.1 Soil Moisture Measurements

Soil moisture is measured using the ECH<sub>2</sub>O system (Decagon Devices Inc.), which mainly includes EC-5 sensors, EM50 data loggers, and a software.

The EC-5 sensor (Figure E.1a) has two prongs with 8.9 cm in length, 1.8 cm in width and 0.7 cm in height, and the measurement radius approximates 2.5 cm. The average measurement time is about 10 ms and frequency is 70 MHz. The accuracy is at least 0.03 m<sup>3</sup>/m<sup>3</sup> ( $\pm 3\%$ ) for all kinds of soils, and with soil-specific calibration, it is about 0.02 m<sup>3</sup>/m<sup>3</sup> ( $\pm 2\%$ ). The resolution is about 0.001 m<sup>3</sup>/m<sup>3</sup> VWC in mineral soils and 0.25% in growing media. The measurement range is 0 to full saturation. EC-5 sensors measure the dielectric permittivity of the surrounding medium using the capacitance built in their probes (i.e., reading electrical voltage between two tongs). The EM50 datalogger that is connected sensors then converts the voltage reading into an analog-to-digital converter number (ADC count). The ADC count can be directly correlated with a change in water content according to the empirical two-point  $\alpha$ -mixing model (Sakaki et al., 2008).



Figure E.1 (a) EC-5 sensor; (b) Em50 data logger.

The Em50 data logger (Figure E.1b) is a 5-port, self-contained data logger, operated by 5 AA Alkaline or Lithium batteries. The communication between the Em50 and EC-5 sensors is through a stereo to USB or stereo to Serial cable to a PC or mobile handheld device. The data storage is 1 MB (i.e., 36,800 scans for all 5 ports). The data stored in the Em50 data logger are configured and downloaded through the ECH2O Utility software.

## E.2 Soil Temperature Measurements

The soil temperature is measured by ECT sensors (Decagon Devices Inc.) shown in Figure E., which are connected to Em50 data loggers mentioned above with a cable to store temperature data. An ECT sensor is 3 cm in length and 0.075 cm in diameter. The accuracy of ECT sensors is about  $\pm 1.0$  °C from -40 to 5 °C,  $\pm 0.5$  °C from 5 to 40 °C, and  $\pm 1.0$  °C from 40 to 50 °C. The resolution is 0.1 °C.



Figure E.2 ECT sensor and Em50 data logger.

The ECT sensor has a thermistor, constructed of semiconductor material with a resistivity that is especially sensitive to temperature. The resistance of a thermistor decreases with increasing temperature. Temperature is calculated from the measured resistance using the Steinhart-Hart equation:

$$\frac{1}{T} = A + B \ln(R) + C [\ln(R)]^3 \quad (\text{E.1})$$

where  $A$ ,  $B$ , and  $C$  are Steinhart-Hart parameters,  $R$  is resistance measured in ohms, and  $T$  is the temperature in Kelvin.  $R$  is determined through:

$$R = D \left( \frac{V_{\text{ex}}}{V_{\text{out}}} - 1 \right) \quad (\text{E.2})$$

where  $D$  is the resistance of the resistor,  $V_{\text{ex}}$  is the applied excitation voltage, and  $V_{\text{out}}$  is the measured output voltage.  $A$ ,  $B$ ,  $C$ , and  $D$  are determined by the ECH<sub>2</sub>O Utilities software, which is used to communicate with Em50 dataloggers, for each device specifically.

### **E.3 Atmospheric Relative Humidity and Temperature Measurements**

Two kinds of measurement methods/devices are used in this research for the atmospheric relative humidity (RH) and temperature.

#### **E.3.1 VP-4**

In phase I and II, the relative humidity and temperature above the soil surface and in the wind tunnel were measured through VP-4 (Decagon Devices, Inc.; USA) as shown in Figure E.3. For the measurement of relative humidity, VP-4 utilizes a capacitance type RH sensor to measure the relative humidity of the surrounding air. The accuracy is about  $\pm 2\%$  RH for temperature 20 – 60 °C and relative humidity 10% – 90%, and the resolution is 0.1%.



Figure E.3 VP-4 sensor.

For the measurement of temperature, VP-4 has a band gap temperature sensor integrated into the sensor electronics. The temperature sensor is located with the RH sensor and accurately measures the sensor temperature. The accuracy of VP-4 is at least about  $\pm 0.3$  °C from 20 to 50 °C,

and increases to about  $\pm 0.9\text{ }^{\circ}\text{C}$  from 20 to  $-40\text{ }^{\circ}\text{C}$ , and about  $\pm 0.7\text{ }^{\circ}\text{C}$  from 40 to  $50\text{ }^{\circ}\text{C}$ . The resolution is  $0.1\text{ }^{\circ}\text{C}$ .

The VP-4 sensor is connected to Em50 data loggers introduced in section E.1 to store measured data. The data are configured and downloaded through the ECH2O Utility software.

### **E.3.2 SHT35-DIS-F**

In phase III, the relative humidity and temperature above the soil surface and in the wind tunnel were measured through SHT35-DIS-F sensor as shown in Figure E.4 manufactured by SENSIRION. The dimension of this sensor is  $2.5 \times 2.5\text{ mm}^2$  and  $0.9\text{ mm}$  high. It is a fully calibrated, linearized, and temperature compensated digital output sensor. It has a I2C interface with communication speeds up to  $1\text{ MHz}$ . The typical accuracy of this sensor is  $\pm 1.5\%$  for relative humidity and  $\pm 0.1\text{ }^{\circ}\text{C}$  for temperature. The resolution for relative humidity and temperature is  $0.01\%$  and  $0.01\text{ }^{\circ}\text{C}$ , respectively.



Figure E.4 SHT3x-DIS sensor.

One sensor is installed on an Arduino board (A000066) together with a real time clock (RTC). A 16GB microSD card is also installed on the Arduino board through a card module. The Arduino board is connected to a computer with a cable for power and real-time data display through Arduino code. The measured humidity and temperature data are also stored in the SD card, which can be downloaded with a card reader.

#### **E.4 Soil Surface Relative Humidity and Temperature Measurements**

Two kinds of relative humidity (RH) and temperature measurement methods/devices are used in this research at soil surface.

##### **E.4.1 EHT**

In phase I and II, the relative humidity and temperature above the soil surface and in the wind tunnel were measured through EHT sensors (Decagon Devices, Inc.; USA) as shown in Figure E.5. This sensor has the same thermistor with that in section E.2 for temperature measurement. For the measurement of relative humidity, the sensor consists of a ceramic substrate on which a thin film of polymer is deposited between two conductive electrodes. The polymer film, which functions as a capacitor, absorbs or releases water proportional to the relative environmental humidity. The change in the capacitance of the capacitor is measured by an onboard electronic circuit and correlated to a relative humidity value. The accuracy for measuring relative humidity is  $\pm 2\%$  from 5% to 90%, and  $\pm 3\%$  from 90% to 100%. The resolution is 0.1%.



Figure E.5 EHT sensor.

##### **E.4.2 AKCP-sensorProbe8 and Sensors**

In phase III, the surface temperature and relative humidity are measured by the AKCP single port temperature and humidity sensor (AKCP, Inc.) shown in Figure E.6. For temperature measurement, the accuracy is maximum  $\pm 2.3$  °C at -40 °C, minimum  $\pm 0.4$  °C at 25 °C, and  $\pm 1.7$  °C at 75 °C. The resolution is 1 °C. For humidity measurement, the accuracy is  $\pm 3\%$  at 25 °C. The sensor is connected to the sensorProbe8 for power and data collection.



Figure E.6 AKCP single port temperature and humidity sensor.

The sensorProbe8 (AKCP, Inc.), shown in Figure E.7 is a high-speed, accurate and intelligent monitoring device. It is a fully embedded host including TCP/IP and a built-in webserver, as well as Email and SNMP functionality. It has 8 auto-sense ports to connect with the above single port temperature and humidity sensor. The sensorProbe8 is connected with a computer to transport measured data for observation in real time.



Figure E.7 AKCP sensorProbe8.

## E.5 Wind Velocity Field Measurements

Three kinds of equipment/technologies are used to measure the wind speed / velocity field in this research.

### E.5.1 Pitot Static Tube

In phase I, the average wind speed in the wind tunnel is measured through the pitot static tube (Dwyer Instruments, Inc.). It includes three main parts, i.e. the pitot tube sensor (Model 167-12), the differential pressure transmitter (Model PX653-0.1D5V), and the multifunction data acquisition (DAQ) module (Model NI USB-6218). The pitot tube has a diameter of 0.32 cm and 30.48 cm insertion length. The accuracy is  $\pm 5\%$ .

Pitot tube measures pressure differences between stagnation pressure and static pressure through the use of a pressure transducer using an electronic strain gauge. The static pressure is the pressure of the fluid and is a measure of the amount of fluid pressure that exceeds local atmospheric pressure. It is measured through a flat opening that is parallel with the fluid flow. The stagnation pressure is also a measure of the amount that fluid pressure exceeds local atmospheric pressure, but it includes the effect of the fluid velocity converted to pressure. It is measured through a flat opening that is perpendicular to the direction of fluid flow and facing into the fluid flow. The average wind speed is calculated based on the Bernoulli's equation:

$$u = \sqrt{\frac{2(p_{\text{stag}} - p)}{\rho}} \quad (\text{E.3})$$

where  $u$  (m/s) is the average wind speed,  $p_{\text{stag}}$  and  $p$  are the stagnation pressure and the static pressure, respectively.  $\rho$  is the air density estimated based on the ideal gas law at the specific temperature and pressure.

### **E.5.2 Hot-wire Anemometry**

In phase II, the Hot-wire Anemometry is used to measure the velocity profiles above the soil surface.

The Hot-wire Anemometry system mainly includes the Constant Temperature Anemometers (CTA) and the sensor probe. The sensor probe consists of the sensor, the sensor support (prongs or substrate) to carry the sensor and lead current, the probe body carrying the sensor support, and the connector which provides electrical connection to the probe support or probe cable. In this research, a miniature wire probe is used, which has a single 5 $\mu\text{m}$  diameter, 1.25 mm long plated tungsten wire sensor welded between two straight prongs (model number 55P11, Dantec Dynamics, Inc.). The probe was mounted on a traverse with the wire perpendicular

to the streamwise flow direction, allowing for the time varying measurement of the streamwise speed normal to the sensor. The main theory of Hot-wire Anemometry to measure wind speed is summarized as follows. An electronic current is sent through the wire to heat the wire. As a fluid (in this study it is the air) flows over the sensor probe, it cools the wire. An energy balance equation can be used to describe the heat transfer process and solved to determine the fluid velocity. During the measurement process, the hot-wire anemometer is operated in a constant temperature configuration using CTA, a five channel AN-1003 model from A.A. Lab.

### **E.5.3 Particle Image Velocimetry**

In phase III, the Particle Image Velocimetry (PIV) is used to measure the velocity field above the soil surface.

PIV is an optical method of flow visualization technology. It can obtain the instantaneous velocity field very fast. The measurement theory is that sufficiently small tracer particles are released to the fluid. The fluid with these entrained particles is illuminated so that particles are visible by the camera. The movement of these particles in the flow fluid is tracked by image analysis technology and their motion is used to calculate the velocity field. PIV is a nonintrusive method to measure the velocity field. The added extremely small particles have negligible influence on the fluid flow development. Compared with the intrusive methods, such as pitot tube and hot-wire anemometry, PIV is capable to measure the entire velocity field simultaneously and fast.

The main components of a PIV system, shown in Figure E.8, include seeding particles, an external laser (Quintel Evergreen Nd:YAG, maximum output 200 mJ per pulse) used to intensify the strength of the scattered light by particles, a sCMOS 2D2C camera (resolution  $2560 \times 2160$  pixels, frame rate 50 fps) with high frame rate, high resolution and high speed, and a computer with

software packages for image processing.

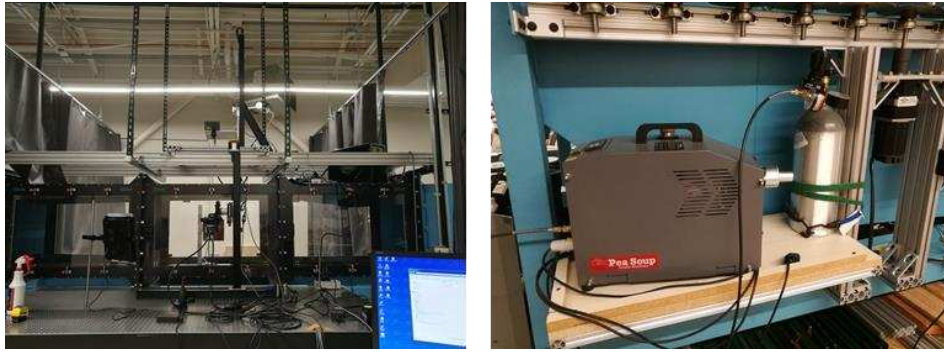


Figure E.8 PIV system. Left figure includes a camera and laser installed on two traverses, respectively. Right figure includes a smoking machine (ViCount Compact 1300).

Before PIV measurement, the system is calibrated first. A calibration target is placed roughly at the location where the images would be obtained by the camera. Start low-power laser and adjust the position of the calibration target to make sure the laser aligns with its front surface. Move the camera to the range of laser and take pictures with low-power laser. Adjust camera angle to hide reflection as much as possible. Power off laser and adjust the focus of the camera. After calibration is finished, start the wind tunnel and set a specific wind speed. Start the smoke machine and release particles until a certain and relatively constant concentration in the air. Move camera and laser together to the location for PIV imaging, adjust laser power, camera aperture and exposure time to meet the demand of image resolution.

Assuming the current position of one particle in a vertical plane is  $[x(t), z(t)]$ , after  $\Delta t$  (exposure time) it arrives at  $[x(t+\Delta t), z(t+\Delta t)]$ . Then its velocity can be estimated by:

$$v_i = \lim_{\Delta t \rightarrow 0} \frac{di(t)}{dt} \approx \frac{i(t+\Delta t) - i(t)}{\Delta t} \quad , \quad i = x, z \quad (\text{E.4})$$

The particle position change is obtained by image analysis based on the camera exposure time. Information from enough particles finally composes to the velocity field.

APPENDIX F

SUPPLEMENTAL ELECTRONIC FILES: EXPERIMENTAL  
AND MODELING OUTPUT DATA

Chapter 3.zip	One experimental dataset	Evaporation amount, #50/70 sand property, soil moisture, soil temperature, surface relative humidity and temperature, atmospheric relative humidity and temperature
	One modeling output dataset	All modeled results under laminar flow state for analysis considering different atmospheric conditions, soil properties, surface geometry
Chapter 4.zip	Three experimental datasets	Boundary layer raw data by HWA
		Processed results of boundary layers
		All evaporation related data, including evaporation amount, surface relative humidity and temperature, atmospheric relative humidity and temperature
One modeling output dataset	All modeled results under turbulent flow state for analysis, considering different atmospheric conditions, soil properties, and surface geometry	
Chapter 5.zip	Seven evaporation related experimental datasets	Atmospheric relative humidity and temperature
		Surface relative humidity and temperature
		Soil moisture
		Soil temperature
		Evaporation amount
		#12&20 sand property
		Field experimental data
	One modeling output dataset	Modeled data used for estimating mass transfer coefficient in section 5.5.2
	One PIV dataset	PIV raw and processed data
	One folder including all figures obtained during parameterization process	Figures from parameterization
One dataset for parameterization analysis in section 5.5.3	Parameterized result analysis	
One dataset for estimating evaporation rate in section 5.6.2 and 5.6.3	Evaporation rate estimation	

## APPENDIX G

### SUPPLEMENTAL ELECTRONIC FILES: COPYRIGHT PERMISSION DOCUMENTS

WRR	Copyright permission from Water Resources Research for Chapter 3
VZJ	Copyright permission from Vadose Zone Journal for Chapter 4
Permission_Rainer	Paper reuse permission from coauthor Dr. Rainer Helmig for Chapter 3
Permission_John	Paper reuse permission from coauthor Dr. John Farnsworth for Chapter 4

## REFERENCES

- Alfredsson, P. H., Örlü, R., & Schlatter, P. (2011). The viscous sublayer revisited—exploiting self-similarity to determine the wall position and friction velocity. *Experiments in Fluids*, *51*(1), 271–280.
- Allegrini, J., Dorer, V., & Carmeliet, J. (2014). Buoyant flows in street canyons: Validation of CFD simulations with wind tunnel measurements. *Building and Environment*, *72*, 63–74. <https://doi.org/10.1016/j.buildenv.2013.10.021>
- Allen, S. J. (1990). Measurement and estimation of evaporation from soil under sparse barley crops in northern Syria. *Agricultural and Forest Meteorology*, *49*(4), 291–309.
- Altevogt, A. S., & Celia, M. A. (2004). Numerical modeling of carbon dioxide in unsaturated soils due to deep subsurface leakage. *Water Resources Research*, *40*(3).
- Andreas, E. L. (1987). A theory for the scalar roughness and the scalar transfer coefficients over snow and sea ice. *Boundary-Layer Meteorology*, *38*(1–2), 159–184.
- Andreas, E. L. (2002). Parameterizing scalar transfer over snow and ice: A review. *Journal of Hydrometeorology*, *3*(4), 417–432.
- Armstrong, J. E., Frind, E. O., & McClellan, R. D. (1994). Nonequilibrium mass transfer between the vapor, aqueous, and solid phases in unsaturated soils during vapor extraction. *Water Resources Research*, *30*(2), 355–368.
- Athanassiadou, M., & Castro, I. P. (2001). Neutral flow over a series of rough hills: A laboratory experiment. *Boundary-Layer Meteorology*, *101*(1), 1–30. <https://doi.org/10.1023/A:1019250801054>
- Baber, K. (2014). Coupling free flow and flow in porous media in biological and technical applications: From a simple to a complex interface description. *Univ. of Stuttgart, Stuttgart, Germany*.
- Baber, K., Mosthaf, K., Flemisch, B., Helmig, R., Müthing, S., & Wohlmuth, B. (2012). Numerical scheme for coupling two-phase compositional porous-media flow and one-phase compositional free flow. *The IMA Journal of Applied Mathematics*, *77*(6), 887–909.
- Bailly, C., & Comte-Bellot, G. (2015). *Introduction to Turbulence*. Springer, Cham. [https://doi.org/10.1007/978-3-319-16160-0\\_1](https://doi.org/10.1007/978-3-319-16160-0_1)
- Basirat, F., Sharma, P., Fagerlund, F., & Niemi, A. (2015). Experimental and modeling investigation of CO<sub>2</sub> flow and transport in a coupled domain of porous media and free flow. *International Journal of Greenhouse Gas Control*, *42*, 461–470.

- Baskaran, V., Smits, A. J., & Joubert, P. N. (1987). A turbulent flow over a curved hill Part 1. Growth of an internal boundary layer. *Journal of Fluid Mechanics*, 182, 47–83.
- Bear, J. (2013). *Dynamics of fluids in porous media*. Courier Corporation.
- Beavers, G. S., & Joseph, D. D. (1967). Boundary conditions at a naturally permeable wall. *Journal of Fluid Mechanics*, 30(1), 197–207. [https://doi.org/DOI: 10.1017/S0022112067001375](https://doi.org/DOI:10.1017/S0022112067001375)
- Benet, J. C., & Jouanna, P. (1982). Phenomenological relation of phase change of water in a porous medium: experimental verification and measurement of the phenomenological coefficient. *International Journal of Heat and Mass Transfer*, 25(11), 1747–1754.
- Bergman, T. L., Incropera, F. P., DeWitt, D. P., & Lavine, A. S. (2011). *Fundamentals of heat and mass transfer*. John Wiley & Sons.
- Binning, P. J., Postma, D., Russell, T. F., Wesselingh, J. A., & Boulin, P. F. (2007). Advective and diffusive contributions to reactive gas transport during pyrite oxidation in the unsaturated zone. *Water Resources Research*, 43(2).
- Bird, R. B. (2002). Transport phenomena. *Appl. Mech. Rev.*, 55(1), R1–R4.
- Bittelli, M., Ventura, F., Campbell, G. S., Snyder, R. L., Gallegati, F., & Pisa, P. R. (2008). Coupling of heat, water vapor, and liquid water fluxes to compute evaporation in bare soils. *Journal of Hydrology*, 362(3–4), 191–205.
- Bixler, N. E. (1985). *NORIA: A finite element computer program for analyzing water, vapor, air and energy transport in porous media*. Sandia National Laboratories Albuquerque, NM.
- Blasius, H. (1907). *Grenzschichten in Flüssigkeiten mit kleiner Reibung*. Druck von BG Teubner.
- Bowling, D. R., & Massman, W. J. (2011). Persistent wind-induced enhancement of diffusive CO<sub>2</sub> transport in a mountain forest snowpack. *Journal of Geophysical Research: Biogeosciences*, 116(G4). <https://doi.org/10.1029/2011JG001722>
- Brutsaert, W. (1979). Heat and mass transfer to and from surfaces with dense vegetation or similar permeable roughness. *Boundary-Layer Meteorology*, 16(4), 365–388.
- Brutsaert, W. (1975). A theory for local evaporation (or heat transfer) from rough and smooth surfaces at ground level. *Water Resources Research*, 11(4), 543–550.
- Brutsaert, W. (2013). *Evaporation into the atmosphere: theory, history and applications* (Vol. 1). Springer Science & Business Media.
- Brutsaert, W., & Stricker, H. (1979). An advection-aridity approach to estimate actual regional evapotranspiration. *Water Resources Research*, 15(2), 443–450.

- Buckles, J., Hanratty, T. J., & Adrian, R. J. (1984). Turbulent flow over large-amplitude wavy surfaces. *Journal of Fluid Mechanics*, *140*, 27–44.
- Budagovskij, A. I. (1964). *Evaporation of soil water*. Izdatelsrvo Nauka (Publishers Nauka), Moscow.
- Businger, J. A., & Yaglom, A. M. (1971). Introduction to Obukhov's paper on 'turbulence in an atmosphere with a non-uniform temperature.' *Boundary-Layer Meteorology*, *2*(1), 3–6.
- Byrne, G. F., Dunin, F. X., & Diggle, P. J. (1988). Forest evaporation and meteorological data: A test of a complementary theory advection-aridity approach. *Water Resources Research*, *24*(1), 30–34.
- Calhoun, R. J., & Street, R. L. (2001). Turbulent flow over a wavy surface: Neutral case. *Journal of Geophysical Research: Oceans*, *106*(C5), 9277–9293.
- Camillo, P. J., & Gurney, R. J. (1986). A resistance parameter for bare-soil evaporation models. *Soil Science*, *141*(2), 95–105.
- Campbell, G. S. (1985). *Soil physics with BASIC: transport models for soil-plant systems* (Vol. 14). Elsevier.
- Canovaro, F., Paris, E., & Solari, L. (2007). Effects of macro-scale bed roughness geometry on flow resistance. *Water Resources Research*, *43*(10).
- Cao, S., & Tamura, T. (2006). Experimental study on roughness effects on turbulent boundary layer flow over a two-dimensional steep hill. *Journal of Wind Engineering and Industrial Aerodynamics*, *94*(1), 1–19.
- Cebeci, T., & Chang, K. C. (1978). Calculation of incompressible rough-wall boundary-layer flows. *AIAA Journal*, *16*(7), 730–735.
- Cheng, N. S. (2007). Power-law index for velocity profiles in open channel flows. *Advances in Water Resources*, *30*(8), 1775–1784. <https://doi.org/10.1016/j.advwatres.2007.02.001>
- Cherukat, P., Na, Y., Hanratty, T. J., & McLaughlin, J. B. (1998). Direct numerical simulation of a fully developed turbulent flow over a wavy wall. *Theoretical and Computational Fluid Dynamics*, *11*(2), 109–134. <https://doi.org/10.1007/s001620050083>
- Chow, F. K., Granvold, P. W., & Oldenburg, C. M. (2009). Modeling the effects of topography and wind on atmospheric dispersion of CO<sub>2</sub> surface leakage at geologic carbon sequestration sites. *Energy Procedia*, *1*(1), 1925–1932.
- Cierniewski, J., & Guliński, M. (2010). Furrow Microrelief Influence on the Directional Hyperspectral Reflectance of Soil at Various Illumination and Observation Conditions. *IEEE Transactions on Geoscience and Remote Sensing*, *48*(11), 4143–4148. <https://doi.org/10.1109/TGRS.2010.2050207>

- Clark, I. (1977). Roke, a computer program for nonlinear least-squares decomposition of mixtures of distributions. *Computers & Geosciences*, 3(2), 245–256.
- Clements, W. E., & Wilkening, M. H. (1974). Atmospheric pressure effects on  $^{222}\text{Rn}$  transport across the earth-air interface. *Journal of Geophysical Research*, 79(33), 5025–5029.
- Coltman, E., Lipp, M., Vescovini, A., & Helmig, R. (2020). Obstacles, Interfacial Forms, and Turbulence: A Numerical Analysis of Soil–Water Evaporation Across Different Interfaces. *Transport in Porous Media*, 1–27.
- Comsol (2016). *COMSOL Multiphysics*. Comsol.
- Crago, R., Hervol, N., & Crowley, R. (2005). A complementary evaporation approach to the scalar roughness length. *Water Resources Research*, 41(6).
- Culler, E. C. E., & Farnsworth, J. A. N. (2019). Higher frequencies in stall flutter moment development. *Journal of Fluids and Structures*, 85, 181–198.
- Davarzani, H., Smits, K., Tolene, R. M., & Illangasekare, T. (2014). Study of the effect of wind speed on evaporation from soil through integrated modeling of the atmospheric boundary layer and shallow subsurface. *Water Resources Research*, 50(1), 661–680.  
<https://doi.org/10.1002/2013WR013952>
- Dawkins, R. A., & Davies, D. R. (1981). The effects of surface topography on momentum and mass transfer in a turbulent boundary layer. *Journal of Fluid Mechanics*, 108, 423–442.  
<https://doi.org/10.1017/S002211208100219X>
- De Bruin, H. A. R., & Moore, C. J. (1985). Zero-plane displacement and roughness length for tall vegetation, derived from a simple mass conservation hypothesis. *Boundary-Layer Meteorology*, 31(1), 39–49.
- De Lemos, M. J. S., & Silva, R. A. (2003). Turbulent flow around a wavy interface between a porous medium and a clear domain. In *ASME/JSME 2003 4th Joint Fluids Summer Engineering Conference, 1 C* (January), 1509–1514. <https://doi.org/10.1115/fedsm2003-45457>
- Deepagoda, T. K. K. C., Smits, K. M., & Oldenburg, C. M. (2016). Effect of subsurface soil moisture variability and atmospheric conditions on methane gas migration in shallow subsurface. *International Journal of Greenhouse Gas Control*, 55, 105–117.
- Deepagoda, T. K. K. C., Smits, K., Ramirez, J., & Moldrup, P. (2016). Characterization of Thermal, Hydraulic, and Gas Diffusion Properties in Variably Saturated Sand Grades. *Vadose Zone Journal*, 15(4). <https://doi.org/10.2136/vzj2015.07.0097>
- Defraeye, T., Blocken, B., & Carmeliet, J. (2010). CFD analysis of convective heat transfer at the surfaces of a cube immersed in a turbulent boundary layer. *International Journal of Heat and Mass Transfer*, 53(1–3), 297–308.  
<https://doi.org/10.1016/j.ijheatmasstransfer.2009.09.029>

- Desborough, C. E., Pitman, A. J., & Iranneiad, P. (1996). Analysis of the relationship between bare soil evaporation and soil moisture simulated by 13 land surface schemes for a simple non-vegetated site. *Global and Planetary Change*, 13(1–4), 47–56.
- Dobberschütz, S. (2014). Stokes-Darcy coupling for periodically curved interfaces. *Comptes Rendus - Mecanique*, 342(2), 73–78. <https://doi.org/10.1016/j.crme.2013.12.003>
- Dong, Z., Gao, S., & Fryrear, D. W. (2001). Drag coefficients, roughness length and zero-plane displacement height as disturbed by artificial standing vegetation. *Journal of Arid Environments*, 49(3), 485–505.
- Erbertseder, K., Reichold, J., Flemisch, B., Jenny, P., & Helmig, R. (2012). A coupled discrete/continuum model for describing cancer-therapeutic transport in the lung. *PLoS One*, 7(3), e31966.
- Faivre, R., Colin, J., & Menenti, M. (2017). Evaluation of methods for aerodynamic roughness length retrieval from very high-resolution imaging lidar observations over the Heihe Basin in China. *Remote Sensing*, 9(1), 63.
- Fan, Y., Clark, M., Lawrence, D. M., Swenson, S., Band, L. E., Brantley, S. L., Brooks, P. D., Dietrich, W. E., Flores, A., Grant, G., & Kirchner, J. W. (2019). Hillslope Hydrology in Global Change Research and Earth System Modeling. *Water Resources Research*, 1–36. <https://doi.org/10.1029/2018WR023903>
- Fetzer, T., Smits, K. M., & Helmig, R. (2016). Effect of turbulence and roughness on coupled porous-medium/free-flow exchange processes. *Water Resources Research*, 114(2), 395–424. <https://doi.org/10.1029/2011WR010685>
- Fetzer, T. (2012). Numerical analysis of the influence of turbulence on exchange processes between porous-medium and free flow. *Dep. of Hydromech. and Model. of Hydrosyst., IWS, Univ. of Stuttgart, Stuttgart, Germany*.
- Fetzer, T. (2018). *Coupled free and porous-medium flow processes affected by turbulence and roughness: models, concepts and analysis*. Stuttgart: Eigenverlag des Instituts für Wasser- und Umweltsystemmodellierung der Universität Stuttgart.
- Finnigan, J. J., & Belcher, S. E. (2004). Flow over a hill covered with a plant canopy. *Quarterly Journal of the Royal Meteorological Society*, 130(596), 1–29. <https://doi.org/10.1256/qj.02.177>
- Fiolitakis, A., Ess, P. R., Gerlinger, P., & Aigner, M. (2014). Modeling of heat transfer and differential diffusion in transported PDF methods. *Combustion and Flame*, 161(8), 2107–2119. <https://doi.org/https://doi.org/10.1016/j.combustflame.2014.01.021>
- Fitzpatrick, N., Radić, V., & Menounos, B. (2019). A multi-season investigation of glacier surface roughness lengths through in situ and remote observation. *The Cryosphere*, 13(3), 1051–1071.

- Forsythe, L. F. (2017). *Numerical and experimental analysis of bare soil resistance in homogeneous and heterogeneous soils*, A. Colorado School of Mines. Arthur Lakes Library.
- Francesco, T. (1987). Separation features of boundary-layer flow over valleys. *Boundary-Layer Meteorology*, 40(3), 295–307.
- Gao, B., Davarzani, H., Helmig, R., & Smits, K. M. (2018). Experimental and numerical study of evaporation from wavy surfaces by coupling free flow and porous media flow. *Water Resources Research*, 54(11), 9096–9117.
- Gao, B., Farnsworth, J., & Smits, K. M. (2020). Evaporation from undulating soil surfaces under turbulent airflow through numerical and experimental approaches. *Vadose Zone Journal*, 19(1), e20038.
- Garratt, J. R., & Hicks, B. B. (1973). Momentum, heat and water vapour transfer to and from natural and artificial surfaces. *Quarterly Journal of the Royal Meteorological Society*, 99(422), 680–687.
- Garratt, John R. (1994). The atmospheric boundary layer. *Earth-Science Reviews*, 37(1–2), 89–134.
- Goyeau, B., Lhuillier, D., Gobin, D., & Velarde, M. G. (2003). Momentum transport at a fluid–porous interface. *International Journal of Heat and Mass Transfer*, 46(21), 4071–4081.
- Guzha, A. C. (2004). Effects of tillage on soil microrelief, surface depression storage and soil water storage. *Soil and Tillage Research*, 76(2), 105–114.  
<https://doi.org/10.1016/j.still.2003.09.002>
- Haghighi, E., & Or, D. (2015a). Evaporation from Wavy Porous Surfaces into Turbulent Airflows. *Transport in Porous Media*, 110(2), 225–250. <https://doi.org/10.1007/s11242-015-0512-y>
- Haghighi, E., & Or, D. (2013). Evaporation from porous surfaces into turbulent airflows: Coupling eddy characteristics with pore scale vapor diffusion. *Water Resources Research*, 49(12), 8432–8442.
- Haghighi, E., & Or, D. (2015b). Interactions of bluff-body obstacles with turbulent airflows affecting evaporative fluxes from porous surfaces. *Journal of Hydrology*, 530, 103–116.
- Haghighi, E., & Or, D. (2015c). Linking evaporative fluxes from bare soil across surface viscous sublayer with the Monin–Obukhov atmospheric flux-profile estimates. *Journal of Hydrology*, 525, 684–693.
- Halder, A., Dhall, A., & Datta, A. K. (2011). Modeling Transport in Porous Media With Phase Change: Applications to Food Processing. *Journal of Heat Transfer*, 133(3), 031010.  
<https://doi.org/10.1115/1.4002463>

- Han, D., Sun, D., & Wang, X. (2014). Two-phase flows in karstic geometry. *Mathematical Methods in the Applied Sciences*, 37(18), 3048–3063.
- Harriott, P. (1962). A random eddy modification of the penetration theory. *Chemical Engineering Science*, 17(3), 149–154.
- Hide, J. C. (1954). Observations on factors influencing the evaporation of soil moisture. *Soil Science Society of America Journal*, 18(3), 234–239.
- Holman, J. P. (2002). *Heat Transfer-Si Units-Sie*. Tata McGraw-Hill Education.
- Huang, Z., Gao, B., Zhang, Y., & Yao, J. (2016). On the coupling of two-phase free flow and porous flow. *ECMOR XV-15th European Conference on the Mathematics of Oil Recovery*, cp-494. European Association of Geoscientists & Engineers.
- Huntingford, C., Allen, S. J., & Harding, R. J. (1995). An intercomparison of single and dual-source vegetation-atmosphere transfer models applied to transpiration from sahelian savannah. *Boundary-Layer Meteorology*, 74(4), 397–418.  
<https://doi.org/10.1007/BF00712380>
- Huxman, T. E., Snyder, K. A., Tissue, D., Leffler, A. J., Ogle, K., Pockman, W. T., Sandquist, D. R., Potts, D. L. and Schwinning, S. (2004). Precipitation pulses and carbon fluxes in semiarid and arid ecosystems. *Oecologia*, 141(2), 254–268.
- Isabelle, P. E., Nadeau, D. F., Rousseau, A. N., Coursolle, C., & Margolis, H. A. (2015). Applicability of the bulk-transfer approach to estimate evapotranspiration from boreal peatlands. *Journal of Hydrometeorology*, 16(4), 1521–1539.
- Ishihara, Y., Shimojima, E., & Harada, H. (1992). Water vapor transfer beneath bare soil where evaporation is influenced by a turbulent surface wind. *Journal of Hydrology*, 131(1–4), 63–104. [https://doi.org/10.1016/0022-1694\(92\)90213-F](https://doi.org/10.1016/0022-1694(92)90213-F)
- Jefferson, J. L., & Maxwell, R. M. (2015). Evaluation of simple to complex parameterizations of bare ground evaporation. *Journal of Advances in Modeling Earth Systems*, 7(3), 1075–1092.
- Jordan, R. E., Andreas, E. L., & Makshtas, A. P. (1999). Heat budget of snow-covered sea ice at North Pole 4. *Journal of Geophysical Research: Oceans*, 104(C4), 7785–7806.
- Katul, G. G., Finnigan, J. J., Poggi, D., Leuning, R., & Belcher, S. E. (2006). The Influence of Hilly Terrain on Canopy-Atmosphere Carbon Dioxide Exchange. *Boundary-Layer Meteorology*, 118(1), 189–216. <https://doi.org/10.1007/s10546-005-6436-2>
- Kaviany, M., & Kanury, A. M. (2002). Principles of heat transfer. *Appl. Mech. Rev.*, 55(5), B100–B102.
- Kellner, E. (2001). Surface energy fluxes and control of evapotranspiration from a Swedish Sphagnum mire. *Agricultural and Forest Meteorology*, 110(2), 101–123.

- Kim, T., Blois, G., Best, J. L., & Christensen, K. T. (2020). Experimental evidence of amplitude modulation in permeable-wall turbulence. *Journal of Fluid Mechanics*, 887.
- Kimball, B. A., & Lemon, E. R. (1971). Air turbulence effects upon soil gas exchange. *Soil Science Society of America Journal*, 35(1), 16–21.
- Kollet, S. J., & Maxwell, R. M. (2008). Capturing the influence of groundwater dynamics on land surface processes using an integrated, distributed watershed model. *Water Resources Research*, 44(2).
- Kondo, J., Saigusa, N., & Sato, T. (1990). A parameterization of evaporation from bare soil surfaces. *Journal of Applied Meteorology*, 29(5), 385–389.
- Kondo, J., Saigusa, N., & Sato, T. (1992). A model and experimental study of evaporation from bare-soil surfaces. *Journal of Applied Meteorology*, 31(3), 304–312.
- Kool, D., Agam, N., Lazarovitch, N., Heitman, J. L., Sauer, T. J., & Ben-Gal, A. (2014). A review of approaches for evapotranspiration partitioning. *Agricultural and Forest Meteorology*, 184, 56–70.
- Kramm, G., Dlugi, R., & Mölders, N. (2002). Sublayer-Stanton numbers of heat and matter for aerodynamically smooth surfaces: basic considerations and evaluation. *Meteorology and Atmospheric Physics*, 79(3–4), 173–194.
- Kruse, N., Kuhn, S., & von Rohr, P. R. (2006). Wavy wall effects on turbulence production and large-scale modes. *Journal of Turbulence*, (7), N31.
- Kustas, W. P., & Agam, N. (2014). Soil Evaporation. *Encyclopedia of Natural Resources-Land-Volume I*, 444.
- Kuzmin, D., Mierka, O., & Turek, S. (2007). On the implementation of the k-epsilon turbulence model in incompressible flow solvers based on a finite element discretization. *International Journal of Computing Science and Mathematics*, 2/3/4, 193–206.
- Lacasse, D., Turgeon, É., & Pelletier, D. (2004). On the judicious use of the k-ε model, wall functions and adaptivity. *International Journal of Thermal Sciences*, 43(10), 925–938. <https://doi.org/10.1016/j.ijthermalsci.2004.03.004>
- Lācis, U., Sudhakar, Y., Pasche, S., & Bagheri, S. (2020). Transfer of mass and momentum at rough and porous surfaces. *Journal of Fluid Mechanics*, 884.
- Launiainen, J., & Cheng, B. (1998). Modelling of ice thermodynamics in natural water bodies. *Cold Regions Science and Technology*, 27(3), 153–178.
- Lawrence, D. M., Thornton, P. E., Oleson, K. W., & Bonan, G. B. (2007). The partitioning of evapotranspiration into transpiration, soil evaporation, and canopy evaporation in a GCM: Impacts on land-atmosphere interaction. *Journal of Hydrometeorology*, 8(4), 862–880.

- Lehmann, P., Assouline, S., & Or, D. (2008). Characteristic lengths affecting evaporative drying of porous media. *Physical Review E - Statistical, Nonlinear, and Soft Matter Physics*, 77(5), 1–16. <https://doi.org/10.1103/PhysRevE.77.056309>
- Lehrsch, G. A., Whisler, F. D., & Römken, M. J. M. (1987). Soil surface roughness as influenced by selected soil physical properties. *Soil and Tillage Research*, 10(3), 197–212. [https://doi.org/10.1016/0167-1987\(87\)90028-6](https://doi.org/10.1016/0167-1987(87)90028-6)
- Lemon, E. R. (1956). The potentialities for decreasing soil moisture evaporation loss. *Soil Science Society of America Journal*, 20(1), 120–125.
- Levintal, E., Dragila, M. I., Kamai, T., & Weisbrod, N. (2017). Free and forced gas convection in highly permeable, dry porous media. *Agricultural and Forest Meteorology*, 232, 469–478.
- Levintal, E., Dragila, M. I., & Weisbrod, N. (2019). Impact of wind speed and soil permeability on aeration time in the upper vadose zone. *Agricultural and Forest Meteorology*, 269–270(February), 294–304. <https://doi.org/10.1016/j.agrformet.2019.02.009>
- Li, Z., Vanderborght, J., & Smits, K. M. (2019). Evaluation of model concepts to describe water transport in shallow subsurface soil and across the soil–air interface. *Transport in Porous Media*, 128(3), 945–976.
- Likos, W. J., & Lu, N. (2004). Unsaturated soil mechanics. *Ed: John Wiley and Sons Inc., New Jersey*.
- Liu, M., Bárdossy, A., Li, J., & Jiang, Y. (2012). *Physically-based modeling of topographic effects on spatial evapotranspiration and soil moisture patterns through radiation and wind*.
- Liu, S., Lu, L., Mao, D., & Jia, L. (2007). Evaluating parameterizations of aerodynamic resistance to heat transfer using field measurements. *Hydrology and Earth System Sciences Discussions, European Geosciences Union*, 11 (2), 769-783.
- Lozano, A., Cherblanc, F., Cousin, B., & Bénet, J. (2008). Experimental study and modelling of the water phase change kinetics in soils. *European Journal of Soil Science*, 59(5), 939–949.
- Maaß, C., & Schumann, U. (1996). Direct Numerical Simulation of Separated Turbulent Flow over a Wavy Boundary. *In Flow Simulation with High-Performance Computers II*, 227-241. [https://doi.org/10.1007/978-3-322-89849-4\\_17](https://doi.org/10.1007/978-3-322-89849-4_17)
- Mahfouf, J. F., & Noilhan, J. (1991). Comparative study of various formulations of evaporations from bare soil using in situ data. *Journal of Applied Meteorology*, 30(9), 1354–1365.
- Maier, M., Schack-Kirchner, H., Aubinet, M., Goffin, S., Longdoz, B., & Parent, F. (2012). Turbulence Effect on Gas Transport in Three Contrasting Forest Soils. *Soil Science Society of America Journal*, 76(5), 1518–1528. <https://doi.org/10.2136/sssaj2011.0376>

- Manes, C., Pokrajac, D., McEwan, I., & Nikora, V. (2009). Turbulence structure of open channel flows over permeable and impermeable beds: A comparative study. *Physics of Fluids*, *21*(12), 125109. <https://doi.org/10.1063/1.3276292>
- Massman, W. J. (2006). Advective transport of CO<sub>2</sub> in permeable media induced by atmospheric pressure fluctuations: 1. An analytical model. *Journal of Geophysical Research: Biogeosciences*, *111*(G3).
- Massman, W. J., & Frank, J. M. (2006). Advective transport of CO<sub>2</sub> in permeable media induced by atmospheric pressure fluctuations: 2. Observational evidence under snowpacks. *Journal of Geophysical Research: Biogeosciences*, *111*(G3).
- Matthias, A. D., Fimbres, A., Sano, E. E., Post, D. F., Accioly, L., Batchily, A. K., & Ferreira, L. G. (2000). Surface Roughness Effects on Soil Albedo. *Soil Science Society of America Journal*, *64*(3), 1035–1041. <https://doi.org/10.2136/sssaj2000.6431035x>
- McIlroy, I. C. (1984). Terminology and concepts in natural evaporation. In *Developments in Agricultural and Managed Forest Ecology* (Vol. 13, pp. 77–98). Elsevier.
- Merta, M., Seidler, C., & Fjodorowa, T. (2006). Estimation of evaporation components in agricultural crops. *Biologia*, *61*(19), S280–S283.
- Millington, R. J., & Quirk, J. P. (1961). Permeability of porous solids. *Transactions of the Faraday Society*, *57*, 1200–1207.
- Mölder, M., & Kellner, E. (2002). Excess resistance of bog surfaces in central Sweden. *Agricultural and Forest Meteorology*, *112*(1), 23–30.
- Mölder, M., & Lindroth, A. (2001). Dependence of kB<sup>-1</sup> factor on roughness Reynolds number for barley and pasture. *Agricultural and Forest Meteorology*, *106*(2), 147–152.
- Monteith, J. L. (1965). Evaporation and environment. *Symposia of the Society for Experimental Biology*, *19*, 205–234. Cambridge University Press (CUP) Cambridge.
- Moradi, A., Smits, K. M., Massey, J., Cihan, A., & McCartney, J. (2015). Impact of coupled heat transfer and water flow on soil borehole thermal energy storage (SBTES) systems: Experimental and modeling investigation. *Geothermics*, *57*, 56–72.
- Moriwaki, R., & Kanda, M. (2006). Scalar roughness parameters for a suburban area. *Journal of the Meteorological Society of Japan. Ser. II*, *84*(6), 1063–1071.
- Morris, E. M. (1989). Turbulent transfer over snow and ice. *Journal of Hydrology*, *105*(3–4), 205–223.
- Morton, F. I. (1983). Operational estimates of areal evapotranspiration and their significance to the science and practice of hydrology. *Journal of Hydrology*, *66*(1–4), 1–76.

- Mosthaf, K. (2014). *Modeling and Analysis of Coupled Porous-Medium and Free Flow with Application to Evaporation Processes*. University of Stuttgart.
- Mosthaf, K., Baber, K., Flemisch, B., Helmig, R., Leijnse, A., Rybak, I., & Wohlmuth, B. (2011). A coupling concept for two-phase compositional porous-medium and single-phase compositional free flow. *Water Resources Research*, 47(10).  
<https://doi.org/10.1029/2011WR010685>
- Mosthaf, K., Helmig, R., & Or, D. (2014a). Modeling and analysis of evaporation processes from porous media on the REV scale. *Water Resources Research*, 50(2), 1059–1079.  
<https://doi.org/10.1002/2013WR014910>.
- Mwendera, E. J., & Feyen, J. (1997). Tillage and evaporativity effects on the drying characteristics of a silty loam: evaporation prediction models. *Soil and Tillage Research*, 41(1), 127–140.
- Nachshon, U., Dragila, M., & Weisbrod, N. (2012). From atmospheric winds to fracture ventilation: Cause and effect. *Journal of Geophysical Research: Biogeosciences*, 117(G2).
- Nield, D. A., & Bejan, A. (2006). *Convection in porous media* (Vol. 3). Springer.
- Obukhov, A. M. (1946). Turbulentnost' v temperaturnoj-neodnorodnoj atmosfere. *Trudy Inst. Theor. Geofiz. AN SSSR*, 1, 95–115.
- Oldenburg, C. M., & Unger, A. J. A. (2004). Coupled vadose zone and atmospheric surface-layer transport of carbon dioxide from geologic carbon sequestration sites. *Vadose Zone Journal*, 3(3), 848–857.
- Oleson, K. W., Dai, Y., Bonan, B., Bosilovich, M., Dickinson, R., Dirmeyer, P., Hoffman, F., Houser, P., Levis, S., Niu, G. Y. and Thornton, P. (2004). *Technical description of the community land model (CLM)*.
- Oleson, K. W., Lawrence, D. M., Gordon, B., Flanner, M. G., Kluzek, E., Peter, J., Levis, S., Swenson, S. C., Thornton, E., Feddema, J., & Heald, C. L. (2010). *Technical description of version 4.0 of the Community Land Model (CLM)*.
- Or, D., Lehmann, P., Shahraeeni, E., & Shokri, N. (2013). Advances in soil evaporation physics - A review. *Vadose Zone Journal*, 12(4), 1–16.
- Ounis, H., Ahmadi, G., & McLaughlin, J. B. (1991). Brownian diffusion of submicrometer particles in the viscous sublayer. *Journal of Colloid and Interface Science*, 143(1), 266–277.
- Owen, P. R., & Thomson, W. R. (1963). Heat transfer across rough surfaces. *Journal of Fluid Mechanics*, 15(3), 321–334.
- Padro, J. (1987). Boundary-layer pollutant concentrations over complex terrain. *Boundary-Layer Meteorology*, 38(1–2), 17–28.

- Pan, H. L., & Mahrt, L. (1987). Interaction between soil hydrology and boundary-layer development. *Boundary-Layer Meteorology*, 38(1–2), 185–202.
- Park, S. J., Park, S. U., & Ho, C. H. (2010). Roughness length of water vapor over land surfaces and its influence on latent heat flux. *Terr. Atmos.*
- Parlange, M. B., Eichinger, W. E., & Albertson, J. D. (1995). Regional scale evaporation and the atmospheric boundary layer. *Reviews of Geophysics*, 33(1), 99–124.
- Pattenden, R. J., Turnock, S. R., & Zhang, X. (2005). Measurements of the flow over a low-aspect-ratio cylinder mounted on a ground plane. *Experiments in Fluids*, 39(1), 10–21.
- Penman, H. L. (1948). Natural evaporation from open water, bare soil and grass. *Proceedings of the Royal Society of London. Series A. Mathematical and Physical Sciences*, 193(1032), 120–145.
- Perry, A. E., Schofield, W. H., & Joubert, P. N. (1969). Rough wall turbulent boundary layers. *Journal of Fluid Mechanics*, 37(2), 383–413.
- Petri, B. G., Fučík, R., Illangasekare, T. H., Smits, K. M., Christ, J. A., Sakaki, T., & Sauck, C. C. (2015). Effect of NAPL source morphology on mass transfer in the vadose zone. *Groundwater*, 53(5), 685–698.
- Poggi, D., & Katul, G. G. (2007a). The ejection-sweep cycle over bare and forested gentle hills: a laboratory experiment. *Boundary-Layer Meteorology*, 122(3), 493–515.
- Poggi, D., & Katul, G. G. (2007b). Turbulent flows on forested hilly terrain: the recirculation region. *Quarterly Journal of the Royal Meteorological Society: A Journal of the Atmospheric Sciences, Applied Meteorology and Physical Oceanography*, 133(625), 1027–1039.
- Poggi, D., Katul, G. G., Albertson, J. D., & Ridolfi, L. (2007). An experimental investigation of turbulent flows over a hilly surface. *Physics of Fluids*, 19(3), 036601. <https://doi.org/10.1063/1.2565528>
- Pokrajac, D., & Manes, C. (2009). Velocity Measurements of a Free-Surface Turbulent Flow Penetrating a Porous Medium Composed of Uniform-Size Spheres. *Transport in Porous Media*, 78(3), 367. <https://doi.org/10.1007/s11242-009-9339-8>
- Pope, S. B. (2001). Turbulent Flows. *Measurement Science and Technology*, 12(11), 2020–2021. <https://doi.org/10.1088/0957-0233/12/11/705>
- Potter, K. N., Horton, R., & Cruse, R. M. (1987). Soil surface roughness effects on radiation reflectance and soil heat flux. *Soil Science Society of America Journal*, 51(4), 855–860.
- Poulsen, T. (2019). Linking below-surface horizontal pore velocity profiles in porous media with near-surface wind conditions and porous medium gas permeability. *European Journal of Soil Science*.

- Poulsen, T., Furman, A., & Liberzon, D. (2018). Effect of near-surface wind speed and gustiness on horizontal and vertical porous medium gas transport and gas exchange with the atmosphere. *European Journal of Soil Science*, *69*(2), 279–289.  
<https://doi.org/10.1111/ejss.12531>
- Poulsen, T. G., & Møldrup, P. (2006). Evaluating effects of wind-induced pressure fluctuations on soil-atmosphere gas exchange at a landfill using stochastic modelling. *Waste Management and Research*, Vol. 24, pp. 473–481.  
<https://doi.org/10.1177/0734242X06066363>
- Poulsen, T. G., Furman, A., & Liberzon, D. (2017). Effects of Wind Speed and Wind Gustiness on Subsurface Gas Transport. *Vadose Zone Journal*, *16*(11).  
<https://doi.org/10.2136/vzj2017.04.0079>
- Pourbakhtiar, A., Poulsen, T. G., Wilkinson, S., & Bridge, J. W. (2017). Effect of wind turbulence on gas transport in porous media: experimental method and preliminary results. *European Journal of Soil Science*, *68*(1), 48–56.
- Qiao, A., & Zhang, S. (2010). Advanced CFD modeling on vapor dispersion and vapor cloud explosion. *Journal of Loss Prevention in the Process Industries*, *23*(6), 843–848.  
<https://doi.org/10.1016/j.jlp.2010.06.006>
- Qiu, G. Y., Miyamoto, K., Sase, S., Gao, Y., Shi, P., & Yano, T. (2002). Comparison of the three-temperature model and conventional models for estimating transpiration. *Japan Agricultural Research Quarterly: JARQ*, *36*(2), 73–82.
- Qualls, R. J., & Brutsaert, W. (1996). Effect of vegetation density on the parameterization of scalar roughness to estimate spatially distributed sensible heat fluxes. *Water Resources Research*, *32*(3), 645–652.
- Raupach, M. R., & Finnigan, J. J. (1997). The influence of topography on meteorological variables and surface-atmosphere interactions. *Journal of Hydrology*, *190*(3), 182–213.  
[https://doi.org/https://doi.org/10.1016/S0022-1694\(96\)03127-7](https://doi.org/https://doi.org/10.1016/S0022-1694(96)03127-7)
- Redeker, K. R., Baird, A. J., & Teh, Y. A. (2015). Quantifying wind and pressure effects on trace gas fluxes across the soil-atmosphere interface. *Biogeosciences*, *12*(24), 7423–7434.
- Riley, W. J., Robinson, A. L., Gadgil, A. J., & Nazaroff, W. W. (1999). Effects of variable wind speed and direction on radon transport from soil into buildings: model development and exploratory results. *Atmospheric Environment*, *33*(14), 2157–2168.
- Rodny, M., Nolz, R., Novák, V., Hlavacikova, H., Loiskandl, W., & Himmelbauer, M. (2016). Modified method of aerodynamic resistance calculation and its application to potential evapotranspiration estimation. *International Agrophysics*, *30*(2).
- Rominger, J. T., & Nepf, H. M. (2011). Flow adjustment and interior flow associated with a rectangular porous obstruction. *Journal of Fluid Mechanics*, *680*, 636–659.  
<https://doi.org/DOI: 10.1017/jfm.2011.199>

- Romkens, M. J., & Wang, J. Y. (1986). Effect of tillage on surface roughness. *Transactions of the ASAE*, 29(2), 429–433.
- Ross, A. N. (2008). Large-eddy simulations of flow over forested ridges. *Boundary-Layer Meteorology*, 128(1), 59–76. <https://doi.org/10.1007/s10546-008-9278-x>
- Sakaguchi, K., & Zeng, X. (2009). Effects of soil wetness, plant litter, and under-canopy atmospheric stability on ground evaporation in the Community Land Model (CLM3. 5). *Journal of Geophysical Research: Atmospheres*, 114(D1).
- Sakai, M., Jones, S. B., & Tuller, M. (2011). Numerical evaluation of subsurface soil water evaporation derived from sensible heat balance. *Water Resources Research*, 47(2).
- Sakaki, T., & Illangasekare, T. H. (2007). Comparison of height-averaged and point-measured capillary pressure-saturation relations for sands using a modified Tempe cell. *Water Resources Research*, 43(12), 1–6. <https://doi.org/10.1029/2006WR005814>
- Sakaki, T., Limsuwat, A., Smits, K. M., & Illangasekare, T. H. (2008). Empirical two-point  $\alpha$ -mixing model for calibrating the ECH2O EC-5 soil moisture sensor in sands. *Water Resources Research*, 44(4).
- Sakaki, T., & Smits, K. M. (2015). Water retention characteristics and pore structure of binary mixtures. *Vadose Zone Journal*, 14(2).
- Schlichting, H., & Gersten, K. (2016). Boundary-layer theory. In *Springer*.
- Schlichting, H., Gersten, K., Krause, E., Oertel, H. J., & Mayes, C. (2000). Boundary Layer Theory Springer. *Eighth Revised and Enlarged Edition*.
- Schlichting, H., & Gersten, K. (2017). Onset of turbulence (stability theory). In *Boundary-Layer Theory* (pp. 415–496). Springer.
- Seager, R., Ting, M., Held, I., Kushnir, Y., Lu, J., Vecchi, G., Huang, H. P., Harnik, N., Leetmaa, A., Lau, N. C. and Li, C. (2007). Model projections of an imminent transition to a more arid climate in southwestern North America. *Science*, 316(5828), 1181–1184.
- Sellers, P. J., Heiser, M. D., & Hall, F. G. (1992). Relations between surface conductance and spectral vegetation indices at intermediate (100 m<sup>2</sup> to 15 km<sup>2</sup>) length scales. *Journal of Geophysical Research: Atmospheres*, 97(D17), 19033–19059.
- Shahraeeni, E., Lehmann, P., & Or, D. (2012). Coupling of evaporative fluxes from drying porous surfaces with air boundary layer: Characteristics of evaporation from discrete pores. *Water Resources Research*, 48(9).
- Shao, W., Coenders-Gerrits, M., Judge, J., Zeng, Y., & Su, Y. (2018). The impact of non-isothermal soil moisture transport on evaporation fluxes in a maize cropland. *Journal of Hydrology*, 561, 833–847.

- Shavit, U. (2009). Special Issue on “Transport Phenomena at the Interface Between Fluid and Porous Domains.” *Transport in Porous Media*, 78(3), 327–330.  
<https://doi.org/http://dx.doi.org/10.1007/s11242-009-9414-1>
- Sherry, M., Lo Jacono, D., & Sheridan, J. (2010). An experimental investigation of the recirculation zone formed downstream of a forward facing step. *Journal of Wind Engineering and Industrial Aerodynamics*, 98(12), 888–894.  
<https://doi.org/10.1016/j.jweia.2010.09.003>
- Shokri, N., & Or, D. (2011). What determines drying rates at the onset of diffusion controlled stage-2 evaporation from porous media? *Water Resources Research*, 47(9), 1–8.  
<https://doi.org/10.1029/2010WR010284>
- Shokri, N. (2014). Pore-scale dynamics of salt transport and distribution in drying porous media. *Physics of Fluids*, 26(1), 12106.
- Shu, F. (1982). Moisture and heat transport in a soil layer forced by atmospheric conditions. *M. Sc. Thesis, Univ. of Connecticut*.
- Shuttleworth, W. J. (1993). *Evaporation In: Maidment, DR Handbook of hydrology*. McGraw-Hill New York.
- Shuttleworth, W. J. (2007). Putting the " vap" into evaporation. *Hydrology and Earth System Sciences Discussions, European Geosciences Union*, 11 (1), 210-244.
- Silva, R. A., & De Lemos, M. J. S. (2003). Laminar flow around a sinusoidal interface between a porous medium and a clear fluid. *In Proceedings of COBEM2003-17th International Congress of Mechanical Engineering*, 1528. <https://doi.org/10.1115/IMECE2003-41452>
- Simpson, R. L. (1996). Aspects of turbulent boundary-layer separation. *Progress in Aerospace Sciences*, 32(5), 457–521.
- Sivykh, G. F. (2000). Turbulent transfer coefficients model for flows over permeable rough surfaces. *Journal of Enhanced Heat Transfer*, 7(1).
- Smits, K. M., Cihan, A., Sakaki, T., & Illangasekare, T. H. (2011). Evaporation from soils under thermal boundary conditions: Experimental and modeling investigation to compare equilibrium-and nonequilibrium-based approaches. *Water Resources Research*, 47(5).
- Souto, E. B., & Müller, R. H. (2008). Cosmetic features and applications of lipid nanoparticles (SLN®, NLC®). *International Journal of Cosmetic Science*, 30(3), 157–165.  
<https://doi.org/10.1111/j.1468-2494.2008.00433.x>
- Stewart, J. B., Kustas, W. P., Humes, K. S., Nichols, W. D., Moran, M. S., & de Bruin, H. A. R. (1994). Sensible heat flux-radiometric surface temperature relationship for eight semiarid areas. *Journal of Applied Meteorology*, 33(9), 1110–1117.

- Su, Z., Schmugge, T., Kustas, W. P., & Massman, W. J. (2001). An evaluation of two models for estimation of the roughness height for heat transfer between the land surface and the atmosphere. *Journal of Applied Meteorology*, 40(11), 1933–1951.
- Sugita, F., & Kishii, T. (2002). Effect of roughness distribution on evaporation processes over non-homogeneous sand surfaces: A wind tunnel investigation. *Hydrological Processes*, 16(11), 2141–2153. <https://doi.org/10.1002/hyp.1147>
- Sumner, D. M., & Jacobs, J. M. (2005). Utility of Penman–Monteith, Priestley–Taylor, reference evapotranspiration, and pan evaporation methods to estimate pasture evapotranspiration. *Journal of Hydrology*, 308(1–4), 81–104.
- Sun, J. (1999). Diurnal variations of thermal roughness height over a grassland. *Boundary-Layer Meteorology*, 92(3), 407–427.
- Sundmacher, K., & Scott, K. (1999). Direct methanol polymer electrolyte fuel cell: analysis of charge and mass transfer in the vapour–liquid–solid system. *Chemical Engineering Science*, 54(13–14), 2927–2936.
- Swenson, S. C., & Lawrence, D. M. (2014). Assessing a dry surface layer-based soil resistance parameterization for the Community Land Model using GRACE and FLUXNET-MTE data. *Journal of Geophysical Research: Atmospheres*, 119(17), 10–299.
- Takle, E. S., Massman, W. J., Brandle, J. R., Schmidt, R. A., Zhou, X., Litvina, I. V., Garcia, R., Doyle, G. and Rice, C. W. (2004). Influence of high-frequency ambient pressure pumping on carbon dioxide efflux from soil. *Agricultural and Forest Meteorology*, 124(3–4), 193–206.
- Tampieri, F. (1987). Separation features of boundary-layer flow over valleys. *Boundary-Layer Meteorology*, 40(3), 295–307.
- Tang, J. Y., & Riley, W. J. (2013). A new top boundary condition for modeling surface diffusive exchange of a generic volatile tracer: theoretical analysis and application to soil evaporation. *Hydrology & Earth System Sciences*, 17(2).
- Taylor, P. A., & Gent, P. R. (1974). A model of atmospheric boundary-layer flow above an isolated two-dimensional ‘hill’; an example of flow above ‘gentle topography.’ *Boundary-Layer Meteorology*, 7(3), 349–362.
- Teng, J., Yasufuku, N., Liu, Q., & Liu, S. (2014). Experimental evaluation and parameterization of evaporation from soil surface. *Natural Hazards*, 73(3), 1405–1418.
- Tezduyar, T. E., Sathe, S., Schwaab, M., & Conklin, B. S. (2008). Arterial fluid mechanics modeling with the stabilized space–time fluid–structure interaction technique. *International Journal for Numerical Methods in Fluids*, 57(5), 601–629.

- Tillman, F. D., & Weaver, J. W. (2005). *Review of recent research on vapor intrusion*. Washington, DC 20460: US Environmental Protection Agency, Office of Research and Development.
- Trautz, A. C. (2015). *Heat and mass transfer in porous media under the influence of near-surface boundary layer atmospheric flow*. Colorado School of Mines.
- Unger, P. W., & Cassel, D. (1991). Tillage implement disturbance effects on soil properties related to soil and water conservation: a literature review. *Soil and Tillage Research*, 19(4), 363–382.
- Van Bavel, C. H. M. (1966). Potential evaporation: the combination concept and its experimental verification. *Water Resources Research*, 2(3), 455–467.
- van de Griend, A. A., & Owe, M. (1994). Bare soil surface resistance to evaporation by vapor diffusion under semiarid conditions. *Water Resources Research*, 30(2), 181–188.
- Van Genuchten, M. T. (1980). A closed-form equation for predicting the hydraulic conductivity of unsaturated soils. *Soil Science Society of America Journal*, 44(5), 892–898.
- van Heerwaarden, C. C. (2011). *Surface evaporation and water vapor transport in the convective boundary layer*.
- Vanderborght, J., Fetzer, T., Mosthaf, K., Smits, K. M., & Helmig, R. (2017). Heat and water transport in soils and across the soil-atmosphere interface: 1. Theory and different model concepts. *Water Resources Research*, 53(2), 1057–1079.
- Ventura, F., Spano, D., Duce, P., & Snyder, R. L. (1999). An evaluation of common evapotranspiration equations. *Irrigation Science*, 18(4), 163–170.
- Verhoef, A., De Bruin, H. A. R., & Van Den Hurk, B. (1997). Some practical notes on the parameter  $k_B^{-1}$  for sparse vegetation. *Journal of Applied Meteorology*, 36(5), 560–572.
- Verma, S. B., & Barfield, B. J. (1979). Aerial and crop resistances affecting energy transport. *Modification of the Aerial Environment of Crops*, 230–248.
- Verma, S. B., & Cermak, J. E. (1974a). Mass transfer from aerodynamically rough surfaces. *International Journal of Heat and Mass Transfer*, 17(5), 567–579.
- Verma, S. B., & Cermak, J. E. (1974b). Wind-Tunnel Investigation of Mass Transfer from Soil Corrugations.pdf. *Journal of Applied Meteorology*, 13(5), 578–587.
- Vickers, D., & Mahrt, L. (2006). Evaluation of the air-sea bulk formula and sea-surface temperature variability from observations. *Journal of Geophysical Research: Oceans*, 111(C5).

- Villagarcía, L., Were, A., Domingo, F., García, M., & Alados-Arboledas, L. (2007). Estimation of soil boundary-layer resistance in sparse semiarid stands for evapotranspiration modelling. *Journal of Hydrology*, 342(1–2), 173–183. <https://doi.org/10.1016/j.jhydrol.2007.05.023>
- Wagner, C., Kenjereš, S., & von Rohr, P. R. (2011). Dynamic large eddy simulations of momentum and wall heat transfer in forced convection over wavy surfaces. *Journal of Turbulence*, (12), N7.
- Wallace, J. S. (1995). Calculating evaporation: resistance to factors. *Agricultural and Forest Meteorology*, 73(3–4), 353–366.
- Wallen, B. M., Smits, K. M., Sakaki, T., Howington, S. E., & Deepagoda T.K.K., C. (2016). Thermal Conductivity of Binary Sand Mixtures Evaluated through Full Water Content Range. *Soil Science Society of America Journal*, 80(3), 592–603. <https://doi.org/10.2136/sssaj2015.11.0408>
- Weaver, J. W., & Tillman, F. D. (2005). *Uncertainty and the Johnson-Ettinger model for vapor intrusion calculations*. US Environmental Protection Agency, Office of Research and Development.
- Whitaker, S. (1977). Simultaneous heat, mass, and momentum transfer in porous media: a theory of drying. In *Advances in heat transfer* (Vol. 13, pp. 119–203). Elsevier.
- White, F. M., & Corfield, I. (2006). The Stability of Laminar Flows. In *Viscous fluid flow* (Vol. 3, pp. 335–392). McGraw-Hill New York.
- Wilcox, B. P., Seyfried, M. S., Breshears, D. D., Stewart, B., & Howell, T. (2003). The water balance on rangelands. *Encyclopedia of Water Science*, 791, 4.
- Xu, X., & Yi, C. (2013). The influence of geometry on recirculation and CO<sub>2</sub> transport over forested hills. *Meteorology and Atmospheric Physics*, 119(3), 187–196. <https://doi.org/10.1007/s00703-012-0224-6>
- Yamanaka, T., Takeda, A., & Sugita, F. (1997). A modified surface-resistance approach for representing bare-soil evaporation: Wind tunnel experiments under various atmospheric conditions. *Water Resources Research*, 33(9), 2117–2128.
- Yang, K., Koike, T., Ishikawa, H., Kim, J., Li, X., Liu, H., Liu, S., Ma, Y., & Wang, J. (2008). Turbulent flux transfer over bare-soil surfaces: characteristics and parameterization. *Journal of Applied Meteorology and Climatology*, 47(1), 276–290.
- Yates, S. R. (2006). Simulating herbicide volatilization from bare soil affected by atmospheric conditions and limited solubility in water. *Environmental Science & Technology*, 40(22), 6963–6968.
- Yuan, J., Rokni, M., & Sundén, B. (2001). Simulation of fully developed laminar heat and mass transfer in fuel cell ducts with different cross-sections. *International Journal of Heat and Mass Transfer*, 44(21), 4047–4058.

- Zhang, C., Werth, C. J., & Webb, A. G. (2008). Investigation of surfactant-enhanced mass removal and flux reduction in 3D correlated permeability fields using magnetic resonance imaging. *Journal of Contaminant Hydrology*, *100*(3–4), 116–126.
- Zilker, D. P., & Hanratty, T. J. (1979). Influence of the amplitude of a solid wavy wall on a turbulent flow. Part 2. Separated flows. *Journal of Fluid Mechanics*, *90*(2), 257–271. <https://doi.org/DOI: 10.1017/S0022112079002196>
- Zobeck, T. M., & Onstad, C. A. (1987). Tillage and rainfall effects on random roughness: A review. *Soil and Tillage Research*, *9*(1), 1–20. [https://doi.org/https://doi.org/10.1016/0167-1987\(87\)90047-X](https://doi.org/https://doi.org/10.1016/0167-1987(87)90047-X)